Willig, Matthias (2013) Contributions to the commutation analysis of uncompensated single phase universal motors. PhD thesis

http://theses.gla.ac.uk/4262/

Contributions to the Commutation Analysis of uncompensated Single Phase Universal Motors

Matthias Willig
Dipl.-Ing.

Submitted to the
School of Engineering,
University of Glasgow,
in fulfilment of the requirements for the
Degree of Doctor of Philosophy.

Glasgow, April 2013

Abstract

In this thesis various aspects of the electromagnetic effects influencing the commutation of uncompensated single phase universal motors are investigated. An introduction to the subject as well as a review of significant literature on the subject are given. The literature review includes classical text books about commutator motors as well as more recent publications about the mathematical analysis of the commutation of universal motors.

Subsequently, the analysis of the most important inductances of the machine is outlined that comprises the analytical and numerical calculation as well as the measurement of the machine inductances using different measurement techniques.

Moreover, a brush model for commutation analysis of small commutator motors is presented. Equivalent circuits of the brush are established for the cases of one coil shorted and two coils shorted by one brush, and a strategy to obtain their elements is proposed. This uses a dedicated finite difference program to calculate the effective brush resistance between all pairs of terminals. The treatment of the boundary conditions is critical in this process. The resulting terminal resistances are regarded as combinations of a set of internal resistances and this nonlinear relationship is inverted to obtain the internal resistors using a modified Newton-Raphson method. Results are presented showing the influence of anisotropy and geometry, and a simplified example of commutation analysis using the model established is given.

In the next step the arcing phenomenon in analysed mathematically. Equations are given for the pre-arcing phase, the arcing phase and the post-arc oscillation. Equivalent circuits for the different phases are proposed and the equations are derived strictly from a circuit point of view. In the analysis a constant arc voltage (confirmed by experimental data and literature on the subject) and a minimum uncommutated residual current necessary for arc ignition are assumed. Those quantities are adopted from reviewed literature and used in the calculations.

The design of a motor test bench is described that allows to measure the motor performance according to the principle of the reaction dynamometer. The load machine is mounted on air bearings to minimize possible torque errors in the measurements. A measured torque speed characteristic of a universal motor is shown as well as the torque as a function of the motor current. These measurements were carried out at reduced motor voltage to keep the shaft speed within reasonable limits.

Furthermore, theoretical and experimental investigations are carried out in order to estimate

how strongly certain rotor coils undergoing rapid current changes affect each other due to mutual coupling and how the mutual coupling changes in the presence of a damping field winding. Several FEA simulations are performed in order to get an insight into the flux pattern if rotor coils are acting on each other and the field winding is allowed to impose its damping effect on the rotor coils. Simple AC measurements are performed as well as di/dt - tests using a more complex oscillating circuit for measurements of the change of the di/dt of a rotor coil with and without the presence of an active field winding. Additionally, investigations are carried out in order to analyse the influence of power cord and source impedances on the ability of the field winding of an uncompensated universal motor to damp flux variations caused by the commutation process. The motor is regarded as a harmonic generator with the power cord and the source impedance acting as a load. Rotational tests are carried out with different loads connected to the field winding and the Fourier spectrums of the field voltage are evaluated.

In the final stage a simulation model is described that uses deductions from the previous chapters and that simulates the electromagnetic behaviour of the machine including the complex problem of brush commutation. Measured and calculated signals suitable for validation of the model were compared in order to evaluate the accuracy of the model with regard to motor performance and commutation analysis.

Contents

List of Tables

List of Figures

xiv

List of Symbols

A	vector potential, area, integration constant
a	number of parallel armature paths
B	magnetic flux density, integration constant
b	stator geometry quantity
C	conductors per radian, capacitance, integration constant
c	number of conductors
D	distance, integration constant
d	diameter
E	induced voltage, electric field strength
e	instantaneous induced Voltage, Euler's Number, relative error
f	general function, frequency
G	conductance
g	general function
h	slot height, brush height, general function
I	current
i	instantaneous current
J	current density
K	linear current sheet, integration constant
k	coefficient, degree of anisotropy
L	inductance
l	length
M	mutual inductance
m	constant, $\{1,2,3,\dots\}$
N	number of turns
n	shaft speed
P	power
p	number of pole pairs
q	tangent of phase shift angle
R	ohmic resistance, magnetic reluctance
r	radius
s	width of slot opening

T	commutation time, torque, coil throw, rotor tooth head, periodic time
t	time, width of rotor tooth tip
U	arc voltage
V	voltage, volume
v	instantaneous voltage
W	energy
w	rotor slot width
X	general function of x
x	Cartesian coordinate
Y	length of interpolar gap, general function of y
y	Cartesian coordinate
Z	total number of armature conductors, impedance
α	pole arc, constant in (0,1)
β	brush shift, brush width, damping coefficient
Γ	high resistance used in simulation
γ	angle between q- and brush axis, rotor position, ratio of angular functions, damping capability
Δ	difference
δ	air gap length
ε	tolerated approximation error
ζ	factor accounting for short pitching, brush to segment width ratio, phase shift angle
η	axial brush length
Θ	MMF
θ	rotor position
κ	electric conductivity
Λ	logarithmic decrement
λ	permeance coefficient, damping term
μ	permeability, width of mica
σ	coil span, commutator segment width
τ	pitch, duration
Φ	magnetic flux
φ	instantaneous magnetic flux, scalar potential, phase shift angle
Ψ	flux linkage

ψ	instantaneous flux linkage
ω	angular velocity, radian frequency
[A]	coefficient matrix
[D]	diagonal matrix
[G]	conductance matrix
[H]	coefficient matrix
[J]	Jacobian matrix
[L]	inductance matrix
[Q]	general matrix
[TD]	tridiagonal matrix
$\vec{A}$	vector of vector potentials
$\vec{b}$	solution vector
$\vec{c}$	solution vector
$d\vec{S}$	differential surface vector
$\vec{E}$	vector of electrical field strength
$\vec{i}$	vector of instantaneous currents
$\vec{J}$	vector of current density
$\vec{R}$	vector of resistances
$\vec{u}$	vector of resistive and rotational voltages
$\vec{v}$	vector of coil voltages
$\vec{x}$	vector of unknown scalar potentials
$\vec{f}$	vector function
$\vec{\xi}$	vector function

Subscripts:

a	armature, flux path a
a,b,c,u,v,w,x,y,z	internal resistances
arc	electric arc
B	internal brush circuit
b, br	brush, flux path b, armature branch
bn	negative brush
bp	positive brush
C	comparison of analytical and numerical calculation
c	commutating coil, capacitive, Carter, conductor, single rotor coil,

	power cord
cf	contact and film
CT	comparison of numerical calculations and measurements
d	d-axis, rotating
e	end windings
em	electromagnetic
ext	external
F	field winding
fa, FA	series connection field and armature
Fc	field coil
FD	Finite Difference
gm	geometric mean
h	main
i	subvector, discrete element
ij	submatrix
int	internal
k	index for mutual inductances
L	inductor
m	mean, magnetic, motor
max	maximum
min	minimum
n	general matrix and vector element index, {1, 2, 3, ….}, slotting
p	pole, parasitic, power source, main winding
p,q	active brush terminals
pq	q-axis component associated with the field poles
q	q-axis
qu	q-axis component associated with turns under pole shoe
qq	q-axis component associated with the interpolar space
r, rd	resistive
s	slot, slot base, supply
sb	brush braid and body
sp	slot pitches
stk	lamination stack
t	tooth

thr	threshold
x	index for mutual inductances, x-direction
y	y-direction
ym	maximum in the interpolar space
α	electric arc, index for integration constant
δ	air gap
δ*Y*	air- and interpolar gap component
ν	commutating coil
σ	leakage, separation
ω	rotational
0	vacuum, source, unknown
0s, 2s, 3s	resistances of delta-star transformation

Acknowledgement

Finally, I want to thank my family for their unconditional support throughout my career and my entire life. Without their encouragement, understanding and motivation I would not have been able to achieve all I have.

Author's Declaration

This thesis is a record of the my own work carried out under the supervision of Emeritus Professor T.J.E.Miller and Mr Calum Cossar in the School of Engineering at the University of Glasgow, United Kingdom, during the period of July 2009 to December 2012.
Clear reference is provided at each stage where I used any work or information from others.

The copyright of this thesis belongs to the author. Acknowledgement must always be made of the use of any material derived from this thesis.

Matthias Willig

This page is intentionally left blank.

1   Introduction

1.1   Background

The field of research this work is carried out in is the analysis of commutation of mechanically commutated machines. The uncompensated single phase commutator motor is examined to acquire a deeper understanding of the commutation process and to draw conclusions that serve as a basis for the implementation of a simulation model of the electromagnetic behaviour of the machine including the commutation.

Even though it has competition such as electronically commutated motors and switched reluctance motors the universal motor is still a competitive drive of home appliances like power tools, washing machines, vacuum cleaners etc. Its high power density also makes it, despite its comparatively low efficiency, the preferred drive of professional mains operated power tools designed to highest standards concerning lifetime, power / weight ratio and reliability.

Much has been written about the design and the calculation of these motors already but as the design optimisation process goes on leading manufactures are not satisfied with the mathematical tools and classical theoretical approaches available anymore. Increasingly the use of transient solvers coupling Finite Element simulations and differential circuit equations is desired. The goal of the layout optimization of universal machines is basically an improved commutation. Currently many manufacturers base the estimation of the quality of the commutation on indicators, which are not fully based on theoretical insights but experience. The main disadvantages of these indicators are that they do not refer to brush material, brush size or related parameters and often neglect the fact that small motors are driven to a high saturation level during operation. Therefore, numerous measurements are necessary to evaluate the commutation quality in universal machines.

The quality of the commutation of a new layout is estimated through the achieved lifetime of the carbon brushes over repeated cycles of endurance tests at no-load and overload conditions in comparison with the standard design. However, due to the high dispersion of the measurements the evaluation is very time consuming, and it could lead the design engineer to

sub-optimal decisions. There are numerous factors affecting the quality of the commutation that can be of either mechanical, thermal, chemical or electrical nature. The main focus of this research work is on the modelling of the electromagnetic system of the machine with focus on the commutation process.

It is expected that a successful mathematical model of the commutation of the universal machine can be established if mathematical approaches for the most critical aspects of brush commutation can be identified, that model the physics of the machine with satisfactory precision and that ideally can be tested separately before putting them together in an overall simulation model of the commutation of the universal machine. Those critical aspects have to be identified during the research, particularly in the literature review, as there have been significant research activities on the subject in the past.

The discussion, however, confines itself to motors excited purely sinusoidally.

1.2   Classification of the Universal Motor

1.2.1   Classification of the universal motor in the area of rotating electrical machines

In Fig. 1.1 classical types of rotating electrical machines are classified according to excitation and power range and examples of typical applications of the respective machine type are given [1]. In this classification the single phase universal motor appears in the lower power range (logarithmic power - axis) where it still remains the preferred drive for applications such as power tools and home appliances.
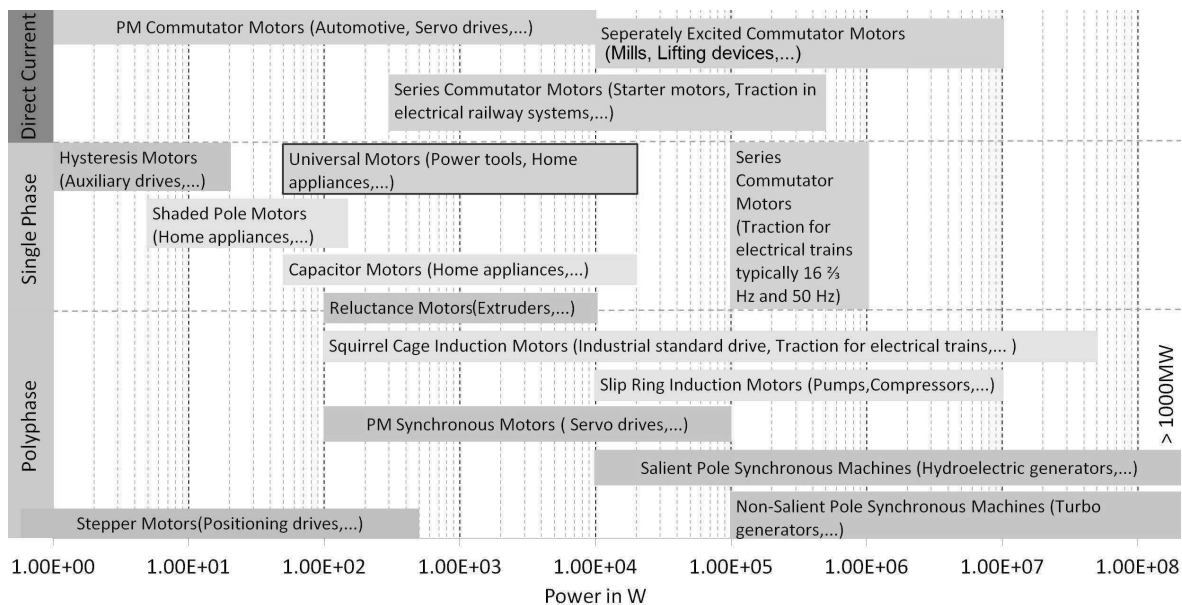
Fig. 1.1 Classification of rotating electrical machines

1.2.2   Application - oriented classification of the universal motor

Fig. 1.2 shows, roughly outlined, the range of rated speed and electrical power of single phase universal motors supplied by a 230V/50Hz grid. Moreover, the applications of the machine are indicated and their electrical power and speed range [2]. One can see that angle grinders are located at the high end of the power range. These power tools not only have a high rated power, the high shaft speed of the motor also ensures a relatively high shaft power.
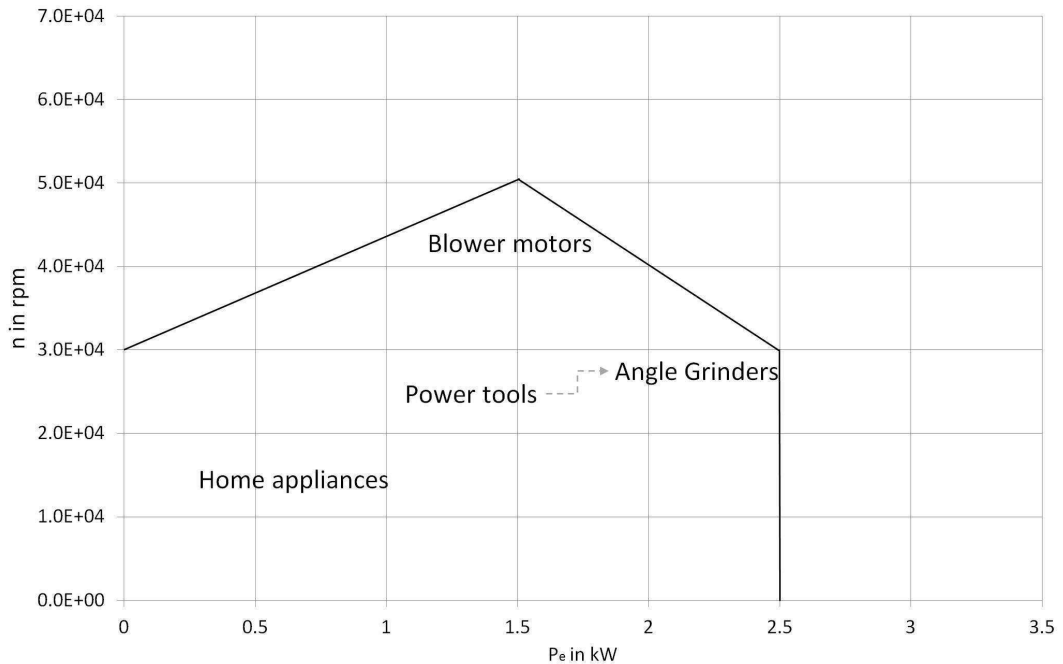
Fig. 1.2 Classification of Universal Motors according to their performance

1.3   Brief Outline of the Problem of Commutation

As stated above, this work is concerned with the electromagnetic aspects of the commutation of the universal motor. In general, the function of the brush - commutator contact is to ensure current reversal in the armature coils in order to achieve the correct direction of torque produced by the interaction of the field winding and the armature conductors, *i.e.* the direction of current in a coil whose terminals (commutator segments) arrive at the brush is reversed after the coil terminals leave the brush. During the current reversal the current progression is in general not ideally linear but under - commutated (delayed - or retarded commutation) or over-commutated (accelerated commutation) . The process of current reversal is shown in Fig. 1.3 for a motor where the stator has two salient poles and the armature has a lap winding.

The problems arising with sub-optimal commutation and the parameters influencing the reversing current are discussed in chapter 2.
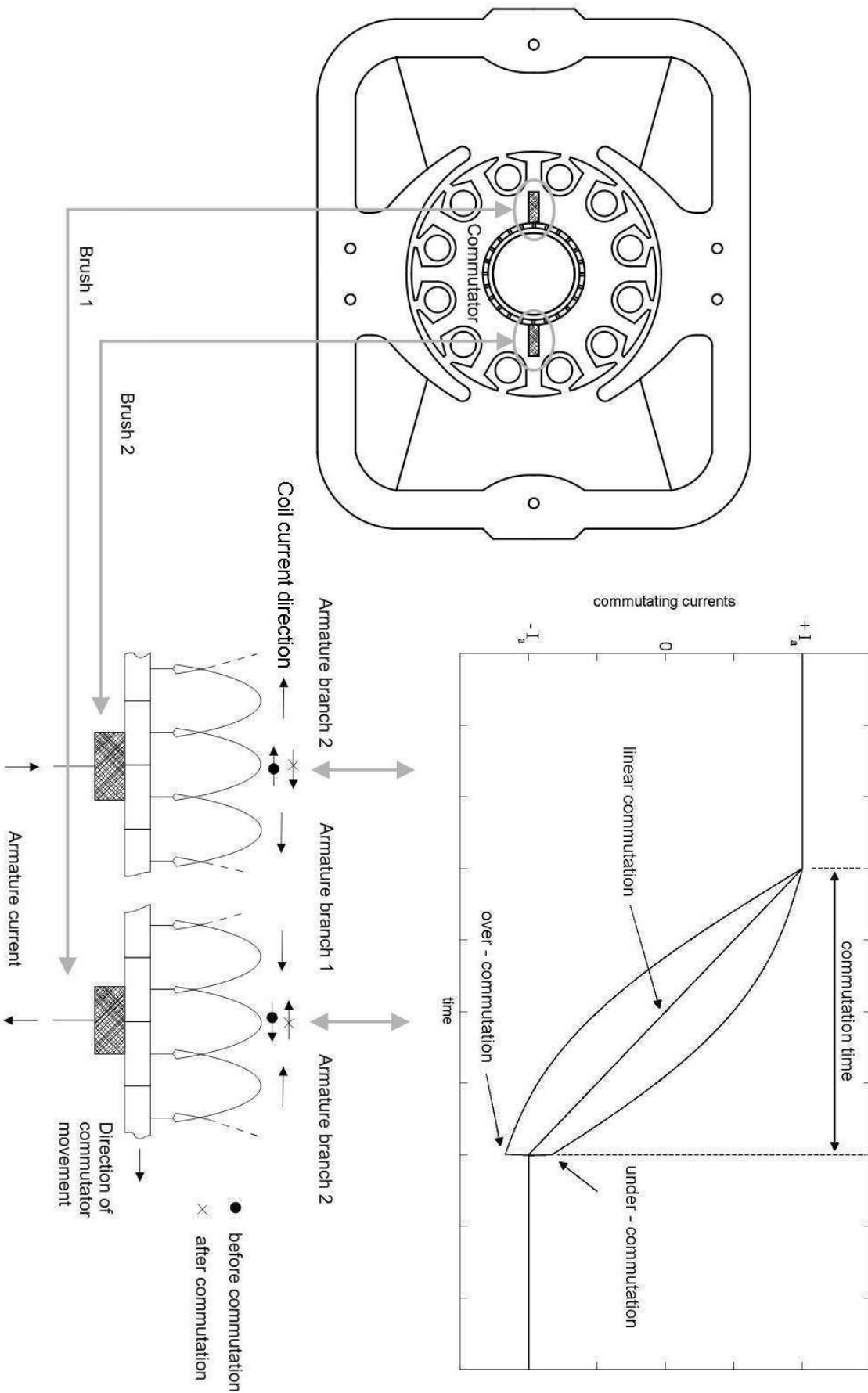
Fig. 1.3 Process of commutation

1.4 Thesis Structure

Chapter 02 is a review of significant books about commutator motors and published articles about the commutation analysis of universal motors.

A commutating circuit is shown and the importance of its elements in the mathematical analysis is pointed out. Classical analytical methods are described as well as semi-numerical approaches to commutation analysis. Moreover, some equations established by other authors are given in order to give some examples of the calculation of the voltages induced in the commutating coils.

Chapter 03 presents the analytical and numerical calculation of the most important self - and mutual inductances of the universal motor. Furthermore, inductance measurement techniques for electrical machines are described where the advantages of DC bridge methods over the simple AC method are demonstrated. Analytically and numerically calculated inductances are compared to measured inductances at a certain rotor position, and numerically calculated and measured inductances are compared over a range of rotor positions.

Chapter 04 describes the development of a model of the resistance of the carbon brush that can be included in the mathematical analysis of commutation. Equivalent circuits of the brush are established for the cases of one coil shorted and two coils shorted by one brush, and a strategy to obtain their elements is proposed. This uses a dedicated finite-difference program to calculate the effective brush resistance between all pairs of terminals. The treatment of the boundary conditions is critical in this process. The resulting terminal resistances are regarded as combinations of a set of internal resistances and this nonlinear relationship is inverted to obtain the internal resistors using a modified Newton-Raphson method. Results are presented showing the influence of anisotropy and geometry, and a simplified example of commutation analysis using the model established is given.

Chapter 05 presents a circuit theory approach to arc modelling in a commutator motor. A literature review on that particular part of the commutation problem is given and the different phases during the arcing are analysed analytically. Equations for arc duration and arc energy are established under the assumption that the arc voltage is constant during arcing.

Subsequently a brief experimental study is carried out in order to verify the assumption of a constant arc voltage in the calculations.

Chapter 06 describes the design of a motor test rig that allows motor performance measurements according to the reaction dynamometer principle. The load machine is mounted on air bearings to minimize torque errors in the measurements and the speed is measured using a built in speed sensor comprising a ferrite ring and a hall sensor. The noisy voltage signal of that sensor is transformed into a series of voltage pulses and evaluated by a flexible electronic controller (FCIV[1]) in order to find the motor speed.
Measured torque - speed and torque - current characteristics are shown that were measured at a reduced motor voltage.

Chapter 07 outlines theoretical and experimental work carried out in order to get a better insight into the interaction of the coils undergoing commutation with and without the presence of a damping field winding that also saturates the magnetic circuit. FEA calculated flux plots are shown that demonstrate the effect of a damping current on the inductance of a rotor coil, the effects of aiding and opposing, and short pitched and full pitched rotor coils on each other. Moreover, an oscillating circuit is used to measure rotor coil inductances at rapid current change with and without field damping effects and the same circuit is used to examine the change of the rate of change of current with time in a rotor coil if another rotor coil experiences a rapid current change. Rotational tests were carried out as well, where the machine was driven by another motor and armature and field circuit were kept separate. A DC current was fed through the armature circuit and the FFT spectrum of the field voltage was evaluated for different circuits connected to the field winding.

Chapter 08 presents a simulation model of the machine including commutation analysis based on the brush model and the arc model established in the previous chapters. As a further deduction the line current is not kept constant during a commutation event in order to allow for damping currents in the field winding. Therefore, the model is voltage-driven and uses precalculated (FEA) inductances in the system of voltage equations and solves the system using Euler's method. Motor current, commutating current and the field voltage are calculated

---

[1]Flexible electronic motor controller developed in the SPEED Laboratory, University
   of Glasgow under direction of Calum Cossar

and comparisons with experimental data are shown.

Chapter 09 gives a brief summary of the previous chapters and recollects the general conclusions from the various aspects of the research carried out in this thesis.

1.5 Original Contributions

The contributions of this thesis believed to be original are summarised in the following points:

■   A complete analysis of the most important inductances of the machine calculated analytically, numerically (FEA) and measured by a simple AC method and Jones' bridge technique (Chapter 3).

■   Equivalent circuits of the carbon brush where the brush body resistances are calculated using the Finite Difference Method where Cholesky factorisation is applied to obtain direct non-iterative solutions (Chapter 4).

■   An algorithm to obtain the elements of the equivalent circuits of the carbon brush by calculating a set of "terminal" resistances one by one and subsequently inverting the relationship between the "terminal" and "internal" resistances using a modified Newton - Raphson method in order to find the "internal" resistances (Chapter 4).

■   An analysis of the influence of brush height and anisotropy on the elements of the equivalent circuits of the carbon brush (Chapter 4).

■   A method to estimate the contact and constriction resistance of the brush to bar contact experimentally by mounting a blank commutator with pairs of inter-connected opposite bars on the shaft of another motor and calculating the resistance from the measured instantaneous voltages and currents (Chapter 4).

■   A set of equations for arc current, duration and energy based purely on circuit theory and which is different from the equations established by other authors (Chapter 5).

■   Flux plots showing the difference of the flux distributions of a non-damped rotor coil and an ideally damped rotor coil where the damping current in the field winding forces the flux into leakage paths and changes the rotor coil inductance from an air gap inductance to a leakage inductance (Chapter 7).

■   An oscillating circuit where capacitors are discharged through certain motor coils (using MOSFETS controlled via FCIV) at different times in order to observe the

change in the *di/dt* of those coils before and after additional coils are switched (Chapter 7).

■   An experimental analysis of the influence of an active field winding on the intensity of the interaction of rotor coils (Chapter 7).

■   An experimental analysis of the influence of additional elements such as power cord parameter (resistance, inductance, capacitance and leakage conductance) in the field circuit on the damping capability of the field winding (Chapter 7).

■   A voltage-driven simulation model that uses the proposed brush model and derives the simulation equations from the most general case introducing simplifications based on findings from the previous chapters and symmetry assumptions (Chapter 8).

2 Literature Review

2.1 The Commutating Circuits

As stated in the introduction, in this chapter the critical aspects of universal motor commutation are identified and approaches to mathematical commutation modelling of other authors are shown.

In the technical literature on the subject of brush commutation variations in terminology for the electromagnetic quantities involved in commutation analysis occur, particularly with regard to the brush voltages and brush resistances. In order to give the reader a clear picture of how the commutating circuits are defined a brief technical exposition needs to be given at this point before moving on to the actual review of the relevant literature.

In Fig. 2.1 a configuration is depicted where a brush makes contact with three commutator segments *i.e.* two coils are undergoing commutation simultaneously at this brush.

Fig. 2.1 Commutating circuits at one brush

For a mathematical analysis of the commutating circuits shown in Fig. 2.1 by means of Faraday's law the voltage equations

$$v_2 - v_1 = R_1 i_1 + \frac{d\psi_1}{dt} \tag{1}$$

and

$$v_3 - v_2 = R_2 i_2 + \frac{d\psi_2}{dt} \tag{2}$$

9

apply for coil 1 and coil 2, respectively. The coil inductances are L_1 and L_2 and the coil flux linkages are ψ_1 and ψ_2. Moreover, the coil currents are i_1 and i_2 and R_1 and R_2 are the coil resistances, i_a the armature current, and the brush voltage drops v_1, v_2 and v_3 include voltages across brush body resistances as well as the highly nonlinear contact resistance comprising the contact constriction resistance in series with the film resistance. The total time derivatives of the flux linkages in (1) and (2) represent the entirety of the induced voltages in the coils. Voltages in the commutating coils are induced due to self induction, mutual coupling with other coils and the rotation of the armature.

In the following review the work of other authors on the subject is outlined. Their arguments are highlighted and circuit equations established are described. Moreover, the meaning of the circuit elements mentioned above as well as their importance in the analysis of commutation are made evident.

Due to the vast amount of literature on the subject in both German and English only a selection of the books and publications can be discussed here. They are chosen to demonstrate best the following aspects:

- The analysis of commutation of AC commutator motors is a classical problem in the area of electric machines and has been vital over a hundred years [3] and still has a lot of significance today [20] - [22].

- Classical text books mainly deal with the commutation of large and medium size machines and generally take purely analytical approaches [3] - [8].

- These approaches require a high level of comprehension of the electromagnetic behaviour of the machine, and give detailed insight about the parameters of the magnetic and electric circuits of the machine that influence commutation.

- More recent publications on the subject take advantage of the advances in computing power and propose transient solvers that use numerical methods to solve the magnetic field equations (*e.g.* FEA) and the electric circuit differential equations (*e.g.* Runge-Kutta) [9] - [14], [17], [20]. The numerical field computations provide a higher level of accuracy for the distorted field in the uncompensated machine and deal with the usually high saturation of the magnetic circuit of universal motors.

- The proposed differential equations describing the commutating circuits are generally very similar although the terminology used by different authors might differ.

- The main difference in the commutation analysis in the more recent publications

appears to be the treatment of the brush to commutator voltage drop or rather the contact resistance (see also chapter 4).

■ There are methods to evaluate the commutation quality by measuring the armature or field voltage rather than modifying the armature winding in order to measure commutating currents directly [15], [16], [21], [22].

2.2   Text Books about Commutator Motors

In the early work about AC commutator motors of Goldschmidt [3] the problem of commutation is already analyzed. It is assumed that the sides of the commuting coils are located in the interpolar space. The problem of sparking at the end of the short circuit if commutation is unfinished is mentioned, and the importance of the length of the period of time available for current reversal is emphasized by stating that, if one tries to commutate too quickly, the current lengthens the commutation by mean of a spark. The delaying effect of the self inductance of the coil undergoing commutation is explained to be associated with the commutation time, which is critical for the EMF generated in the coil due to self inductance. As a possibility to achieve more time available for commutation an increase in brush thickness (see Fig. 2.3) is suggested and the consequence of this measure, namely an increased number of coils short circuited by one brush and therefore an increased current load in the brush is pointed out. Moreover, the unfavorable interaction of the coils commutating at the same time is mentioned as well as circulating currents caused by EMFs induced in the commutating circuits. The circulating currents contribute to the current loading of the brush and it is stated that a hard carbon brush, *i.e.* a brush with a very high contact resistance would have a more or less governing influence on the current distribution at the brush - commutator interface where the segment leaving the brush. The possibility to aid current reversal by means of a brush shift against the direction of rotation (in a motor) is correlated to the rotational EMF that is a result of that measure and tends to reverse the current. However, due to the field weakening effect the author does not recommend brush shift in an uncompensated plain series motor. Another EMF induced in the commutating coil, caused by the alternating flux the coil encloses and which therefore is a transformer EMF also contributes to the circulating currents mentioned above.

It is assumed that if the current is reversed without the influence of the self induction the current progression is linear and will change to a delayed progression if self induction is effective. The EMF induced by the main flux can be beneficial or unfavorable for commutation depending on whether the resulting circulating current is falling or rising.

This work, however, is more concerned with large machines rotating at slow speeds (<1000 rpm) and having several hundreds of commutator segments.

In Taylor's book [4] about AC commutator motors a graph is shown (Fig. 2.2) which illustrates one of the main differences between commutation in a DC machine and commutation in an AC machine.
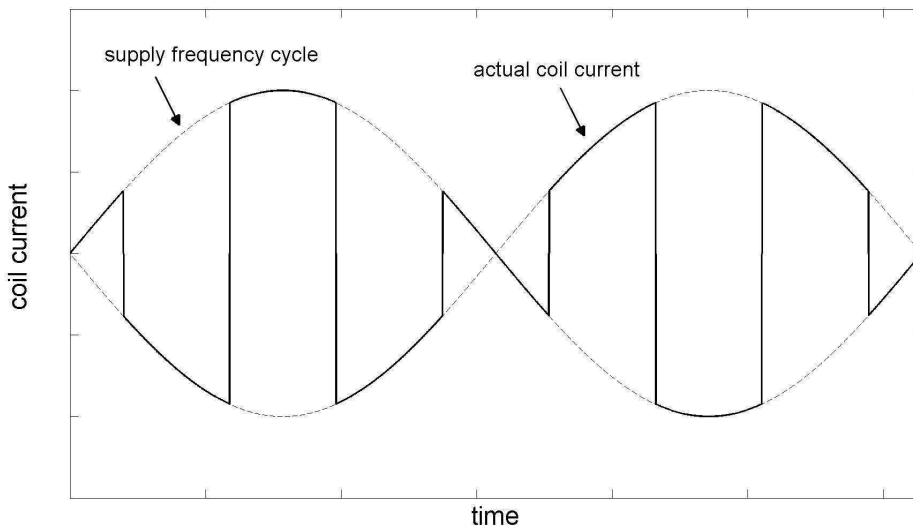
Fig. 2.2 Current in one armature coil in an AC machine

In the DC machine, the current to be reversed is a DC value whereas in an AC machine the current to be reversed is the instantaneous value of the armature current.

The different induced voltages that occur in the commutating coil are distinguished as:

- reactance EMF
- rotational EMF
- transformer EMF

It is stated the rate of change of current due to commutation is large compared to the rate of change due to its cyclic variation and therefore the calculation of the reactance EMF can be

carried out by methods generally applied to DC machines. This calculation is then based on the assumption that the commutation takes place in all conductors of a slot simultaneously and thus an average EMF induced in a conductor during the time of commutation can be applied. Moreover, only the leakage flux of the coil undergoing commutation is considered for the calculation. High frequency ripples in the reaction voltage caused by slots, segments and non-uniform rate of change of current are mentioned as well.

Simplifications are introduced in order to establish an analytical expression to calculate the rotational voltage. The simplifications are that the axis of the alternating (but stationary in space) flux is at 90° to the short circuited coil axis.

Fig. 2.3 Brush commutator contact

Moreover, it is assumed that the short circuited coil always occupies the same positions relative to the flux. The transformer EMF is described to be the result of the mutual coupling of the coil undergoing commutation and the main winding producing alternating flux in the single phase machine. It is stated that the voltage drop across the brush from entering to leaving edge is in general more than the voltage drop between two adjacent commutator segments making contact with the brush and should be kept to a minimum.

The radio interference of the machine is mentioned which is generated due to the abrupt change of current during commutation as well as the sparking that may occur and cause high frequency voltages that appear across the armature of a commutator machine.

In Clayton's book [5] about direct current machines the EMF induced in each coil of the armature is considered having a frequency that is equal to the product of the rotor speed and the number of pole pairs. Ideally, current reversal of a coil should take place at the instant when the EMF induced in that coil is zero. The nature of the brush resistance is explained to be by no means constant which complicates the problem of current reversal significantly. The brush resistance is considered the main resistance in the commutating circuit and largely depends on the current density at the contact interface.
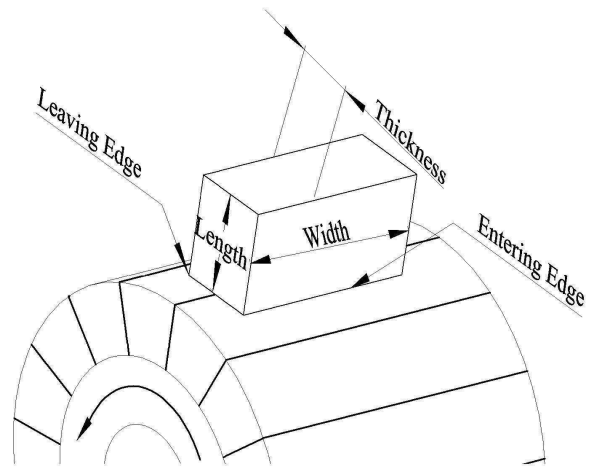
Distinguishing between the positive and the negative brush the author emphasizes that for a dynamo at low temperature the contact drop is less at the positive brush than at the negative brush and the converse holds for a motor. In addition to that the very large extent to which the contact voltage drop depends on the composition of the brush is mentioned.

In Fig. 2.3 a brush sitting on a commutator is shown where the geometry parameters of the brush are indicated using the notation of the author. The author discusses several commutation curves, such as retarded and accelerated commutation in comparison with a linear commutation curve (see Fig. 1.3). Moreover, a curve of sinusoidal commutation is shown which has, according to the author, the advantage that $di/dt = 0$ both at the beginning and at the end of commutation and is slightly retarded before and accelerated after the zero crossing (see Fig. 2.4).
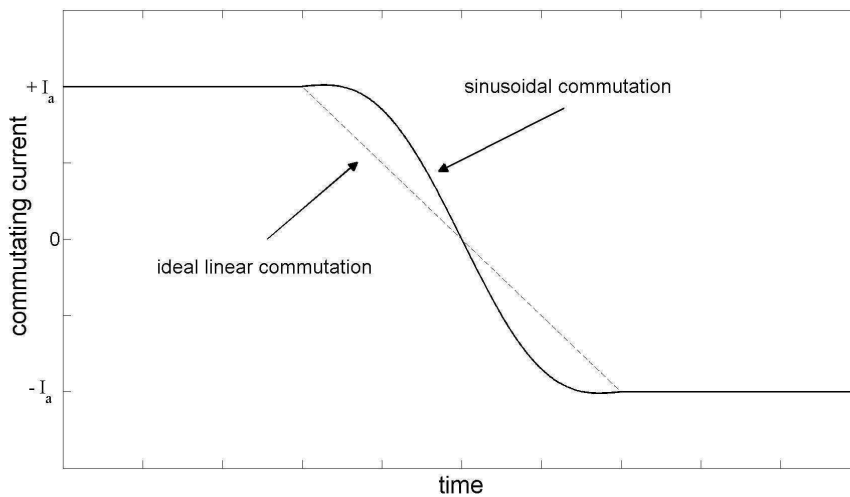
Fig. 2.4 Sinusoidal commutation

It is emphasized that even if a small EMF is induced in the commutating coil and also the coil resistance is not negligible the voltage drop at the brush is the most important term in the commutating circuit and the resistance of the brush contact alone can suffice to ensure satisfactory commutation.

The total EMF induced in the coil undergoing current reversal is explained to be the total rate of change of flux linkage in the coil. Changes in flux linkage occur in the DC machine due to motion of the coil through the stationary magnetic field in the motor and due to change of current in the coil itself or neighboring coils.

The author gives an account of how armature reaction and brush shift influence commutation. If the brushes are located in the quadrature axis and the magnetic neutral axis is shifted due

to armature reaction against the direction of rotation in a motor a dynamic EMF in the commutating coil therefore produces retarded or under-commutation[2]. On the other hand a brush shift against the direction of rotation beyond the magnetic neutral axis will cause the dynamic EMF to be in such a direction as to accelerate commutation. If the brush shift is too large over-commutation will occur.

The static EMF due to the inductance of the coil is always present such as to retard commutation. The fact that there is always retarding EMF makes it essential to develop a reversing EMF in the coil to be commutated in order to rapidly reverse the current.

The inductance of a coil undergoing commutation is considered to be a leakage inductance comprising slot leakage, tooth tip leakage and end connection leakage (see Fig. 2.5 and Fig. 2.6). The reduction of the coil inductance to a pure leakage component is justified by stating that the reversal of the current in the coil does not appreciably affect the value of its total flux due to armature reaction but serves to alter the manner in which this flux links the coil.
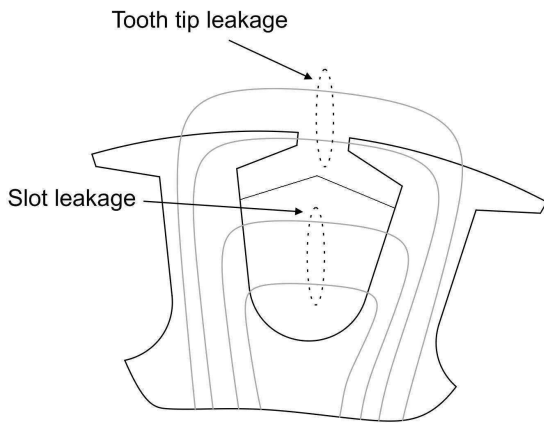
Fig. 2.5 Tooth tip and slot leakage   Fig. 2.6 End winding leakage
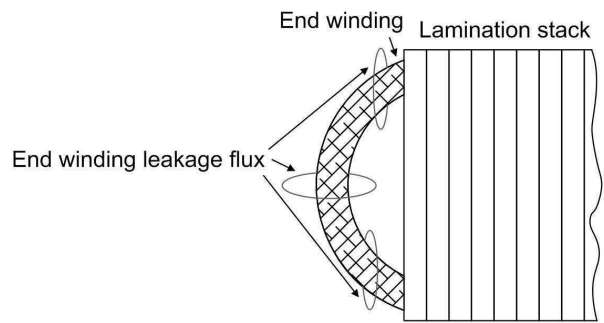
In the book about DC machines by Liwschitz-Garik [6] the length of the period of time of the short circuit of a winding element is described to be critical as sparking under the brush may occur if the short circuit time is too short which is to be avoided.

The author closely relates sparking with commutation and states that "good commutation" is to be understood as current reversal where no sparking at the brushes occurs. The short circuit period of time is proportional to the brush thickness (see Fig. 2.3). One part of the current carried by the short circuited coil is considered an internal current which circulates in

---

[2] Statements given for non-interpole machines

the short circuit path made up of the coil , the commutator risers, both commutator bars and the brush. Moreover, it is emphasized that if the current density at the instant of separation of the trailing edge of the brush and the commutator segment becomes too large sparking appears under the brush which leads to both increased commutator - and brush wear. During the time of commutation the short circuited winding element moves a fixed distance through the cross flux of the armature (see Fig. 2.7b) which delays commutation. Moreover an EMF is induced by the pole flux (Fig. 2.7a) if the brushes are displaced from the neutral axis. This EMF is described to be of either accelerating or delaying character with regard to commutation of a winding element (rotor coil section). The effect depends upon the position of the coil in the main flux during the commutation period. The statement is given that in general commutation in a motor is accelerated by shifting the brushes opposite to the rotation, and is delayed by shifting the brushes in the direction of rotation. The self-induced EMF due to current reversal in the coil is explained to oppose any change in coil current and therefore delays commutation. For the total EMF *e* induced in a commutating coil the expression

$$e = -\left[L\frac{di}{dt} + \sum_{x} M_x \frac{di_x}{dt} \right] \tag{3}$$

is given where the first term represents the EMF due to self induction with the leakage inductance *L*, and the sum in the second term represents the EMFs induced by all other motor coils that carry varying currents, including other coils commutating at the same time.

a) Stator winding excited only   b) Rotor winding excited only   c) Stator and rotor winding excited
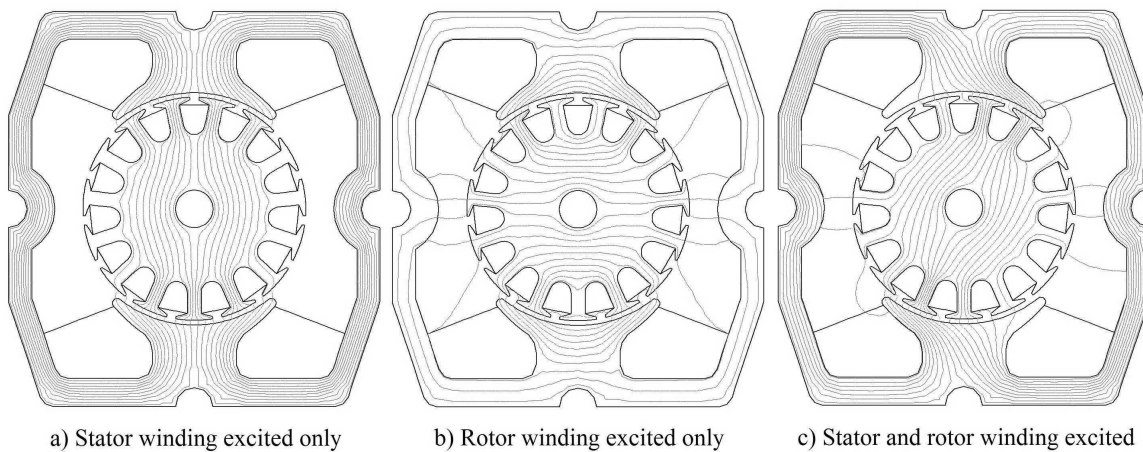
Fig. 2.7 FE-flux plots of armature reaction and shift of magnetic neutral axis

Hawkins [7] describes sparking at the brushes as to shorten the lifetime of the commutator and brushes and its suppression thus is desirable. The sparks are described to be small arcs between a commutator sector edge and the brush edge that will, if allowed to continue, sooner or later

pit the commutator surface and heat the brushes. This will lead to an untrue commutator , worn into deep and rugged grooves and thus brush bounce and increased sparking. A similar expression as (3) is introduced to calculate the total EMF in the commutating coil. Moreover, the expression "apparent" self inductance is introduced owing to the damping effect of the field magnet due to the great mutual coupling between the commutating coil and the field winding. Also the retarding effect of the self induced EMF is mentioned. The EMF induced due to the rotation of the shorted coil through the field produced by the stator winding (distorted by the armature reaction) is expressed as a function of time $f(t)$ and it is stated that a reversing $f(t)$ is achieved shifting the brushes against the direction of rotation in a motor. It is pointed out that a reversing EMF is needed as the carbon brush cannot be expected by its own unaided action to effect the commutation of a coil with considerable inductance without sparking.

The current in the coils undergoing commutation is divided into two parts, one part corresponds to a straight line (ideal, linear commutation) and an additional part which accounts for any deviation from the straight line current. It is emphasized that such a resolution of the actual current is entirely artificial.

In the book about AC commutator motors by Richter [8] a stationary EMF is introduced that would be induced in the commutating coil due to the pulsating flux produced by the field magnet if the rotor was stationary. The transformer coupling between the field winding and the coil shorted by the brush is described to be the reason for that EMF. The short circuited armature coil behaves in this case like a short circuited secondary of a transformer with the field winding acting as a primary. Also the repercussions for the field winding are mentioned. Then, the consideration of this transformer EMF is expanded to the case where the armature is rotating. The currents (contributing to brush erosion) caused by that EMF are assumed to decrease with increasing speed as they cannot build up to their maximum due to the short period of time the coil is short circuited. In addition, due to this short period of time the transformer EMF is considered constant. The main influential element in the commutating circuit is stated to be the brush to bar contact resistance (if no additional resistors are inserted into the circuit).

The EMF due to current reversal is shown to be in phase with the armature current in a motor and will oppose any change in coil current. The calculation of the EMF is done using a self

inductance of the coil comprising slot- and end winding leakage inductance. As the decisive quantity for brush sparking the sum of the three EMFs described is contemplated.

With regard to current harmonics it is stated that current waveforms with sharp peaks are likely to cause more brush wear which is referred to the higher harmonic content in the induced EMF.

In the text books classical analytical approaches have been taken in order to analyze commutation mathematically where simplifications were introduced that hold for large or medium size machines. In recent scientific articles on the subject more modern approaches can be found using numerical field calculations and coupled magnetic field - and electrical circuit transient solvers. The accuracy improvements obtained by these methods permit the application of those methods to commutation analysis of small uncompensated high speed universal motors where the simplifications introduced for larger machines tend to be too coarse.

2.3   Publications on Commutation Analysis of Universal Motors

Di Gerlando and Perini [9] analyze the commutation of an universal motor with a typical configuration of two salient stator poles, a set of two brushes, four coil sides per armature slot and an armature slot to commutator bar ratio of 1:2. A commutating coil section is characterized by a resistance[3] R, a self inductance L and mutual inductances M_x (representing the mutual coupling between coil sections undergoing commutation simultaneously), and an instantaneous EMF e induced by the main flux which is due to the current in the field winding and the non-shorted armature coils. It is emphasized that the relative positions of stator and rotor are symmetric after turning the rotor over one slot pitch. Moreover, the line current is assumed to be practically constant during the very short time a coil section is undergoing commutation where this time period can be lengthened by an arc.

The self - and mutual inductances are found multiplying the number of turns of the coil by the difference quotient of the magnetic flux linking the coil and the respective current. Magnetic saturation and the frequency dependent penetration depth of the magnetic field are considered.

---

[3] Variable names may differ from cited references in order to establish uniform annotations.

It is not made entirely clear how the magnetic fluxes are determined yet it is stated that a numerical method must be applied as some quantities are nonlinear.

As the three flux paths related to the self and mutual inductances of a commutating coil section the authors name

- the slots around the coil sides
- the path around the end windings
- the path through the air gap, closing in the main ferromagnetic circuit of the machine

and state that only the third path, the most important one, depends on the rotor position. Yet the authors do not take the position dependence into account in their simulations.

For the brush - commutator contact voltage the authors distinguish between a static curve of voltage as a function of current density where the current density is constant and a dynamic characteristic that takes into account the instantaneous current density. Both characteristics contain constants that need to be found experimentally.

In addition to the consideration of the brush to commutator voltage drop the electric arc is also taken into account in the mathematical analysis by means of Ayrton's equation which also relies on parameters identified from measured curves.

The authors present a graph showing two calculated (per unit) commutating currents. The coil sections are assumed to be short circuited by the same brush and are located in the same pair of rotor slots. The coils sections start commutating at different instants and their interaction becomes evident at the instant the second coil starts commutating. The coil that has already started commuting before that instant experiences a considerable current increase due to the opposing EMF caused by the high di/dt in the coil section that has just started commutating and the strong coupling of the two coils sharing the same slots.

Wang and Walter [10] use an equivalent circuit in their commutation analysis as depicted in Fig. 2.8. The motor examined is a two pole universal motor with one coil side per armature slot. The authors combine the field winding and the armature winding (non-shorted armature coils) to one winding, the main winding. Moreover, the two commutating coils (resulting from the motor topology) are also combined to one winding, the commutating winding. The voltage equation for the commutating winding is of the same form as (1) and (2) and the brush voltages v_1 and v_2 are calculated from a matrix equation deduced from Fig. 2.8 using a brush

resistance matrix that includes both the brush contact resistances R_{cf1} and R_{cf2} and the brush body resistances calculated using a 2D FEA package. The brush leading and trailing edges in contact with the commutator are considered Dirichlet boundaries with given voltages but also the end surface of the brush in normal direction to the commutator is defined as a Dirichlet boundary condition with a voltage equal to zero. The brush body resistances are calculated from the field solution using an energy formulation. The brush contact resistances are calculated using an empirical expression where the full resistance is found

$$R_{full} = \frac{V_{br}}{I_a} \tag{4}$$

and V_{br} is the average contact voltage drop provided by the brush material manufacturer and I_a is the current at which the commutator surface is filmed. Subsequently, the position dependent contact resistances R_{cfn} are found as follows, where A_{full} is the apparent (see 4.6) contact area at full overlap of the carbon brush and a commutator segment and A_n is the apparent contact area at a certain rotor position $(A_n \leq A_{full})$.

$$R_{cfn} = R_{full} \left[\frac{A_{full}}{A_n} \right]^{0.75} \tag{5}$$

The flux linkage in the commutating winding is found using its self inductance and its mutual inductance with the main winding calculated by FEA. These inductances are then multiplied by the commutating current and the current in the main winding, respectively.

A state space formulation is derived using flux linkage as state variable which is then integrated numerically.
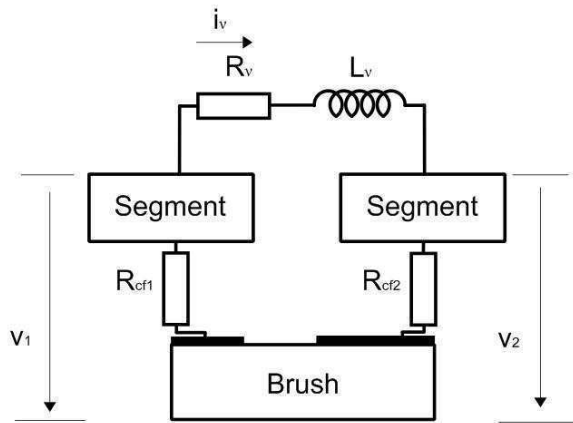
Fig. 2.8 Commutating circuit

Also the electric arc is modeled in the simulation. Near the end of commutation the current density and the associated electric field strength become extremely high at the trailing edge of the brush. The threshold electric field strength for arc formation is given by $E_{thr} = 10^6$ V/m. Once this threshold is reached, R_{cf2} (see Fig. 2.8) is replaced by an arc model in the simulation. The arc resistance applied is the threshold field strength E_{thr} multiplied by a constant film thickness of $20 \cdot 10^{-6}$ m and divided by the arc current.

A curve is presented that shows a calculated commutating current which progresses slightly accelerated. Due to the motor configuration and the combination of the two coils commutating simultaneously to one commutating winding the graph does not show effects caused by interaction of the commutation coils.

In a later publication by the authors [11] the simulation is extended to motors with two coil sides per armature slot. A maximum of two coils shorted by one brush is now allowed in their simulations. Three windings are considered, the main winding comprising the field winding and the non-shorted armature coils, the first and the second commutated coil. The two voltage equations established for the commutating coils are equivalent to (1) and (2). Again matrix equations are solved in order to obtain the brush voltages whose number have now increased to three, and inductances are calculated by use of FE-software.

The authors reduce the order of the required inductance matrix to the order of two by applying a transformation that treats two coil flux linkages as independent variables only although three windings are considered. This is done for what the authors call type-1 commutation. This commutation type is referred to the case of coils undergoing commutation are located in the same rotor slots. If the coils are located in neighboring slots the authors denote that type-2 commutation. The authors show simulated commutating current waveforms where type-1 and type-2 commutation alternate.

Benedičič *et al.* [12] present a similar approach. Their machine model allows for configurations of two and three commutator segments connected to one brush and therefore up to two coils can commutate simultaneously per brush. The voltage equations for the two coils shorted by one brush is equivalent to (1) and (2). Inductances are taken from magnetostatic calculations using a commercially available FEA package. Subsequently the flux linkages are calculated as functions of current and rotor angle. The entries of the resistance matrix are calculated in the same manner as in [10]. The arc model presented is based on a constant arc voltage of 16.5 V which is the average of an anodic and a cathodic brush. The current at which the arc extinguishes is I_{min} = 0.22 A which is again the mean value of an anodic and a cathodic brush. If the conditions for arc ignition are satisfied an apparent contact resistance is calculated by maintaining the constant arc voltage drop. However, after the segment leaves the brush a *V/I* arc characteristic is applied. If the current falls below the minimum arc current I_{min} the arc stops in the simulation. Moreover, the "charred layer" is discussed where due to arcing under the brush a blackened charred layer develops which grows

in the opposite direction of armature rotation. This increases the brush to bar contact resistance.

In addition to the model described another model is established that includes capacitors in parallel to the commutating coils to demonstrate their arc reducing effects.

Kurihara *et al.* [13] also analyze a motor with two salient stator poles, twelve rotor slots and twenty four commutator segments. The equivalent circuits of the commutating coils are similar to the one shown in Fig. 2.8, with the main difference that brush voltages are used rather than brush resistances in the analysis. The voltage equations for two coils short circuited by one brush are expressed by

$$e_1 + R_1 i_1 - v_1 + v_2 + L_{\sigma 1}\frac{di_1}{dt} = 0 \tag{6}$$

and

$$e_2 + R_2 i_2 - v_2 + v_3 + L_{\sigma 2}\frac{di_2}{dt} = 0 \tag{7}$$

where e_1 and e_2 denote the induced voltages in the commutating coils 1 and 2, respectively. The coil currents are i_1 and i_2, and R_1 and R_2 are the coil resistances. $L_{\sigma 1}$ and $L_{\sigma 2}$ denote the end winding leakages of the coils and v_1, v_2 and v_3 the contact voltage drops at the brush to commutator bar interfaces. The induced voltage e in each coil is found using the line integral over the time derivative of the vector potential $\vec{A}$ as follows

$$e = \frac{d}{dt}\oint \vec{A}\,\vec{ds} \tag{8}$$

where the vector potentials are found from FEA and the brush to bar voltage drops calculated from a mathematical expression that relies on constants derived from a measured curve. The argument by the authors is that a conventional brush voltage - current density characteristic does not show the saturating behaviour of the measured curve and therefore introduces a large error in the simulation and thus the saturating, parameterised expression is proposed.

Matsuda *et al.* [14] base their commutation analysis on the assumptions that the contact voltage characteristic is the same for anode and cathode brushes, the thickness of the commutator segment insulation can be ignored and the armature current and the revolving speed are constant under a constant load.

Moreover, the AC voltage source is replaced by two AC current sources in the parallel armature circuits in the simulation. Due to the small variations of the 50 Hz or 60 Hz AC wave

during the period of commutation the authors believe that it is possible to ignore any error caused by the approximation of constant armature current. A mathematical model is established that takes into account self and mutual inductances of up to four coils (two per brush), transformer and speed EMFs and combined static and dynamic characteristics of the brush contact voltage.

The magnetic circuit parameters are calculated using a 2D numerical model which takes magnetic nonlinearity into account.

The speed EMF in a commutating coil is found from a difference quotient of flux linkage and time where the magnetic vector potential is calculated before and after a small angular step of the rotor with current in all coils kept constant.

Self - and mutual inductances are found from difference quotients of flux linkage and current where the flux linkages are determined before and after a small current variation in a certain coil.

Fujii [15] divides the period of time in which a coil is undergoing commutation into three intervals

- ■ the period just after the start of commutation where the current is still almost constant
- ■ the period where the current is decreasing but has not changed polarity yet
- ■ the period after the zero crossing

The author states that in an ordinary case the commutation period is far smaller than the electrical time constant of the commutating coil and a high jump of commutating current occurs at the end of commutation and thus a high reactance voltage is induced. This voltage appears between the brush and the commutator and the author measures it as pulses in the armature terminal voltage waveform. Moreover, it is concluded that the main flux is under the influence of the commutating current.

In the later commutation analysis by Fujii and Hanazawa [16] the excessive voltage pulses at field or armature of the motor caused by rapid current change at the end of commutation are described again. The integration of the waveform of these pulses is considered to give information on the commutation quality. Due to the short commutation period of an armature coil the current is assumed to jump to its designated value at the end of commutation and thus

the large voltage pulses are induced. The authors regard these pulses as indication of poor commutation.

The integration of the field - and armature voltage gives the waveform of the saw toothed flux that is generated by the harmonic contents of the commutating currents. Regarding the brush contact resistance the authors state that it affects the time constant of the commutating coil and varies not only as the armature input current varies but also as the motor running time elapses. It is found that the brush contact resistance in case of AC operation is larger than in case of DC operation. Moreover, the authors present some suppressing circuits to improve commutation *i.e.* diminish the voltage pulses.

The influence of a mechanically unstable brush contact is discussed too. Vibrating brushes are found to downgrade commutation quality to an extent where electrical measures, *i.e.* the suppressing circuits shown by the authors do not lead to satisfactory commutation.

Therefore it is emphasized to improve the mechanical configuration first and then to apply electrical measures to improve commutation.

Doppelbauer [17] uses a different mathematical approach in his analysis. He points out that the quality of an universal motor depends much more strongly on the quality of the commutation than it is the case with DC machines.

As a strong simplification of the problem magnetic saturation effects in the lamination steel are neglected. The current transfer from the brush to the commutator is described to be one of the key problems in the mathematical analysis. It is pointed out that for commutation simulations the progression of the brush to bar contact resistance has to be known precisely. To include the brush resistance in the calculations the author performs a set of measurements to establish characteristics for certain brush types. Subsequently, these brush resistance characteristics are emulated section by section by linear functions and second or higher order parabola functions. The time dependent currents are considered as Fourier series with complex coefficients. The same is done for the self - and mutual inductances. Therefore the inductances are precalculated using 2D Finite Difference magnetic field analysis.

The flux linkage is calculated by multiplying the currents by the respective inductances and the brush voltage drops are calculated by multiplication of the brush resistance and the current through the commutator bar. Hence, multiplications of complex Fourier series are required. After the set up of the complex system of equations it is transformed into a real system of the same order to decrease computing time.

Roye and Poloujadoff [18] claim to be the first to give a quantitative evaluation of the EMFs in a commutating coil of an universal motor. The authors point out that all fractional horsepower motors present some characteristics which are fundamentally different from those of the medium sized and large machines. Moreover, an "ideal commutation" reference case is defined. The commutation is described to be ideal if the variation of the coil current is such that the magnetic field does not move. For a commutating coil the authors present a voltage equation as follows

$$v_2 = Ri + \frac{d\phi}{dt} + v_1 \qquad (9)$$

where φ is denoted the flux in the commutating coil (the turns are not mentioned at this point therefore it can be assumed the authors use the expression "flux" for what other authors denote "flux linkage" where the turns are already considered). The brush voltages v_1 and v_2 are calculated following the laws indicated by the brush manufacturer which is a function of current density. The magnetic parameters of the voltage equations are obtained by measurements of the coil flux linkages as functions of current. Thus, saturation of the steel is taken into account. The obtained curves are then approximated by mathematical functions. The authors obtain curves for several different rotor positions and state that they approximated more than 200 curves.

Subsequently, the electric circuit equations are solved by a computer program. In the calculated motor current the repercussions of the commutation are notable. It is emphasized that the sudden short circuit of a rotor coil causes a relatively large voltage drop across the rotor terminals. As a consequence the input motor current rises very rapidly as the network impedance is always too small to limit these variations. The increase of the line current tends to cause an increase of the flux through the commutating coil which decreases the commutating current by transformer action.

The authors explain that if the commutating current decreases too rapidly the magnetic neutral line may rotate in a direction opposite to the rotor movement and causes the speed EMF to increase or even change sign which then causes a delay in current reversal. At the instant the current reversal in the coil ends the sudden variation is assumed to have several consequences such as sparking due to change of stored energy, and the shift of the magnetic axis in the same direction as the armature movement.

Bradley and Ismail [19] point out that, in a universal motor, the armature coils undergoing commutation share a similar winding axis to the AC excited field coils and appear as shorted turns producing an opposing MMF where the number of shorted armature turns is an appreciable fraction of the field turns in the small series machines. The authors present a voltage equation for a commutating coil as follows

$$v_c = R_c i_c + \frac{d\psi_{Fc}}{dt} + \frac{d\psi_{Ac}}{dt} + \frac{d\psi_c}{dt} + v_{bp} - v_{bn} \tag{10}$$

where the subscripts F, A and c refer to field, armature and the commutating coil, respectively, and the time derivative of the flux linkage is resolved into the mutual parts between F and c, A and c, and the self flux linkage of the commutating coil.

The voltages v_{bp} and v_{bn} are the brush contact voltages at each side of the commutating coil. The derivatives of the flux linkages are expanded as follows

$$\frac{d\psi}{dt} = \frac{\partial\psi}{\partial i}\frac{di}{dt} + \frac{\partial\psi}{\partial\theta}\frac{d\theta}{dt} \tag{11}$$

which takes its dependence on the current i and the rotor position θ into account.

In a case of two coils undergoing commutation simultaneously (one coil at each brush) the coils can be represented by a single coil only when exactly similar conditions apply at each brush. To solve the electric circuit equations pre-calculated magnetic fluxes are used obtained for a variety of currents and rotor positions (lookup tables). Due to the high amount of required magnetic field solutions the authors decided to use a simplified magnetic network rather than FEA.

The authors show in their simulation results that the transformer EMF dominates the initial change of the current in the commutating coil and it is not until well into the commutation process that the brush contact voltage drop starts to dominate the current change as the current density under the brush rises rapidly.

Niwa and Akiyama [20] analyse a universal motor with a rated speed of 33000rpm. An equation for a commutating coil is presented as follows

$$L\frac{di}{dt} + Ri + \left(\frac{R_b T}{T-t}\right)(I+i) - \frac{R_b T}{t}(I-i) + e = 0 \tag{12}$$

where the inductance L of the commutating coil is calculated using FEA, the resistance R is the sum of the coil resistance and the commutator riser resistance, T is the commutation time and R_b is the contact resistance which is modeled by a time response that varies between an "on" and an "off" value. The current I is assumed constant whereas i is instantaneous, and e is the commutation EMF. The authors present a graph showing calculated brush voltage waveforms of a low resistance brush and a high resistance brush. One can see that the voltage at the low resistance brush has significantly higher spikes than the voltage at the high resistance brush. These voltage spikes are assumed to be an indication of commutator sparking.

A non-mathematical analysis is carried out by Möckel and Oesingmann [21], [22]. The authors are concerned with the evaluation of the commutation of an operating machine that requires a minimum of modification of the machine. As it is aimed not to modify the armature to measure the commutating current directly an indirect method of commutation evaluation is proposed. This is based on the repercussions of the commutation for the field winding.

It is stated that there is a contribution of the commutating coils to the air gap flux that links the field winding. Hence, a high rate of change of flux caused by commutation will be notable in the voltage drop across the field winding.

The induced spikes in the field voltage are described to be positive with respect to voltage polarity if the current at the instant of separation of the brush and the commutator bar is over-commutating. If the current is under-commutated the voltage spike that appears in the field voltage is negative. It is shown that at AC operation the commutation near the peak value of the motor current is generally unfinished and that just before the motor current reaches its peak value the voltage peaks change polarity *i.e.* there is a transition from over- to under-commutation. Between the over- and the under-commutation zones there is a small period when nearly ideal commutation takes place which is indicated by the absence of the voltage peaks at the conclusions of commutation periods.

Moreover, the discrepancy between the theoretical and actual width of the contact zone of brush and commutator is examined. Due to the charring at the trailing edge of the brush or eroded commutator bars the actual contact width can, in extreme cases become less that one commutator pitch even though the theoretical (mechanical) contact width may be 1.5 commutator pitches.

3 Inductance Calculations and Measurements

3.1 Inductances in Commutation Analysis

As shown in the literature review, inductances are commonly used in the analysis of commutation. They represent the capability of a coil to build up a magnetic field that opposes any change in flux that links the coil and therefore are important indicators of how strongly the current reversal is affected by the rate of change of currents in the coils. The inductances depend on the magnetic circuit, *i.e.* the cross section geometry of the motor and the position of the rotor, and the state of saturation of the steel. Hence, the inductances reveal how the coupling of the coils changes with rotor position, modifications of the motor geometry and the choice of steel.

Today, FEA is commonly used in universal motor analysis to calculate inductances. In this chapter important inductances of the universal machine calculated using FEA are compared to inductances calculated analytically and measured inductances to verify the application of numerical magnetostatic field analysis. The analysis is carried out for a 230V mains-operated power tool motor.

3.2 Analytical Calculations

3.2.1 Calculation of the armature inductance

As shown in [23] the analytical calculation of the armature inductance of a salient pole machine that has brush shift can be carried out by subdividing the full inductance into a d-axis part and a q-axis part.

To calculate the q-axis inductance L_q with respect to the armature current (see Fig. 3.1 and Fig. 3.2) the flux linkage of that axis Ψ_q has to be calculated. This flux linkage has three components. The first component Ψ_{pq} is associated with the flux Φ_{pq} that is circulating under the salient field poles (see Fig. 3.1). Assuming a smooth unslotted rotor with a linear current sheet $K = CI_a/a = ZI_a/(2\pi a)$ where Z is the number of total armature conductors, I_a is the armature current and a is the number of parallel armature branches, the incremental flux $d\Phi$
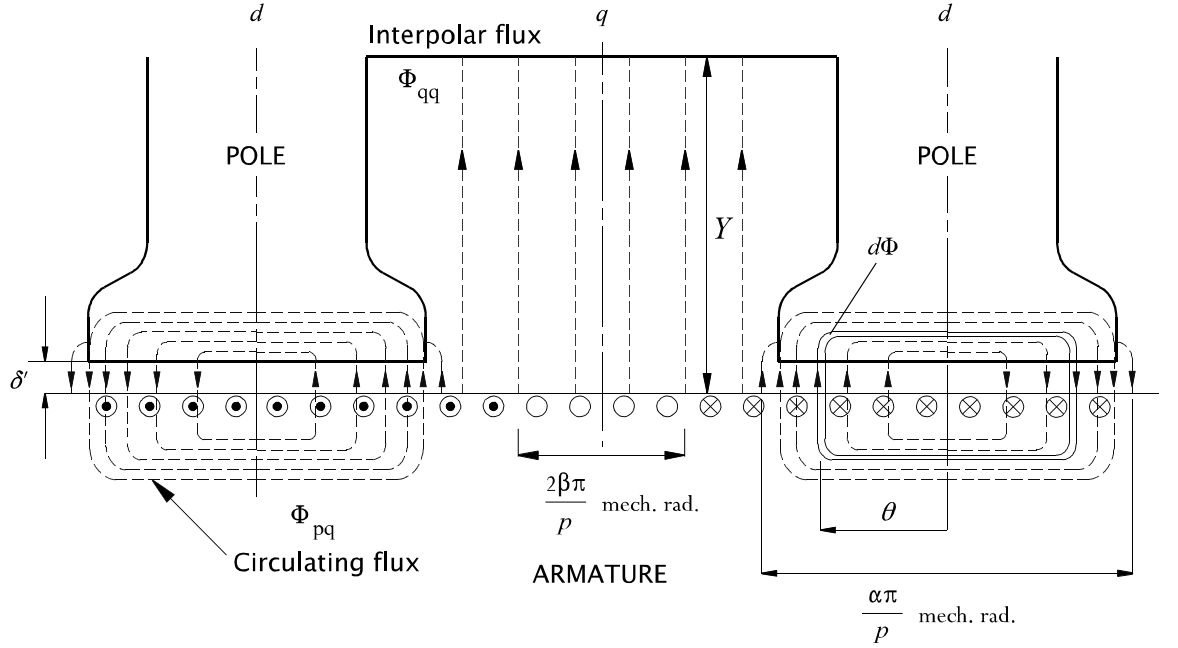
Fig. 3.1 q-axis analysis [23]

links $2C\theta$ armature conductors with reference to Fig. 3.1. Hence $d\Psi_{pq}=2C\theta d\Phi$ where

$$d\Phi = \mu_0 \frac{K\theta}{\delta'} r l_{stk} d\theta, \tag{13}$$

r is the rotor radius, l_{stk} is the lamination stack length and δ' is the air gap modified by Carter's coefficient.

Hence

$$\Psi_{pq} = \frac{2p}{a} \int_0^{\frac{\alpha\pi}{2p}} d\Psi_{pq} = \frac{2p}{a} \mu_0 2C^2 \frac{I_a r l_{stk}}{a\ 3\delta'} \left[\frac{\alpha\pi}{2p} \right]^3 = L_{pq} I_a \tag{14}$$

where α is the per unit pole arc and p is the number of pole-pairs.

A second component Ψ_{qq} is associated with the flux crossing the interpolar space between adjacent poles. The flux is assumed to cross that distance Y in straight lines so that the incremental flux loop now becomes

$$d\Phi = \mu_0 \frac{K\theta}{Y} r l_{stk} d\theta. \tag{15}$$

Now, with $\gamma = 1 - 2\beta$, where β is the per unit brush shift angle and $d\Psi_{qq}=2C\theta d\Phi$ one obtains

$$\Psi_{qq} = \frac{2p}{a} \int_{\frac{\alpha\pi}{2p}}^{\frac{\gamma\pi}{2p}} d\Psi_{qq} = \frac{2p}{a} \mu_0 2C^2 \frac{I_a r l_{stk}}{a\ 3Y} \left[\frac{\pi}{2p} \right]^3 (\gamma^3 - \alpha^3) = L_{qq} I_a \tag{16}$$

29

which is the second component of Ψ_q. Moreover a third component Ψ_{qu} must be added as there are N_u armature turns which are located under the pole shoes and are linked by the flux

$$\Phi_{qq} = 2\mu_0 \frac{Krl_{stk}}{Y} \int_{\frac{\alpha\pi}{2p}}^{\frac{\gamma\pi}{2p}} \theta d\theta = \mu_0 \frac{Krl_{stk}}{Y}\left[\frac{\pi}{2p}\right]^2 (\gamma^2 - \alpha^2) \tag{17}$$

as therefore can be calculated as follows

$$\Psi_{qu} = \frac{2p}{a} N_u \Phi_{qq} = L_{qu} I_a \tag{18}$$

where $N_u = \alpha Z/(4p)$.
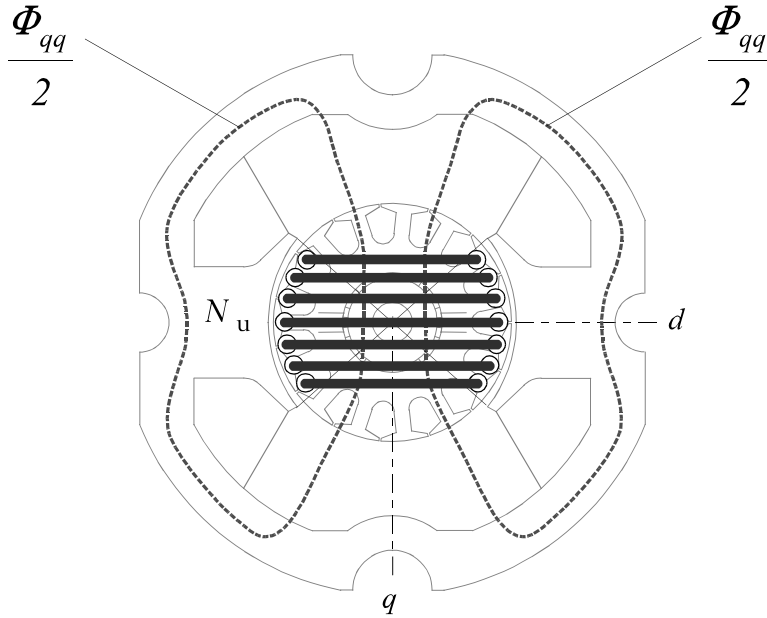
Fig. 3.2 Flux linkage component Ψ_{qu} [23]

The q-axis component of the armature inductance is the sum

$$L_q = L_{pq} + L_{qq} + L_{qu} \tag{19}$$

As the motor examined has a brush shift $\beta < (1 - \alpha) / 2$ the d-axis flux produced by the armature can simply be calculated as follows (see Fig. 3.3)

$$\Phi_d = \mu_0 K \alpha \beta \left[\frac{\pi}{p}\right]^2 \frac{rl_{stk}}{\delta'} \tag{20}$$

and the d-axis flux linkage is

$$\Psi_d = \frac{2p}{a} C \beta \frac{\pi}{p} \Phi_d = L_d I_a \tag{21}$$
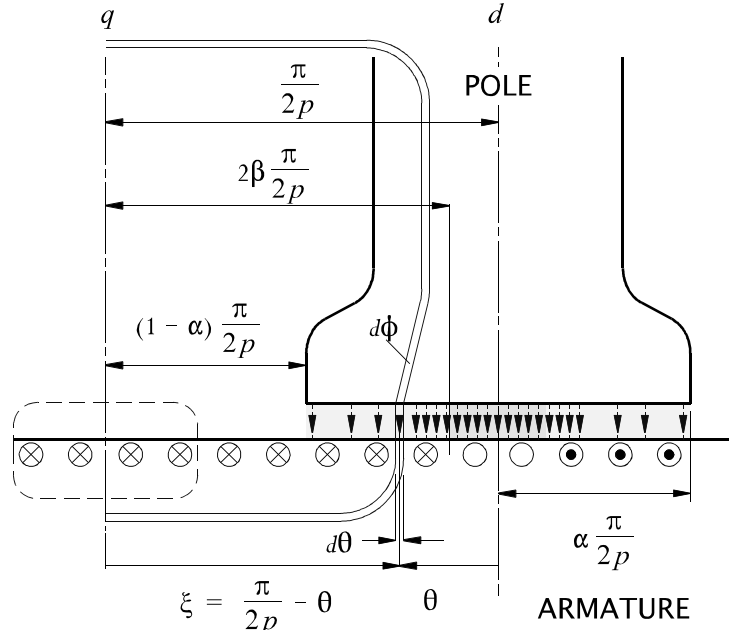
Fig. 3.3 d-axis flux [23]

In order to find the effective air gap for the calculations above one can apply Carter's coefficient k_c found using for example [24]

$$k_c = \frac{\tau_s}{\tau_s - q\delta_m} \tag{22}$$

where τ_s is the slot pitch and $\delta_m = (\delta_{min} + \delta_{max})/2$ is the mean air gap and

$$q = \frac{(s/\delta_m)^2}{5 + s/\delta_m}, \tag{23}$$

where s is the width of the slot opening and the modified air gap is now found as follows

$$\delta' = k_c \delta_m. \tag{24}$$

Now, in order to determine the slot leakage inductance $L_{\sigma s}$ of the armature winding [25] the slot permeance coefficients $\lambda_s = 0.25h/w$ and $\lambda_t = t/s + 2T/(w+s)$ are defined with reference to Fig. 3.4. With these permeance terms the armature winding's slot leakage inductance becomes

$$L_{\sigma s} = \frac{N_s}{a^2} \mu_0 l_{stk} c_s^2 \left[\frac{4}{3} \lambda_s + \lambda_t \right] \tag{25}$$

where N_s is the number of armature coils and c_s is the number of conductors per slot.

31
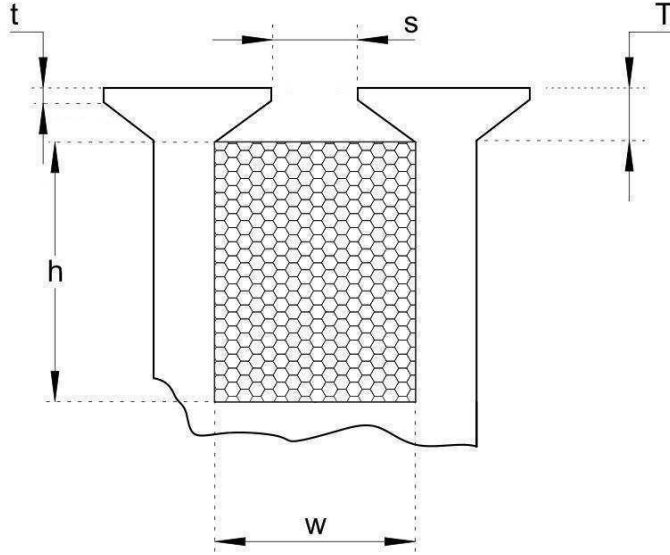
Fig. 3.4 Slot geometry parameters

The end winding leakage inductance $L_{\sigma e}$ of the armature winding [25] is found using the geometric mean distance D_{gm} of the conductors located in the same pair of slots. Hence, using the cross sectional area A_c of a conductor, D_{gm} can be found as follows

$$D_{gm} = 0.447\sqrt{A_c c_s /2} \tag{26}$$

and with the diameter d, that is found assuming that the end windings of the two ends of a coil are taken together to form a circular coil whose diameter d, is equal to the chord spanned by the coil so that

$$d = 2r_s \sin(\sigma/2) \tag{27}$$

where r_s is the radius from the mid point of the rotor to the slot base and the coil span $\sigma = 2\pi/N_s \cdot T_{sp}$ with the coil throw T_{sp} in slot pitches. The end winding leakage inductance $L_{\sigma e}$ of the armature winding can be found as follows

$$L_{\sigma e} = \frac{N_s}{a^2}\frac{1}{8}\mu_0 d c_s^2 \ln\left[\frac{4d}{D_{gm}} - 2\right] \tag{28}$$

and the full armature inductance L_a is

$$L_a = L_q + L_d + L_{\sigma s} + L_{\sigma e} \tag{29}$$

The parameters of the motor examined as well as the calculated flux linkages and inductances are summarised in table 3.1.

32

Table 3.1 Parameters of L_a calculation

Parameter	Annotation	Value	Dimension
Z	total armature conductors	504	—
a	parallel armature branches	2	—
α	per unit pole arc	13/18	—
β	per unit brush shift angle	1/8	—
p	number of pole pairs	1	—
Y	interpolar gap length	6.330	mm
r	rotor radius	17.500	mm
l_{stk}	lamination stack length	56.000	mm
τ_s	slot pitch	$\pi/6$	rad
s	slot opening	2.000	mm
δ'	modified air gap	0.658	mm
I_a	armature current	0.500	A
N_s	number of armature coils	24	—
c_s	conductors per rotor slot	42	—
λ_s	slot permeance coefficient	0.350	—
λ_t	slot permeance coefficient	0.620	—
A_c	conductor cross section	0.475	mm^2
r_s	slot base radius	11.000	mm
T_{sp}	rotor coil throw	5	—
Ψ_q	flux linkage q-component	3.000	mVs
Ψ_d	flux linkage d-component	1.100	mVs
L_q	inductance q-component	6.000	mH
L_d	inductance d-component	2.200	mH
$L_{\sigma s}$	slot leakage inductance	0.810	mH
$L_{\sigma e}$	end winding leakage inductance	0.080	mH
L_a	full armature inductance	9.090	mH

3.2.2 Calculation of the inductance of the field winding

The calculation of the unsaturated air gap component of the field winding inductance is straightforward and based on the assumption of a constant magnetic flux density in the air gap B_δ under each pole *i.e.* slotting is not considered and B_δ can be calculated as follows

$$B_\delta = \mu_0 \frac{N_{Fc} I_F}{\delta'} \tag{30}$$

where N_{Fc} is the number of turns per field coil and I_F is the field current. Now with the flux linking one field coil $\Phi_{Fc} = B_\delta\, r\, l_{stk}\, \alpha\pi/p$ the air gap component of the inductance of the field winding $L_{F\delta}$ can be obtained as follows

$$L_{F\delta} = 2\mu_0 N_{Fc}^2 \frac{\alpha\pi r l_{stk}}{\delta'} . \tag{31}$$

In order to find the leakage component $L_{F\sigma}$ of the field winding inductance one has to consider the leakage in the stator slots characterised by the leakage flux $\Phi_{F\sigma s}$ and the leakage at the end windings of the field coils characterised by the leakage flux $\Phi_{F\sigma e}$.

These leakage fluxes are found taking into account the geometry of the stator [26] (see Fig.3.5) and are calculated as follows

$$\Phi_{F\sigma s} = \frac{1}{2}\mu_0 l_{stk} N_{Fc} \frac{h_F}{b_F} I_F \tag{32}$$

$$\Phi_{F\sigma e} = \frac{1}{2}\frac{\mu_0}{\pi} b_p N_{Fc} \ln\left[\frac{h_p}{r_F}\right] I_F \tag{33}$$

where r_F is the radius of the field coil. As the field leakage flux can be expressed as the sum of the two leakage parts $\Phi_{F\sigma s}$ and $\Phi_{F\sigma e}$ one obtains the leakage inductance as follows

$$L_{F\sigma} = \frac{1}{2}\mu_0 N_{Fc}^2 \left[\frac{h_F}{b_F} l_{stk} + \frac{b_p}{\pi}\ln\left[\frac{h_p}{r_F}\right]\right] \tag{34}$$

and the parameters and results for the motor examined can be found in table 3.2 where α is slightly augmented to allow for fringing. Table 3.2 contains the relevant stator geometry parameters, rotor geometry and air gap parameters are listed in table 3.1. The stack length is the same for stator and rotor.
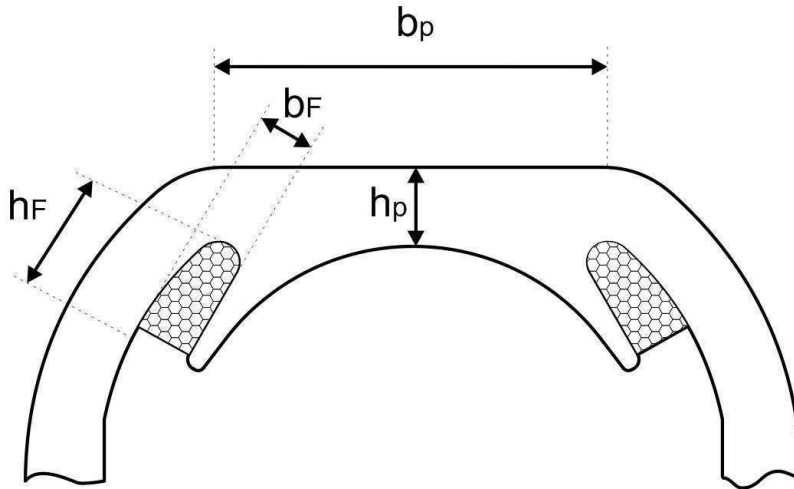
Fig. 3.5 Relevant stator geometry parameters

Table 3.2 Parameters of L_F calculation

Parameter	Annotation	Value	Dimension
N_{Fc}	turns per field coil	87	—
α	per unit pole arc	3/4	—
h_F	see Fig. 3.5	12.820	mm
b_F	see Fig. 3.5	4.740	mm
b_p	see Fig. 3.5	40.000	mm
h_p / r_F	—	≈ 2	—
$L_{F\delta}$	air gap inductance	67.000	mH
$L_{F\sigma}$	leakage inductance	0.760	mH
L_F	full field inductance	67.760	mH

The full field inductance L_F is calculated as the sum of the air gap component and the leakage component as follows

$$L_F = L_{F\delta} + L_{F\sigma} \tag{35}$$

3.2.3   Calculation of the inductance of a single rotor coil

Although in scientific articles dealing with the analytical calculation of a single rotor coil inductance of a universal motor often series expansions of the magnetic flux density or the winding- and air gap distribution are proposed, (*e.g.* [25], [27]) the calculation of a single rotor coil inductance in this chapter is based on simplified magnetic networks. Due to the value of α (table 3.2) and the value of β (table 3.1) one can assume that one side of the first coil of one of the armature branches is located under the fringe of a tip of a salient stator pole as indicated in Fig. 3.6. Due to the short pitching (table 3.1) the other side is not located under the tip of an adjacent pole. The other coil side is located between the second pole tip of the same pole and the q-axis. Therefore one can establish a magnetic network per half pole assuming the flux paths indicated in Fig. 3.6. The half pole paths are denoted path a and path b and the magnetic networks are shown in Fig. 3.7 where the elements are calculated as follows

$$R_\delta = \frac{2\delta'}{\mu_0 \alpha \pi r l_{stk}} \tag{36}$$

$$R_{\sigma a} = \frac{4Y}{\mu_0 \pi r l_{stk}} \tag{37}$$

$$R_{\sigma b1} = \frac{12Y}{\mu_0 \pi r l_{stk}} \tag{38}$$

$$R_{\sigma b2} = \frac{6Y}{\mu_0 \pi r l_{stk}} \tag{39}$$
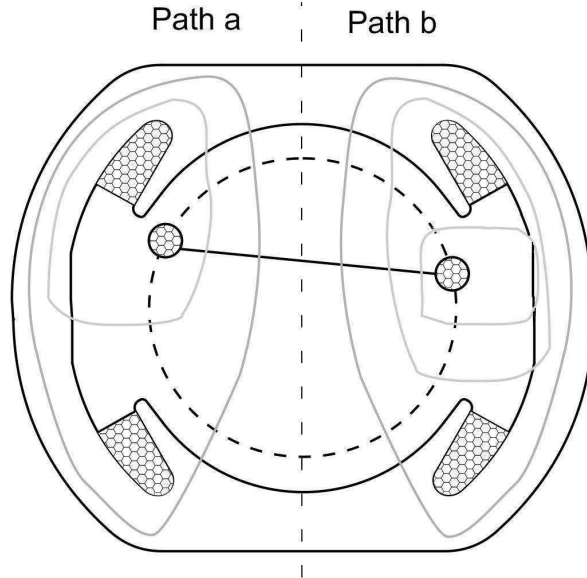
Fig. 3.6 Flux of single rotor coil

Path a

Path b
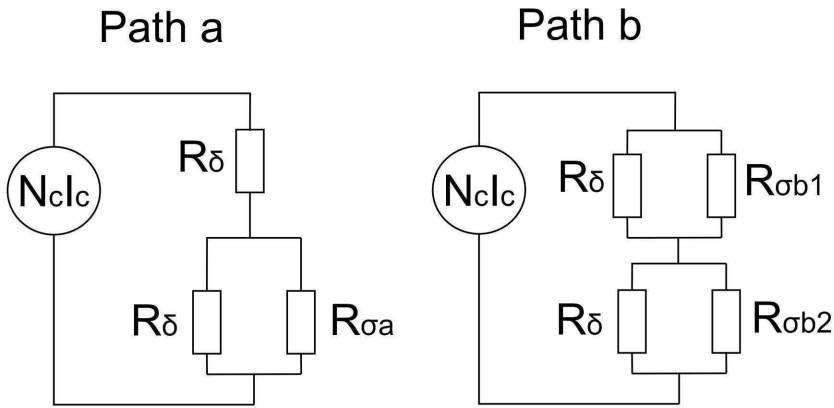
Fig. 3.7 Magnetic networks

and the magnetic reluctances of the paths a and b become

$$R_{ma} = R_\delta\left[1 + \frac{1}{1+R_\delta/R_{\sigma a}}\right] \tag{40}$$

and

$$R_{mb} = R_\delta\left[\frac{1}{1+R_\delta/R_{\sigma b1}} + \frac{1}{1+R_\delta/R_{\sigma b2}}\right] \tag{41}$$

which yields the air- and interpolar gap component $L_{c\delta Y}$ of the single rotor coil

$$L_{c\delta Y} = N_c^2\left[\frac{1}{R_{ma}} + \frac{1}{R_{mb}}\right] \tag{42}$$

with the number of turns of the rotor coil N_c.

Now, to find the slot leakage and end winding leakage components of the single rotor coil inductance according to [25], the relevant parameters from table 3.1 can be used. The slot leakage component $L_{c\sigma s}$ is

$$L_{c\sigma s} = 4\mu_0 l_{stk} N_c^2 \left[\frac{5}{6}\lambda_s + \frac{1}{2}\lambda_t \right] \tag{43}$$

and, with

$$d_{gm} = 0.447\sqrt{A_c N_s} \tag{44}$$

the end winding leakage component $L_{c\sigma e}$ is

$$L_{c\sigma e} = \frac{1}{2}\mu_0 d N_c^2 \ln\left[\frac{4d}{d_{gm}} - 2 \right] \tag{45}$$

and the full coil inductance is found as follows

$$L_c = L_{c\delta Y} + L_{c\sigma s} + L_{c\sigma e}. \tag{46}$$

The results are listed in table 3.3.

Table 3.3 Parameters of L_c calculation

Parameter	Annotation	Value	Dimension
N_c	turns of rotor coil	11	—
R_{ma}	reluctance path a	877.670	kA/Vs
R_{mb}	reluctance path b	876.810	kA/Vs
$L_{c\delta Y}$	air gap inductance	275.870	µH
$L_{c\sigma s}$	slot leakage inductance	18.720	µH
$L_{c\sigma e}$	end winding leakage inductance	3.660	µH
L_c	full coil inductance	298.250	µH

3.2.4 Calculation of the mutual inductance of two rotor coils with coinciding coil axes

If two rotor coils are located in two different pair of slots in a way that their coil axes coincide one can assume that the flux crossing the air gaps produced by one coil c_1 links the other coil c_2 so that $M_{c2c1} \approx L_{c1\delta Y}$ *i.e.* in the case of a coil located as shown in Fig. 3.6 we obtain for the mutual inductance with another coil with coinciding coil axis $M_{c2c1} \approx 275.87\mu H$.

3.2.5   Calculation of the mutual inductance of one rotor coil and the armature winding

Considering the armature winding as the current carrying winding whose flux links a single armature coil that is assumed to be separated from the rest of the armature winding and located as shown in Fig. 3.6 one can assume, with regard to Fig. 3.1 that the q-axis flux will cancel out in that armature coil and it is only linked by the d-axis flux produced by the armature. However, now there are N_c conductors missing locally in the belt of armature conductors producing d-axis flux and (20) needs to rewritten as

$$\Phi_d = (C\beta\pi/p - N_c)\frac{I_a}{a}\mu_0\alpha\frac{\pi}{p}\frac{rl_{stk}}{\delta'} \tag{47}$$

and with

$$\Psi_{ca} = N_c\zeta\Phi_d = M_{ca}I_a \tag{48}$$

with the factor $\zeta = 5/6$ accounting for short pitching one obtains a mutual inductance of $M_{ca} = 424.29\mu H$.

3.2.6   Calculation of the mutual inductance of one rotor coil and the field winding

Considering the field winding as the current carrying winding whose flux links a single armature coil located as shown in Fig. 3.6. Assuming that the angle between the coil axis and the d-axis is negligible, i.e the armature coil links the full air gap flux produced by the field winding (just slightly reduced due to short pitching) one obtains for the mutual inductance

$$M_{cF} = \mu_0 N_{Fc} N_c\zeta\frac{\alpha\pi}{p}\frac{rl_{stk}}{\delta'} \tag{49}$$

with a value for the armature coil shown in Fig. 3.6 of $M_{cF} = 3.35mH$.

3.2.7   Calculation of the mutual inductance of the armature winding and the field winding

Considering the armature winding as the current carrying winding one can assume that the field winding is linked by the d-axis flux produced by the armature and therefore

$$M_{Fa} = 2\mu_0 N_{Fc}\frac{Z}{2\pi a}\alpha\beta\left[\frac{\pi}{p}\right]^2\frac{rl_{stk}}{\delta'} \tag{50}$$

which yields a value $M_{Fa} = 11.60mH$.

3.3   Numerical Inductance Calculations using FEA

3.3.1   Inductance from Finite Element Analysis

In many FE-programs the inductances are found from energy formulations taking into account the magnetostatic field distribution and co-energy [61]. However, a more rigorous approach is to use the vector potential $\vec{A}$ obtained from FEA directly [28]. Via use of Stoke's law the magnetic flux can be expressed as

$$\Phi = \int_S \vec{B}d\vec{S} = \int_S rot\vec{A}d\vec{S} = \oint_l \vec{A}d\vec{l} \tag{51}$$

which in the 2D case yields

$$\Phi = (A_2 - A_1)l_{stk} \tag{52}$$

and the inductance of a coil with N turns carrying a current I is found as follows

$$L = \frac{N}{I}(A_2 - A_1)l_{stk}. \tag{53}$$

The vector potentials are taken at the coil side locations and represent the respective z-component of the $\vec{A}$ - vector if the magnetostatic problem is solved in the x-y-plane.

The commercial software package PC-FEA [55], a module of the SPEED motor design software [79], is used to obtain the vector potentials. As the PC-FEA meshing stage is optimised for the use with motor geometries created in the SPEED motor design programs, the time required for the automatic meshing (triangular elements) is considerably short compared to other available FEA programs. Hence, FE-results can be obtained within comparably low computing times which is important due to the high amount of required computations. The created meshes can be checked and customised if necessary [55].

3.3.2   FE-calculation of the armature inductance

Due to the complex armature circuit where, in the universal machine examined, two branches are in parallel and the individual armature coils share their "go" and "return" slots with other coils that are in the same branch and in the respective other branch, the calculation of the armature inductance using FEA is not straightforward but requires a careful establishment of the correct excitation and summation of the branch flux linkages. The distinction "go" and "return" slot is chosen to clarify that in the two slots the coil sides are located in the current flows in opposite directions.

a) Meshed machine cross section   b) FE flux plot
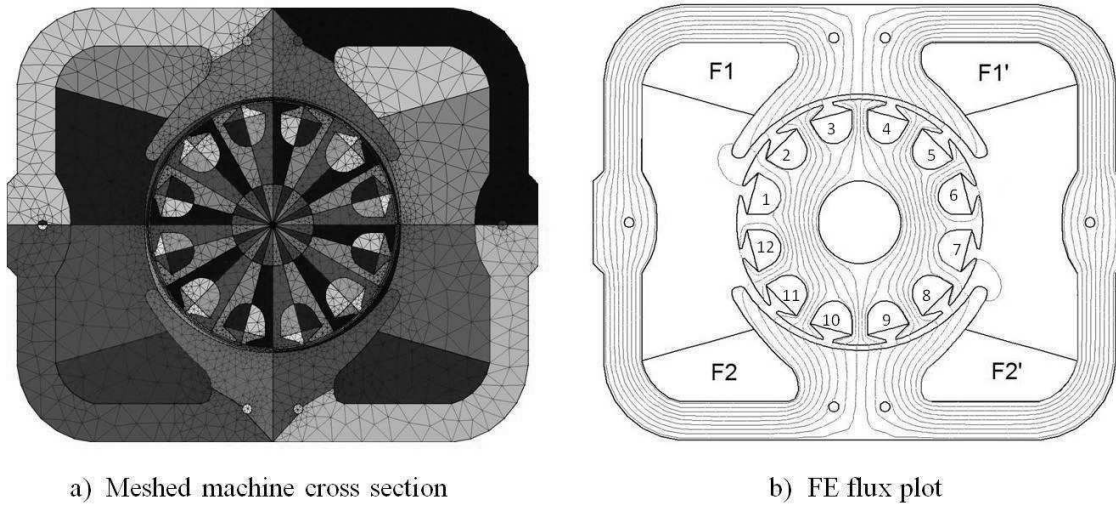
Fig. 3.8 PC-FEA plots and slot numbering convention, $\theta = 0°$

Table 3.4 Rotor slot MMF distribution

Slot No.	Slot MMF
1	$-2N_cI_a/2$
2	$-4N_cI_a/2$
3	$-4N_cI_a/2$
4	$-4N_cI_a/2$
5	$-4N_cI_a/2$
6	$-2N_cI_a/2$
7	$2N_cI_a/2$
8	$4N_cI_a/2$
9	$4N_cI_a/2$
10	$4N_cI_a/2$
11	$4N_cI_a/2$
12	$2N_cI_a/2$

Taking into account the parameters of the armature lap winding of the motor examined (table 3.1) and with regard to the slot numbering convention shown in Fig. 3.8b) one obtains the slot MMFs required to simulate the armature field listed in table 3.4. This slot MMF distribution corresponds to a reference position of $\theta = 0°$. Letting the rotor rotate with that armature slot MMF distribution fixed is equivalent to a stationary rotor with a rotating brush gear where the brushes span less than the width of the inter-segment gap.

The MMF distribution shown in table 3.4 assumes point contacts on opposite commutator segments where no coil is short circuited by carbon brushes. This is in compliance with the way the armature resistance and inductance are measured in practice.

Now, in order to find the full armature inductance the branch inductances have to be found first. In the motor examined the armature winding has two parallel branches which are mutually coupled which leads, taking the $N_s = 24$ armature coils into account, to the apportionment of armature coils between the two parallel armature branches 1 and 2 listed in table 3.5 where, again, fixed point contacts are assumed.

Table 3.5 Apportionment of armature coils

Coil No.	Armature Branch	"go" Slot	"return" Slot
1	1	6	1
2	1	5	12
3	1	5	12
4	1	4	11
5	1	4	11
6	1	3	10
7	1	3	10
8	1	2	9
9	1	2	9
10	1	1	8
11	1	1	8
12	1	12	7
13	2	7	12
14	2	6	11
15	2	6	11
16	2	5	10
17	2	5	10
18	2	4	9
19	2	4	9
20	2	3	8
21	2	3	8
22	2	2	7
23	2	2	7
24	2	1	6

After running FEA with the rotor slot MMF distribution listed in table 3.4 and the field winding left unexcited the armature branch inductances L'_{a1} and L'_{a2} can now be found using the calculated vector potentials and taking into account the apportionment of armature coils listed in table 3.5. As L'_{a1} and L'_{a2} include the mutual effects between the two parallel branches the armature inductance is found

$$L_a = \frac{L'_{a1} \, L'_{a2}}{L'_{a1} + L'_{a2}} \, .$$
(54)

For deeper comprehension of the apportionment of armature coils between the two parallel armature branches 1 and 2 a typical armature winding diagram of a universal motor armature lap winding with two coil sides per layer, twelve slots and a throw of five slot pitches is shown in the appendix A1.

3.3.3 FE-calculation of the field inductance

Similar to the analytical calculation the FE-calculation of the field winding is straightforward. The armature is left unexcited and the coil sides of the field winding (see Fig. 3.8) are carrying the MMFs $\Theta_{F1} = \Theta_{F2} = I_F N_{Fc}$ and $\Theta_{F1'} = \Theta_{F2'} = -I_F N_{Fc}$.

Now, the inductances L'_{F1} and L'_{F2} of the two field coils can be calculated from the vector potentials. As L'_{F1} and L'_{F2} include the mutual coupling between the two field coils the field inductance as a series connection of the two field coils can be found as follows

$$L_F = L'_{F1} + L'_{F2}. \tag{55}$$

3.3.4 FE-calculation of the inductance of a single rotor coil

Assuming a coil in the slots 1 and 6 with regard to Fig. 3.8 the slot MMF required is $\Theta_1 = -\Theta_6 = I_c N_c$ and all other coils are left unexcited. The single coil inductance is then found using the vector potentials in slot 1 and slot 6.

3.3.5 FE-calculation of the mutual inductance of two rotor coils with coinciding coil axes

Two rotor coils are assumed to be located in two different pair of slots in a way that their coil axes coincide. For convenience these pairs of slots are chosen to be 1;6 and 12;7. Now, with the same excitation as in 3.3.4 the mutual inductance can be deduced from the vector potentials in the slots 12 and 7.

3.3.6 FE-calculation of the mutual inductance of one rotor coil and the armature winding

The single rotor coil is assumed to be located in the slots 1 and 6. The armature winding is considered the current carrying winding and assumed to be separated from the single rotor coil. Hence, the rotor slot MMF distribution in table 3.4 only needs to be changed for slot 1 to $-N_c I_d/2$ and for slot 6 to $-3N_c I_d/2$. Subsequently, FEA is performed and the mutual inductance can be deduced from the vector potentials in the slots 1 and 6.

3.3.7 FE-calculation of the mutual inductance of one rotor coil and the field winding

The single rotor coil is assumed to be located in the slots 1 and 6. The field winding is considered the current carrying winding. Now, with the same excitation as in 3.3.3 the mutual inductance can be deduced from the vector potentials in the slots 1 and 6.

3.3.8   FE-calculation of the mutual inductance of the armature winding and the field winding

Considering the armature winding as the current carrying winding the slot MMFs are the same as in table 3.4 and the mutual inductance with the field winding is found from the vector potentials taken from the locations of the coil sides of the field coils.

3.4   Inductance Measurements

3.4.1   AC measurements

The AC method is often chosen to determine inductances in power systems. It is simple to setup and evaluate. To measure the self inductance of a coil its ohmic copper resistance R is determined first using 4 wire or DC bridge measurements [29]. Subsequently, the coil is excited with an AC voltage of known frequency f, and the rms values of the coil current I_c and the voltage across the coil terminals V_c are measured. The coil inductance L_c is then found solving the AC impedance formulation for L_c as follows

$$L_c = \frac{1}{2\pi f}\sqrt{\left[\frac{V_c}{I_c}\right]^2 - R^2}$$

(56)

and the mutual inductance M_{12} between two coils 1 and 2 is found

$$M_{12} = \frac{1}{2\pi f}\frac{V_1}{I_2}$$

(57)

where V_1 is the rms value of the voltage measured across the terminals of coil 1 and I_2 is the rms value of the current in coil 2.

However, despite its simplicity the AC method should not be the method of choice to determine inductances of electrical machines. Due to resistance and parasitic induced currents in conductive components in the neighbourhood of the circuit whose inductance is to be measured, AC methods are of questionable value [28]. Not only these currents lead to incorrect test data, their influence is also supply frequency dependent owing to the eddy currents induced in the lamination stack [30]. To overcome these difficulties Jones' bridge method [31] is applied which is explained in the next subsection.

Due to the uncertainties arising with the use of an AC inductance measurement it is only applied here to demonstrate its weakness compared to DC bridge techniques [30], [31].

3.4.2   Jones Bridge measurements

In this method described by C. V. Jones [31] to measure the self inductance of a coil the problems of measurement errors due to currents in coupled circuits (including eddy currents) are avoided. The principle is based on a balanced DC bridge that compensates for the ohmic copper resistance of the coil whose inductance is to be measured. If the DC supply voltage is removed or reversed after the bridge is balanced, a transient disturbance occurs in the bridge which causes the voltage across the bridge to take non-zero values before it reaches the final steady-state condition which is again balance. Thus, the voltage across the bridge is integrated during the transient disturbance to obtain the inductance of the coil. In the measurements, the current through the coil was reversed using an H-bridge. The circuit diagram of the test setup can be seen in Fig. 3.9.
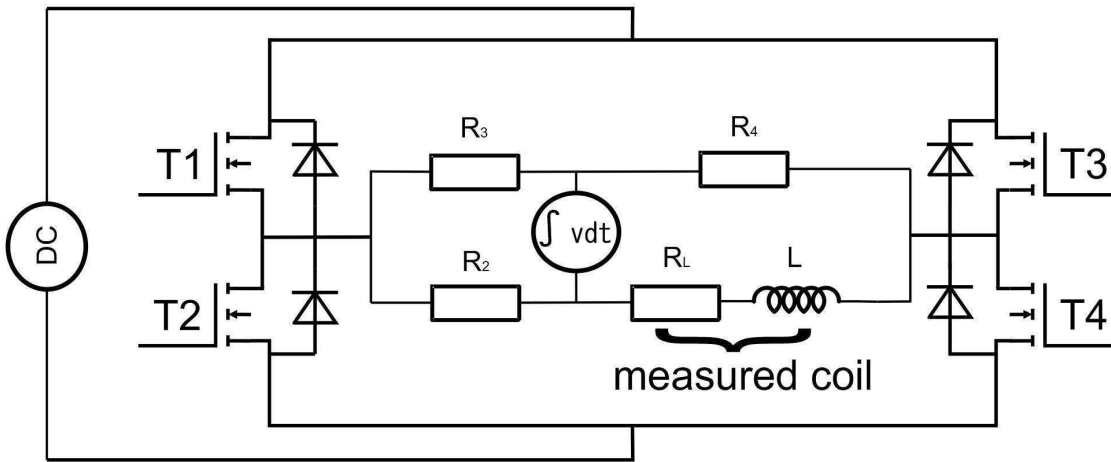
Fig. 3.9 Circuit diagram of self inductance measurement

After the bridge circuit comprising the measured coil (copper resistance R_L, inductance L) and the non-inductive resistors R_2, R_3, and R_4 is balanced with resistor variable R_2 the integrating voltmeter across the two bridge branches indicates a value of zero. Subsequently, the current in the bridge is reversed by switching the pair of conducting transistors T1 and T4 off and, after a dead time of approximately 1 µs, switching the pair of transistors T3 and T2 on. The transient disturbance causes a voltage drop across the integrating voltmeter which is analysed [28] using the voltage drop v_p across the parallel circuit i.e the sum of the voltage drops across R_3 and R_4 which is equal to the sum of the voltage drops across R_2 and the measured coil. Hence

$$v_p = (R_2 + R_L)i_L + L\frac{di_L}{dt} \tag{58}$$

where i_L is the current in the coil, and for the voltage drop v_2 across R_2 one obtains

$$v_2 = \frac{R_2}{R_L + R_2}\left[v_p - L\frac{di}{dt}\right]. \tag{59}$$

Moreover, the voltage drop v_3 across R_3 is

$$v_3 = \frac{R_3}{R_3 + R_4}v_p \tag{60}$$

and the voltage v across the integrating voltmeter is

$$v = v_2 - v_3 \tag{61}$$

and, the balanced condition

$$\frac{R_3}{R_3 + R_4} = \frac{R_2}{R_L + R_2} \tag{61}$$

yields

$$v = -\frac{R_2}{R_L + R_2}L\frac{di_L}{dt} \tag{62}$$

for the bridge voltage drop.

Hence, if the current in the coil is reversed from I to $-I$ the integrating voltmeter reads

$$\Psi = \int_0^\infty v\,dt = -\frac{R_2}{R_L + R_2}L\int_I^{-I} di \tag{63}$$

which yields for the inductance

$$L = \frac{1}{2}\left[1 + \frac{R_L}{R_2}\right]\frac{\Psi}{I}. \tag{64}$$

Now, in order to determine the mutual inductance between two coils the method proposed in [31] again uses an integrating voltmeter which is connected across the terminals of an open

circuit coil which is magnetically coupled to another coil that is undergoing a current reversal.

Again, the H-bridge was used to reverse the current in one coil 1 (in this case from $-I_1$ to I_1)

and the integrating voltmeter across the terminal of the second coil 2 reads

$$\Psi = \int_0^\infty v_2 \, dt = M_{21} \int_{-I_1}^{I_1} di_1 \tag{65}$$

and the mutual inductance can be found as follows

$$M_{21} = \frac{\Psi}{2I_1}. \tag{66}$$

The measurements of self - and mutual inductances were performed as described below.

For the measurement of the armature inductance supply leads were soldered to two opposite commutator bars. This ensured a fixed armature slot MMF distribution as shown in table 3.4. Subsequently the armature inductance was measured with the Jones bridge.

The measurement of the field winding was straightforward, the two field coils were connected in series (aiding in the d-axis, as connected in normal operating conditions) and the self inductance of the field winding was measured with the Jones bridge.

In the measurements of the self inductance of a single armature coil only a single rotor coil was galvanically isolated from the rest of the armature winding and its self inductance was measured with the Jones bridge.

For the measurements of the mutual inductance between a single armature coil and the armature winding the single coil was left isolated from the rest of the winding and the gap in the armature winding caused by its exclusion was bridged by a piece of copper wire. The current supplied through the soldered leads to the armature was then reversed using the H-bridge and the voltage caused by that current reversal in the single armature coil was integrated in order to find the mutual inductance.

In order to measure the mutual inductance between two single rotor coils located in different pairs of slots with coinciding coil axes these coils were isolated from the armature winding and the voltage in one coil caused by current reversal in the other coil was integrated.

The measurement of the mutual inductance between the field winding and the single rotor coil was done in the same manner, the current in the field winding was reversed and the voltage in the single rotor coil was integrated.

The mutual inductance the field winding and the armature winding is found reversing the current in the armature and integrating the voltage inducted in the field winding.

The non-inductive resistors used are of substrate film type (see Fig. 3.10) and the H-bridge transistors were controlled by an FCIV controller[4] (see Fig. 3.11).
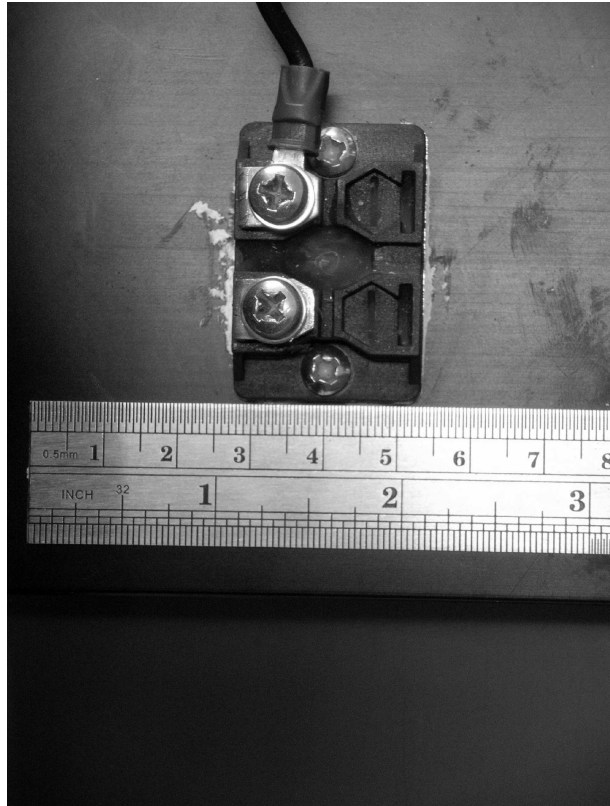
Fig. 3.10 Non-inductive film resistor

Fig. 3.11 FCIV controller

---

[4] The transistor switching algorithm was implemented by Mr Calum Cossar, researcher and lecturer at the School of Engineering, University of Glasgow

3.5   Comparison of calculated and measured Inductances

3.5.1   Comparison at fixed rotor position

Here, the analytically and numerically calculated inductances are compared to the measured inductances at the rotor position of $\theta = 0°$. The commutator lead of the armature used of $22.5°$ is considered in both the analytical and the numerical calculations. It is equivalent to a brush shift against the direction of rotation and yields the per unit brush shift of $\beta = 1/8$ used in the analytical calculations. In the numerical calculations the excitations are set as described above and the armature is turned to $\theta = 22.5°$ to account for the commutator lead. The comparison of measured and calculated inductances can be found in table 3.6. In addition to the analytical calculations and the FEA data there is an additional column for the FEA data corrected for end winding leakage (analytically calculated as shown above; applicable to self inductances only) as well as columns showing the errors between analytical calculations and FEA data (corrected for end winding leakage for self inductances) e_C, FEA data and AC measurements e_{CT1}, and FEA data and Jones' measurement technique e_{CT2} ($100\% \cdot (1 - \text{FEA value} / \text{comparison value})$). One can see that for almost every inductance measured and calculated the measurement technique proposed by Jones is significantly more precise than the AC method and should therefore be the preferred inductance measurement method for electrical machine inductances. The AC method gives errors of up to 26 % and is not further pursued.

Table 3.6 Comparison of calculated and measured inductances

Inductance	Calculations			Measurements		Errors		
	Analytical	FEA	FEA + End Windings	AC Test	Jones' Bridge	e_C [%]	e_{CT1} [%]	e_{CT2} [%]
L_A [mH]	9.090	8.560	8.640	8.220	8.710	4.950	5.109	0.804
L_F [mH]	67.760	70.800	70.900	56.050	68.500	4.634	26.494	3.504
L_c [µH]	298.250	281.460	285.120	238.000	292.000	4.402	19.798	2.356
M_{cc} [µH]	275.870	245.010	-	207.000	266.000	11.186	18.362	7.891
M_{Ac} [µH]	424.290	425.150	-	438.000	413.000	0.203	2.934	2.942
M_{Fc} [mH]	3.350	3.300	-	3.900	3.000	1.493	15.385	10.000
M_{FA} [mH]	11.600	12.400	-	10.900	11.700	6.896	13.761	5.983

3.5.2   Comparison at several rotor positions

In order to cover the change of inductance with rotor position FEA was performed as described in 3.3 over the full range of $360°$ and measurements were performed as described in 3.4.2 in

a range of 42° in 6° steps. For exact positioning in the measurements the motor was mounted on a dividing head as shown in Fig. 3.12.
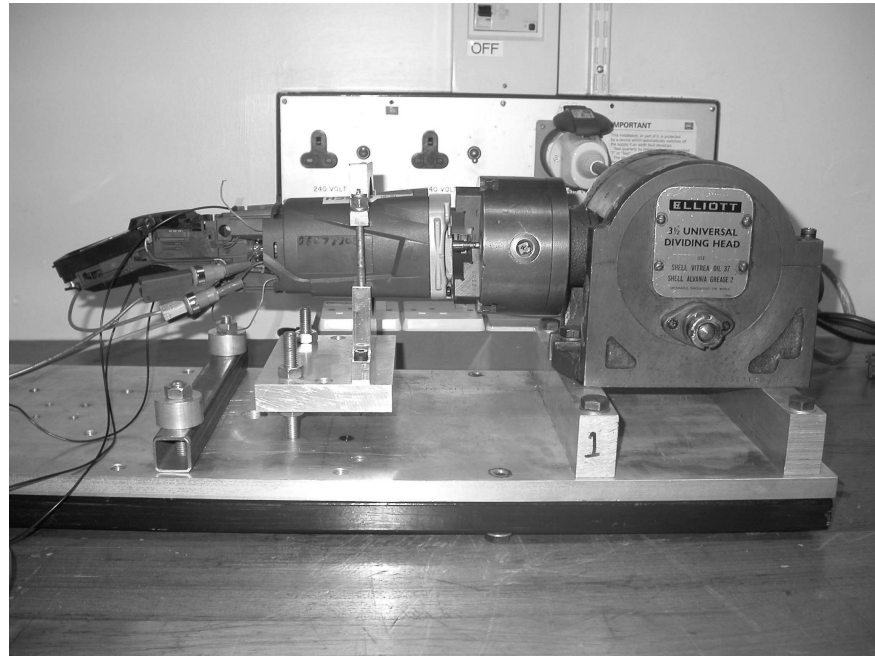
Fig. 3.12 Universal motor mounted on dividing head

The inductances calculated using FEA and measured [31] can be seen in Fig. 3.13 to Fig. 3.19 corrected for the commutator lead.
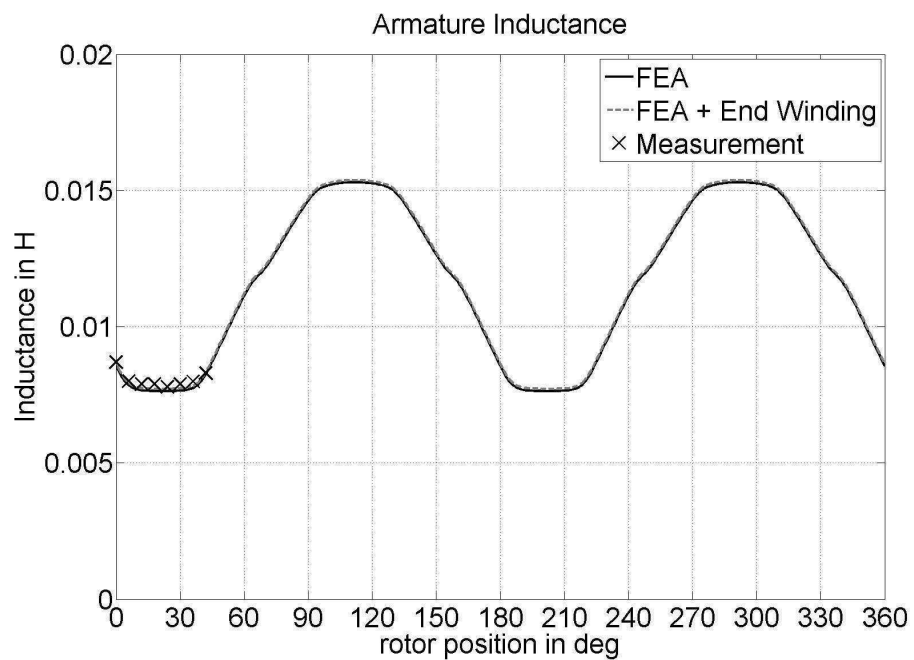
Fig. 3.13 Armature Inductance
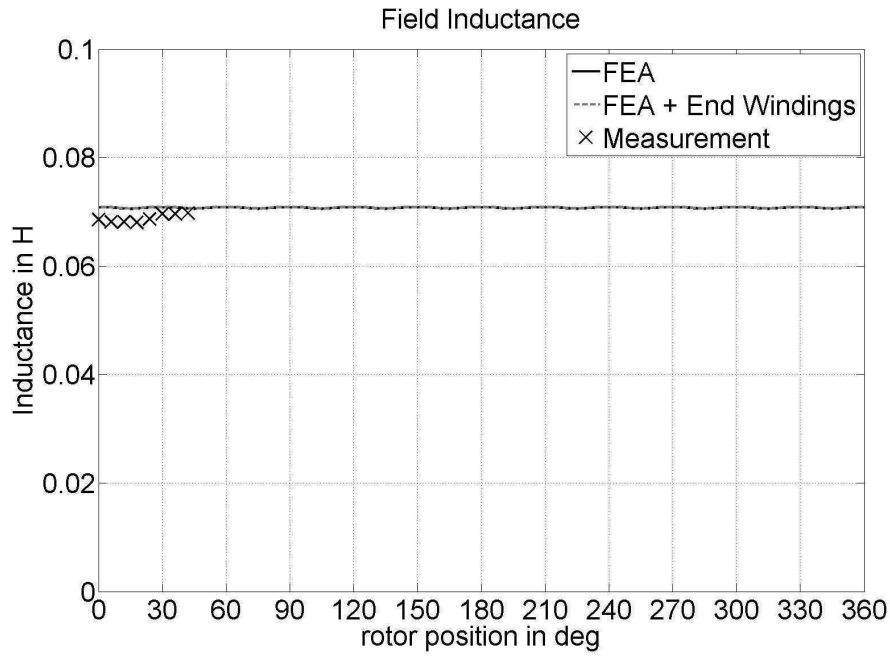
Fig. 3.14 Field Inductance
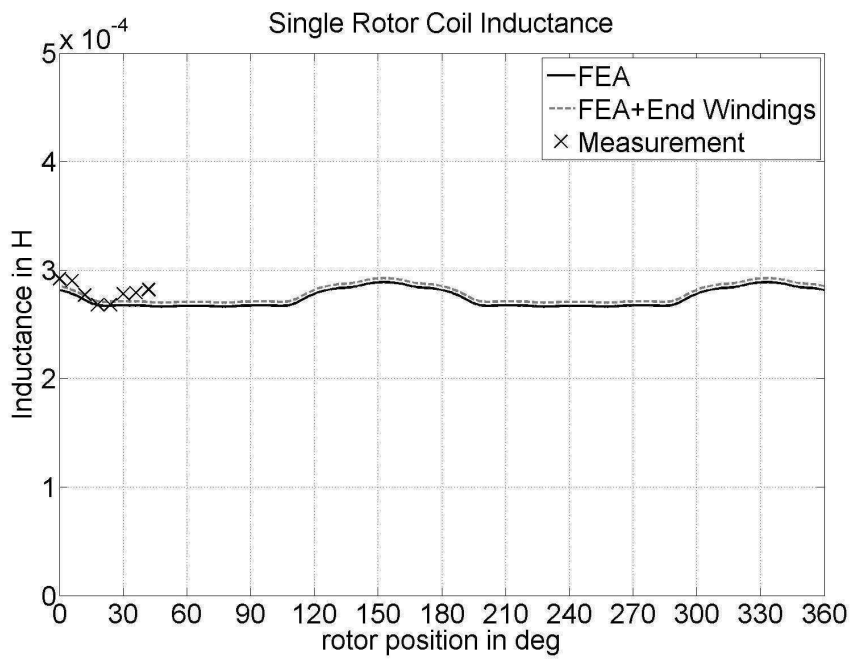
Fig. 3.15 Single rotor coil inductance
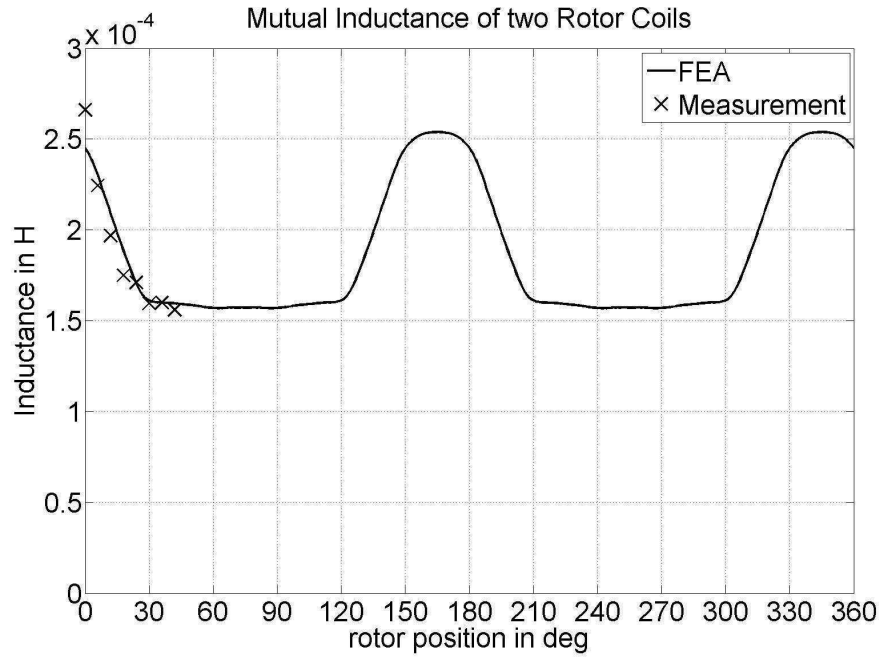
Fig. 3.16 Mutual inductance of two rotor coils
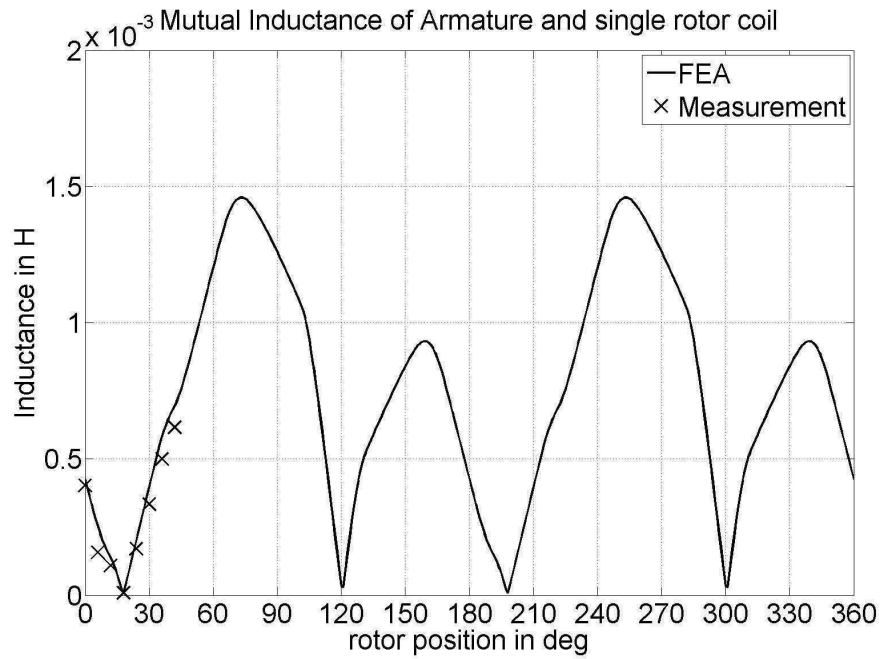
Fig. 3.17 Mutual inductance of single rotor coil and armature winding
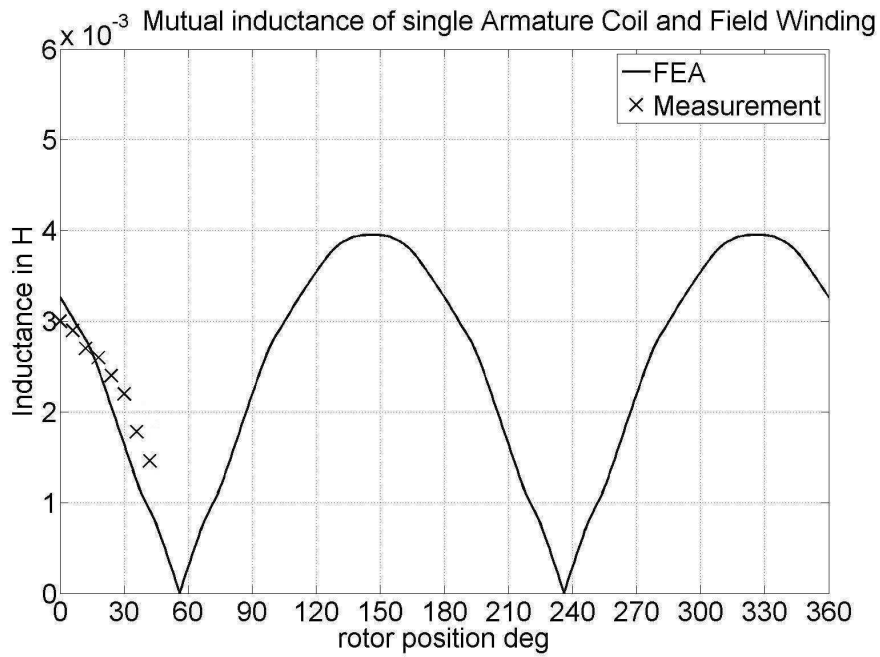
Fig. 3.18 Mutual inductance of single rotor coil and field winding
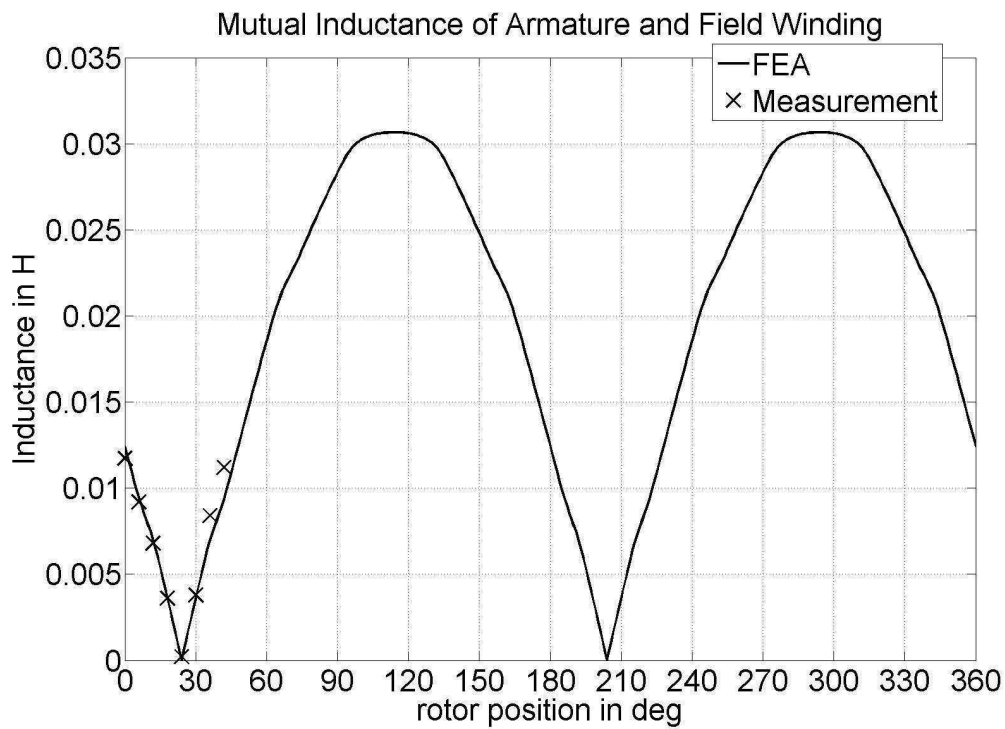
Fig. 3.19 Mutual inductance of armature and field winding

3.6   Discussion of Saturation Effects

As universal machines are usually driven into high saturation during operation at rated power a brief discussion of the change of inductance with current will be given at this point. Due to the high utilisation of the ferromagnetic material *i.e.,* the relationship of flux linkage and current in a coil becomes highly nonlinear [61], the effective coil inductance decreases. The saturation level of the machine will mainly change with the motor current. Small changes that may occur due to commutating currents [10] are not taken into consideration. Hence, the full motor inductance (series connection of field and armature inductance) at a fixed rotor position was calculated for different currents using FEA. In the calculation all rotor coils and the field coils were excited so the calculated motor inductance contains all mutual effects between rotor and stator. Similar to [10] the variation of the per unit inductance (normalised to the unsaturated value of 65.8 mH) with current can be seen in Fig. 7.20.
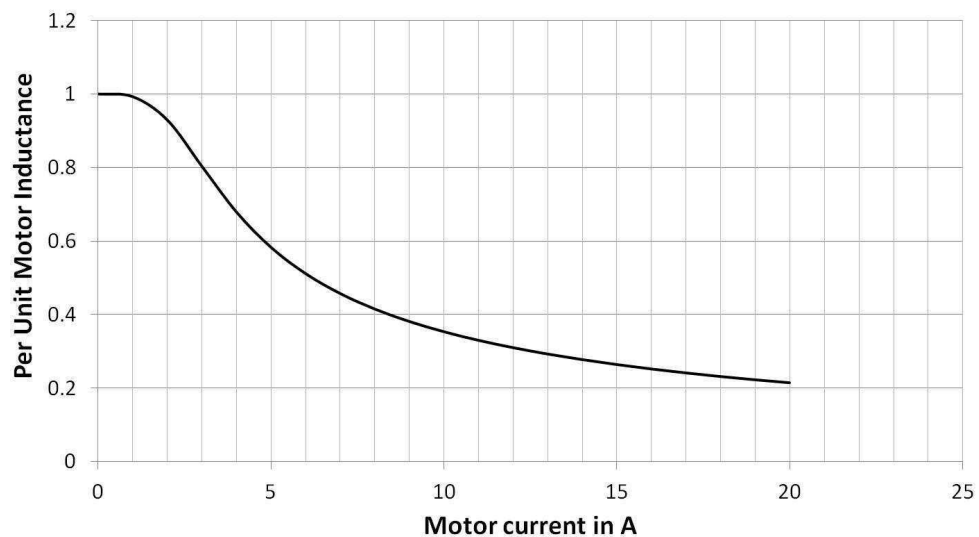
Fig. 3.20 Effect of saturation on motor inductance

It can be observed that the saturation already starts at a motor current of 1A and the motor inductance decreases steadily from this point. At 20A its value has diminished to approximately 20% of the unsaturated value.

For the self inductance of a commutating coil, the saturation will affect the air gap component of that inductance (if not damped, see chapter 7). Also mutual inductances associated with flux paths through the ferromagnetic part of the machine will be affected by saturation. FEA is a computing tool in the mathematical machine analysis capable of dealing with the difficulties arising with saturation.

3.7   Conclusions

In this chapter it was demonstrated that, for unsaturated universal machines, analytical calculations of self and mutual inductances of salient pole machines are an important comparative method in order to verify the use of FEA in motor analysis. The agreement of the analytical calculations and FEA is satisfying and the correction for end winding leakage does not seem to be necessary for the FE-calculated inductances. Moreover, in the analytical equations the influence of certain geometry parameters is highlighted which, despite the limitations with regard to magnetic saturation and slotting effects, makes the analytical calculation an essential tool in motor analysis.

Furthermore, measurement techniques are applied to verify the mathematical analysis. It can be demonstrated that with the method proposed in [31] good accuracy can be achieved whereas a simple AC method proves to be inadequate for electrical machine inductances.

The influence of saturation effects on the motor inductance is discussed, too. The change of the motor inductance with motor current can be seen from a curve computed using FEA. The inductance starts decreasing at a motor current of 1A due to saturation of the steel.

With regard to a machine simulation model FEA is a tool capable of dealing with variations of the machine inductances with rotor position and motor current. Hence, FEA is applied to calculate the machine inductances in the overall simulation model (see chapter 8).

4   A Brush Model for detailed Commutation Analysis

4.1   Brush Models in Commutation Analysis

In the past the analysis of commutation of universal motors has received considerable attention and many significant works on that subject have been published such as [9]-[22]. In this chapter the problem of modelling the brush resistance in commutation analysis by means of equivalent circuits is examined. In Fig. 2.1 it can be seen that the voltage in a commutating coil is equal to the difference of the brush voltages at the two adjacent commutator bars the coil is connected to. Hence, brush resistance has to be considered in the mathematical analysis of commutation. This problem has already been addressed by other authors in previous works such as [10], [11] where a brush resistance matrix is used that includes the brush and contact resistances . The brush resistances are calculated by means of 2D finite element conduction field solutions where Dirichlet boundary conditions are applied to brush - commutator interfaces and the opposite surface of the brush. The resistances of the brush body are calculated using an energy formulation. The contact resistances (see Fig. 2.8) are found using an empirical equation. In [12] the procedure is very similar, the resistor network representing the brush is found using a commercial finite element software package.

A curve of the brush to bar voltage drop is used in [13] instead of a resistor network. The argument is that the saturation in the brush to bar voltage curve is not covered sufficiently by use of contact resistance. A mathematical expression is derived from a measured saturating brush to bar voltage curve which is then used in the analysis.

Formulations for brush to bar voltage drops using parameters obtained in tests are also applied in [9] and [14] whereas in [9] the distinction between a static (constant current density) and a dynamic (time dependent currents) voltage drop characteristic is made.

In [18] the brush voltage drop is obtained following the guidelines of the carbon brush manufacturer which leads to a voltage drop expressed as a function of current density.

Although these approaches are quite practical this chapter develops a more rigorous method using resistor networks. The highly nonlinear contact resistance between the brush and the

commutator bar taken from experimental work provides reliable data in support of this method.

The resistor networks established are considerably different from the networks established by other authors.

4.2   Mathematical Formulations

4.2.1   Formulation of the conduction problem

A brush making contact with 2 commutator segments is depicted in Fig. 4.1. It is assumed there is a uniformly distributed current density J_1 at the top of the brush and two further current densities J_2 and J_3 at the brush-to-segment contact areas. In this case J_1 is flowing into the brush and J_2 and J_3 are flowing out of the brush. Similar to a nodal point in an electric network the sum of currents entering the brush must be equal to the sum of currents emerging from the brush. Hence, the summation of current density $\vec{J}$ over the whole surface $\vec{S}$ of the brush must be zero and Kirchhoff's law applies [32], so that

$$\oint \vec{J} d\vec{S} \ = \ 0 \tag{67}$$

which yields

$$div \ \vec{J} \ = \ 0 \ . \tag{68}$$

The current density $\vec{J}$ is linked to the electric field strength $\vec{E}$ via the conductivity κ. Furthermore it is well known that the electric field strength is the negative gradient of the scalar potential φ. Hence,

$$div \kappa \vec{E} \ = \ - \ \kappa \, div \, grad \, \varphi \ = \ 0 \tag{69}$$

and

$$div \, grad \, \varphi \ = \ 0 \tag{70}$$

where (70) represents Laplace's equation which in a 2D problem can be rewritten as

$$\frac{\partial^2 \varphi}{\partial x^2} \ + \ \frac{\partial^2 \varphi}{\partial y^2} \ = \ 0 \ . \tag{71}$$
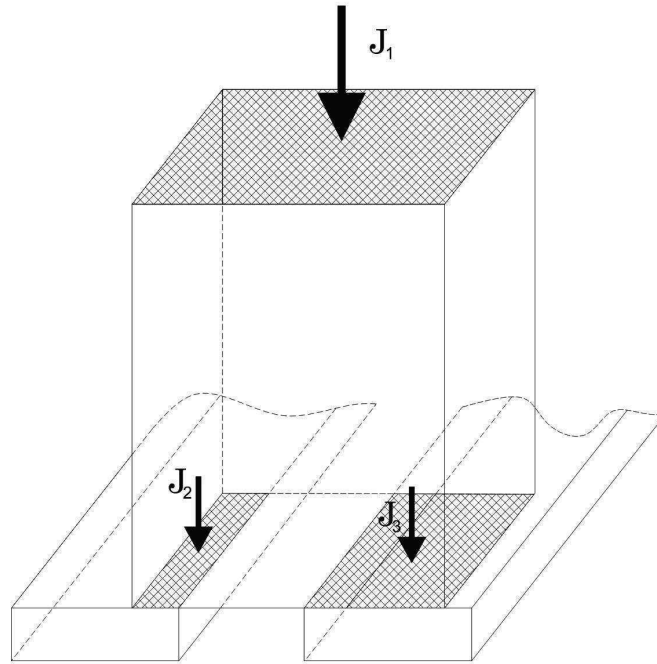
Fig. 4.1 Current densities at brush contact

4.2.2 Formulation of the numerical problem

The way of solving the conduction problem was chosen to be a finite differences algorithm implemented in Pascal. A 5-star point is depicted in Fig. 4.2. For convenience an equidistant grid is implemented. Hence, the linear system to be solved is

$$[A]\vec{x} = \vec{b} \tag{72}$$

where $[A]$ is the coefficient matrix, $\vec{x}$ is the vector of unknown node potentials and $\vec{b}$ is the solution vector according to the boundary conditions. The matrix $[A]$ has only certain bands of non-zero elements. These bands consist of reoccurring tridiagonal matrices $[TD]$ and diagonal matrices $[D]$. The structure of a coefficient matrix $[A]$ with 36x36 elements can be seen in Fig. 4.3. Less than 12% of the elements are non-zero elements in that matrix. The advantage of that structure is clear. Only the non-zero elements of the tridiagonal matrix $[TD]$ need to be stored and, as all diagonal elements of $[D]$ are equal, all matrix multiplications involving $[D]$ can be reduced to a simple element-wise multiplication which reduces the memory consumption significantly and reduces computing time. $[A]$ can thus be written

57

$$
[A] = \begin{bmatrix} [TD] & [D] & & [0] \\ [D] & \ddots & \ddots & \\ & \ddots & \ddots & [D] \\ [0] & & [D] & [TD] \end{bmatrix}.
\tag{73}
$$
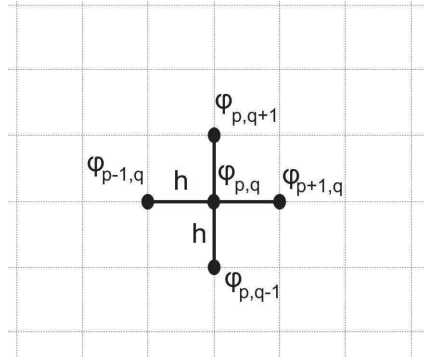
Fig. 4.2 5-point star
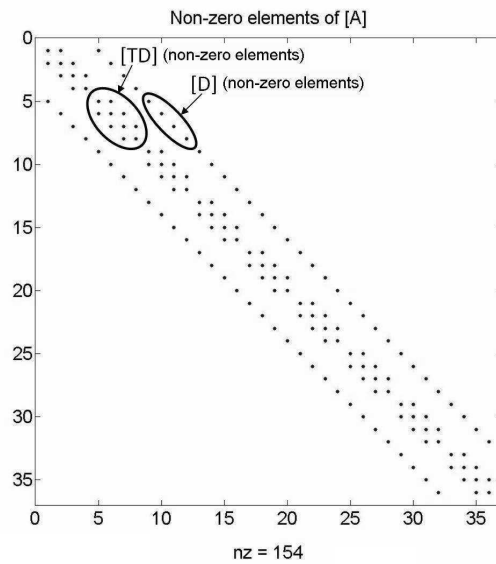
Fig. 4.3 Structure of coefficient matrix

For block tridiagonal systems that are also symmetric *i.e.* $[A_{n+1n}] = [A_{n+1n}]^T$ it is favourable to execute a transformation into a block bidiagonal system [33]. Using an extension of the Thomas algorithm which aims at transforming [A] into a block bidiagonal matrix [H], the whole system is transformed into a new one maintaining the vector $\vec{x}$ as follows

$$
[A]\vec{x} = \vec{b} \quad \Rightarrow \quad [H]\vec{x} = \vec{c}
\tag{74}
$$

Let $[Q^C]$ be the Cholesky factorization of a matrix $[Q]$ so that $[Q] = [Q^C]^T[Q^C]$ [34] and $[H_{ij}]$ a submatrix of $[H]$, and $[A_{ij}]$ a submatrix of $[A]$, respectively. Moreover, let $\vec{x}_i$ and $\vec{c}_i$ be subvectors of $\vec{x}$ and $\vec{c}$, respectively.

Thus, with $[H_{11}] = [A_{11}^{\,C}]$ we get the first row of the new system

$$[H_{11}]^T[H_{11}]\vec{x}_1 + [A_{21}]\vec{x}_2 = \vec{b}_1 \quad | \cdot [H_{11}]^{-T}$$
$$[H_{11}]\vec{x}_1 + [H_{11}]^{-T}[A_{21}]^T\vec{x}_2 = [H_{11}]^{-T}\vec{b}_1 \quad | [H_{21}] = [H_{11}]^{-T}[A_{21}]^T, \vec{c}_1 = [H_{11}]^{-T}\vec{b}_1$$

$$[H_{11}]\vec{x}_1 + [H_{21}]\vec{x}_2 = \vec{c}_1 \tag{75}$$

Accordingly, the second row becomes

$$[H_{21}]^T[H_{11}]\vec{x}_1 + [A_{22}]\vec{x}_2 + [A_{32}]^T\vec{x}_3 = \vec{b}_2 \quad | - \left\{ [H_{21}]^T \cdot eq.\,(75) \right\}$$
$$([A_{22}] - [H_{21}]^T[H_{21}])\vec{x}_2 + [A_{32}]^T\vec{x}_3 = \vec{b}_2 - [H_{21}]^T\vec{c}_1 \quad | \cdot [H_{22}]^{-T},$$
$$[H_{22}]^T[H_{22}] = ([A_{22}] - [H_{21}]^T[H_{21}])$$
$$[H_{22}]\vec{x}_2 + [H_{22}]^{-T}[A_{32}]^T\vec{x}_3 = [H_{22}]^{-T}(\vec{b}_2 - [H_{21}]^T\vec{c}_1) \quad | [H_{32}] = [H_{22}]^{-T}[A_{32}]^T,$$
$$\vec{c}_2 = [H_{22}]^{-T}(\vec{b}_2 - [H_{21}]^T\vec{c}_1)$$

$$[H_{22}]\vec{x}_2 + [H_{32}]\vec{x}_3 = \vec{c}_2 \tag{76}$$

where the unknown $\vec{x}_1$ is eliminated. This procedure is continued for all rows leaving

$$[H_{nn}]\vec{x}_n = \vec{c}_n \tag{77}$$

in the last row. Subsequently, the system can be solved by block back substitution starting at the last row by solving (77) for $\vec{x}_n$. Subsequently all remaining subvectors of $\vec{x}$ are calculated row by row. This algorithm simplifies remarkably due to the fact that $[A_{ii}]=[TD]$ and $[A_{i+1i}]=[A_{i+1i}]^T=[D]$. Non-zero elements of $[H]$ are stored in one dimensional arrays for the main diagonal and the upper secondary diagonal. This algorithm provides a stable direct calculation of the linear system where no iteration is needed.

At this point the algorithm was tested against an analytical solution as shown in the appendix A2. Good agreement of numerically and analytically calculated scalar potentials could be observed. In these simplified tests cases Dirichlet boundary conditions only were applied in order to obtain unique analytical solutions.

However, under normal conditions the analysis of the brush - commutator problem needs to be treated with mixed Dirichlet - and Neumann boundary conditions. As an unique analytical solution for mixed boundary conditions can only be found in exceptional cases [35] the numerical algorithm is necessary to obtain reliable results.

4.3   The equivalent Circuits of the Brush

4.3.1   The reference system

The model was created for universal motors with a brush width to commutator segment width ratio $\zeta \in [1; 2]$ as the most common ratios in practice are in this range. Therefore, a maximum of three commutator segments in contact with a brush at a time occurs and a minimum of one commutator segment in contact with a brush occurs depending on ζ. Thus it is necessary to distinguish between the different cases in order to establish the appropriate circuit. The case where only one commutator segment is connected to a brush can be modelled by a single resistor and is irrelevant for commutation analysis as no coil is short circuited. However, the different cases occur in cyclic transitions and therefore, the equivalent circuits of the brush change in cyclic transition as well.
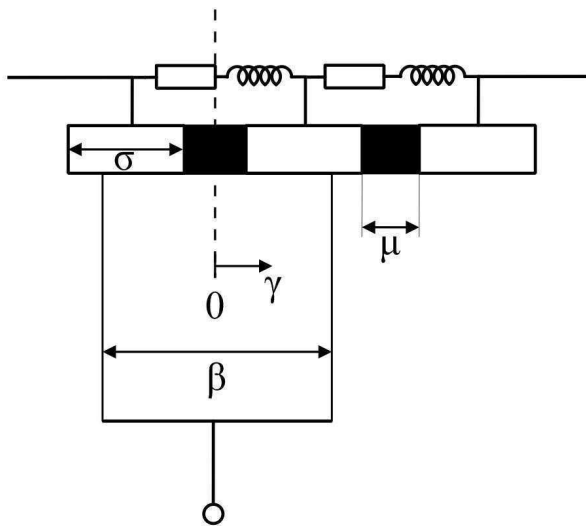
Fig. 4.4 Reference system

In Fig. 4.4 the reference system is depicted, where σ is the commutator segment width, μ is the width of the insulating layer between two segments, β is the brush width and γ is the rotor position angle; all measured in radians. The commutator is moving in positive direction of γ. The reference point $\gamma = 0$ is located where the centre axis of the insulation layer is aligned with the brush centre axis.

If $\beta \leq 2\mu + \sigma$ there is a transition from one to two segments in contact with the brush only. Starting from $\gamma = 0$, where two segments are in contact with the brush, the transition from two to one connected segments takes place at $\gamma_1 = 1/2(\beta - \mu)$. Subsequently, the transition from one to two segments takes place at $\gamma_2 = \gamma_1 + 2\mu + \sigma - \beta$ and the next transition from two to one segment in contact with the brush at $\gamma_3 = \gamma_2 + \beta - \mu$ etc. As mentioned above the case of one segment in contact with the brush only *i.e.* no coil is shorted by that brush is modelled by a single resistor and more important for motor performance analysis than commutation analysis.

If $\beta > 2\mu + \sigma$ a cyclic transition between the cases of two and three segments in contact with the brush takes place. The case of one segment making contact with the brush does not occur. At $\gamma = 0$ two segments are connected to the brush until the angle $\gamma_1 = 1/2(3\mu - \beta) + \sigma$ is reached where the transition from two to three segments in contact with the brush takes place. The next transition from three to two segments takes place at the angle $\gamma_2 = \gamma_1 + \beta - 2\mu - \sigma$ and the consecutive transition to three segments connected to the brush occurs at $\gamma_3 = \gamma_2 + 3\mu + 2\sigma - \beta$ etc.

According to the defined transition angles, the corresponding resistor networks are taken into account in an overall commutation analysis. Hereinafter, only the cases of more than one commutator segment in contact with a brush at a time are going to be analysed.

It has to be pointed out that the brush resistances are contact area dependent and vary between a minimum value and an infinitely high resistance (segment not in contact with the brush). In the simulation model the resistance cannot become infinite and has to be limited to a reasonably high value Γ. Due to the usually high conductivity of the brush material a value of $\Gamma = 500\ \Omega$ is sufficient.

4.3.2   Two segments in contact with the brush

The brush is a conductive body which theoretically allows current flow between all its terminals[5]. It can thus be considered a resistor between every pair of terminals. Maintaining the convention of terminal numbering in Fig. 2.1 the equivalent circuit of the brush for this case is the circuit depicted in Fig. 4.5 where terminal 0 denotes the top of the brush, terminal 1 the first segment connected to the brush, terminal 2 the second segment connected to the brush. Those represent the circuit terminals of the brush body resistor network whilst 0, 1' and 2' represent the terminals of the full brush circuit including contact resistances. R_a, R_b and R_c are the internal resistances of the network. It is obvious that resistances measured across two terminals $\{0, 1, 2\}$ are combinations of R_a, R_b and R_c. The equations describing this relationship are

$$R_{01} = \frac{R_a(R_b + R_c)}{R_a + R_b + R_c} \tag{78}$$

$$R_{02} = \frac{R_b(R_a + R_c)}{R_a + R_b + R_c} \tag{79}$$

---

[5]The brush terminals are referred to the parts of the carbon brush where current can flow into or out of the brush.

and

$$R_{12} = \frac{R_c(R_a + R_b)}{R_a + R_b + R_c}.$$
(80)
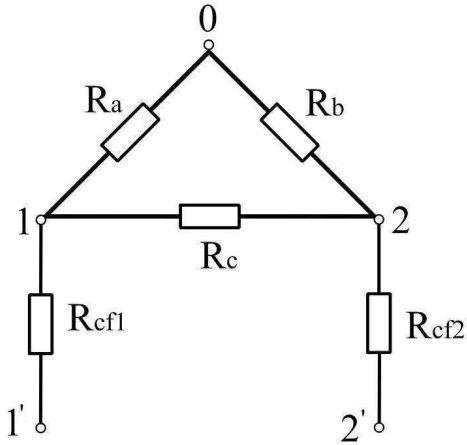
Fig. 4.5 Equivalent circuit of a brush in contact
with two commutator bars

So far only the brush body resistances have been annotated. Yet in order to establish a complete circuit of the brush resistance active in the operating motor the nonlinear contact resistance has to be considered, too. This resistance represents the contact constriction resistance in series with the film resistance [36]. In the circuit (Fig. 4.5) this resistance is added at both brush commutator interfaces and denoted R_{cf1} and R_{cf2}. A method to obtain these resistances is discussed later on.

4.3.3 Three segments in contact with the brush

The number of internal resistors doubles in the case of three segments in contact with the brush, *i.e.* two coils commutating at this brush, compared to the previous case (two segments in contact with the brush). This is due to the fact that again, a resistor is considered between every pair of terminals. A resistance measured across two terminals {0, 1, 2, 3} is a combination of the internal resistors. The use of six resistors in this case allows a unique set of equations of the terminal resistances R_{01}, R_{02}, R_{03}, R_{12}, R_{23} and R_{13} as functions of the internal resistances R_u, R_v, R_w, R_x, R_y and R_z (see Fig. 4.6) and appears to be the most natural circuit for this configuration.

Also, the contact resistances R_{cf1}, R_{cf2} and R_{cf3} are considered.

The relationship between terminal resistances

Fig. 4.6 Equivalent circuit of a brush in contact
with three commutator bars

and internal resistances now becomes more complex as shown in the appendix A3. For example, the resistance measured between terminal 0 and terminal 1 can be found redrawing the circuit in Fig. 4.6 to the one depicted in Fig. 4.7a) (contact resistances omitted). After using the delta - star transformation shown in Fig. 4.8 the circuit becomes the one in Fig. 4.7b) where

$$R_{0s} = \frac{R_v R_w}{R_v + R_w + R_y} \tag{81}$$

$$R_{2s} = \frac{R_v R_y}{R_v + R_w + R_y} \tag{82}$$

$$R_{3s} = \frac{R_w R_y}{R_v + R_w + R_y} \tag{83}$$

a) Before Delta - Star - Transformation

b) After Delta - Star - Transformation
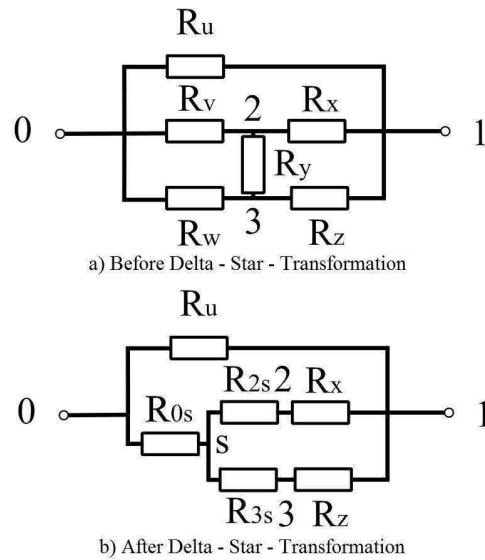
Fig. 4.7 Circuits to obtain R_{01}
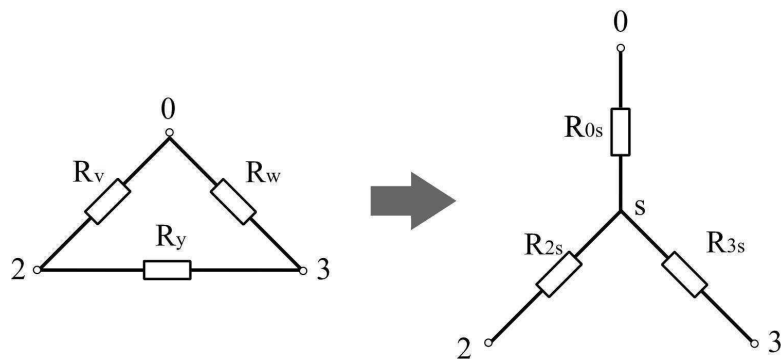
Fig. 4.8 Delta - Star transformation

and the expression for R_{01} derived from this circuit can be found in appendix A3.

4.4   The Strategy to obtain the Internal Resistances of the Brush

At the first stage, the terminal resistances R_{01}, R_{02}, and R_{12} in the case of 4.3.2 or R_{01}, R_{02}, R_{03}, R_{12}, R_{23} and R_{13} in the case of 4.3.3 are calculated one by one. This is done by allowing current flow between two terminals only, *i.e.* setting Dirichlet boundary conditions there, and setting Neumann boundary conditions at all remaining parts of the brush periphery to prevent any current flow there. This way of proceeding is shown for the resistances in the case of 4.3.3 in Fig. 4.9. The scalar potentials φ at the Dirichlet boundaries are set externally. Subsequently, Laplace's equation is approximated by a five-point-star finite-difference method with user-defined mesh density using the transformation to a block bidiagonal system as described above.
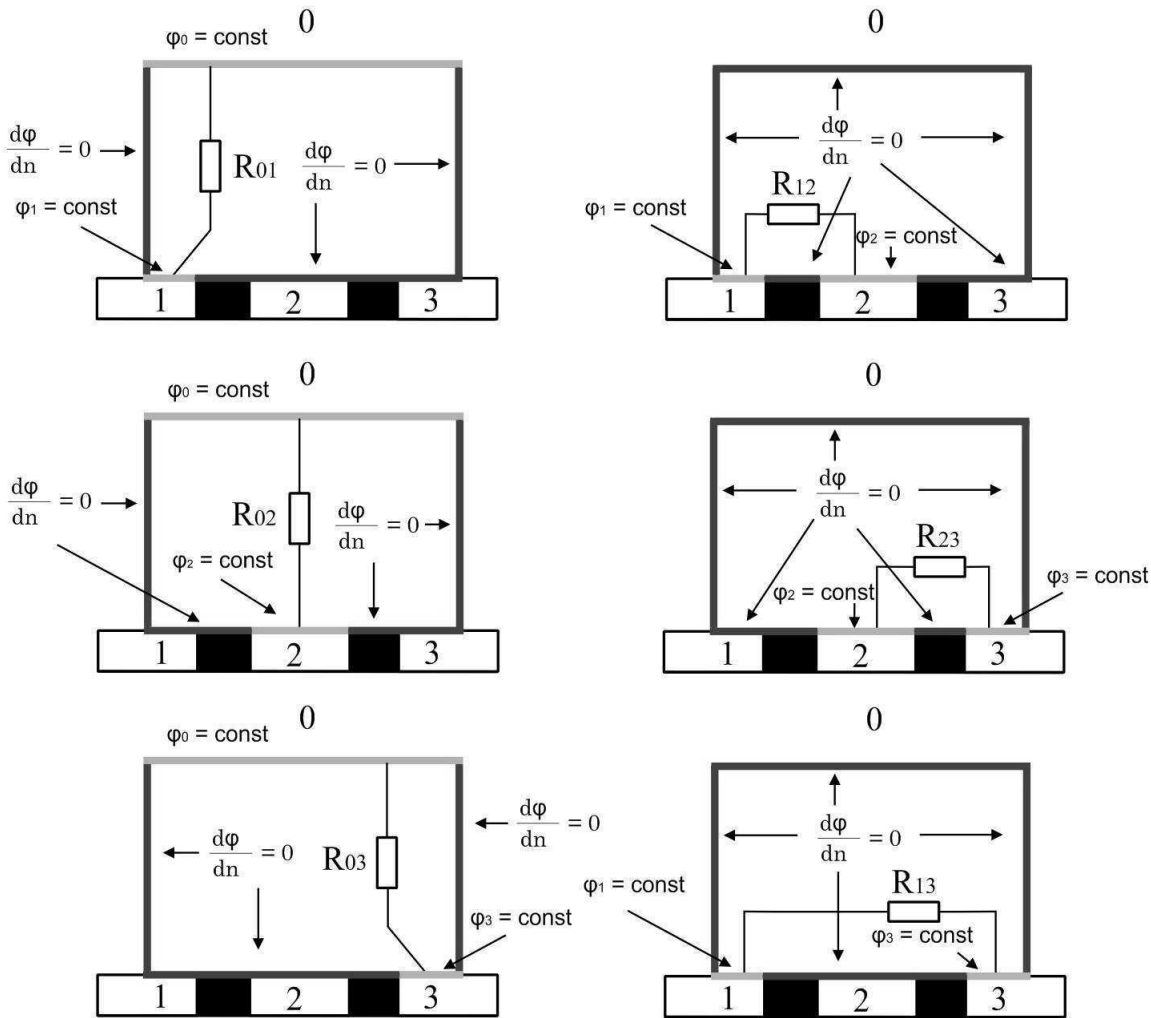
Fig. 4.9 Boundary conditions used in external resistance calculation

To calculate the power dissipated in the isotropic or the anisotropic brush correctly the field distribution in the brush has to be covered sufficiently as the current flow in the brush will be distorted due to different degrees of anisotropy [37]. Therefore the volume integral of the product of vectors of current density $\vec{J} = \langle \kappa \rangle \, \vec{E}$ and electric field strength $\vec{E} = -\text{grad } \varphi$ is applied as follows

$$P = \int_V \vec{J}\vec{E}\,dV \approx \sum_{i=1}^{m} \left[\frac{J_x^2}{\kappa_x} + \frac{J_y^2}{\kappa_y} \right] V_i \qquad (84)$$

where m is the number of grid points, V_i a discrete volume element and the conductivities κ_x and κ_y can differ from each other in an anisotropic brush.

Now, the resistance active between two terminals p and q can be found as follows

$$R_{pq} = \frac{(\varphi_p - \varphi_q)^2}{P} \qquad (85)$$

This is done consecutively for all pairs of terminals of the equivalent circuit of the brush. It is important at this stage to point out that if there are more than two terminals "active", *i.e.* current is flowing in or out, rigorously speaking the dissipated power cannot be resolved into the parts dissipated at different internal resistances. This arguments becomes clear regarding Fig. 4.10. The calculated vector field of the current density is depicted for a case where three segments are in contact with the brush. Current flow is allowed between all four terminals at the same time by applying Dirichlet boundary conditions at all current carrying terminals ($\varphi_0 \neq \varphi_1 \neq \varphi_2 \neq \varphi_3$).

The calculated dissipated power P cannot be resolved in the parts dissipated at R_u, R_v, R_w, R_x, R_y and R_z (see Fig. 4.6). This is the reason the strategy of calculating the terminal resistors one by one is proposed.
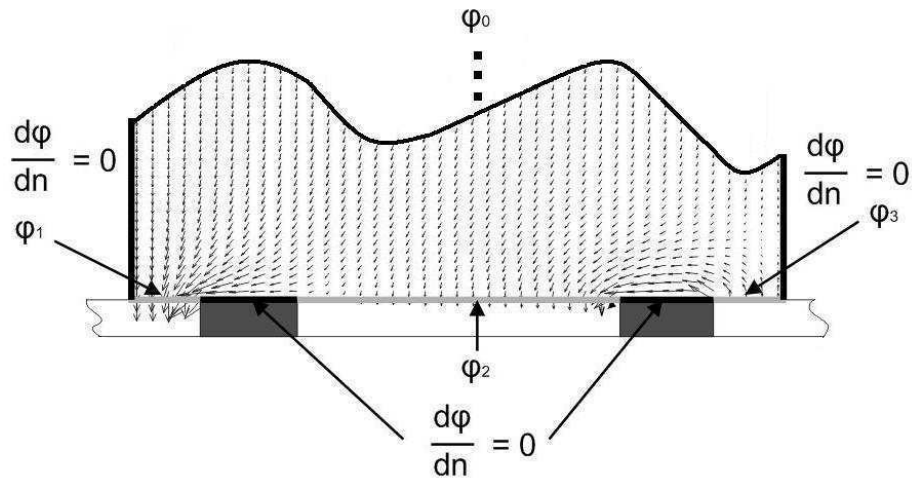
Fig. 4.10 Calculated current density vector field with four terminals active

After all external (terminal) resistances have been determined at a certain rotor position the nonlinear system

$$\vec{R}_{ext} = \vec{\xi}(\vec{R}_{int}) \tag{86}$$

where $\vec{R}_{ext}$ is the vector of external resistances and $\vec{R}_{int}$ is the vector of internal resistances, (86) needs to be inverted. To solve

$$\vec{R}_{int} = \vec{\xi}^{-1}(\vec{R}_{ext}) \tag{87}$$

it is transformed into a problem of finding zeros as follows

$$\vec{f}(\vec{R}_{int}) = \vec{\xi}(\vec{R}_{int}) - \vec{R}_{FD} = 0 \tag{88}$$

where $\vec{R}_{FD}$ is the vector of external resistances $(= \vec{R}_{ext})$ calculated by the finite difference method. More - dimensional Newton - Raphson's method was chosen to solve (88).

4.5   Newton - Raphson's Method applied to calculate the internal Resistances

In the general Newton - Raphson's method the iterative solution for (88) of the linearised problem is found solving

$$^{n+1}\vec{R}_{int} = {}^{n}\vec{R}_{int} - [J({}^{n}\vec{R}_{int})]^{-1}\vec{f}({}^{n}\vec{R}_{int}) \tag{89}$$

until the stop criterion is satisfied, where

$$[J] = \begin{vmatrix} \dfrac{\partial R_{01}}{\partial R_a} & \dfrac{\partial R_{01}}{\partial R_b} & \dfrac{\partial R_{01}}{\partial R_c} \\[3mm] \dfrac{\partial R_{02}}{\partial R_a} & \dfrac{\partial R_{02}}{\partial R_b} & \dfrac{\partial R_{02}}{\partial R_c} \\[3mm] \dfrac{\partial R_{12}}{\partial R_a} & \dfrac{\partial R_{12}}{\partial R_b} & \dfrac{\partial R_{12}}{\partial R_c} \end{vmatrix} \tag{90}$$

is the Jacobian matrix of the system in the case of 4.3.2 and

$$[J] = \begin{bmatrix} \dfrac{\partial R_{01}}{\partial R_u} & \dfrac{\partial R_{01}}{\partial R_v} & \dfrac{\partial R_{01}}{\partial R_w} & \dfrac{\partial R_{01}}{\partial R_x} & \dfrac{\partial R_{01}}{\partial R_y} & \dfrac{\partial R_{01}}{\partial R_z} \\[2mm] \dfrac{\partial R_{02}}{\partial R_u} & \dfrac{\partial R_{02}}{\partial R_v} & \dfrac{\partial R_{02}}{\partial R_w} & \dfrac{\partial R_{02}}{\partial R_x} & \dfrac{\partial R_{02}}{\partial R_y} & \dfrac{\partial R_{02}}{\partial R_z} \\[2mm] \dfrac{\partial R_{03}}{\partial R_u} & \dfrac{\partial R_{03}}{\partial R_v} & \dfrac{\partial R_{03}}{\partial R_w} & \dfrac{\partial R_{03}}{\partial R_x} & \dfrac{\partial R_{03}}{\partial R_y} & \dfrac{\partial R_{03}}{\partial R_z} \\[2mm] \dfrac{\partial R_{12}}{\partial R_u} & \dfrac{\partial R_{12}}{\partial R_v} & \dfrac{\partial R_{12}}{\partial R_w} & \dfrac{\partial R_{12}}{\partial R_x} & \dfrac{\partial R_{12}}{\partial R_y} & \dfrac{\partial R_{12}}{\partial R_z} \\[2mm] \dfrac{\partial R_{23}}{\partial R_u} & \dfrac{\partial R_{23}}{\partial R_v} & \dfrac{\partial R_{23}}{\partial R_w} & \dfrac{\partial R_{23}}{\partial R_x} & \dfrac{\partial R_{23}}{\partial R_y} & \dfrac{\partial R_{23}}{\partial R_z} \\[2mm] \dfrac{\partial R_{13}}{\partial R_u} & \dfrac{\partial R_{13}}{\partial R_v} & \dfrac{\partial R_{13}}{\partial R_w} & \dfrac{\partial R_{13}}{\partial R_x} & \dfrac{\partial R_{13}}{\partial R_y} & \dfrac{\partial R_{13}}{\partial R_z} \end{bmatrix} \tag{91}$$

is the Jacobian matrix of the system in the case of 4.3.3. However, to achieve convergence the initial guess needs to be chosen sufficiently close to the desired solution. Otherwise, Newton - Raphson's method may diverge [38]. For the more-dimensional problem to be solved where resistances vary according to the rotor position an accurate choice of the starting point is therefore difficult. Hence, Newton - Raphson's method was modified in order to achieve global convergence [33], [38]. This is done by adding a damping term $\lambda \in (0; 1)$ in (89) which now needs to be rewritten as

$$^{n+1}\vec{R}_{int} = {^n}\vec{R}_{int} - \lambda [J({^n}\vec{R}_{int})]^{-1} \vec{f}({^n}\vec{R}_{int}) \tag{92}$$

The strategy is to force the iteration progression to decrease monotonically so that $\|\vec{f}\|_2 > \|\vec{g}\|_2$ where λ is initially set to 1 to try a full Newton step and

$$\vec{g}(\vec{R}_{int}) = \vec{\xi}(\vec{R}_{int} - \lambda [J(\vec{R}_{int})]^{-1}\vec{f}(\vec{R}_{int})) - \vec{R}_{FD} \tag{93}$$

and the Euclidean vector norms of $\vec{f}$ and $\vec{g}$ are calculated for comparison. If $\|\vec{f}\|_2 > \|\vec{g}\|_2$ is not achieved, then λ is multiplied by a constant $\alpha \in (0, 1)$ and $\vec{g}$ is calculated again. This is repeated until $\|\vec{f}\|_2 > \|\vec{g}\|_2$ is satisfied. Subsequently, the next iteration is found using (92) and λ is set to 1 again. This procedure is repeated until all elements of $\vec{f}$ are smaller than the tolerated approximation error ε. An overview of the procedure described can be found in Fig. 4.11 where $\vec{R}*$ is the starting point of the Newton - Raphson method and f_n is an element of $\vec{f}$.
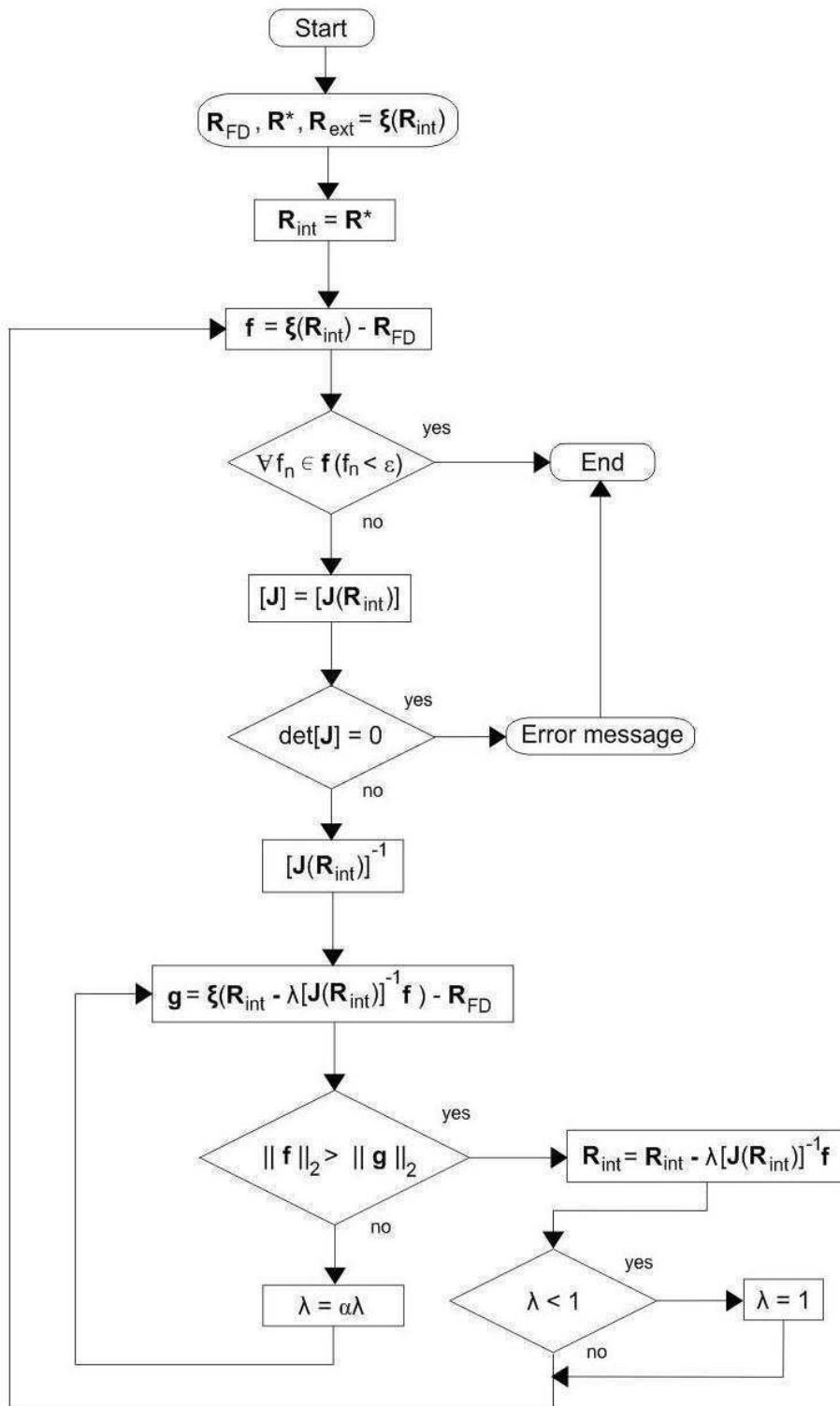
Fig. 4.11 Flow chart of modified Newton - Raphson method

4.6   Proposed Procedure to obtain R_{cf}

As already mentioned the resistance R_{cf} represents the contact constriction resistance in series with the film resistance. In Fig. 4.12 the contact properties of a brush - commutator interface are depicted (greatly zoomed) . The constriction resistance is due to the fact that the actual contact between surfaces is made through microscopic contact spots where the current lines are being constricted and current density is increased. The film resistance is the resistance of the thin oxide layer (film) on the commutator surface. It is the nature of a copper surface that it, once exposed to air, develops oxide layer mainly consisting of Cu_2O. However in the brush - commutator sliding contact also brush particles are incorporated in the film. Moreover, water molecules are part of the film due to condensation as well.

The contact resistance is subjected to many "outer", non-electrical influence parameters such as surface roughness, spring pressure, surrounding atmosphere and material hardness [36]. Additionally, the electrical parameters such as current density in the contact spots and conductivity of the film have a significant influence. Due to such complexity it is explicable that no successful model for the brush contact resistance has been established in the literature and in order to include it into the simulation empirical models or measured values have to be used.

However, in order to include the contact resistance into the calculations as shown in Fig.4.5 and Fig. 4.6 it is identified experimentally.
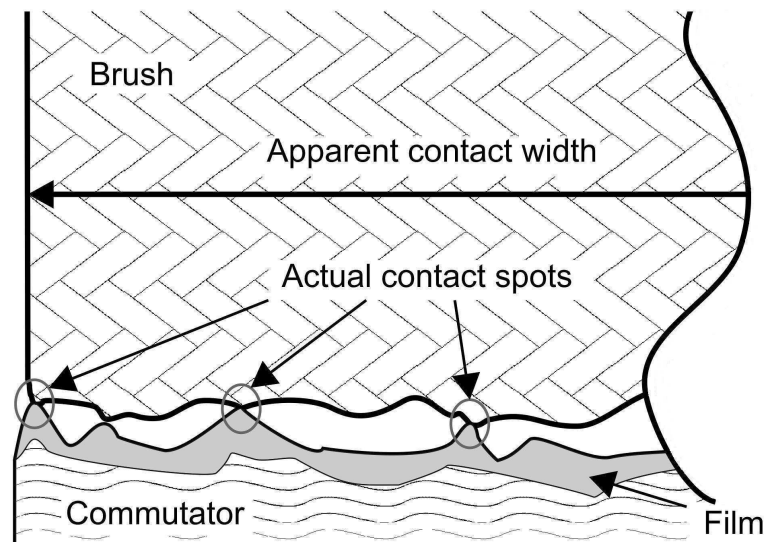
Fig. 4.12 Contact constriction and film at one instant of time

The brush voltage drop comprises the voltage drop along the brush braid and the braid to brush contact, the brush body and the constriction and film resistance [36]. In order to separate the constriction and film resistance from the remaining components of the brush resistance the following procedure is proposed. A blank commutator with 24 segments is mounted on the shaft of an AC motor. Subsequently the brush holder of a motor with an identical commutator is mounted on the housing of the AC motor using an adapter plate (see Fig. 4.13). This ensures that the brushes have the same play and spring pressure they would have under normal motoring conditions. At the blank commutator three pairs of opposite segments are interconnected and the brushes are connected to a DC source. This principle can be seen in Fig. 4.14. It allows six periods of conduction during one revolution as shown in Fig. 4.15.
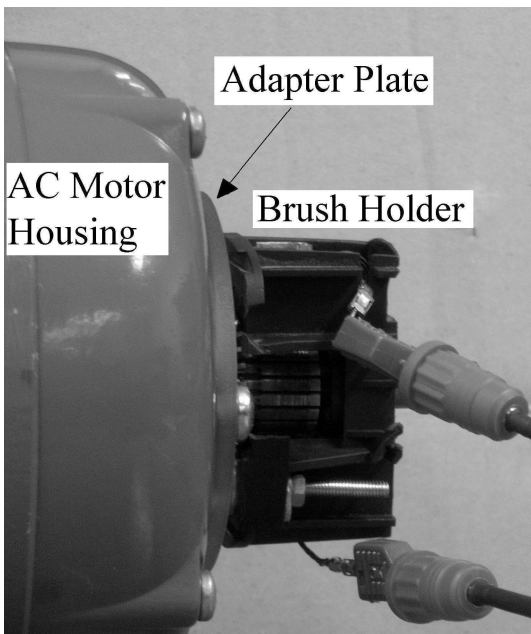
Fig. 4.13 Brush holder and commutator mounted on AC motor shaft
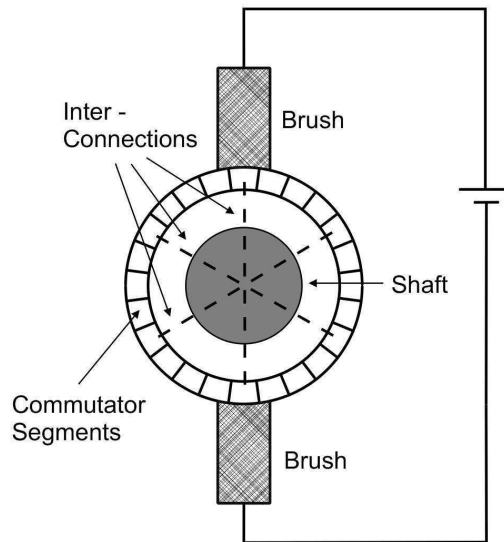
Fig. 4.14 Test setup schematic
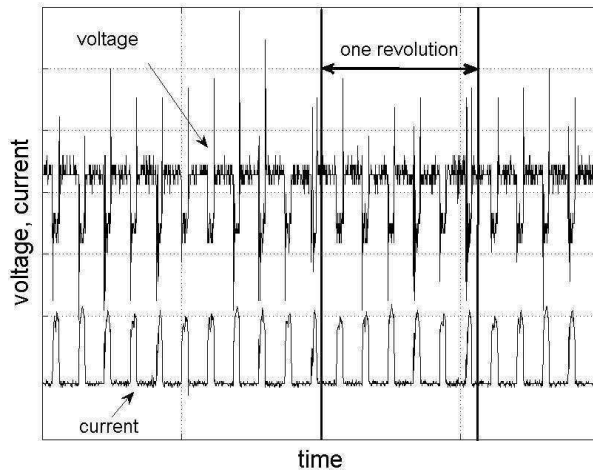
Fig. 4.15 Current and Voltage during tests

70

The AC motor was run until the commutator had a clearly visible film. Then, the voltage and current in the circuit were recorded using a digital oscilloscope. Subsequently, the resistance of the circuit was found as the quotient of instantaneous voltages and currents. In Fig. 4.16 the resistance time waveform can be seen during a period of conduction. Only the resistance during the period of time where the contact areas at both brushes are constant and the resistance is reasonably constant is of interest. The mean value of that resistance of several periods of conduction was used. The tests were repeated for different speeds and currents as the resistance is a function of both.
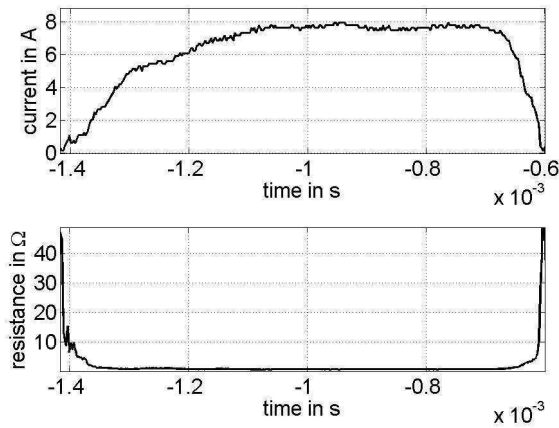
Fig. 4.16 Current and resistance during one period of conduction

Regarding Fig. 4.14 it is obvious that the resistance R measured across the brush-braid terminals is equal to the sum of $2R_{sb}$ (resistances of braids and brush bodies) and $2R_{cf}$ as the resistances of the commutator bars and the inter-connections are negligible. It is well known that the voltage drops are different for anodic and cathodic brushes, yet, as the model is used for AC commutator machines where both brushes become anodic and cathodic during an AC cycle, the use of a mean value seems justified. Now, to determine R_{sb} 4-wire-measurements were performed as shown in Fig. 4.17 and Fig. 4.18. Subsequently, in order to find R_{cf} as a function of the contact area a similar expression as in [10], [11] and [12] is applied.
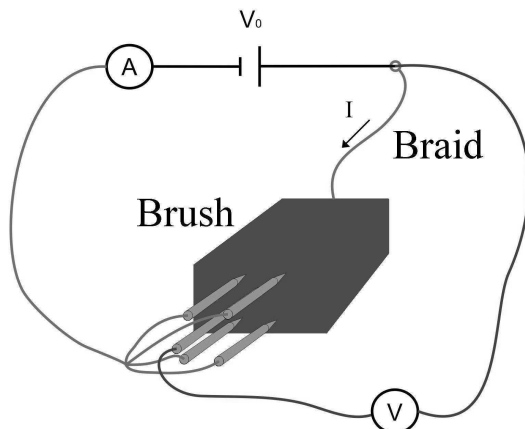
Fig. 4.17 Test principle to determine brush body resistance
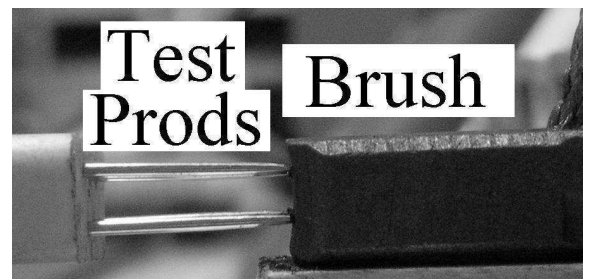
Fig. 4.18 Carbon brush with test prods

For the 4-wire measurements a single brush was connected to a DC source in a way that the brush strand was connected to one terminal of the source and four test prods where connected to the bottom of the brush on one side and connected together to the second terminal of the source on the other side and the current in this circuit was measured. A fifth test prod was applied in the midpoint of the bottom of the brush to measure voltage between this point and the top of the brush stand. Tests were carried out at several currents and it was found that the brush strand and body resistance remained reasonably constant with current. Results can be found in table 4.1.

For the tests described above several sets of brushes of the same type where used in order to obtain expressive results.

Table 4.1 Results of 4-wire tests

I in Amps	V in Volts	R_{sb} in Ω
0.500	0.050	0.100
1.000	0.100	0.100
2.000	0.198	0.099
3.000	0.301	0.100
4.000	0.392	0.098
5.000	0.497	0.099

Now, the contact restriction and film resistance can be found as follows

$$R_{cf} = \frac{1}{2}R - R_{sb} \qquad (94)$$

The highly position dependent R_{cf1}, R_{cf2} and R_{cf3} are then found using the expression

$$R_{cfn} = R_{cf}\frac{A_{full}}{A_n}. \qquad (95)$$

where A_{full} is the apparent contact area at full overlap of the carbon brush and a commutator segment and the position dependent contact areas are found as follows

$$A_1(\gamma) = \begin{cases} (0.5(\beta - \mu) - \gamma)r_c\eta & \gamma \in [0;\gamma_2) \\ 0 & \gamma > \gamma_2 \end{cases} \qquad (96)$$

$$A_2(\gamma) = \begin{cases} (0.5(\beta - \mu) - \gamma)r_c\eta & \gamma \in [0; \gamma_1 - \mu) \\ A_{full} & \gamma \in [\gamma_1 - \mu; \gamma_2 + \mu) \\ A_{full} - (\gamma - (\gamma_2 + \mu))r_c\eta & \gamma \in [\gamma_2 + \mu; p_c) \end{cases} \tag{97}$$

$$A_3(\gamma) = \begin{cases} 0 & \gamma < \gamma_1 \\ (\gamma - \gamma_1)r_c\eta & \gamma \in [\gamma_1; p_c) \end{cases} \tag{98}$$

with the data required taken from table 4.2.

Table 4.2 Parameters of brush during simulation

Parameter	Annotation	Value	Dimension
μ	width of mica	0.053	rad
σ	commutator bar width	0.209	rad
β	brush width	0.405	rad
p_c	commutator pich	$\pi/12$	rad
ζ	β / σ	1.938	–
η	axial brush length	8.000	mm
r_c	commutator radius	12.350	mm
h	brush height	16.000	mm
A_{full}	$\eta\sigma$	20.649	mm^2

The resistance R_{cf} obtained as a function of current density for two different shaft speeds can be seen in Fig. 4.19.
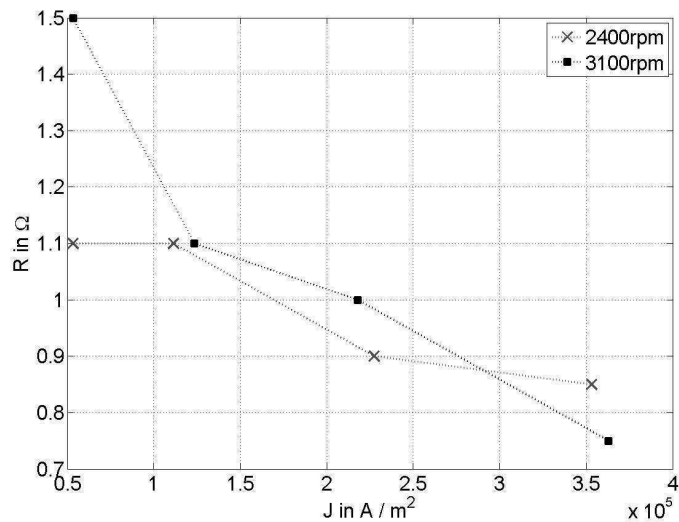
Fig. 4.19 R_{cf} as a function of speed and current density

4.7 Results and Discussion

4.7.1 Simulation results

Simulations were carried out for a brush with the parameters listed in table 4.2. In Fig. 4.20 the calculated external resistances, normalised to Γ, are depicted over about one commutator pitch and the transition points γ_1 and γ_2 are indicated. They are highly position dependent and behave inversely proportional to the contact areas of the commutator bars and the brush. For each position the more-dimensional Netwon-Raphson's method was applied, distinguishing between the three- and the six resistor circuit, to calculate the internal resistances which can be seen in Fig. 4.21. It has to be pointed out that for example R_{a1} progresses to R_u etc. during the cycle. In the annotation the labels of the resistances are chosen with regard to the distinction made in Fig. 4.5 and Fig. 4.6. There is one transition from the three- to the six resistor network (γ_1) and one transition from the six- to the three resistor network (γ_2) within one commutator pitch. In can be seen that the internal resistors show the same behaviour with rotor position as the external ones.
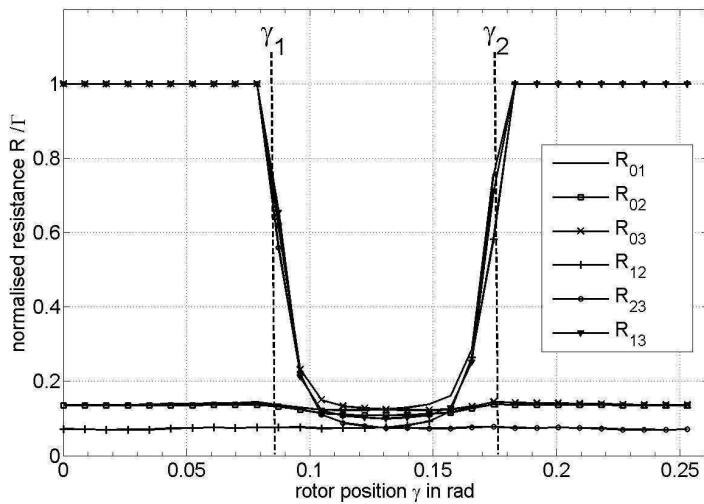
Fig. 4.20 Calculated external resistances
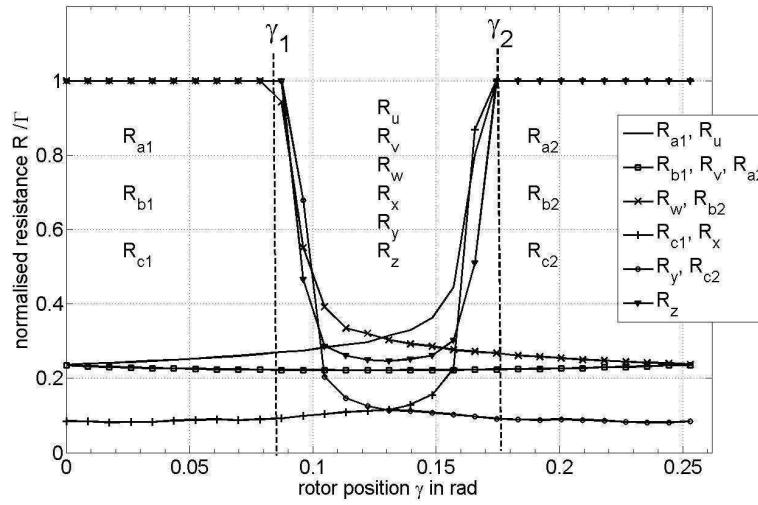
Fig. 4.21 Calculated internal resistances

In the following the effect of anisotropy on the internal resistors is investigated. In order to simplify the annotation only the subscripts u, v, w, x, y and z are used for the resistances. Now, a degree of anisotropy $k = \kappa_y / \kappa_x$ is defined [37] where κ_y is held constant and κ_x is decreased in order to vary k. It is important to note here that in the anisotropic case k needs to be multiplied to the term $\partial^2 \varphi / \partial y^2$ in (71) which, however, does not affect the symmetry of the system (72). The effect on the internal resistors in orthogonal direction to the commutator R_u, R_v and R_w can be seen in Fig. 4.22, moreover the effect on the ones in transversal direction to the commutator R_x, R_y and R_z can be seen in Fig. 4.23. The anisotropy has an effect on all internal resistances, yet it can be noticed that the influence on the transversal ones is considerably higher. As the conductivity κ_x is decreased, the current is drawn more into y-direction due to the higher κ_y, current paths and thus resistances are increased [37]. In the next step the influence of the brush height h on the internal resistances is investigated. The brushes simulated here are isotropic and the height is decreased starting at $h = 16$ mm. The results can be found in Fig. 4.24 and Fig. 4.25. Here the influence of h on the orthogonal and transversal resistances is illustrated. The influence on the orthogonal ones is quite significant (Fig. 4.24) while the influence on the transversal ones (Fig. 4.25) is negligible. In practice this means that R_u, R_v and R_w are strongly affected by brush wear while R_x, R_y and R_z are barely affected. For good recognizability of the effects examined Γ was limited to 5Ω in Fig. 4.20 to Fig. 4.25.
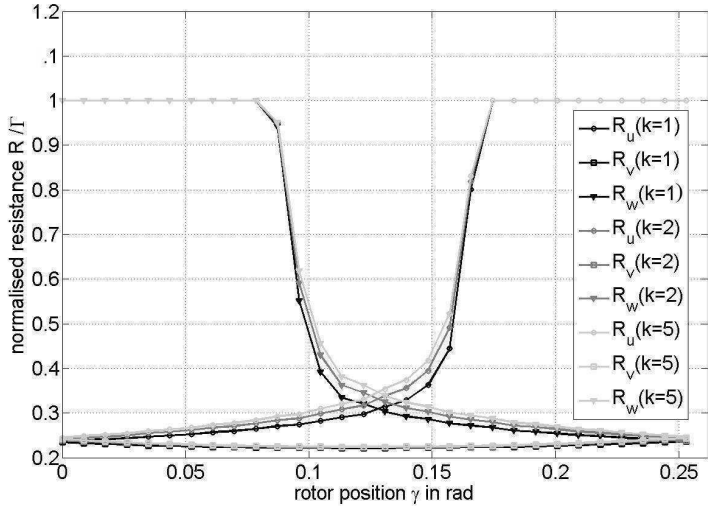
Fig. 4.22 Influence of anisotropy on internal resistances R_{uvw}
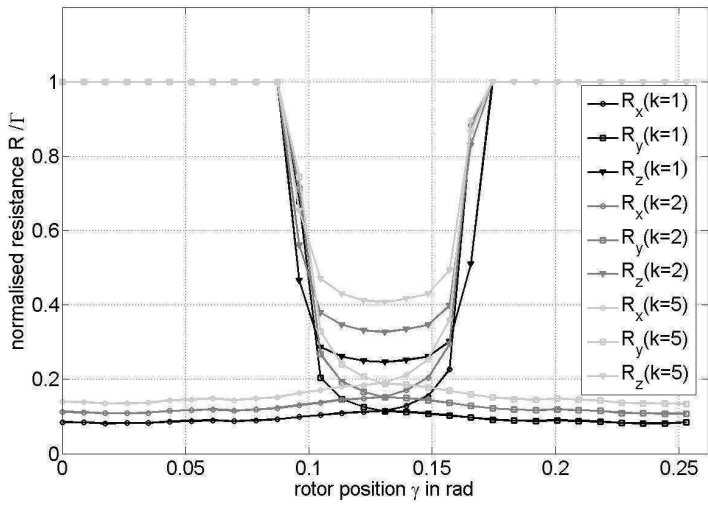
Fig. 4.23 Influence of anisotropy on internal resistances R_{xyz}
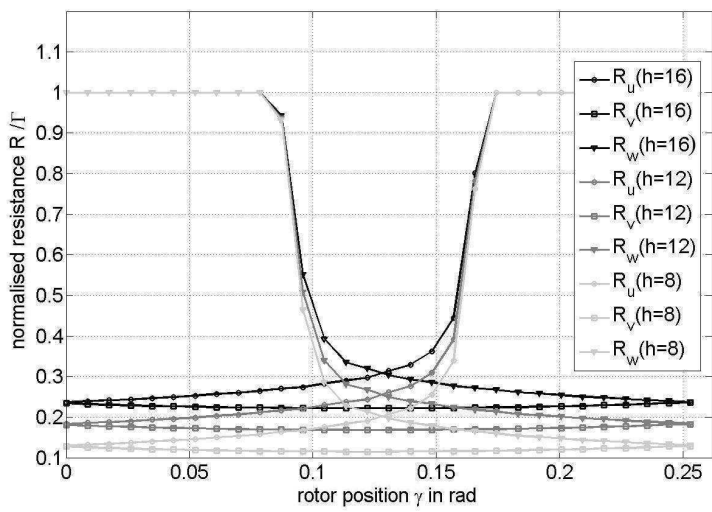
Fig. 4.24 Influence of radial brush height on internal resistances R_{uvw}
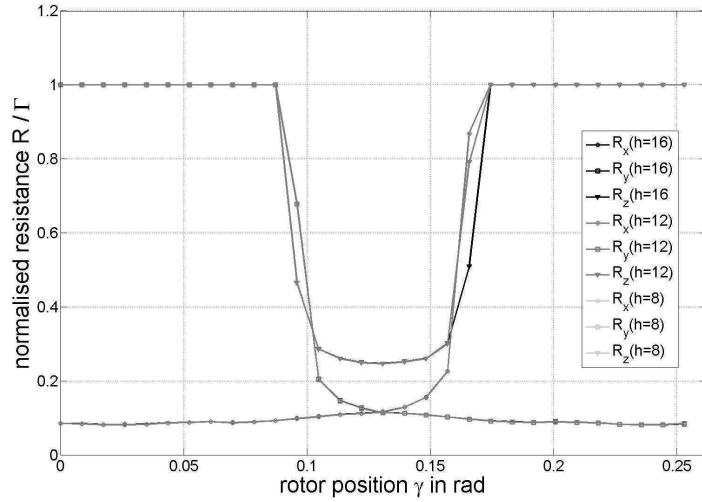
Fig. 4.25 Influence of radial brush height on internal resistances R_{xyz}

4.7.2 Simplified application example of the brush model

To demonstrate prospective use of the brush model a simplified commutating circuit is analysed here. It is assumed that two coils are being short circuited by one brush. The current in the armature I_a is 10A and assumed constant during commutation. Hence, the governing circuit is the one in Fig. 4.26. It is assumed that the coil c_1 which started commutating first is carrying 1A and coil c_2 which started commutating later is carrying a current of 4A.

Using the method described above to obtain R_{cf} for a brush with the parameters listed in table 4.2 a value of 0.325 Ω was found at full contact between the brush and a commutator segment.
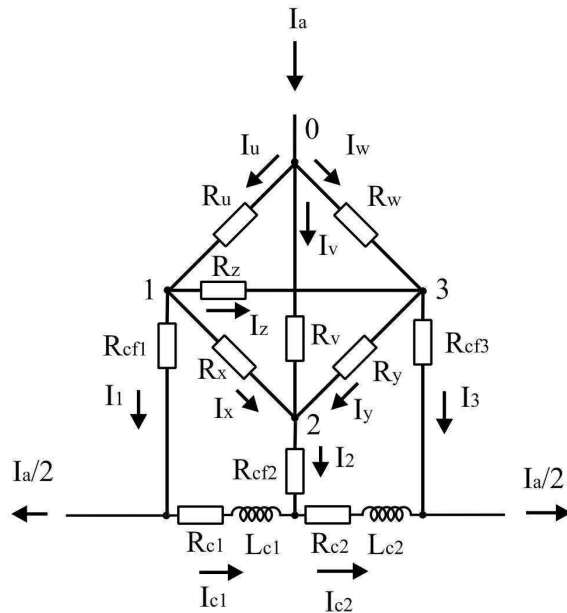
Fig. 4.26 Analysed commutating circuits

The currents emerging from the brush can now be found as follows

$$I_1 = \frac{I_a}{2} + I_{c1} \tag{99}$$

$$I_2 = I_{c2} - I_{c1} \tag{100}$$

$$I_3 = \frac{I_a}{2} - I_{c2} \tag{101}$$

and in order to find the remaining currents in the circuit the node voltage method is applied which gives

$$\begin{bmatrix} V_{02} \\ V_{12} \\ V_{32} \end{bmatrix} = [G]^{-1} \begin{bmatrix} I_a \\ -I_1 \\ -I_3 \end{bmatrix} \tag{102}$$

where [G] is the conductance matrix

$$[G] = \begin{bmatrix} \dfrac{1}{R_u} + \dfrac{1}{R_v} + \dfrac{1}{R_w} & -\dfrac{1}{R_u} & -\dfrac{1}{R_w} \\[2mm] -\dfrac{1}{R_u} & \dfrac{1}{R_u} + \dfrac{1}{R_x} + \dfrac{1}{R_z} & -\dfrac{1}{R_z} \\[2mm] -\dfrac{1}{R_w} & -\dfrac{1}{R_z} & \dfrac{1}{R_w} + \dfrac{1}{R_y} + \dfrac{1}{R_z} \end{bmatrix} \tag{103}$$

and the calculated voltages V_{02}, V_{12} and V_{32} can be used to find all branch currents in the brush circuit as follows

$$I_u = \frac{V_{02} - V_{12}}{R_u} \tag{104}$$

$$I_v = \frac{V_{02}}{R_v} \tag{105}$$

$$I_w = \frac{V_{02} - V_{32}}{R_w} \tag{106}$$

$$I_x = \frac{V_{12}}{R_x} \tag{107}$$

$$I_y = \frac{V_{32}}{R_y} \tag{108}$$

$$I_z = \frac{V_{12} - V_{32}}{R_z}. \tag{109}$$

Considering the currents to be instantaneous, the expressions

$$\frac{di_{c1}}{dt} = \frac{1}{L_{c1}}(R_{cf2}i_2 - R_{cf1}i_1 - R_{c1}i_{c1} + R_x i_x) \tag{110}$$

and

$$\frac{di_{c2}}{dt} = \frac{1}{L_{c2}}(R_{cf3}i_3 - R_{cf2}i_2 - R_{c2}i_{c2} - R_y i_y) \tag{111}$$

can be derived from the circuit, and can be used to calculate the time waveforms of the commutating currents based on the simplifications mentioned below applying Euler's method (112) and (113).

$$^{n+1}i_{c1} = {^n}i_{c1} + \frac{^n di_{c1}}{dt}\Delta t \tag{112}$$

$$^{n+1}i_{c2} = {^n}i_{c2} + \frac{^n di_{c2}}{dt}\Delta t \tag{113}$$

The simulated waveforms can be seen in Fig.4. 27. The circuit was simulated to the point where current reversal in coil c_1 finishes. The influence of the sudden increase of resistance just before the end of commutation can be seen in the time waveform of i_{c1}. The time waveform of i_{c2} is still unaffected as the coil c_2 is still considerably far away from the end of commutation. In addition to table 4.2 $\kappa_x = \kappa_y = 40kS/m$ and $\Gamma = 500\ \Omega$. A mechanical speed $\omega = 80\pi\ s^{-1}$ was assumed.
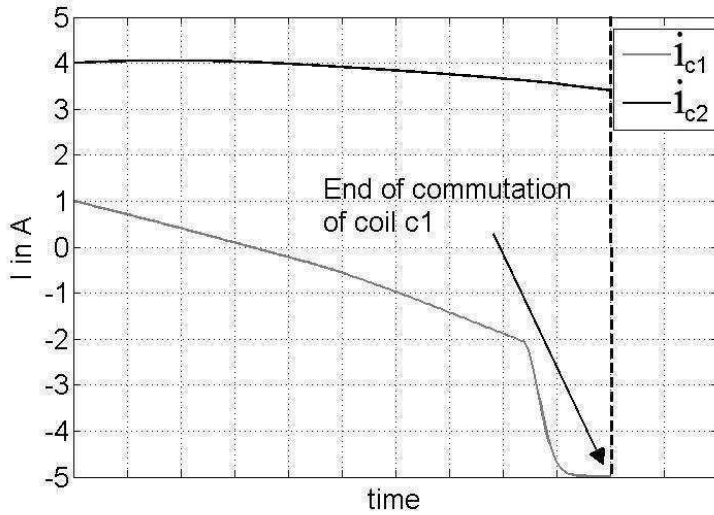
Fig. 4.27 Simulated commutating currents

As shown in this chapter, the brush body resistances are influenced by anisotropy and radial brush height. It could be observed that the anisotropy has a stronger effect on the resistances in transversal direction R_x, R_y and R_z than on the resistances in orthogonal direction R_u, R_v, and R_w. Moreover, it could be observed that the influence of the radial brush height has significant influence on R_u, R_v, and R_w whereas its influence on R_x, R_y and R_z seems negligible. Now, in order to observe the influence of the brush body resistances on the commutating currents i_{c1} and i_{c2} the transverse and orthogonal resistances were, starting from the resistance values used to calculate the transients in Fig. 4.27, increased manually by factors 5 and 20 and the commutation transients i_{c1} and i_{c2} were recalculated. It was found that there is no significant influence on i_{c2} and the effect on i_{c1} is not until it reaches the phase of rapid resistance increase towards the end of commutation as shown in Fig. 4.28. The increase of the brush body resistances causes the commutating current i_{c1} to reach its designated value of $-I_a / 2 = -5A$ earlier i.e accelerated commutation is achieved. Especially the increase of the transverse resistances has an accelerating effect on i_{c1}. The commutation current reaches $-5A$ the fastest with increased transverse resistances by factor 20 and increased orthogonal resistance by factor 5 within the examined range.

Before the phase of rapid resistance increase (trailing brush edge reaches the end of commutator bar) no influence of increased brush body resistances is evident which may lead to the conclusion that up to this point the main resistance in the commutating circuit is the contact resistance R_{cf} in combination with the ohmic coil resistance.
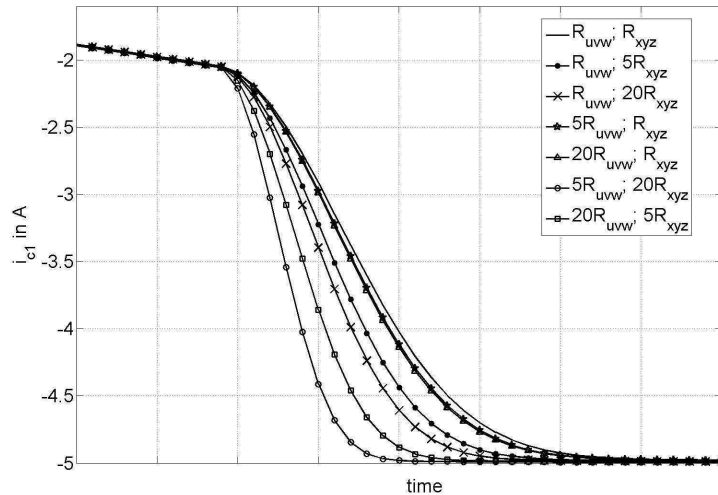
Fig. 4.28 Simulated commutating currents with different brush body
resistances

4.8   Conclusions

A brush model has been developed that can be used to investigate the influence of brush parameters such as dimensions, conductivity and anisotropy on the currents in the brush, the commutating circuit and the power dissipated in the brush at each operation point. A rigorous approach was taken where the resistances between two terminals of the brush were calculated by a quick and dedicated finite difference program which uses Cholesky factorisation in order to obtain a direct non-iterative solution. Subsequently, Newton-Raphson's method is applied to calculate the internal resistances of the brush referring to resistor networks established for both a three- resistor case and a six-resistor case. It is shown that the brush body resistances are influenced by anisotropy and radial brush height. The anisotropy has a stronger effect on the resistances in transversal direction than on the resistances in orthogonal direction with respect to the commutator circumference. Moreover, it could be observed that the influence of the radial brush height has significant influence on the resistances in orthogonal direction whereas its influence on the resistances in transversal direction seems negligible. Moreover, in a simplified application example commutation transients are shown as well as the influence of the brush body resistances on the progression of the commutating currents. The commutation was fastest with increased transversal resistances by factor 20 and increased orthogonal resistance by factor 5 within the examined range. The progression of the calculated currents shows that the brush resistance is a critical quantity in commutation analysis. Hence, the brush model will be included in the detailed commutation model. (See chapter 8)

5 Circuit Theory Approach to model the Brush Contact Arc in a Commutator Motor

5.1 Arc Modelling in Commutation Analysis

In this chapter it is intended to calculate the currents in the commutating coil and the commutation arc that ignites due to a non - zero difference of the current in the commutating coil and the armature branch current (see Fig. 5.2 and Fig. 5.8) at contact separation. This current difference is denoted the uncommuted residual current and the analysis is carried out strictly from an external circuit point of view as the values of the circuit elements are under the control of the motor designer. Therefore the current in the arc is calculated by means of circuit resistance and inductance as well as the armature branch current and the current in the commutating coil applying Kirchhoff's law. From the arc current and arc voltage, the arc energy can be calculated as well as the arc duration as a function of circuit resistance, inductance and the uncommuted residual current.

So-called black-box models are widely used to model electric arcs especially in circuit breakers. The most important ones are the models of Cassie and Mayr and in scientific articles such as [39], [40], [41] and [42] many further developed and extended versions can be found. However, the parameters of those models have to be identified using test data. It is very difficult to produce repeatable test conditions for a commutation arc [43] as the conditions are subject to ongoing changes with current density, temperature, humidity, the condition of the commutator film as well as the brush polarity during the AC cycle and the state of wear of the contact members.

To model the commutation arc of universal or DC machines, in [9] and [44] Ayrton's equation is proposed, which also requires constants that have to be identified experimentally. Moreover, in [44] a brief overview of some equations modelling the arc voltage as a function of the arc current is given as well as the simple method of modelling the arc using a constant voltage. In [10] it is assumed that the ignition of the arc takes place if a certain electric field strength is reached and the electric field strength and the conductivity in the arc are constant during

arcing. The arc length is defined as the thickness of the commutator film. The arc model is included into the overall simulation as a simple resistance.

In [45] and [46] a very deep analysis of the arc physics is carried out. The commutator switching arc is assumed to be a short arc (which under certain circumstances might become a drawn arc which is a long arc with a higher voltage required to persist) which ignites at the minimum arc voltage U_m and becomes extinct at a sufficiently low arc current I_{min}. The theoretical analysis includes ionisation of air near the electrodes, tunnel effect and the problem of differently ionised layers between the commutator bar and the trailing edge of the brush. Average values of ignition voltage (which is slightly higher than the arc voltage) and extinction current are taken from Holm's works and confirmed experimentally. The values differ depending on whether the brush is anodic or cathodic. The average values for those two cases are given by U_m = 16.6V and I_m = 0.22A.

Graphs of commutating current and commutating voltage are shown in [47]. At the conclusion of commutation an oscillation can be noted in the commutating current taking place *after* arcing (this oscillation is also shown in [48]). It is stated that if the current at the brush contact at the end of commutation is high, the trailing edge is exposed to an enormous current density and the contact bridges (actual contact spots, see Fig. 4.12) between the brush trailing edge and the commutator bar burst. If there is enough energy stored in the inductance, the arc ignites after contact burst. During the dynamic phase of commutation *i.e.* the phase where the trailing brush edge reaches the end of the commutator bar (see Fig. 5.1), the brush to bar contact voltage rises proportionally to the rise of the brush resistance as the contact area decreases towards zero. The arc is characterised by a constant voltage and the initial arc current is the current difference of the commutating current and the armature branch current at the instant of separation (see Fig. 5.2). At the instant of separation a capacitive current starts flowing into the parasitic capacitance (see Fig. 5.3). Hence the voltage rise at the open contact is oscillatory. Arcing takes place as soon as the ignition voltage is reached. It is stated that *contact wear during arcing is proportional to arc energy* and the arc current is approximated as a linear function as the resistance of the commutating coil is neglected. The arc energy depends directly on the uncommuted residual current.

A similar approach is taken in [49] where arcing is considered a very significant influence parameter on brush wear. Electric heating causes contact bridge burst at the end of commutation and a large amount of the stored energy is dissipated as heat in the phase of

rapidly rising contact resistance. The remainder of the stored energy is dissipated in the arc. Again, the commutation arc is referred to as a short arc which ignites once the ignition voltage is reached. Moreover the voltage at which the last contact bridges burst is given by 5V. The short arc voltage is assumed to be constant during arcing and given by 12.2V. Similar as in [47] the resistance of the carbon brush is neglected and the arc current is assumed to decrease linearly. However, it is stated that in practice the brush resistance will cause the current to decrease exponentially.

In [43] the different stages in the commutator sparking (the authors refer to arcing as sparking) are defined. The pre-arcing voltage rise is referred to as the period of time where physical contact separation between brush and commutator bar takes place and a parasitic capacitance comprising the parasitic inter-segment capacitance and the distributed coil capacitance is being charged by a capacitive current. This causes an oscillatory voltage rise where the arc ignition voltage is reached within the first quarter of a period. The frequency is determined by the effective coil inductance and the parasitic capacitance (see Fig. 5.3).

Once the arc ignites it is described to persist at constant 12V. This is referred to as sparking or post-commutating short arc. The high-frequency oscillation at the conclusion of sparking is mentioned and it is assumed that it has the same frequency as during the pre-arcing voltage rise. As the short arc voltage is almost constant the arc duration is governed only by circuit conditions *i.e.* it depends on resistance, inductance and capacitance in the circuit. The arc extinguishes when the current reaches a minimum short-arc current which is different for anodic and cathodic brushes.

Reference [36] introduces the terms "brush fire" and "brush sparks" as synonyms for commutator arcs. Here a minimum arc length of $5 \cdot 10^{-8}$m is specified referring to Holm. Due to the short arc length there is no anode fall and the voltage is mainly constant and drops rapidly to zero at the end of arcing. As there is also capacitance in the circuit the system is vibratory. The voltage across the inter-segment gap also includes contact resistance of the brush to bar interface. The ignition voltage is higher than the arcing voltage and given by 20V. The arcing voltage is given by 12V...17V for an anodic brush and 17V...20V for a cathodic brush. Arc current decrease is assumed linear.

Reference [50] states that oscillations in a closed circuit containing resistance, inductance and capacitance can be maintained by an arc. Moreover, it is said that in any practical contact circuit there is resistance, inductance and capacitance and that in order to prevent an arc from

being set up the local self inductance must be exceedingly low. The ability to strike an arc on opening contacts is stated to depend on the instantaneous potential difference between the electrodes, and the nature of the gas and the resistance of the arc depends on the current.

In [26] it is stated that in the best case scenario, the voltage at contact separation does not reach the value that causes the contact bridges to burst. After contact burst the brush and the commutator bar are galvanically separated and a capacitive current starts flowing (see Fig. 5.3). A strong reference to [43] is made. The voltage rise across the separation gap is oscillatory and if the uncommutated residual current is not sufficiently small after separation the arc ignition voltage is reached within nanoseconds.

5.2   Interpretation of Terms

In the literature the usage of the terms sparking and arcing is not quite unified. Therefore it is necessary for any further steps in theoretical analysis to define those terms and retain those definitions throughout. This definition of terms also includes a definition of different time intervals during conclusion of commutation.

■   Interval 1 : Pre-arcing; period of contact bridge bursts

This is the period of time where the last contact bridges burst (at approx. 5 V [49]) and glowing carbon material flies out. This interval is from now on referred to as *sparking*.

■   Interval 2 : Arcing

This is the period of time where articles differ in their terminology. One can find the term sparking (for example in [36] and [43]) as well as post-commutating short arc [43], short arc (for example [46],[49]) or electric arc (*e.g.* [9], [10]). This period will be referred to as *arcing* and is generally considered to be the main reason for electrical wear at the contact members.

■   Interval 3 : High frequency oscillation at the end of commutation

This oscillation is shown in [47] and [48] and is mentioned in [43]. This will be referred to as *post-arc oscillation.*

5.3　Theoretical Analysis of the different Time Intervals

5.3.1　Pre-arcing

This is the period of time where the physical contact area between the brush and a certain commutator segment approaches zero (see Fig.5.1). The last remaining contact bridges burst at approximately 5V due to high current density and glowing carbon material flies out as sparks.
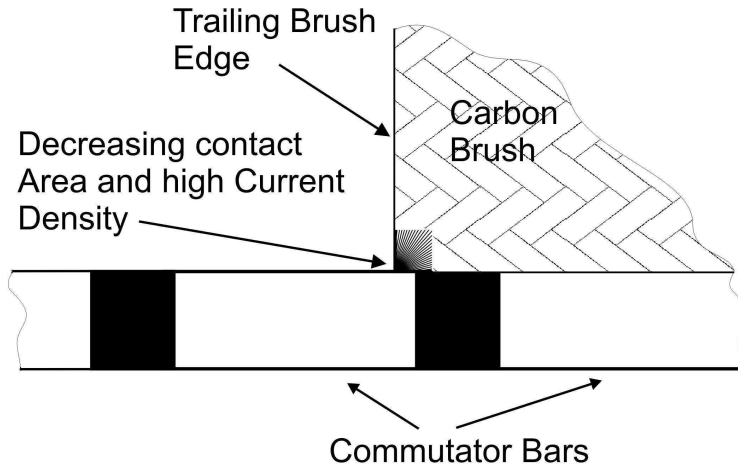
Fig. 5.1 Brush leaving segment

At the instant of separation $t = t_\sigma$ a certain amount of energy has been dissipated in the contact resistance. If there is still a difference (see Fig. 5.2) of the current in the commutating coil and the armature branch current (half of the armature current) a capacitive current starts flowing and the governing circuit is the one depicted in Fig. 5.3. The theoretical commutation time is the brush width divided by the commutator velocity.
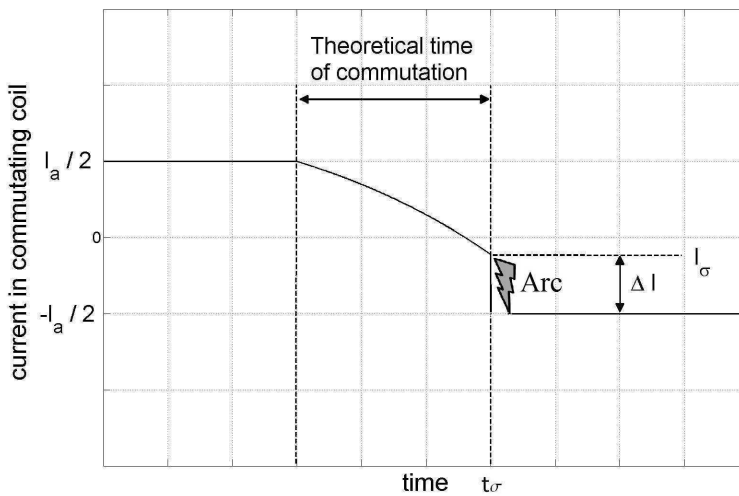
Fig. 5.2 Commutating current at separation
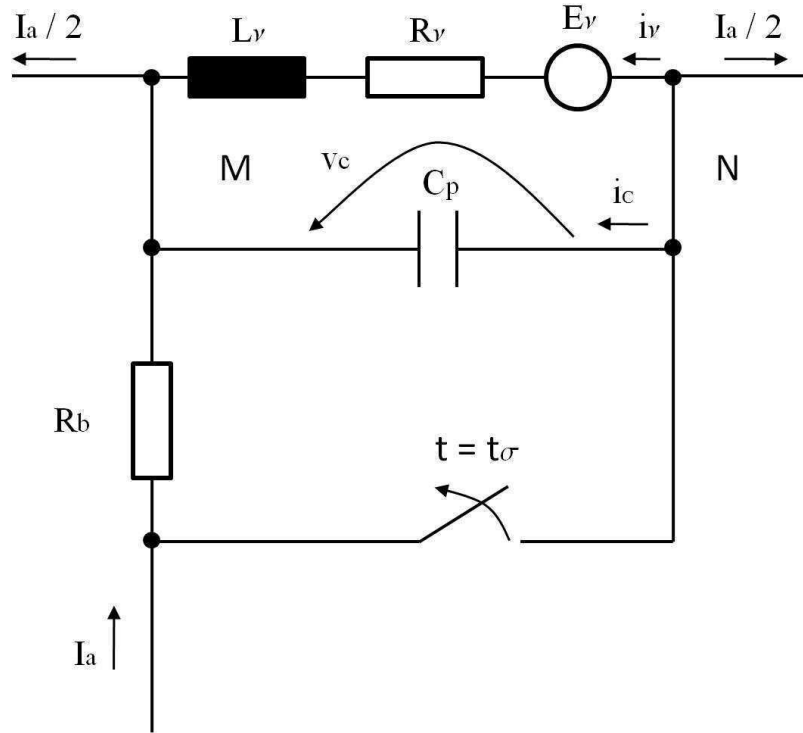
Fig. 5.3 Circuit after separation

In Fig. 5.3 the index v is associated with the commutating coil where E_v is the induced voltage due to coupling with other circuits. C_p is the parasitic capacitance (10^{-10} ... 10^{-15} F, [26]) and R_b is the series connection of the brush to bar contact resistance and the film resistance between the leading edge of the brush and the respective segment. The resistance R_b and the armature current I_a will be assumed constant during the calculations.

It can be seen, that the circuit is valid for a brush shorting one armature coil.

For nodal point N we get the equation

$$i_c + i_v + \frac{I_a}{2} = 0 \qquad (114)$$

and for mesh M we get

$$v_c = R_v i_v + L_v \frac{di_v}{dt} + E_v \qquad (115)$$

where L_v is assumed constant during the calculation as I_a is also expected to be constant and a single armature coil is not considered capable of changing the saturation level of the machine significantly.

If we now use

$$i_c = C_p \frac{dv_c}{dt} \tag{116}$$

in (114) and replace i_v in (115) we get

$$v_c = R_v \left[-C_p \frac{dv_c}{dt} - \frac{I_a}{2} \right] - L_v C_p \frac{d^2 v_c}{dt^2} + E_v \tag{117}$$

and ultimately

$$\frac{d^2 v_c}{dt^2} + \frac{R_v}{L_v} \frac{dv_c}{dt} + \frac{v_c}{L_v C_p} = \frac{1}{L_v C_p} \left[E_v - R_v \frac{I_a}{2} \right] \tag{118}$$

with the general solution

$$v_c(t) = A e^{-\beta t} \sin(\omega t + \varphi_0) + E_v - R_v \frac{I_a}{2} \tag{119}$$

where

$$\beta = \frac{R_v}{2 L_v} \tag{120}$$

and

$$\omega = \sqrt{\frac{1}{L_v C_p} - \beta^2}. \tag{121}$$

Now to determine A and φ_0 in (119) we change the time coordinate t to t' for convenience as depicted in Fig. 5.4.
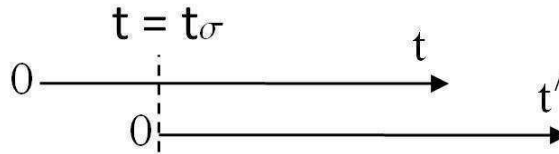
Fig. 5.4 Time coordinates

The voltage at contact separation now becomes $V_\sigma = v_c(t = t_\sigma) = v_c(t' = 0) = 5\text{V}$ and the current at separation becomes $I_\sigma = i_v(t = t_\sigma) = i_v(t' = 0)$ which depends on the circuit history up to the point of contact separation (see Fig. 5.2).

Now with (114) and

$$- \frac{I_a}{2} + \Delta I = I_\sigma \tag{122}$$

(See Fig. 5.2) we get

$$i_c(0) = - I_\sigma - \frac{I_a}{2} = - \Delta I = C_p \left. \frac{dv_c}{dt'} \right|_{t' = 0} \tag{123}$$

and, assuming E_v is constant, with (119) we get

$$V_\sigma = A \sin(\varphi_0) + E_v - R_v \frac{I_a}{2} \tag{124}$$

with (119) equation (123) becomes

$$A (\omega \cos(\varphi_0) - \beta \sin(\varphi_0)) = - \frac{\Delta I}{C_p} \tag{125}$$

and solving (124) and (125) for A yields

$$\frac{C_p}{\Delta I} \left[V_\sigma - E_v + R_v \frac{I_a}{2} \right] = \frac{\sin(\varphi_0)}{\beta \sin(\varphi_0) - \omega \cos(\varphi_0)} \, . \tag{126}$$

To solve (126) we set $\gamma = C_p (V_\sigma - E_v + R_v I_a/2)/\Delta I$ and $q = \tan(\varphi_0)$ which gives

$$\gamma = \frac{q \cos(\varphi_0)}{\beta q \cos(\varphi_0) - \omega \cos(\varphi_0)} = \frac{q}{\beta q - \omega} = \frac{1}{\beta - \omega/q} \tag{127}$$

which yields

$$q = \frac{\gamma \omega}{\gamma \beta - 1} = \frac{\omega}{\beta - 1/\gamma} = \tan(\varphi_0) \, . \tag{129}$$

Thus

$$\varphi_0 = \arctan \left[\frac{\omega}{\beta - 1/\gamma} \right] \tag{130}$$

and, with (124) one obtains

$$A = \frac{V_\sigma - E_v + R_v I_a/2}{\sin(\varphi_0)} = V_0 \tag{131}$$

89

which gives the analytical expression

$$v_c(t') = V_0 e^{-\beta t'}\sin(\omega t' + \varphi_0) + E_v - R_v\frac{I_a}{2} \tag{132}$$

for the voltage drop across the capacitor. The voltage v_c is plotted in Fig. 5.5 simulated for a set a set of parameters as shown. The plot stops at the point where the voltage reaches the ignition voltage of 16.6V. The voltage starts rising at $t' = 0$ and reaches the ignition voltage within approximately half a nanosecond.
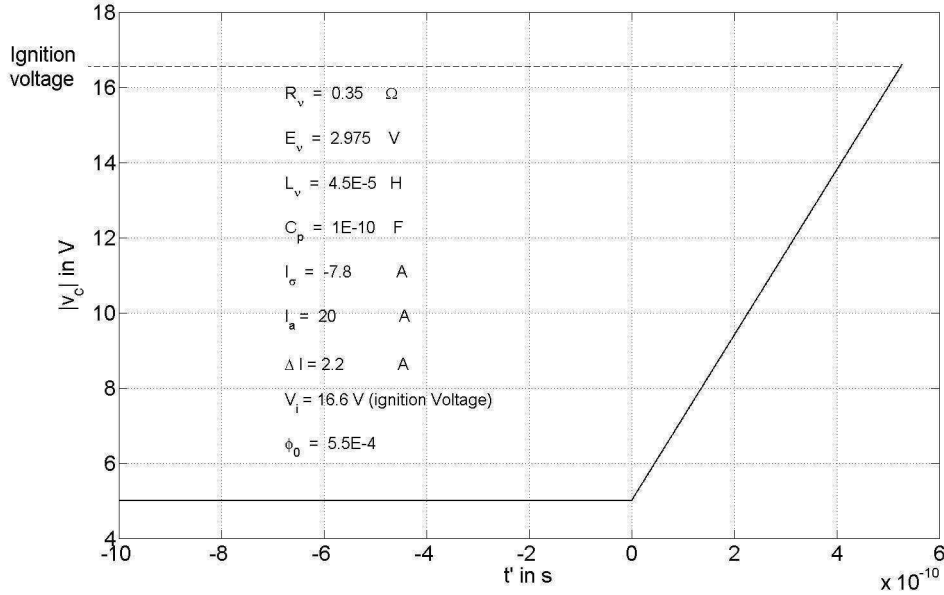
Fig. 5.5 Capacitive voltage rise

Another important point to consider is the change of current in the commutating coil during the voltage rise. With (114), (116) and (132) we get for the current

$$i_v(t') = -C_p V_0 e^{-\beta t'}[\omega\cos(\omega t' + \varphi_0) - \beta\sin(\omega t' + \varphi_0)] - \frac{I_a}{2} \tag{133}$$

For the same parameters as in Fig. 5.5 the current during the voltage rise is shown in Fig. 5.6.
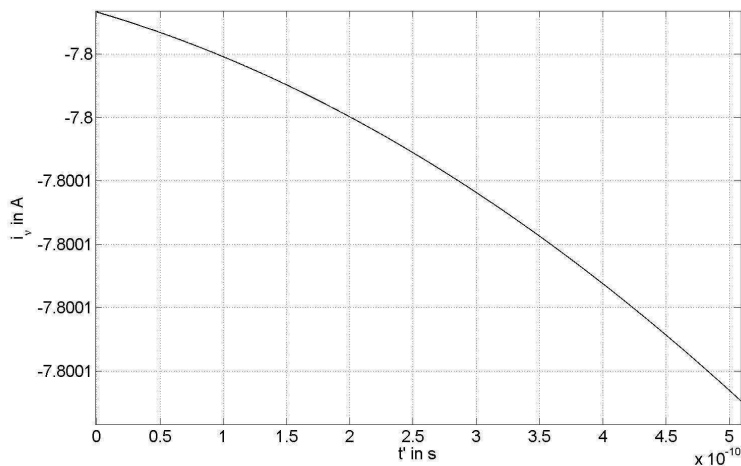
Fig. 5.6 Current during voltage rise

90

It can be observed that the change of current during the voltage rise is negligibly small. Hence, the initial current for the next phase, the arcing, can still be assumed to be I_σ.

5.3.2 Arcing period

It is assumed that the arc has been fully established during the phase where the voltage decreases from ignition voltage to constant arc voltage (See Fig. 5.7).

Hence for this phase a constant arc voltage is assumed. Due to the constant arc voltage and the assumption that the voltage drop across R_b is mainly determined by the armature current I_a, which is held constant during the calculation as mains frequency is much lower than commutation frequency, changes in the voltage across C_p are neglected. From (116) it follows that there will be no capacitive current during that phase and therefore the governing circuit for this phase is the one in Fig. 5.8. The sign conventions in the circuit have been chosen for convenience. As mentioned above the initial current in the commutating coil for this phase will be the current at separation I_σ.
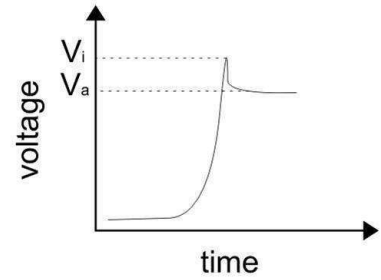
Fig. 5.7 Ignition and arc voltage
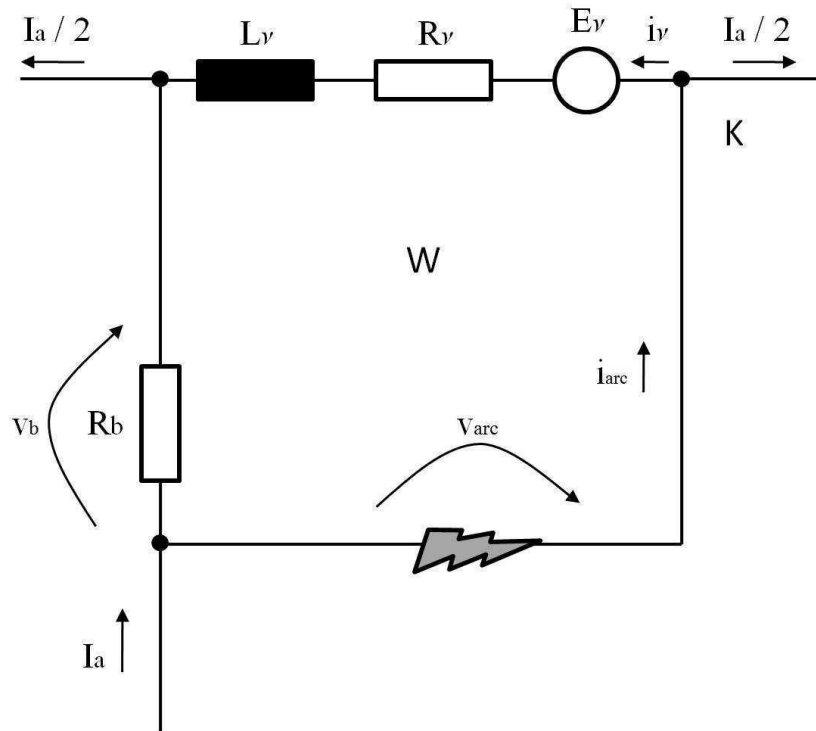
Fig. 5.8 Circuit during arcing

91

For nodal point K we get

$$i_{arc} = i_v + \frac{I_a}{2} \tag{134}$$

and for mesh W we get

$$R_v i_v + L_v \frac{di_v}{dt} + E_v = v_b - v_{arc} \tag{135}$$

where

$$v_b = R_b(I_a - i_{arc}) \tag{136}$$

and

$$v_{arc} = V_\alpha = const. \tag{137}$$

Now, combining (134), (135), (136) and (137) gives

$$(R_v + R_b)i_v + L_v \frac{di_v}{dt} + E_v = R_b \frac{I_a}{2} - V_\alpha \tag{138}$$

and, after differentiating with respect to time

$$\frac{d^2 i_v}{dt^2} + \frac{R_v + R_b}{L_v} \frac{di_v}{dt} = 0 \tag{139}$$

with the solution

$$i_v(t) = K_1 + K_2 e^{-\frac{R_v + R_b}{L_v}t} \tag{140}$$

To find the constants K_1 and K_2 a new time coordinate t'' is introduced so that $i_v(t = t_\alpha) = i_v(t'' = 0)$ where t_α is the instant where the arc voltage reaches the constant value V_α. (See Fig. 5.9). With regard to Fig. 5.2 the constants can be found as follows

$$i_v(t'' = 0) = I_\sigma = K_1 + K_2 \tag{141}$$

$$\lim_{t'' \to \infty} i_v = -\frac{I_a}{2} = K_1 \tag{142}$$

$$K_2 = I_\sigma + \frac{I_a}{2} = \Delta I \tag{143}$$

and, with (142) and (143), (140) can be rewritten as

$$i_v(t'') = \Delta I e^{-\frac{R_v + R_b}{L_v}t''} - \frac{I_a}{2}. \tag{144}$$

Thus with (134) we obtain for the arc current

$$i_{arc}(t'') = \Delta I e^{-\frac{R_v + R_b}{L_v}t''}.$$ (145)
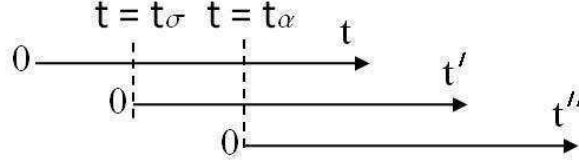
Fig. 5.9 Time coordinates

It can be seen that the theoretical time needed for the arc current to become zero is infinite. To keep this time in practical limits it is taken into account that the arc extinguishes at a sufficiently small current I_{min}.

Hence, solving

$$I_{min} = \Delta I e^{-\frac{R_v + R_b}{L_v}\tau_\alpha}$$ (146)

for τ_α gives

$$\tau_\alpha = -\frac{L_v}{R_v + R_b}\ln\left[\frac{I_{min}}{\Delta I}\right]$$ (147)

Now, to calculate the energy dissipated in the arc we get

$$W_{arc} = V_\alpha \int_{t''=0}^{t''=\tau_\alpha} i_{arc}\, dt'' = \frac{V_\alpha \Delta I L_v}{R_v + R_b}\left[1 - e^{-\frac{R_v + R_b}{L_v}\tau_\alpha}\right] = \frac{V_\alpha L_v}{R_v + R_b}\left[\Delta I - I_{min}\right]$$ (148)

which is closely related to the arc erosion of the contact members [6], [7],[70],[71],[72].

5.3.3   Post-arc oscillation

This phase starts at the instant the arc has extinguished. As stated above this happens if the arc current falls below I_{min}. As there is no current flow from the trailing edge of the carbon brush to the commutator bar any longer (re-ignition is not considered) the governing circuit for this phase is again the one in Fig. 5.3 with the instant of extinction $t = t_\alpha + \tau_\alpha$. With (114), (115) and (116) we get the differential equation of i_v

$$\frac{d^2 i_v}{dt^2} + \frac{R_v}{L_v}\frac{di_v}{dt} + \frac{i_v}{C_p L_v} = -\frac{1}{C_p L_v}\frac{I_a}{2} \tag{149}$$

with the general solution

$$i_v(t) = Be^{-\beta t}\sin(\omega t + \zeta_0) - \frac{I_a}{2} \tag{150}$$

where B and 0 are found applying another time coordinate t''' as depicted in Fig. 5.10. Note that β and ω have the same values they had in the pre-arcing phase as given in (120) and (121).
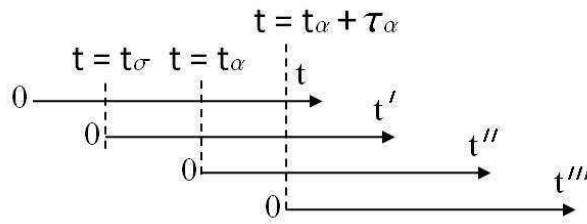
Fig. 5.10 Time coordinates

Now, assuming that at the instant $t''' = 0$ the arc voltage is still V_α which drops to zero instantly afterwards, and the current in the commutating coil at the same instant is $-I_a/2 + I_{min}$ we obtain a relationship similar to (126)

$$\frac{I_{min}}{\lambda} = \frac{\sin(\zeta_0)}{\omega\cos(\zeta_0) - \beta\,\sin(\zeta_0)} \tag{151}$$

where

$$\lambda = \frac{1}{L_v}[R_b(I_a - I_{min}) - R_v(-\frac{I_a}{2} + I_{min}) - E_v - V_\alpha]. \tag{152}$$

Using $q = \tan(\zeta_0)$ gives

$$\zeta_0 = \arctan\left[\frac{\omega}{\beta + \lambda/I_{min}}\right] \tag{153}$$

and subsequently B can be found as follows

$$B = \frac{I_{min}}{\sin(\zeta_0)} = I_0 \tag{154}$$

and (150) can be rewritten as

$$i_v(t''') = I_0 e^{-\beta t'''} \sin(\omega t''' + \zeta_0) - \frac{I_a}{2}. \tag{155}$$

5.4   Results

5.4.1   Full simulation including all phases

The current in the commutating coil was emulated using a simple exponential function controlled by a parameter that determines the value I_σ at contact separation. From this instant the current i_v at every stage is calculated as described above. The calculated current for a certain set of parameters can be seen in Figs. 5.11 and 5.12. Moreover the resulting arc current can be seen in Fig. 5.13. The arc voltage is set to 12V.
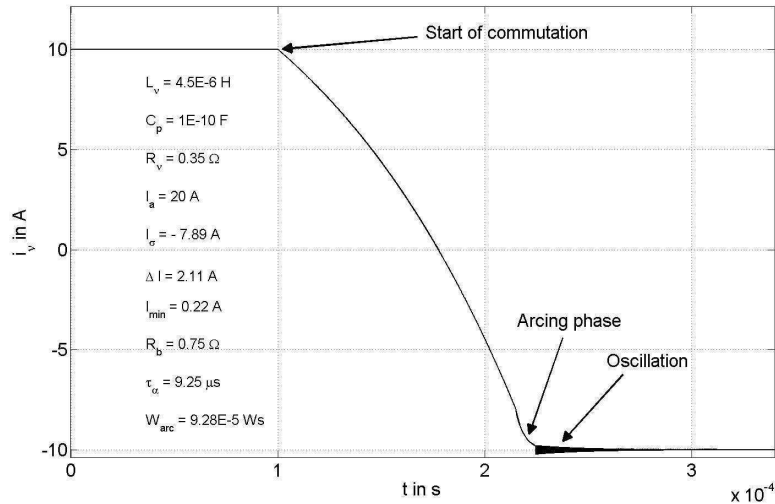
Fig. 5.11 All phases
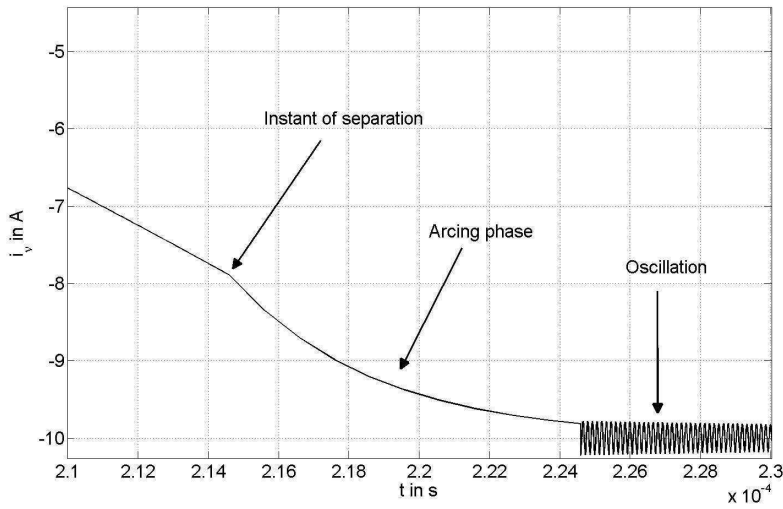
Fig. 5.12 Zoomed view of Fig. 5.11
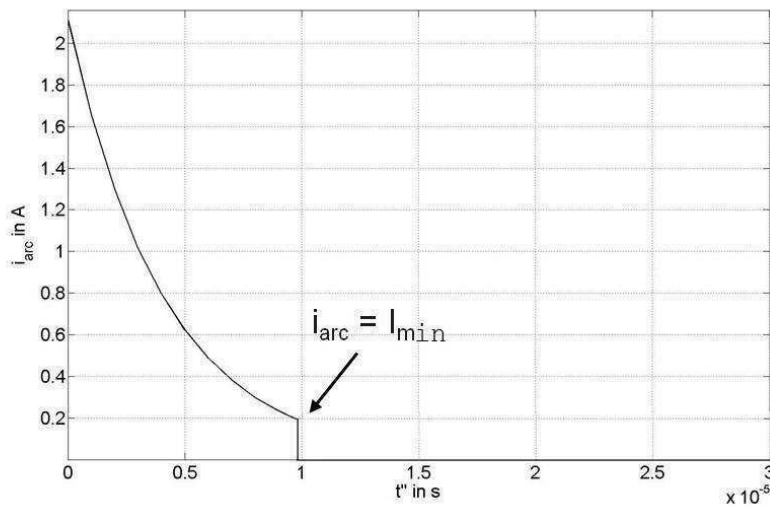
Fig. 5.13 Resulting arc current

5.4.2 Arc energy and arc duration as functions of current at separation

In Fig. 5.14 the uncommutated residual current ΔI, the arc duration τ_α and the arc energy W_{arc} are plotted against the value of current in the commutating coil at the instant of separation I_σ. All other parameters were held constant during the calculation. It can be seen that the normalised graph of W_{arc} very closely follows the normalised graph of ΔI which emphasises their proportionality.
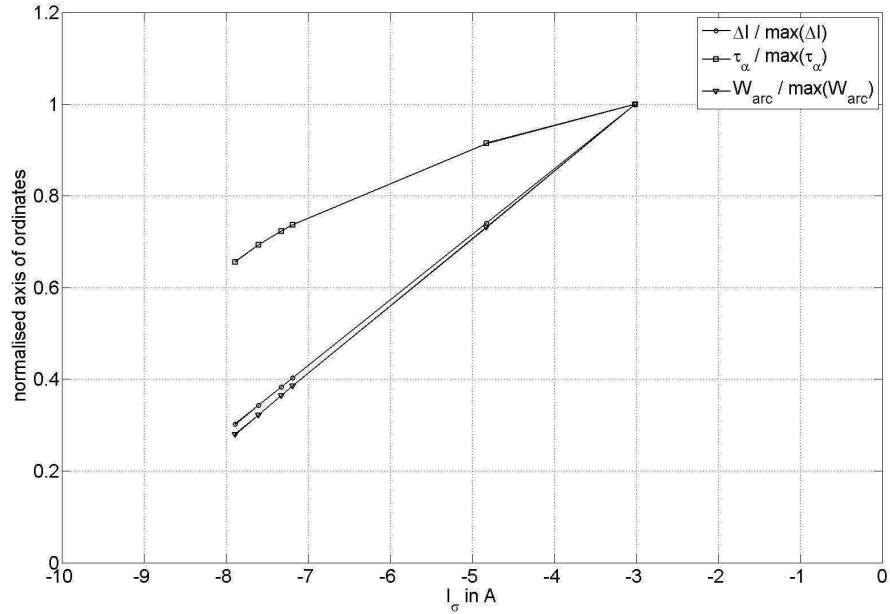
Fig. 5.14 Arc parameters as functions of I_σ

Moreover, the arc energy is plotted against the arc duration. The graph can be seen in Fig. 5.15.
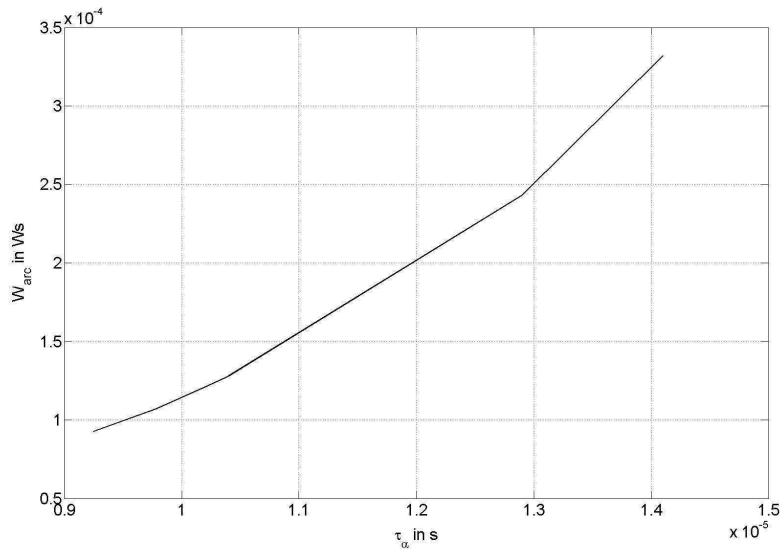
Fig. 5.15 Arc energy as a function of arc duration

5.4.3 Arc energy and arc duration as functions of inductance

The inductance was increased by decimal power steps and all other parameters were held constant. The best way to present the resulting graphs was found to be a doubly logarithmic figure (Fig. 5.16) where it can be seen that the graphs of arc energy and arc duration are parallel with a proportionality factor of approximately 10.
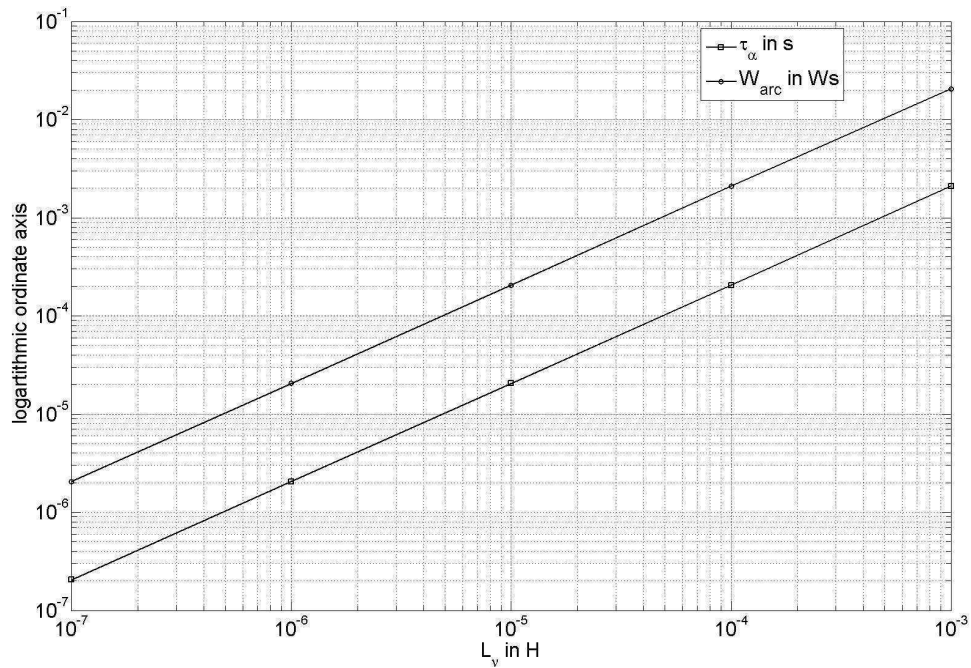
Fig. 5.16 Arc energy and arc duration as functions of L_v

5.4.4 Arc energy and arc duration as functions of R_b

The resistance R_b was increased in small steps of 0.15Ω and all other parameters were held constant. The influence of R_b might be significant with regard to parameters such as spring pressure that have significant influence on the contact resistance. The graphs are shown in Fig. 5.17. where the ordinate axis is scaled logarithmically for better presentability.
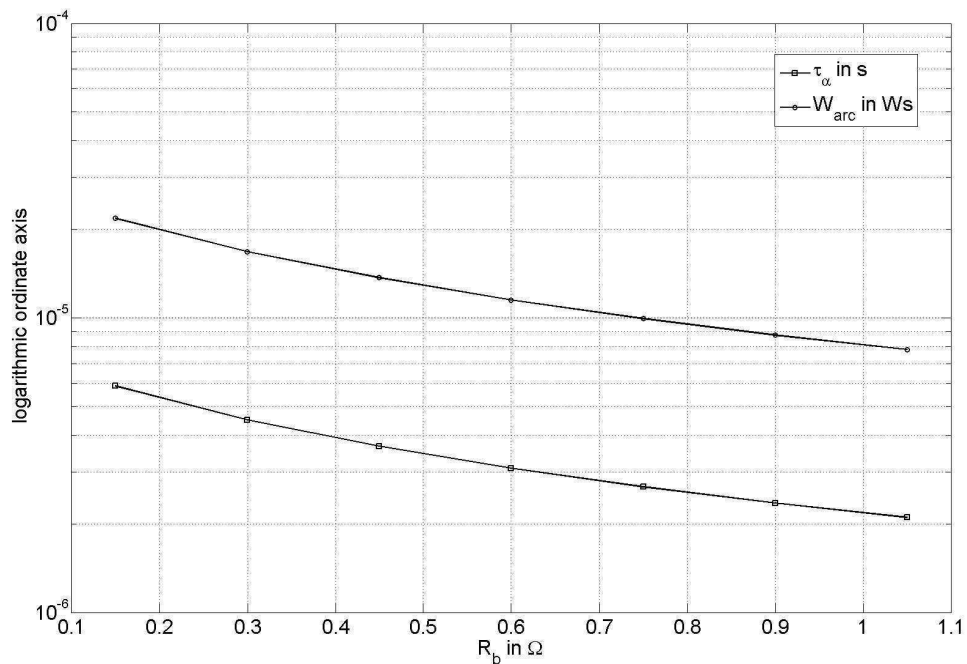
Fig. 5.17 Arc energy and arc duration as functions of R_b

5.5   Experimental Study

In order to verify the mathematical analysis the current in the commutating coil during arcing is measured and compared to the current simulated using the appropriate simulation parameters. The application of slip rings on the shaft has not been pursued as the motor used does not provide the space required for them between commutator and bearing or, on the other end, rotor end turns and fan impeller or between fan impeller and bearing. Therefore it would be necessary to through-bore the shaft in axial direction to provide space to bring out the connector leads for the sliprings. As the shaft is only 8mm in diameter this would pose significant stability problems and possibly result in the loss of the rotor. Therefore, the following measurement technique is proposed.

The rotor is clamped using a lever arm that is connected to a tension spring as depicted in Fig. 5.18. A photograph of the setup is shown in Fig. 5.19. Now, applying force to the lever arm on the opposite end to the spring builds up a force in the spring that will cause the rotor to quickly turn a certain angle once the initial force is removed. This angular step allows the commutator bars associated with the coil with the shunt resistor inserted to travel across the carbon brush from entering edge to leaving edge. The advantages of that method is that leads can be soldered to the coil examined directly without the use of slip rings. To measure the current in a single rotor coil during arcing a non-inductive, low value resistor (0.03Ω) is inserted by breaking the coil's connection to a commutator segment and bridge the gap created with the resistor (see Fig. 5.20). Subsequently, the voltage across the shunt resistor is measured which has essentially the same progression as the current in the coil which can then be found using Ohm's law. Moreover, the voltage drop between the brush and the trailing segment is recorded as well (see Fig. 5.21) in order to determine the beginning and the end of the arcing. The recorded voltage and coil current can be seen in Fig. 5.22. These waveforms were obtained feeding the rotor circuit with a DC current of 7A and leaving the field circuit unexcited. Hence, the single rotor coil inductance is not affected by any field damping effects (see chapter 7) and the value of $L_v = 280\mu H$ determined as shown in chapter 3 is assumed. It can be seen that the assumption of a constant arc voltage seems justified and the value of 14V is in good agreement with the values found by other authors. Moreover, it can be seen that at the instant the arc ignites the difference ΔI between the coil current and $-I_d/2 = -3.5A$ is almost exactly 2A. This is emphasised because ΔI is an important parameter to be used in the simulation. Another important parameter taken from the measurement is $V_\alpha = 14V$. The brush

contact resistance $R_b = 0.325\Omega$ (see 4.7.2) was used in the simulation as well as a measured coil resistance $R_v = 0.25\Omega$. For the minimum arc current I_{min} a value of $0.22A$ was applied [45], [46].
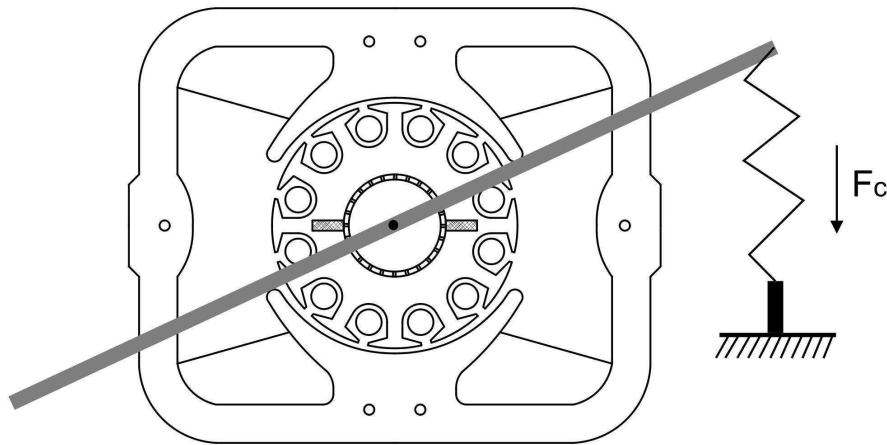
Fig. 5.18 Test Setup
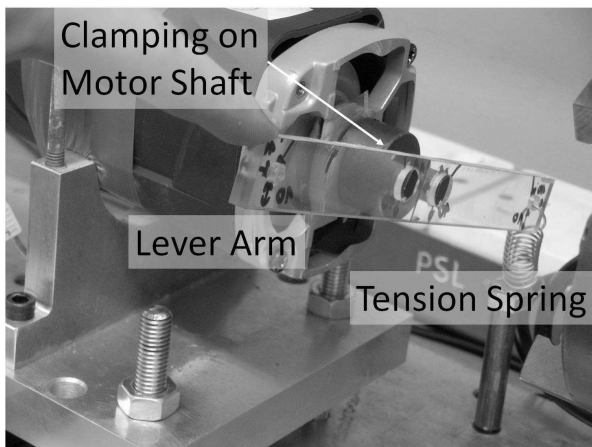
Fig. 5.19 Photograph of Setup
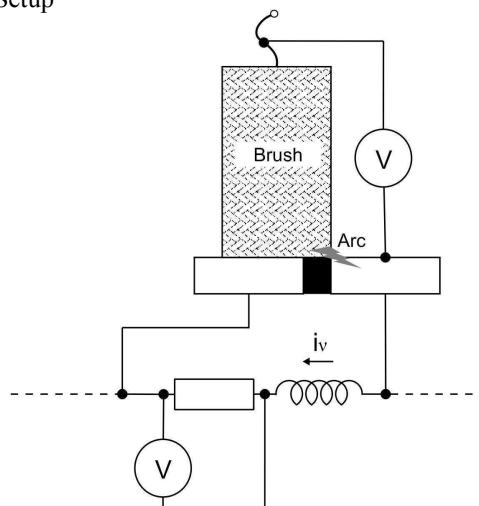
Fig. 5.21 Voltage measurement
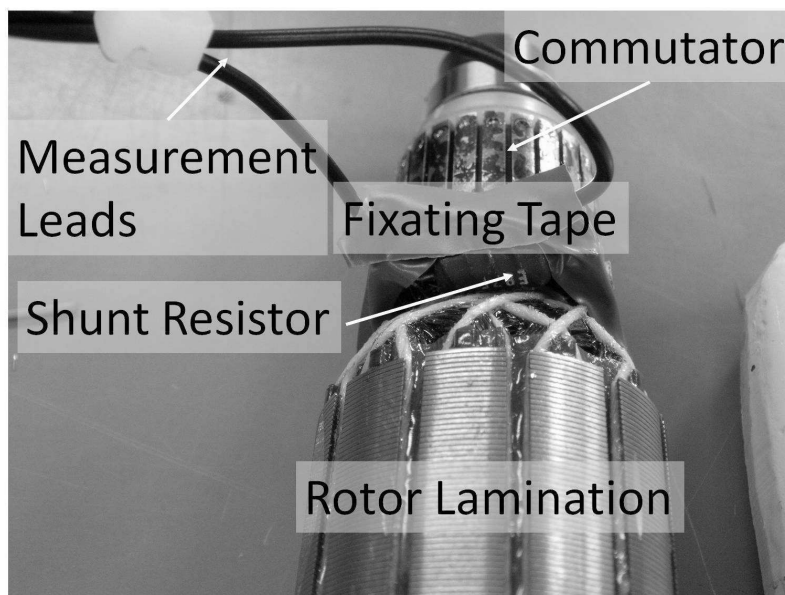
Fig. 5.20 Shunt resistor for coil current measurement
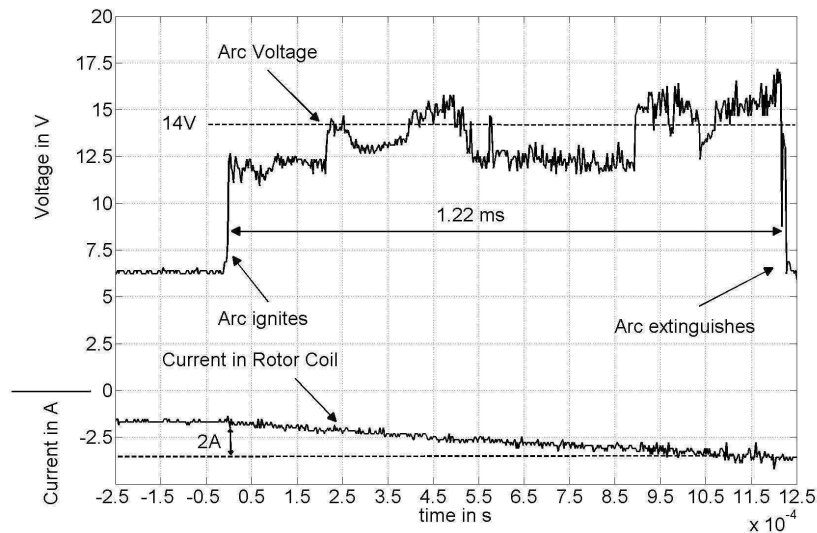
Fig. 5.22 Brush to bar voltage and coil current during arcing

Using the parameter extracted from tests, the current in the commutating coil was simulated and compared to the measured current as shown in Fig. 5.23. Up to the point where the arc extinguishes in the simulation good agreement of simulated and measured current can be observed. At the point where the post-arc oscillation starts one can see that the frequency seems to be too high which is possibly due to insufficient knowledge of the actual inter-segment capacity ($C_p = 10^{-10}$ F used in the simulation).

Although the result looks quite promising the limitations of the measurement technique described have to be pointed out. As we can see in Fig. 5.22 the characteristic ignition voltage at the instant of arc ignition as described by other authors ([36], [45], [46], [47], [49], [43]) is not evident in the tests which suggests that the behaviour of the sliding contact is different in the test and under normal operating conditions. This is comprehensible as under normal operating conditions the friction between the brushes and the commutator rotating at high speed causes additional heating and therefore the conditions at which the last contact bridges burst will be different from the test conditions. For this reason, and the fact that the voltages induced in the commutating coil will be different if the armature is rotating, the testing method cannot be applied to determine the commutating current in any other phase than during the arcing. However, the test and simulation results suggest that the measurement technique is valid for the period of arcing. The arc duration in the test was identified as 1.22ms (see Fig. 5.22) and the calculated arc duration for the set of parameters shown in Fig. 5.23 is 1.10ms. The good agreement indicates that the critical parameters ΔI, L_v, V_a, R_b, and R_v have been identified reasonably precisely.
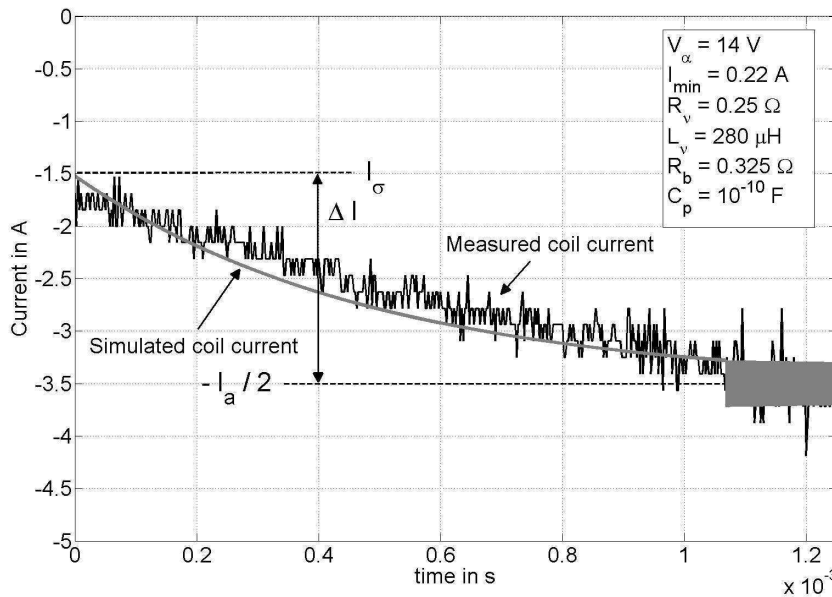
Fig. 5.23 Simulated and measured rotor coil current during arcing

It has to be pointed out that the determined arc duration seems very high although the value of $\Delta I = 2A$ used is not unreasonable. However, under normal operating conditions damping of the field and the armature winding as well as saturation will cause a reduction of the effective coil inductance which will have significant influence on the arc duration. This problem needs to be addressed by an overall motor model based on numerical field computation that can fairly precisely predict the effective inductance of the commutating coil under the influence of all other motor coils and the state of saturation of the machine.

The constant arc voltage applied together with the effective coil inductance found by numerical computations is expected to give a good approximation of the coil current during the arcing phase.

5.6   Conclusions

A circuit theory approach was taken in order to model the arc at the conclusion of commutation. The different time intervals after contact separation are analysed theoretically and mathematical expressions for the build-up of the critical voltage drop across the inter-segment capacity, the progression of current in the commutating coil and the arc current are derived. Certain simplifications had to be applied that were adopted after an extensive literature review on the subject.

It was shown that, taking into account the inter-segment and parasitic coil capacitance, the theoretical voltage rise time to a typical arc ignition voltage is less than a nanosecond. The inter-segment and parasitic coil capacitance was neglected in the mathematical analysis of the arcing phase and it was found that, taking the brush resistance into account, the arc current as well as the current in the commutating coil during arcing decrease exponentially towards their designated values. Equations for arc energy and arc duration were derived that reveal the strong dependency of both quantities on brush resistance, coil resistance, effective coil inductance and the difference of armature branch current and the coil current at contact separation. The mathematical analysis is based on the assumption of a constant arc voltage adopted from reviewed literature. Moreover, a simplified measurement technique was applied in order to verify the theoretical analysis. Even though the technique is limited to the arcing phase the results suggest that the equations established model the commutation arc with satisfactory precision and thus can be applied in an overall motor simulation model including commutation.

6 Design of the Motor Test Bench

6.1 The Reaction Dynamometer

In order to obtain reliable test data to verify the results of the motor simulation (see chapter 08) a precision test bench needs to be used. The design of this test bench is explained in this chapter.

In order to avoid an in-line torque transducer which requires a setup with two couplings and which also poses the possible problem of torque transients exceeding the rated torque of the torque transducer full scale rating [28] it was decided to use a reaction dynamometer. It combines the capability of braking the motor under test (MuT) to the desired speed and straightforward and precise torque measurements.

The principle of the reaction dynamometer is based on the force between stator and rotor in an electrical machine. If a MuT drives the dynamometer (load machine) with a certain torque (not no-load) the torque provided by the MuT is also effective between stator and rotor of the dynamometer. The stator of the load machine is pivoted and its movement is restricted by a lever arm that is connected to the stator of the load machine on one end and connected to a force gauge on the other end. Therefore the torque provided by the MuT can be found by multiplying the force obtained from the force gauge multiplied by the length of the lever arm. The principle of a reaction dynamometer with a commutator machine applied as load machine is depicted in Fig. 6.1. The shaft is rotating in the two bearings B_1 and B_2 mounted inside the machine housing.
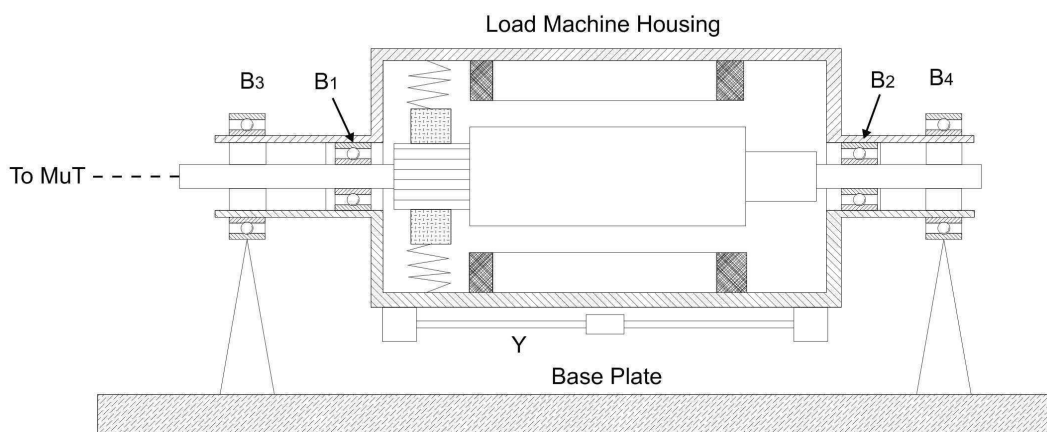
Fig. 6.1 Reaction dynamometer

The housing is pivoted on a base plate via the two bearings B_3 and B_4. This means that nearly all forces are transmitted to the housing of the load machine (apart from a small amount of force created by the air stream of the fan impeller) [29]. The bearings B_3 and B_4 are a source of torque error if not chosen to be of low friction type. The oblique bracket Y is part of the lever system where the actual lever arm restricting the angular displacement of the machine housing in B_3 and B_4 is connected to the midpoint of Y orthogonally to the 2D illustration in Fig. 6.1.

To tackle the problem of the torque error introduced by B_3 and B_4 it was decided to apply air bearings as they have many technical advantages such as near zero friction and wear, high speed and high precision capabilities, and no oil lubrication requirements [51]. As a load machine a universal machine from a power tool (angle grinder) is used. It was decided to leave the universal machine in the tool polyamide housing and insert the housing into an aluminium tube with the required surface finish and outside diameter of 75.000mm [52]. The schematic of the load machined described is shown in Fig. 6.2.

Compressed air used to supply an air bearing must be properly cleaned and dried. Air bearing performance and useful lifetime greatly depends on the quality of the compressed air. General-purpose filters are used to remove the bulk of particles before it gets downstream and damages the coalescing filter. The coalescing filter is used to remove oil and liquid water, including all the particles that passed through the general-purpose filter. The desiccant dryer is used to remove the water vapour before it condenses [51]. The equipment used can be seen in Fig. 6.3. The rated input pressure of the compressed air is 0.41MPa which leads to an air film in the 4 micron air gap [52] between metal tube and air bearing that provides frictionless motion and therefore avoids need for correction for bearing friction in the torque measurement. As mentioned above the torque is measured via a lever arm connected to a force gauge. A 3D view of the load machine assembly without the air supply system is shown Fig. 6.4.

This setup enables a very precise adjustment of the desired operating point in order to get reliable test data. Test data of the motor performance is required to compare simulation results with measurements in order to evaluate the simulation model (see chapter 8) with regard to its accuracy.

To minimise angular, parallel or axial misalignment when coupling the MuT to the dynamometer, the MuT was mounted on a linear slide system with spindles in x - y - z - direction and locking mechanisms for each spindle. Subsequently the slide system was mounted on the common base plate.
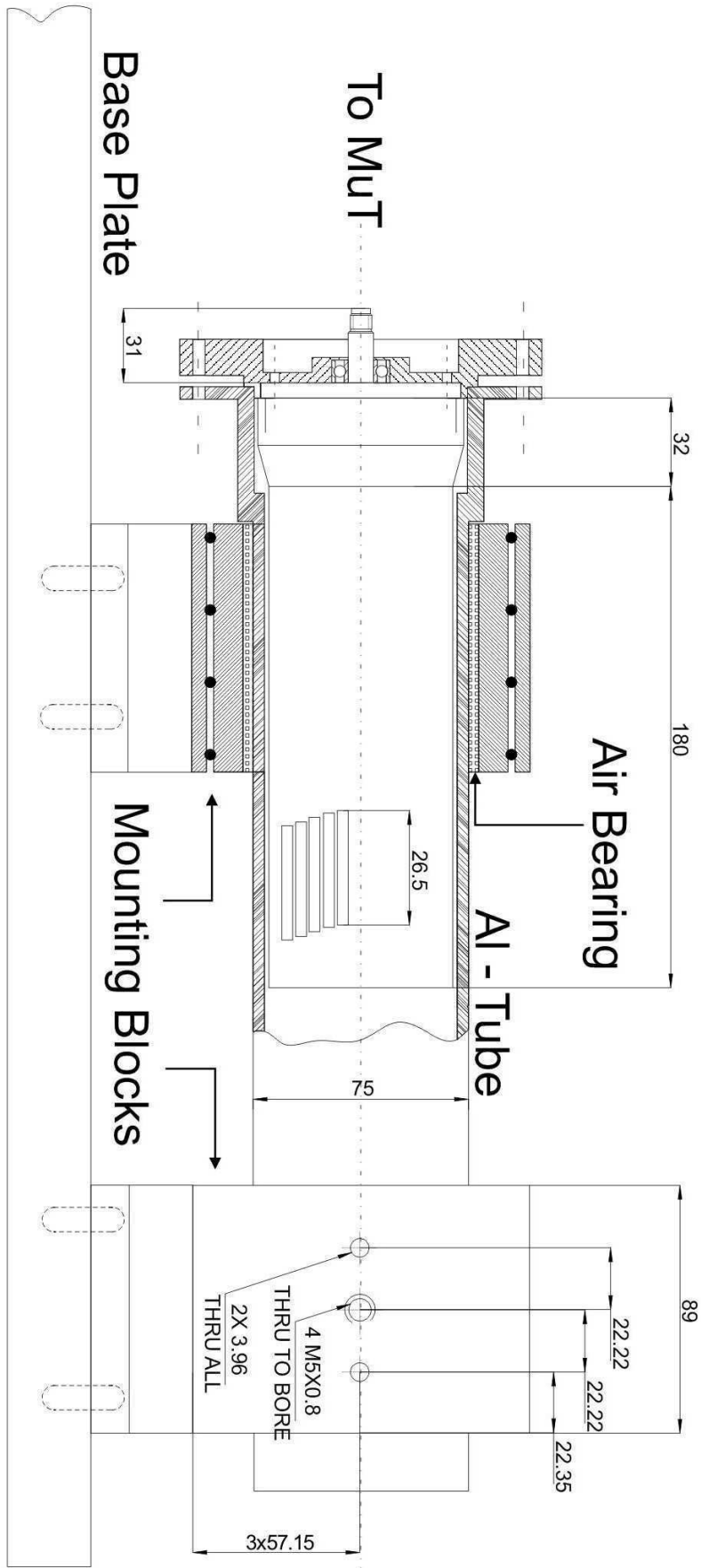
Fig. 6.2 Dynamometer on air bearings
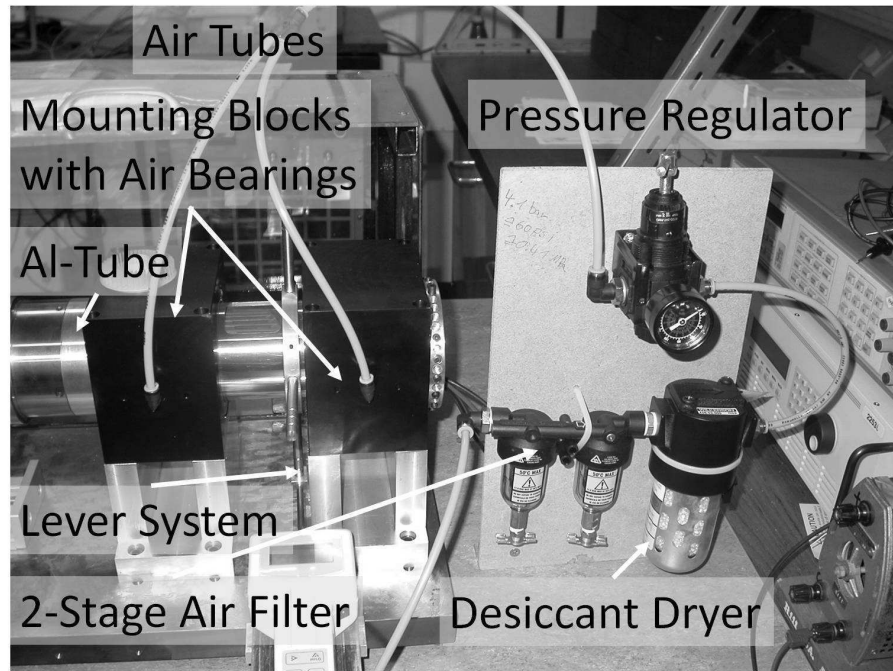
Fig. 6.3 Air supply system
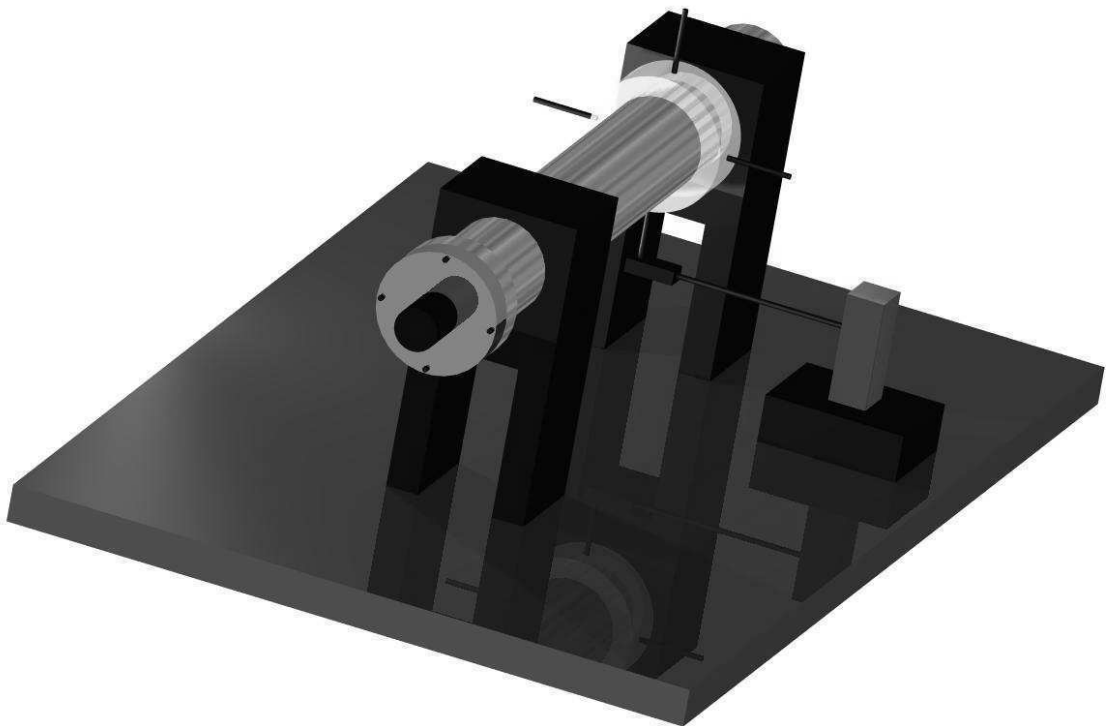
Fig. 6.4 Load machine assembly

The load machine and the MuT were connected using a BSD Thomas coupling of 965 (CBC) type (see Fig. 6.5). This coupling has compensating capabilities for the types of misalignment mentioned above. It was applied using a dial indicator to check if the axial, angular and parallel offset are within the tolerated values for this coupling, and if required the x - y - z - spindles were used to make adjustments and subsequently locked. The lesser misalignment faults, the higher compensation capacity, lifetime and smooth running during operation [53].
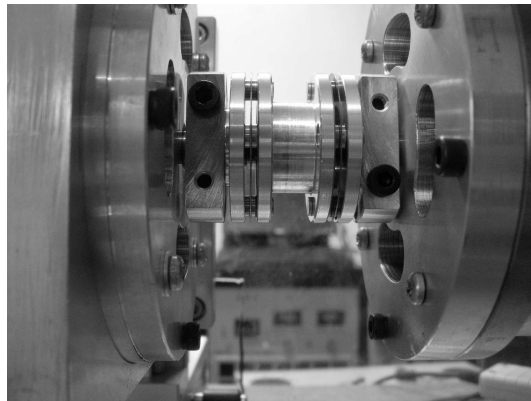
Fig. 6.5 Coupling of MuT and Load machine
shafts

It has to be pointed out that both the MuT and the load machine remained in their original polyamide housings and the gearboxes that are normally used in these tools were removed so that the two armature shafts were coupled directly. The full assembly[6] can be seen in Fig. 6.6.
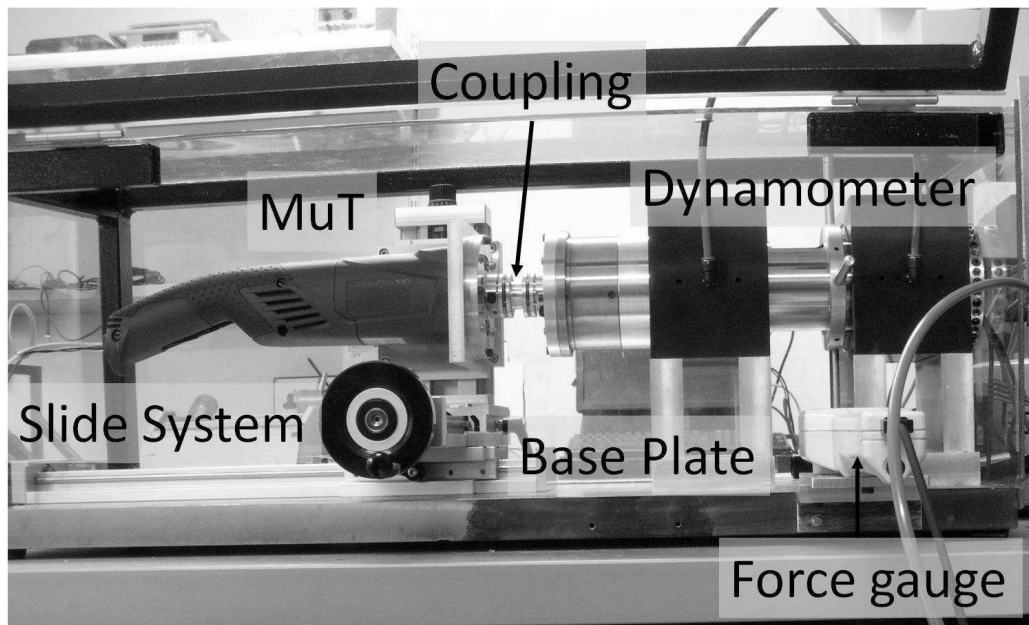
Fig. 6.6 Full assembly

[6]The author would like to acknowledge the distinguished work on the assembly by the late Mr Jimmy Kelly, technician at the mechanical workshop, James Watt Building, University of Glasgow

6.2   Measurement of Torque and Speed

As stated above the torque is measured using a lever arm connected to a force gauge. The torque is equal to the measured force multiplied by the length of the lever arm. The force gauge is a digital SHIMPO force gauge of the DFS series. It has an RS232 communications output that allows to directly control the force gauge with a PC and download the test data from the internal force gauge memory.

To measure the rotor speed it was decided to use the built-in speed sensor comprising a ferrite ring and a hall sensor (see Fig. 6.7) that provides the speed signal to the speed controller at normal operation of the machine as a power tool drive. The ferrite ring is mounted onto the motor shaft and is multi-polarly magnetized. The hall sensor is located in the motor housing right beside the ferrite ring. It produces a noisy voltage signal as shown in Fig. 6.8. In order to quantify the information available from this voltage signal the number of pole pairs of the ferrite ring was identified using a Gaussmeter. The number of pole pairs was found to be eight as shown in Fig. 6.9[7].
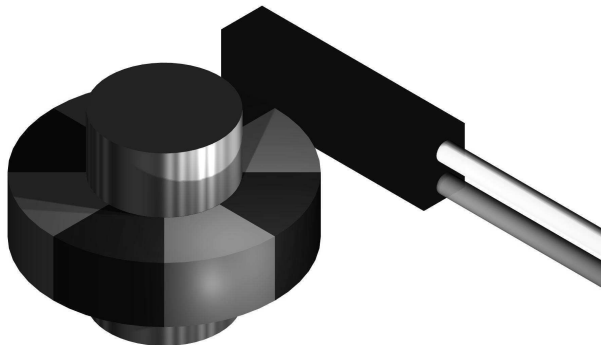
Fig. 6.7 Typical power tool built-in speed sensor
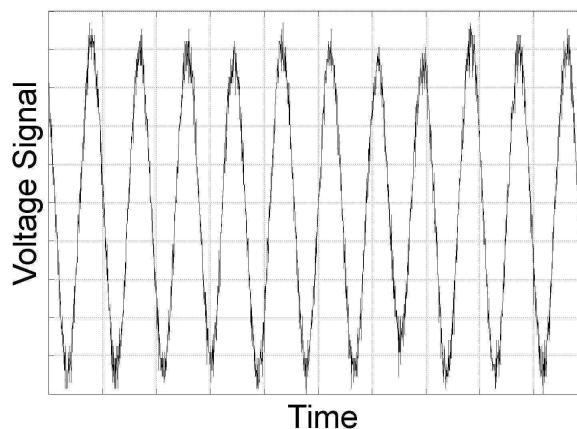
Fig. 6.8 Voltage signal produced by speed sensor

---

[7]The measured graph ultimately is periodic over $360°$ even though this appears not to be the case due to the coarse resolution.
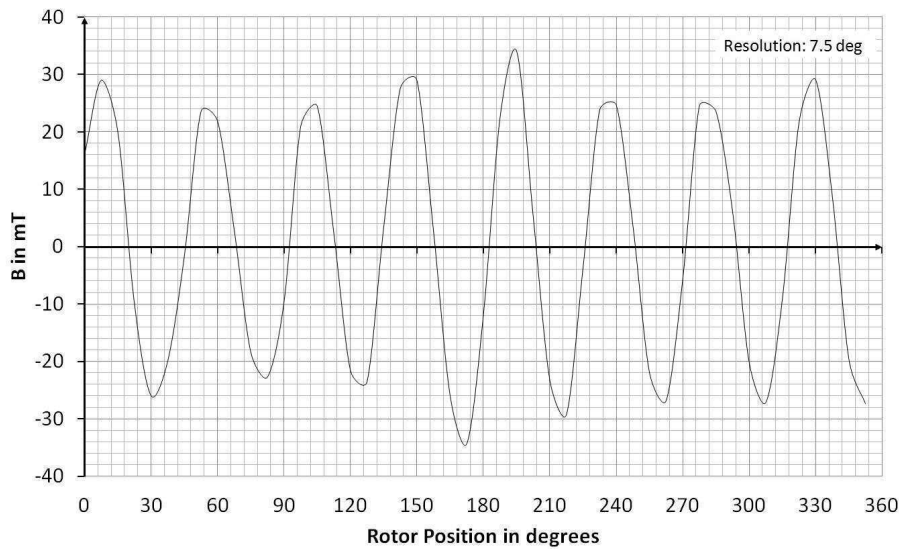
Fig. 6.9 Measured radial flux density

This information was used in order to determine the speed of the machine. An electronic circuit converts the voltage signal shown in Fig. 6.8 into a series of voltage pulses that were evaluated over a certain time interval in order to determine the shaft speed. The evaluation is done using an FCIV controller (see Fig. 3.11). The circuit[8] takes into account the positive half cycle of the noisy voltage signal and, if a certain threshold value is reached converts it into a voltage pulse that ends if the signal voltage drops below the defined threshold. A detailed circuit diagram can be found in appendix A4. As stated above the series of generated pulses is evaluated using the FCIV controller and the speed is made available to the user by FCIV - PC communication as shown in Fig. 6.10.
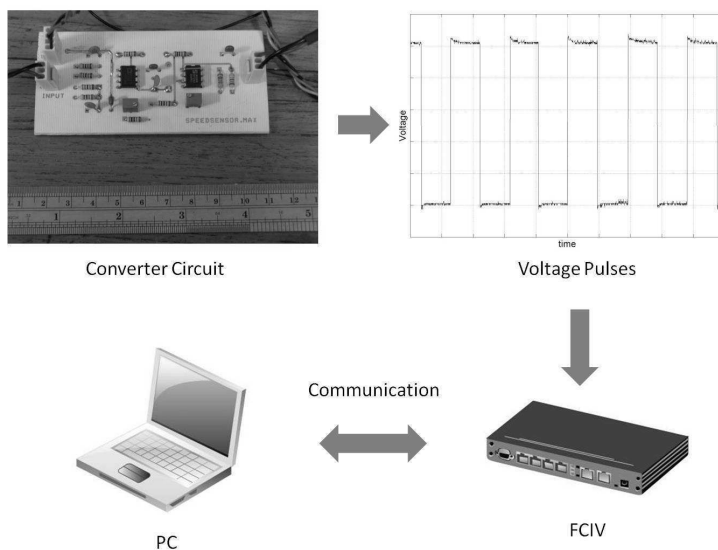
Fig. 6.10 Speed measurement

---

[8]The circuit was designed by Mr Ian Young, technician at the School of Engineering, University of Glasgow

This method of speed measurement was checked against an optical speed sensor with good agreement.

6.3   Measured Motor Performance

To measure the torque speed characteristic the motor voltage was reduced to 25V (rms, 50Hz) for laboratory safety reasons. This is because the gear boxes of both MuT and load machine were removed and therefore the motor shafts were coupled directly. To reduce the risk of damaging the coupling during the measurement the speed and therefore the motor voltage had to be limited. At high speeds ejected objects, despite the polycarbonate shielding, pose a potential threat to health and safety. Moreover the coupling used is an expensive piece of equipment. The motor used was designed to operate from a 120V grid. Hence, the motor was operated at 20.8% of its nominal voltage during the measurements. The torque - speed characteristic of the motor was measured for five operating points.

At each operation point the force gauge was set on "continuous memory mode" where 100 measurements are performed and the gauge provides the average force as well as the standard deviation. The measured torque - speed characteristic can be found in Fig. 6.11 and table 6.1.
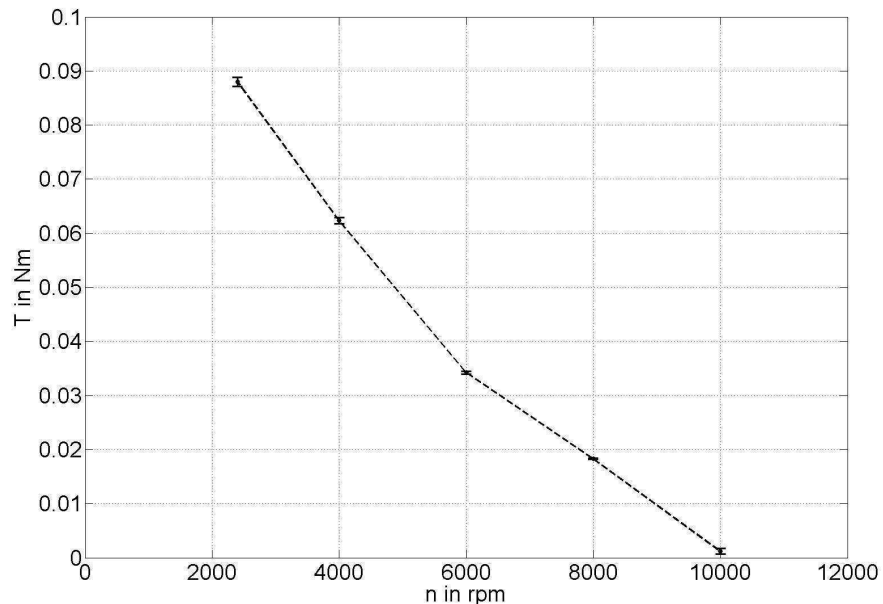
Fig. 6.11 Measured torque - speed characteristic at reduced voltage

Moreover, the torque as a function of motor current (rms) is shown in Fig. 6.12. It can be seen that the progression of the torque as a function of the motor current is approximately linear although the functional correlation of torque and current is quadratic in this machine [1]. This indicates that the machine is saturating and therefore, as flux now increases only minimally with current, the relationship of torque and current becomes linear.
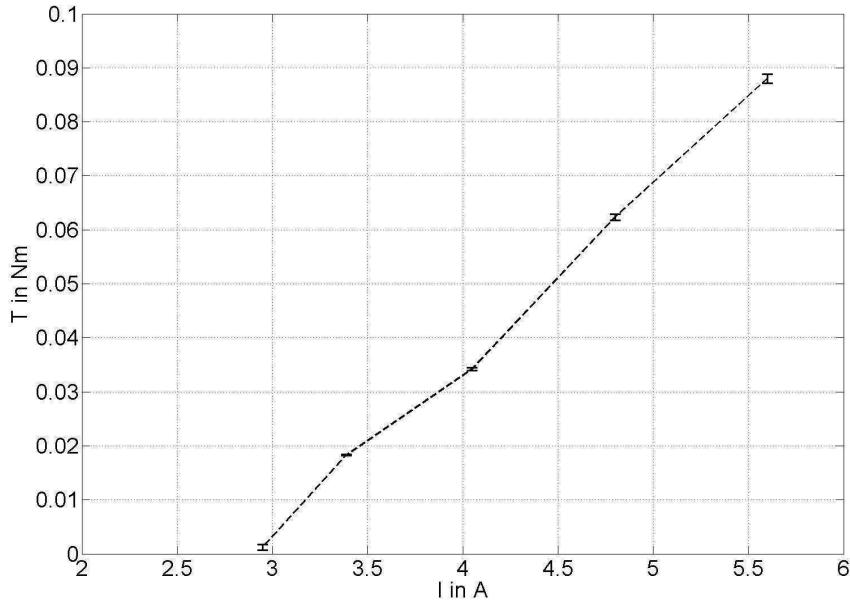
Fig. 6.12 Torque as a function of motor current at reduced voltage

Table 6.1 Test results

n[rpm]	M[Nm]	I_rms[A]
10000	1.22E-03±4.89E-04	2.95
8000	1.83E-02±1.22E-04	3.39
6000	3.42E-02±2.45E-04	4.05
4000	6.23E-02±6.11E-04	4.80
2400	8.80E-02±8.56E-04	5.60

6.4 Conclusions

A motor test bench has been built that allows to measure the motor performance according to the principle of the reaction dynamometer. The load machine is mounted on air bearings to minimize possible torque errors in the measurements. The speed is measured using the built in speed sensor comprising a ferrite ring and a hall sensor. The noisy voltage signal of that sensor is transformed into a series of voltage pulses and evaluated by a FCIV controller in order to find the speed.

A torque speed characteristic of a universal motor was measured as well as the torque as a function of the motor current. These measurements were carried out at reduced motor voltage to keep the shaft speed within reasonable limits.

The test bench could now be used for several rotational tests involving generator tests (see 7.5.2) and due to the capability to reliably set the desired operational points of the motor, test data could be obtained in order to check the accuracy of the mathematical model of the machine (see chapter 8).

7   The Interaction of Commutating Coils and Field Winding

7.1   Characterisation of the Coil Interactions in Technical Literature

The interaction of the commutating coils is shown in several publications dealing with the subject of commutation. For example in [9] graphs are shown where the computed waveforms of the currents of two commutating coils are depicted. The coil that started commutation first is decreasing towards its designated value of 50% of the armature current. At the instant the second coil starts commutating the current in the current in the first coil increases before it decreases again. This effect is due to the mutual coupling of the commutating coils which varies depending on the locations of the commutating coils (rotor position, same slots/ different slots) and the state of saturation of the machine.

In [11] also a graph with two calculated commutating currents can be seen where the interaction of these coils is evident. Here an increase of current in the commutating coil can be observed at the instant the respective other commutating coil reaches the end of commutation.

Measured curves of commutating curves are shown in [45] during arcing where the effect of the commutating coils on each other becomes evident.

In the work about DC machines [54] the authors describe an EMF in the commutating coils due to the rates of change of currents in each of the conductors in the same pair of slots. It is described to be composed of three parts, a central component due to commutation of the coils at a given brush arm and two equal components of similar form but smaller magnitude, respectively, displaced right and left by the chording, due to commutation at neighbouring brush arms.

Among others the publications mentioned above give an adequate image of the interaction of commutating coils. However, the description of the interaction of the field winding and the commutating coils is often limited to the transformer voltage induced in the commutating coils by the field winding in AC commutator motors *e.g.* [8]. The effect of field damping is only rarely described.

In [7] it is stated that for rapid changes of current, like the frequency of commutation, the

effect of a secondary with negligible resistance closely coupled to the commutating coil (considered the primary) nearly counterbalances the action of a short circuited coil which then has very little effective self inductance.

Moreover, the author states that any change in total flux linked with the exciting coils is, in fact, damped by the great mutual inductance between a short circuited coil regarded as a primary and the field coils regarded as a secondary.

In this chapter some theoretical investigations and measurements are carried out in order to get a better insight into these processes.

7.2 Theoretical Investigations

7.2.1 Simulation of ideal field damping using FEA

We assume that the (full pitched) coil *c* located as shown in Fig. 7.1 and Fig. 7.2, is excited, no other rotor coil is carrying a current, and the damping effect of the armature winding is neglected. L_σ is the leakage inductance, L_h is the main (air gap) inductance and M is the mutual inductance of the field winding and coil c. The current I_c in the armature coil c causes an emf in the field winding that is represented by $j\omega M I_c$. The effect caused by the field current I_F in coil *c* is represented by $j\omega M I_F$. The full inductance of a single coil comprises the leakage and the main inductance ($L = L_\sigma + L_h$). Moreover, if we neglect the copper resistances of the coils and assume sinusoidal excitation the voltage equation for the field winding is

$$V_F = j\omega L_F I_F + j\omega M I_c \tag{156}$$

and the voltage equation for rotor coil *c* is

$$V_c = j\omega L_c I_c + j\omega M I_F \tag{157}$$

Setting $V_F = 0$ (ideal damping, *i.e.* field winding short circuited) the current in the field winding necessary to cancel out the main flux between *F* and *c* can be found as follows

$$I_F = -\frac{M_{Fc}}{L_F} I_c. \tag{158}$$

Concerning the damper effect of the field coils in the d-axis there are two ways of looking at the problem.

a) The field coils are connected in series and short circuited.

In this case the self inductance of the series connection of the field coils becomes

$$L_F = L_{F1} + L_{F2} + M_{F1F2} + M_{F2F1} \tag{159}$$

Furthermore, coupling between the field winding F and the single rotor coil c is

$$M_{Fc} = M_{F1c} + M_{F2c} \tag{160}$$

And the required damping current is calculated using (158).

b) The two field coils are short circuited individually.

Now, the voltage equations for the two individual field coils must be considered. Again, the copper coil resistance is neglected as it does not play a role in the FE-calculations.

$$V_{F1} = j\omega L_{F1}I_{F1} + j\omega M_{F1c}I_c + j\omega M_{F1F2}I_{F2} \tag{161}$$

$$V_{F2} = j\omega L_{F2}I_{F2} + j\omega M_{F2c}I_c + j\omega M_{F2F1}I_{F1} \tag{162}$$

Setting $V_{F1} = V_{F2} = 0$ to achieve short circuit conditions from (161) and (162)

$$I_{F1} = -\frac{M_{F1c}I_c + M_{F1F2}I_{F2}}{L_{F1}} \tag{163}$$

and

$$I_{F2} = -\frac{M_{F2c}I_c + M_{F2F1}I_{F1}}{L_{F2}} \tag{164}$$

are found.

Solving the system (163), (164) for I_{F1} and I_{F2} gives

$$I_{F1} = \frac{M_{F1F2}M_{F1c} - L_{F2}M_{F1c}}{L_{F1}L_{F2} - M_{F1F2}^2}I_c \tag{165}$$

and

116

$$I_{F2} = \frac{M_{F2F1}M_{F2c} - L_{F1}M_{F2c}}{L_{F1}L_{F2} - M_{F1F2}^2}I_c \qquad (166)$$

for the damping currents in field coil *F1* and field coil *F2* respectively.

Now, the self and mutual inductances were calculated from the vector potential obtained from FEA as described in chapter 3. The software used was PC-FEA [55]. It is important to point out that these investigations have been carried out for non-saturated conditions.

The calculated inductances per turn and per metre stack length for the cross section depicted in Fig. 7.1 and Fig. 7.2 are listed in table 7.1.

<div align="center">Table 7.1 Calculated Inductances</div>

Inductances [µH/m]					
L_{F1}	L_{F2}	M_{F1F2}	M_{F2F1}	M_{F1c}	M_{F2c}
29.000	29.000	25.000	25.000	25.500	25.500

With the inductances computed using FEA and an injected current in coil *c* of $I_c = 17.933$A one obtains for the damping current required in the field coils calculated by (158), (165) and (166) $I_F = I_{F1} = I_{F2} = -8.468$A which suggests that it is unimportant if the field winding is considered to be two single coils that are both short circuited or a short circuited series connection of the two field coils. However, this only holds if $M_{F1c} = M_{F2c}$ which is not necessarily true for short pitched rotor coils at certain rotor positions.

The resulting field plot can be seen in Fig. 7.1. It can be observed that no mutual flux links the rotor coil *c* and the field winding *F*. This behaviour is similar to the process in a transformer undergoing a sudden short circuit of the secondary winding. The shorted secondary winding attempts to maintain the flux it is linking at the instant of the short circuit. It drives a short circuit current that opposes the change in linked flux. The fluxes of *c* and *F* are forced into leakage paths and do not link the respective other coil. The apparent inductance of *c*, L_c per turn and per metre stack length is found from the calculated vector potentials $\vec{A}$ and the injected current I_c as follows:

$$L_c = \frac{1}{I_c}\oint_s \vec{A}\vec{ds} = 6.35\frac{\mu H}{m} \qquad (167)$$
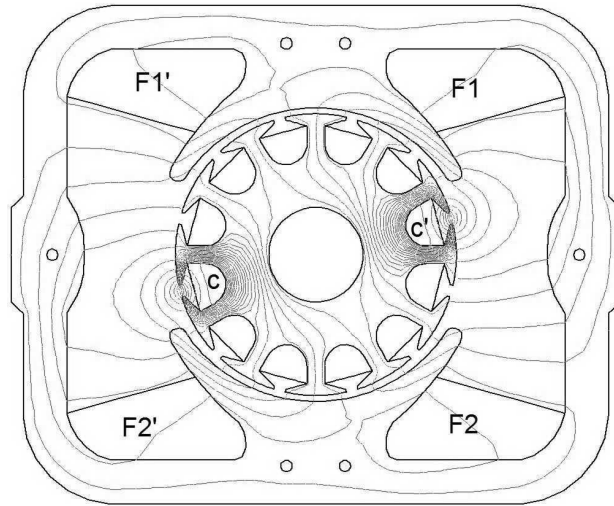
Fig. 7.1 Ideal field damping

To compare the inductances of the ideally damped and the non-damped case the flux pattern of the non-damped case is depicted in Fig. 7.2. Coil *c* is excited only and the field coils *F1* and *F2* are linked by the flux produced by *c*. The same current in c as in the damped case leads to an inductance of $L_c = 30.05$ µH/m. Ideal field damping causes a reduction of the apparent coil inductance to approximately one fifth compared to the non-damped case for the motor cross section used in the calculations. Non - ideal damping will cause a value that is between the non-damped and the ideally damped case.
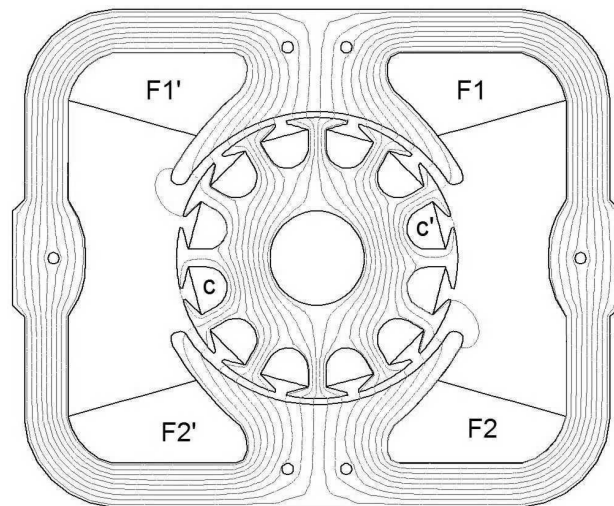
Fig. 7.2 No field damping

One can see from the field plots (Fig. 7.1 and Fig. 7.2) that the ideally damped armature coil inductance is almost solely a leakage inductance whilst the non-damped inductance is solely an air gap (main) inductance. An inductance of an electric machine generally contains both parts, leakage- and air gap inductance. In normal operating conditions field damping will force a part of the flux produced by commutating coils to leakage paths and therefore increase the leakage inductance of the commutating coil although the full inductance of the coil may decrease.

7.2.2 Simulation of interaction of rotor coils using FEA

The program PC-FEA was used to simulate the field in a universal motor for the cases when only two armature coils are excited and all other coils do not carry any current. The excited armature coils were chosen in a way that they represent short pitched, full pitched, aiding or opposing coils close to the interpolar (quadrature [23]) axis.

Fig. 7.3 shows the flux caused by two aiding coils in the armature. It is obvious that this flux distribution is valid for two full pitched as well as two short pitched coils. In this configuration those rotor coils are aiding in the polar (d-) axis and are opposing in the interpolar (q-) axis.
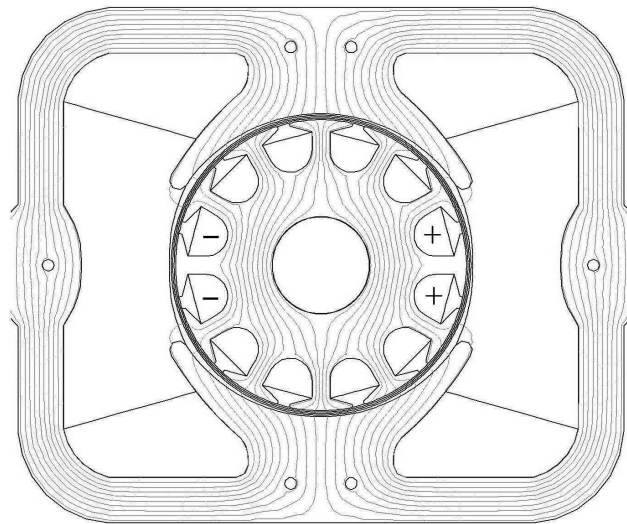
Fig. 7.3 Two aiding rotor coils

It is a different case if the armature coils are opposing in the d - axis. Their fluxes cancel out in the d-axis and sum up in the q-axis in a way that there is only leakage flux left and the field coils are not linked as depicted in Fig. 7.4 for two full pitched coils.
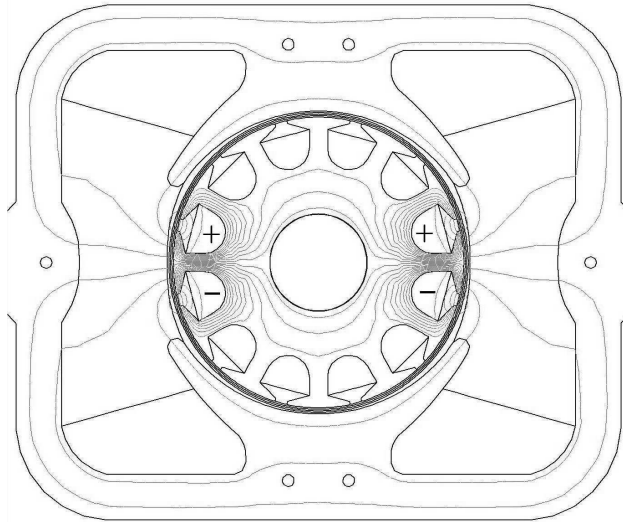
Fig.7.4 Two opposing full pitched coils

If the two opposing coils in the armature are short pitched as depicted in Fig.7.5 *i.e.* they do not cross over, there is flux crossing the air gap in the d-axis and linking the field coils. However, this d-axis flux does not link both field coils at the same time. Hence it can also be considered leakage flux of the armature coils. The effects on both poles cancel out.
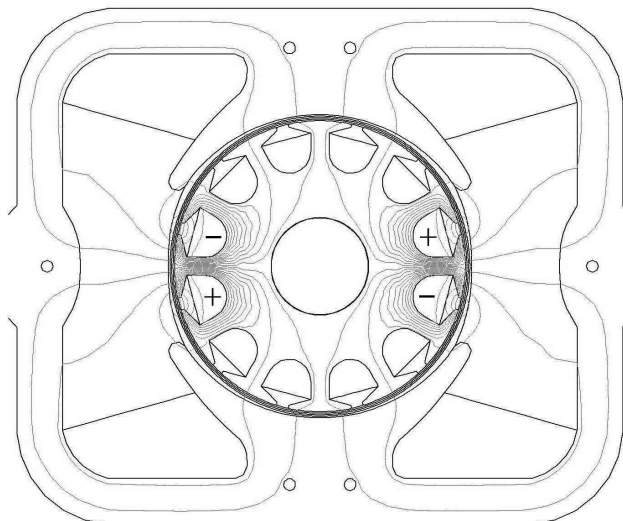
Fig. 7.5 Two opposing short pitched coils

7.3   Static AC Measurements

7.3.1 Test setup

An empty rotor and empty stator lamination were used to examine the effects observed in the FE plots. On each pole of the stator a field coil was wound. According to the motor data sheet each field coil got 87 turns. An actual pre-wound machine stator could not be used as the machine-wound field coils do not leave space for the sense coils to be placed around the salient stator poles. Around each field coil a sense coil with 10 turns was wound. Additionally a sense coil with 10 turns was wound around the stator yoke. On the rotor two short pitched and two full pitched coils were wound (10 turns each) and another sense coil was wound around a tooth to examine tooth leakage. The full configuration can be seen in Fig. 7.6.
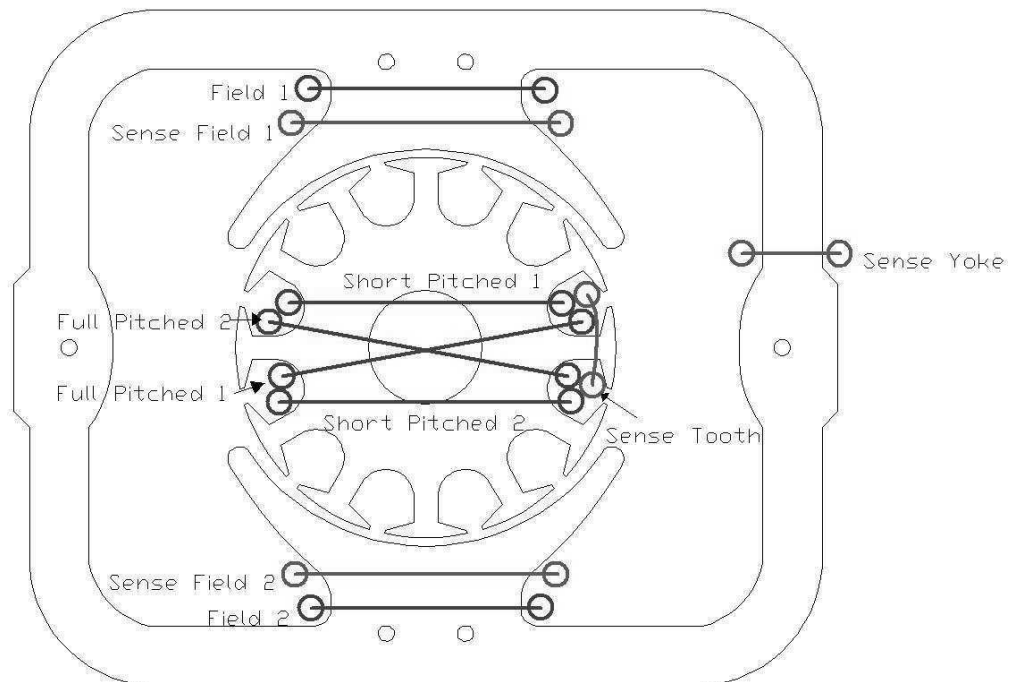
Fig. 7.6 Locations of coils

A minimum air gap of 0.5 mm in the d-axis at each pole is ensured by the use of plastic shims. The rotor and the plastic shims were inserted into the stator and the terminals of all the coils were brought out to connector blocks (see Fig. 7.7 and Fig. 7.8).

121
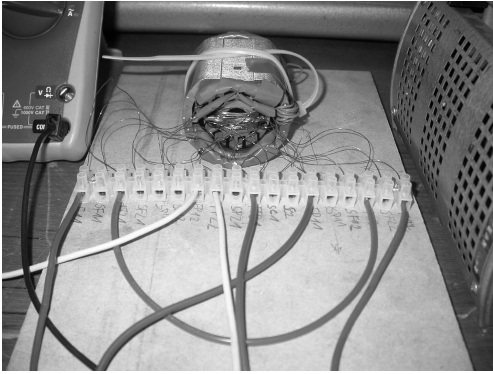
Fig. 7.7 Setup view 1

Fig. 7.8 Setup view 2

The adhesive tape was used to protect the wire insulation as it is very likely that the sharp corners of the lamination cause damage to the insulation which leads to short circuits in the coils and between the coils and the lamination.

7.3.2   Tests with field winding left open circuit

At first, the field coils were left open circuit whilst current was injected into the armature coils. As the connections at the connector block may have different resistances the excitation circuit of the armature coils got variable resistors to ensure the current in the armature coils is equal. The excitation circuit is shown in Fig. 7.9.
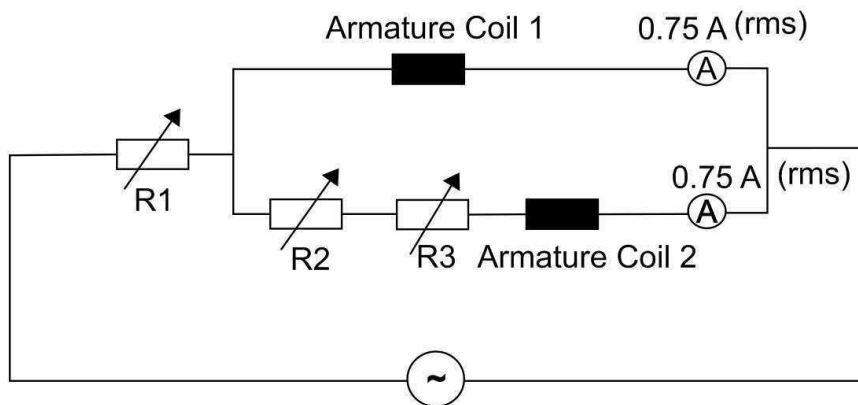
Fig. 7.9 Armature circuit

The resistor R1 serves as a current limiter as the coil resistances are very small. R2 is a variable resistor with a coarse range and R3 is a variable resistor with a fine range. The combination of R2 and R3 is used to adjust the current. An AC source was used to apply a sinusoidal current to the coils. To avoid saturation the current was kept reasonably low. (0.75 A (rms) at 60 Hz)

The following measurements were carried out with the field coils open circuit:

- M1: One full pitched coil excited
- M2: Two full pitched coils excited (aiding)
- M3: Two full pitched coils excited (opposing)
- M4: One short pitched coil excited
- M5: Two short pitched coils excited (aiding)
- M6: Two short pitched coils excited (opposing)

7.3.3   Tests with field winding short circuited

At the next stage, the field coils were connected in series and short circuited. Subsequently, the following measurements were performed:

- M7: One full pitched coil excited
- M8: Two full pitched coils excited (aiding)
- M9: Two full pitched coils excited (opposing)
- M10: One short pitched coil excited
- M11: Two short pitched coils excited (aiding)
- M12: Two short pitched coils excited (opposing)

7.3.4   Results

The results of M1 - M12 can be found in table 7.2. They are in compliance with the findings from the finite element simulations. Comparing M1 and M2 it can be seen that the flux in the yoke increases significantly while the tooth leakage flux seem to vanish in case of M2. This agrees very well with Fig. 7.2 and Fig. 7.3. Moreover, if M2 and M3 are compared the opposite effect can be observed. The flux in the yoke decreases significantly while the tooth leakage becomes very high as expected from Fig.7.3 and Fig. 7.4. Basically the same effects take place with the short pitched coils. However, there is a difference in the cases M1 and M4. The coupling of a single short pitched coil to the sense coils on the field poles is not equal at the rotor position shown in Fig. 7.6. This effect and be confirmed using 2D FEA. In addition there is more flux linking the coils on the field poles in M6 than in M3. This was to be expected with regard to the field plots in Fig. 7.4 and Fig. 7.5.

Now the open circuit cases and the short circuit cases are to be compared. The damping is significant in M7, M8, M10 and M11 compared to M1, M2, M4 and M5 respectively. This could be expected regarding Fig. 7.1. Again, regarding Fig. 7.4 and 7.5 the insignificant damper effect in M12 compared to M6, and M9 compared to M3 becomes plausible. There is no or very little flux in the poles so the short circuited field coils do not seem to have an effect.

Table 7.2 Measurement results

Measurement	Voltages in Sense coils / mV			
	S-Field 1	S-Field 2	S-Tooth	S-Yoke
M1	34.9	35.1	3.9	16.7
M2	76.7	76.8	0.8	37.6
M3	0.8	0.7	7.8	0.9
M4	36.8	33.9	3.9	17.6
M5	77	77.2	0.6	37.6
M6	2.8	3	7.6	0.9
M7	16.5	16.6	3.8	7.9
M8	34.1	34.1	0.5	16.6
M9	0.6	0.6	7.6	0.7
M10	17.8	16.1	3.8	8.4
M11	34.3	34.4	0.6	16.6
M12	3.2	3	7.4	0.8

7.4 Static Inductance and *di/dt* - Tests using an oscillating Circuit

7.4.1 Purpose of measurements

Desired is an estimation of the inductance when a single coil experiences a sudden current rise *i.e.* a high *di/dt*. Furthermore the change of this inductance if other coils also experience a high *di/dt* is to be investigated. The change of this inductance highly depends on the other coils carrying currents that lead either to aiding or opposing fields in the d - axis and q - axis, respectively. The influence of damping and saturation is another interesting aspect in that matter and will be observed as well.

Moreover, the effect of a sudden current injection into a coil on the *di/dt* of another coil will be examined. The resultant accelerating or braking effect can give some indication about beneficial or unfavourable current reversal conditions from an electromagnetic point of view.

7.4.2   The motor used

For the measurements a 2 pole universal motor was used. The field circuit has 2 field coils and the armature circuit comprises 24 coils distributed in 12 armature slots. There are 4 coil sides per slot and the rotor coils are short pitched with a throw of 6 - 1 = 5. The rotor winding is a lap winding.

The number of turns in one field coil is 87, the average number of turns in one armature coil is 10.5. It is known for the rotor that a commutator lead of 30 mechanical degrees is applied equivalent to a brush shift of 30 mechanical degrees against the direction of rotation. The slot pitch is 30 degrees and the commutator pitch is 15 degrees. A typical armature winding configuration for this motor can be seen in appendix A1.

7.4.3   The commutation scenarios examined

The reference system described in 4.3 shows that there is a cyclic transition of the configurations 4 coils commutating - 2 coils commutating - 4 coils commutating - ... in this machine, with different lengths of the intervals 4 coils commutating and 2 coils commutating. Illustrated in Fig. 7.10 is an overview of the number of coils commutating simultaneously at certain rotor angles where coils shorted by brush 1 are labelled with odd numbers and coils shorted by brush 2 are labelled with even numbers. The reference point $0°$ in Fig. 7.10 corresponds to a brush position on the commutator where the brush centre axis is aligned with a commutator bar centre axis.
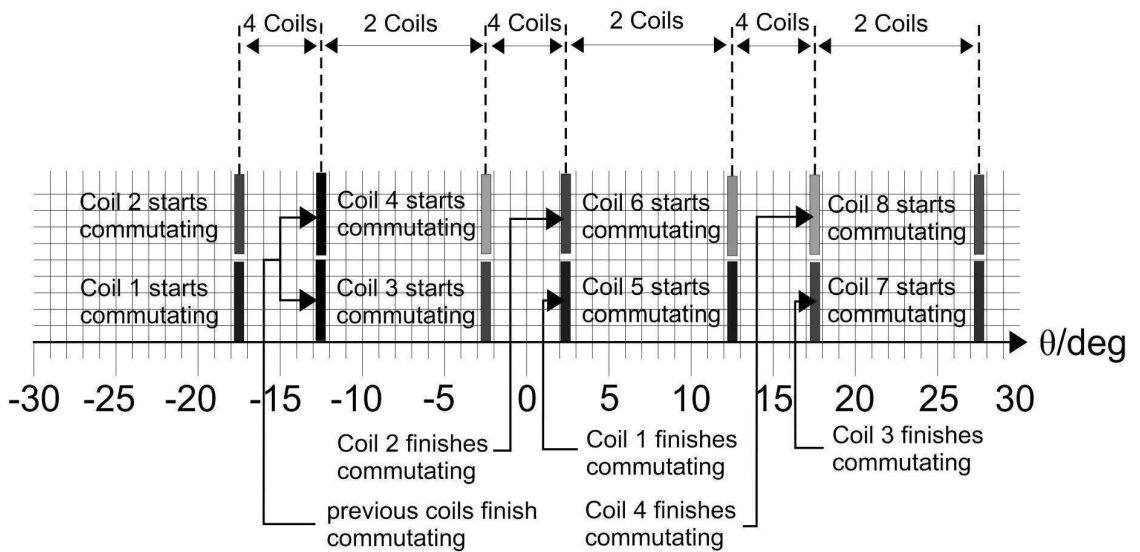
Fig. 7.10 Commutation scenarios

Now the positions of the coils undergoing commutation at different rotor positions can be determined. The coil positions in the motor at different rotor positions are shown in Fig. 7.11 - 7.15. The direction of rotation is clockwise with respect to the commutator.

Fig. 7.11 θ = 0°

Fig. 7.12 θ = 10°

Fig. 7.13 θ = 15°

Fig. 7.14 θ = 20°
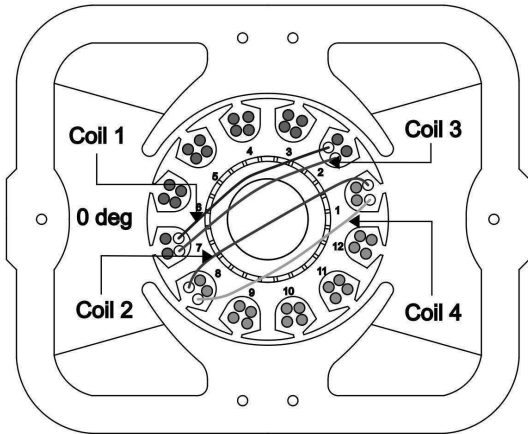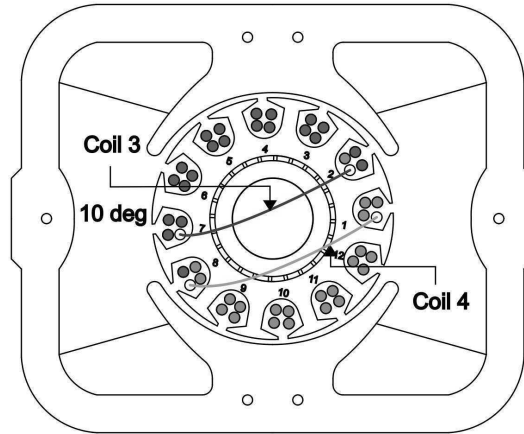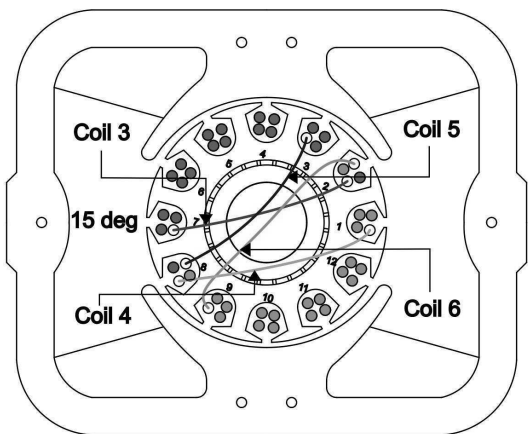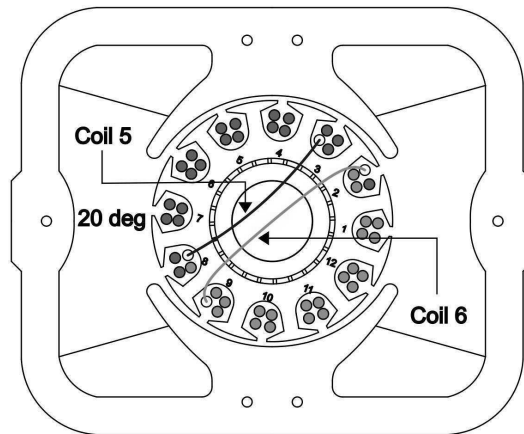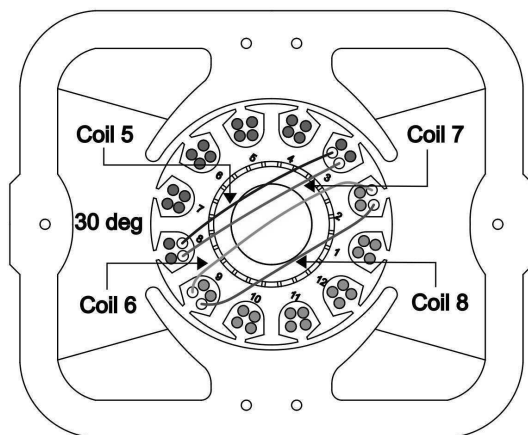
Fig. 7.15 θ = 30°

It can be seen from Fig. 7.11 and Fig. 7.13 that the case of 4 coils commutating has two different configurations. In Fig. 7.11 the coils undergoing commutation at one brush are located in the same slots whilst in Fig. 7.13 the coils are in different slots and cross over which is likely to cause quite different field distributions in the q- and the d- axis as shown in 7.2. In Fig. 7.15 the commutating coils after one slot pitch (30°) are indicated. The configuration is the same as at 0° just with other coils involved. Hence the current reversal process of this motor is 30° - cyclic.

7.4.4 Proposed inductance and *di*/*dt* test method

In order to apply a rapid current change to one or several coils at a time or at different times to observe changes in inductance or in the *di*/*dt* an oscillating circuit (see Fig. 7.16) was found suitable for this purpose.

The idea is to charge a capacitor with known capacitance C using a DC source. Then, the DC source is disconnected from the capacitor and the capacitor is discharged through the coil to be investigated (coil resistance R; coil inductance L). The appearing decaying current oscillation is recorded with a current probe and a digital oscilloscope.
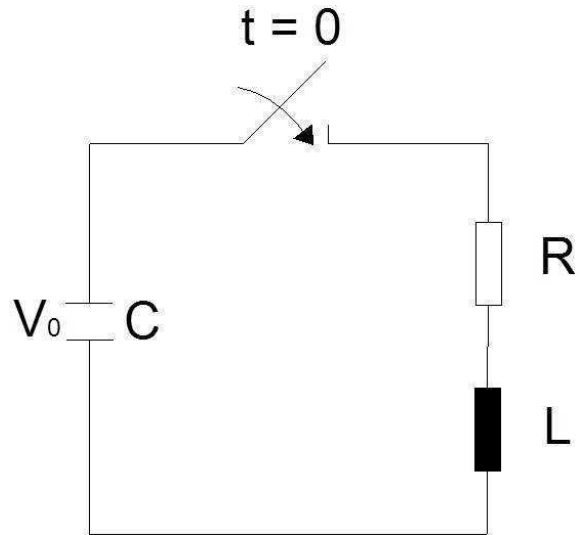
In the test - circuit the disconnection of the capacitor from the DC source is done by a relay. The capacitor is then discharged

Fig. 7.16 RLC circuit

through the coils using electronic switches (N – channel MOSFETS) controlled via a FCIV controller. The choice of electronic switches was due to the requirement of fast switching and negligible contact bounce. The circuit will be explained in detail later on.

The capacitor C is charged to the voltage V_0 and is discharged through R and L via the switch at the instant $t = 0$. After the switch is closed the governing differential equation for the current is

$$\frac{d^2 i(t)}{dt^2} + \frac{R}{L}\frac{di(t)}{dt} + \frac{1}{LC}i(t) = 0 \tag{168}$$

with the solution

$$i(t) = I_0 e^{-\beta t} \sin(\omega' t - \varphi_0) \tag{169}$$

where

$$\beta = \frac{R}{2L}, \tag{170}$$

$$\omega_0 = \frac{2\pi}{T_0} = \frac{1}{\sqrt{LC}} \tag{171}$$

and

$$\omega' = \frac{2\pi}{T'} = \sqrt{\omega_0^2 - \beta^2}. \tag{172}$$

Moreover, the unknown parameters I_0 and φ_0 can be found using the initial conditions as follows

$$i(0) = 0 = I_0 \sin(-\varphi_0) \implies \varphi_0 = 0 \tag{173}$$

and

$$v_C(0) = V_0 = L\frac{di(t)}{dt}(0) = L\omega' I_0 \implies I_0 = \frac{V_0}{\sqrt{\dfrac{L}{C} - \dfrac{R^2}{4}}}. \tag{174}$$

The graph of (169) is depicted in Fig. 7.17. From the current waveform the logarithmic decay

$$\Lambda = \ln\left[\frac{I_n}{I_{n+1}}\right] = \beta T' \tag{175}$$

can be determined as well as the oscillating period T'. Subsequently, with the knowledge of the capacitance C active in the circuit and the voltage V_0, the parameters β, L, R, I_0 and ω' can be found using (175), (170), (171), (172) and (174). This also deals with the problem of knowing the value of resistance in the circuit as it might vary for different circuits and change due to warming of the conductors and eddy currents (skin effect) due to the high frequency.

Furthermore the inductance determined is the inductance active in the circuit which includes mutual coupling with other active coils as well as damping effects of the field coils or the remainder of the armature circuit, eddy currents and saturation effects.
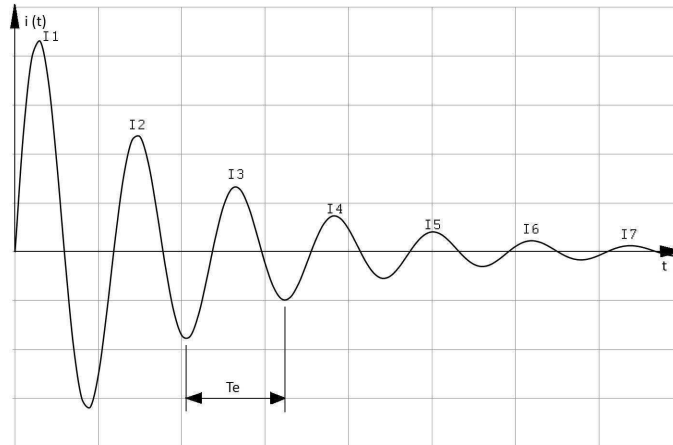
Fig. 7.17 Decaying current (Te = T')

7.4.5 The test circuit

As shown in 7.4.3 there is a maximum of 4 coils undergoing commutation simultaneously in this motor. Hence, a capacitor bank of 4 identical AC film capacitors was set up in order to supply 4 rotor coils independently. The circuit can be seen in Fig. 7.18. The capacitors are charged through a DC source and subsequently disconnected from the source and each other using 2 relays capable of switching 2 circuits each. Furthermore each capacitor is connected to a rotor coil (R and L) through 2 electronic switches (N – channel MOSFETS).

There is need for 2 switches in each branch because all the armature coils are connected in series round the commutator. The first switch needs to be between the capacitor and the coil to make sure that no other capacitor discharges through that coil when its lower switch is open. The second switch needs to be located between the coil and ground. As the capacitors are connected to one ground the second switch makes sure that the capacitor switched does not discharge through more than one coil. If there was no second switch the capacitor would discharge through a parallel connection of several coils connected to the same ground. The MOSFETS are driven by 2 different gate drives. One drives the 4 "upper" switches between the capacitors and the coils and the other one drives the 4 "lower" switches between the coils and ground. These two gate drives were originally designed for H - bridges and are isolated from the power side. There is need for 2 different gate drives for upper and lower switches as the two MOSFETS in one branch have two be switched at the same time *i.e.*

triggered by the same gate signal. This means that both transistors need to have the same reference which would lead to the coil to be shorted out if there was only one gate drive. The gate drives are controlled by a FCIV controller via an interface that converts the signal transmitted via optical fibre to the input signals of the gate drives. The switching instants of the MOSFETS can be user defined on the PC and sent to FCIV via parallel port.
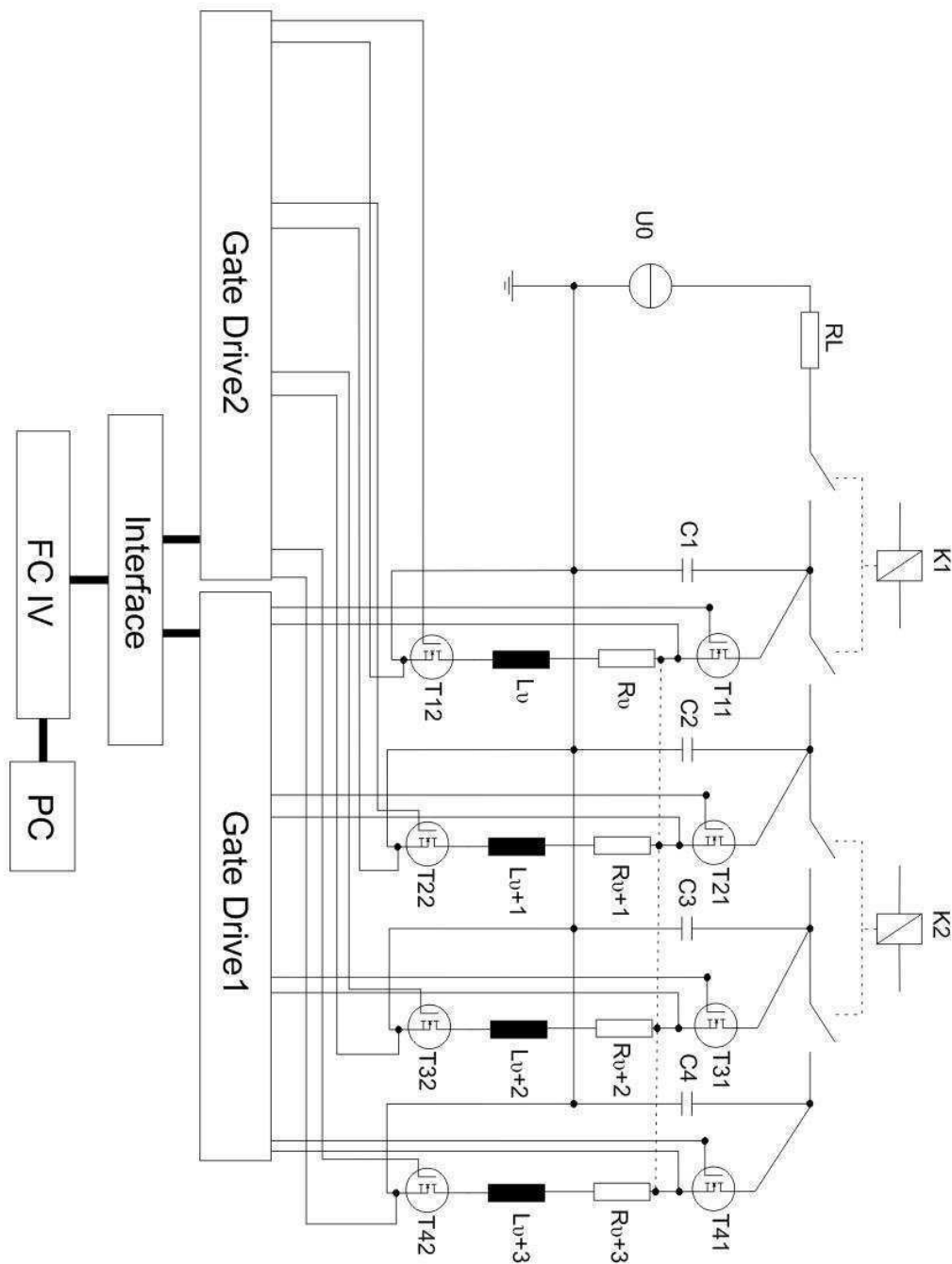
Fig. 7.18 Test circuit

The gate drive and interface circuits were provided by Ian Young, the capacitor bank and the relays were provided by Peter Miller, and the switching algorithm of for the FCIV - controlled MOSFETS was provided by Calum Cossar, all members of the Systems, Power and Energy Research Division, School of Engineering, University of Glasgow.

The circuit diagram of the interface for the MOSFET control and photographs of the test setup can be found in appendix A5.

7.4.6 Evaluation of the parasitic inductance of the capacitors used

It is well known that the impedance frequency response of a capacitor has a minimum at the resonant frequency f_0. If the frequency is increased further the impedance starts rising. This effect is due to the parasitic inductance of the capacitor. In Fig. 7.19 the typical impedance frequency response of a capacitor is depicted.

A frequency generator was used to supply a sinusoidal voltage of variable frequency to the capacitor and its impedance was measured. The minimum was found at f_0 = 9MHz. The capacitance of the capacitor is 1μF. Hence Thomson's equation

Fig. 7.19 Frequency response of capacitor

$$f_0 = \frac{1}{2\pi\sqrt{LC}} \tag{176}$$

yields

$$L = \frac{1}{C(2\pi f_0)^2} = 3.127 \cdot 10^{-10} H \tag{177}$$

Hence, the parasitic inductance of the AC film capacitor can be considered negligible as the expected measured coil inductance is not smaller than several μH.

7.4.7 Identification of coils located in one slot

To set up the different commutation scenarios as depicted in Fig. 7.11 - 7.15 the reference position θ = 0 ° needs to be identified first. It can be seen in Fig. 7.11 that in this case 4 coils are commutating simultaneously whereas the coils being commutated by one brush are located in the same slots. To find a configuration of 4 coils where 2 coils are connected to one side of the commutator and located in the same slots and the other 2 coils are connected to the opposite side of the commutator and on their part located in the same slots the following was done:

The two field coils were connected in series and connected to an AC source. The supply voltage was 3V (rms) at 50 Hz and the induced voltages in the rotor coils were measured across two adjacent commutator segments in each case. The rotor was in a position where a tooth axis aligns with the interpolar axis as depicted in Fig.7.20. The profile of induced voltages can be seen in Fig. 7.21. The segments with minimum induced voltage measured across represent the terminals of the 4 coils indicated in Fig. 7.20.
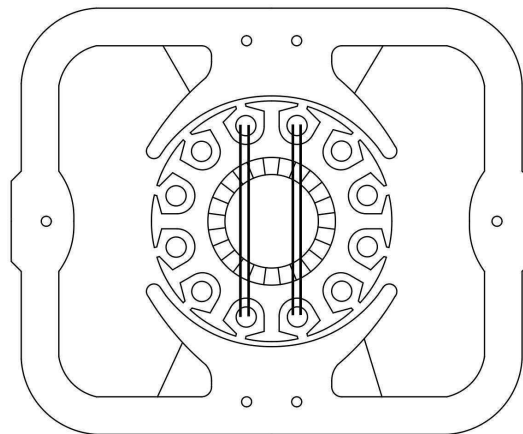
Fig. 7.20 Rotor coils with minimum induced voltage
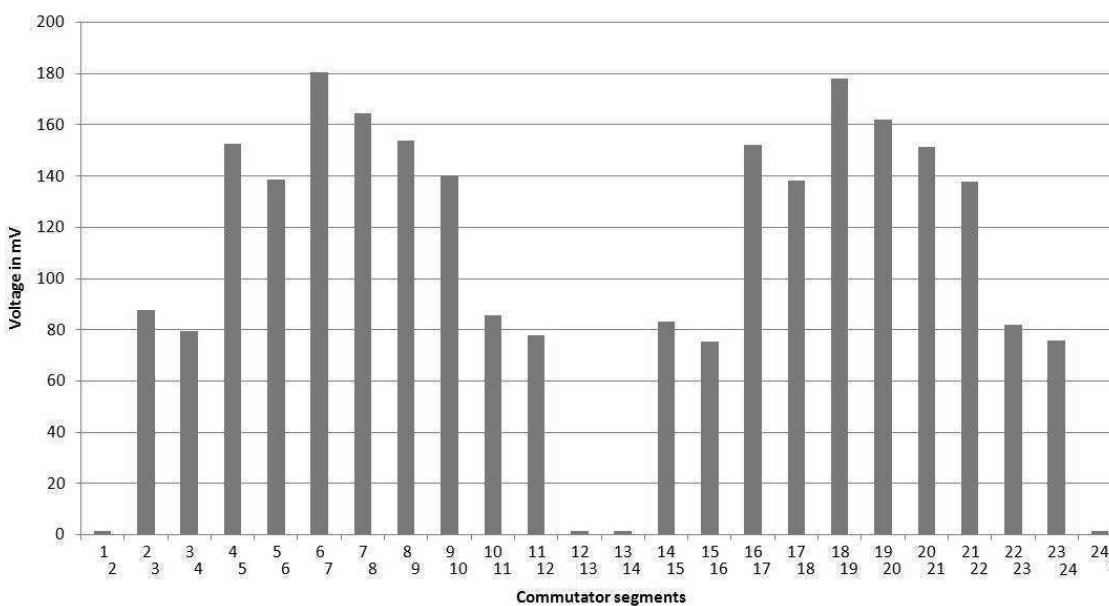
Fig. 7.21 Profile of induced voltages

From Fig. 7.21 it can be seen that the minima of the induced voltages are measured across commutator segments 1-2,12-13,13-14 and 24-1 where the coils connected to segments 24-1 and 1-2 are located in the same slots and the coils connected to segments 12-13 and 13-14 are located in the same slots, respectively. Therefore those 4 coils were selected to represent the 4 coils undergoing commutation in Fig. 7.11. Those coils are from now on denoted coil1, coil2, coil3 and coil4. To bring those coils in the position shown in Fig. 7.11 the rotor was turned into a position where the centre axes of segments 1 and 13 align with the q - axis. It has to be pointed out here that the rotor was inserted into the stator using plastic shim to ensure a minimum air gap of 0.5 mm in the d - axis at each salient pole and to hold the rotor in place.

7.4.8   Insertion of sense coils in the q - axis

To capture leakage flux in the q - axis straying from teeth to the stator yoke across the interpolar axis 2 sense coils with 10 turns each were inserted into the interpolar gaps of the motor. These coils are fixed in position and do not change location if the armature is turned. See Fig. 7.22.
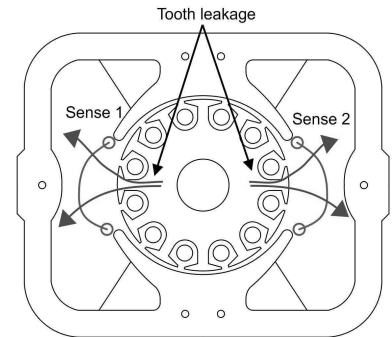
Fig. 7.22 Position of sense coils

7.4.9   Access to armature coils

To measure the current through a single armature coil it was necessary to break the armature winding at several points to solder additional loops in which were brought out to current probes. Comparing Fig. 7.11 and Fig. 7.15 the magnetic properties will be the same in both cases so tests were carried out for the cases in Fig. 7.11 - 7.14 only and therefore 6 loops were soldered into the armature circuit (see Fig. 7.23 and 7.24).
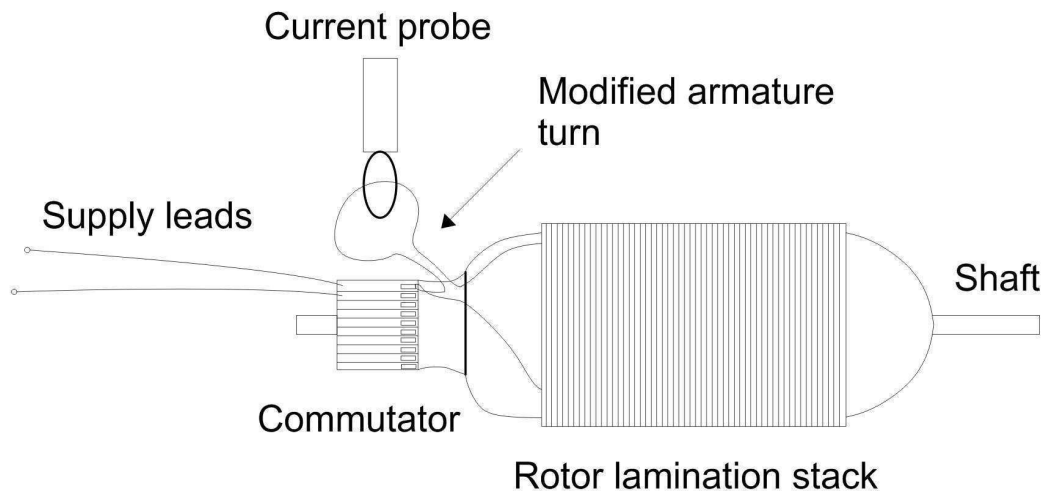
Fig. 7.23 Modified armature loop
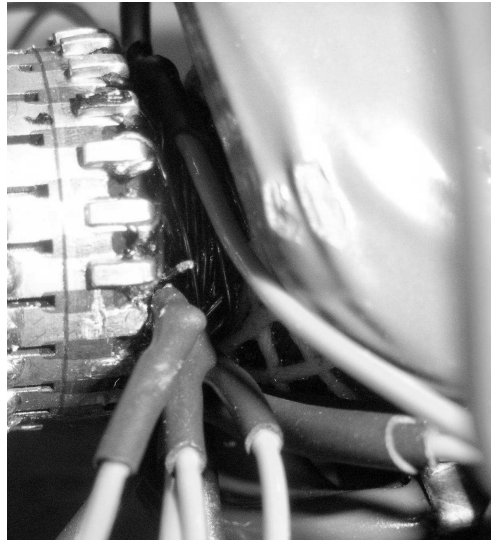
Fig. 7.24 Access to armature coils

7.4.10 Inductance measurements

■ Tests at θ = 0°

For these tests the circuit in Fig. 7.18 was set up in a way that coil1, coil2, coil3 and coil4 were connected to a capacitor each. The capacitors were charged in parallel to a DC voltage $V_0 = 30V$. Subsequently, the capacitors were separated from the DC source and discharged through the coils using the electronic switches.

The coils were switched one by one without interaction between them. The decaying current in coil1 when the field winding is left open circuit can be seen in Fig. 7.25. The inductance estimated using the logarithmic decrement Λ and the period T' is $L = 99\mu H$.
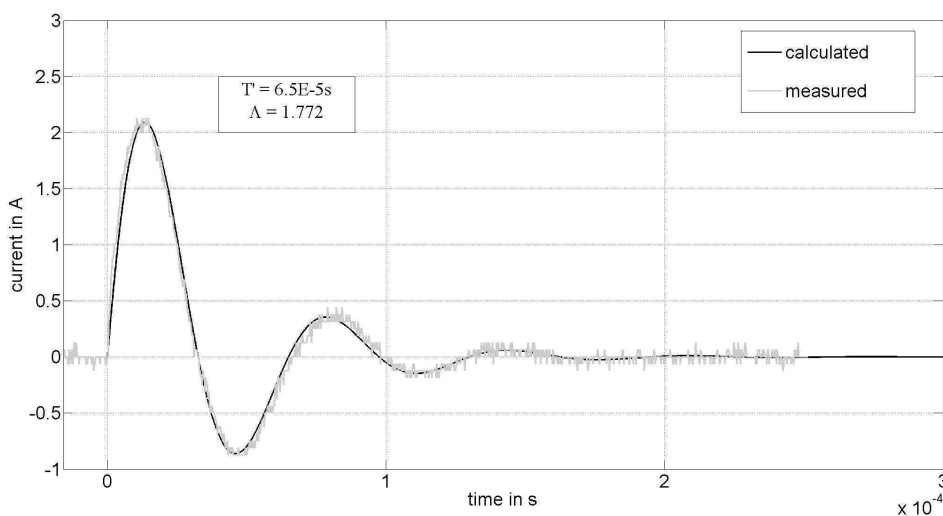
Fig. 7.25 Calculated and measured waveforms of coil1

The logarithmic decrement Λ and the oscillating period T' can be obtained from the measured time waveforms. Subsequently, β, L, R, I_0 and ω' can be calculated as described above. Those parameters can now be used to calculate the current waveform using (169). Both the measured and calculated current waveforms are then plotted against time in the same diagram for comparison.

It can be seen that even though the peaks of the current waveform change significantly over the measured period of time the calculated and the measured curves agree very well over the full measured range. This indicates that the parameters of the decaying oscillation do not vary significantly during the measurement. One could expect that the parameters change due to saturation and the measured curve starts deviating from the calculated one at some point but the low number of turns of a single armature coil (10.5 average) is not enough to drive the magnetic circuit into considerable saturation.

In the next step, the influence of a field winding current on the single rotor coil inductances is examined. Therefore, the field winding was supplied by a DC source and the field current was increased successively. The inductance of coil1 as a function of the field current is shown in Fig. 7.26.
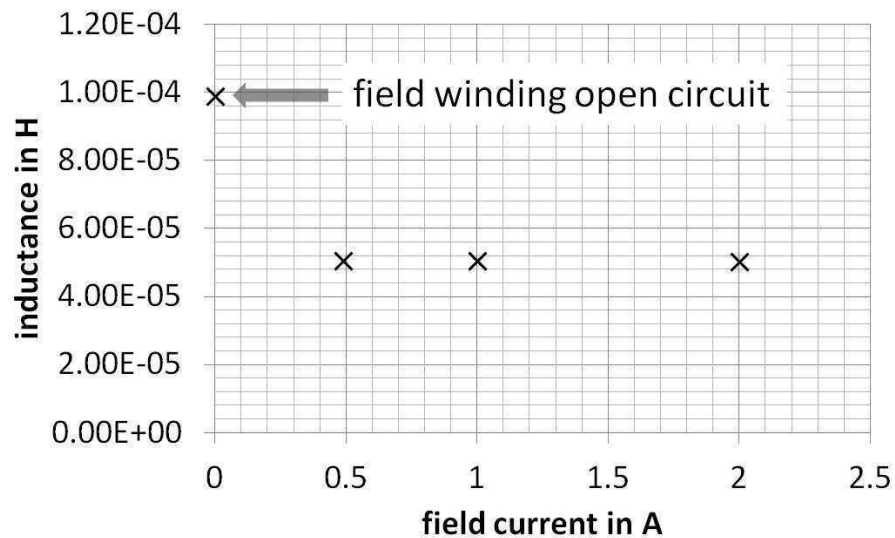
Fig. 7.26 Rotor coil inductance as function of DC field current

From the graph one can see that the inductance decreases significantly after the DC source is connected to the field winding but then remains almost constant with field increasing field current. It is known that the motor used starts saturating at about 1A motor current (peak or DC value) therefore saturation does not seem to have a strong influence on the inductance of

a rotor coil experiencing a rapid current change. The decrease of the inductance is more likely to be caused by the damping currents in the field winding caused by a high rate of change of flux linking the field winding due to the high *di/dt* in the rotor coil.

Therefore, in the following tests only one value of field current (2A) is applied in order to examine the influence of the presence of a saturating and damping field winding. In table 7.3 the inductances of coil1, coil2, coil3 and coil4 are listed for the cases of field winding open circuit and field winding carrying a DC current of 2A.

Table 7.3 Measured inductances

	Inductance / 10^{-5} H			
coil switched	1	2	3	4
field open circuit	9.9138	9.765	9.7311	9.7783
field current 2A	5.0226	4.8425	4.9308	4.8491

One can see that the single coil inductances decrease to approximately 50% of their value if the field winding is active.

This was confirmed by the same tests at the other rotor positions shown in Fig. 7.12 - 7.14.

The current oscillation in the rotor coils causes a voltage in the sense coils that is a decaying oscillation as well. At the instant the current starts flowing in one or more rotor coil the voltage in the sense coils jumps to a certain value instantaneously and starts decaying sinusoidally with the current. The following approach to evaluate this voltage signal is proposed:

The area enclosed by one half cycle of the voltage and the time axis represents the flux linkage in that coil during this period of time. Choosing the first completely originated half cycle and dividing the calculated area by the number of turns (10) of the sense coil gives the maximum interpolar flux Φ_{ym} captured by a sense coil (comprising rotor coil - and field leakage, see Fig. 7.1) in the duration of current flow. The idea is outlined in Fig. 7.27. This quantity will be used to compare the sense coil voltages of the different tests. This comparison can be found in table 7.4. For the two sense coils the average value of Φ_{ym} has been taken into account for each test.
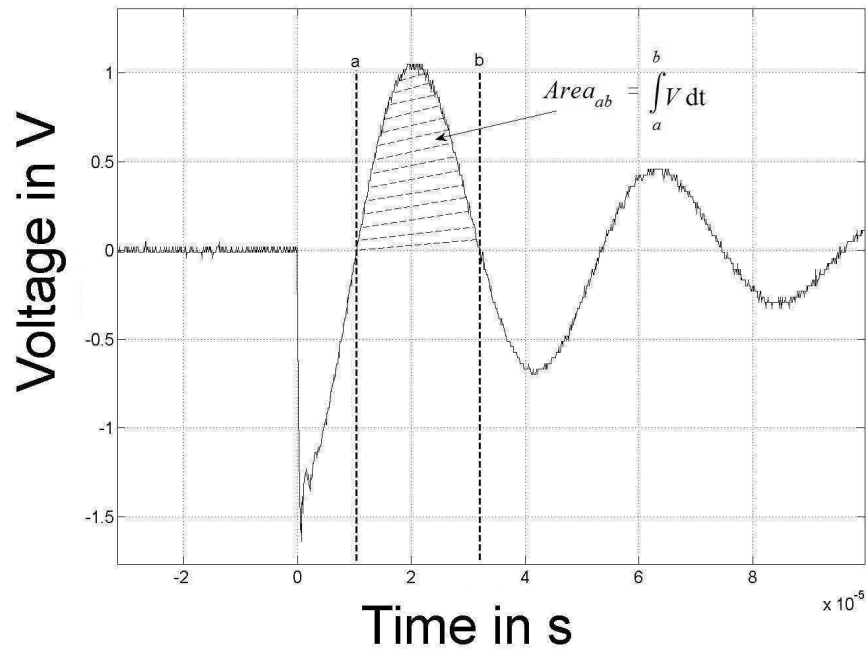
Fig. 7.27 Sense coil signal

Table 7.4 Sense coil fluxes

	Φ_{ym} / 10^{-7} **Wb**			
coil switched	1	2	3	4
field open circuit	2.41	2.6	2.17	2.77
field current 2A	4.98	5.34	4.21	5.27

Table 7.4 confirms the conclusions drawn above. The flux Φ_{ym} increases to approximately twice the amount if the field winding is active. This is an indicator that the flux produced by the rotor coils as well as a part of the flux produced by the field winding is forced to leakage paths.

7.4.11 *di/dt* tests

In the *di/dt* - tests coils are switched at $t = 0$. Subsequently, at $t = \Delta t$ other coils are switched and their influence on the *di/dt* of the coils switched at $t = 0$ is examined. This is done to see if there is a significant braking or accelerating effect which is an important insight regarding current reversal.

▪ coil1 switched at $t = 0$ and coil3 switched at $t = 5\mu s$ / no source connected to field circuit

In this test the pair of coil1 and coil3 is switched only with time delay of 5μs between coil1 and coil3. This simulates the case of one coil undergoing commutation and then a second coil starts commutating as the rotor moves forward and the brush makes contact with one more commutator segment. A reversing effect can be observed in Fig. 7.28. The rise of current per second has been estimated using linear fits before and after the switching instant of coil3. At the instant coil3 is switched and starts carrying a current with a $di/dt = 8.0583 \cdot 10^5$ A/s the di/dt of coil1 changes from $2.8730 \cdot 10^5$ A/s to $-5.5051 \cdot 10^5$ A/s. This is roughly the difference of the di/dt of coil1 before coil3 is switched and the di/dt of coil3. The significantly higher di/dt of coil3 at the switching instant $t = 5\mu s$ compared to the di/dt of coil1 at the switching instant $t = 0$ is due to the fact, that the sudden current reversal in coil1 at $t = 5\mu s$ leads to a pair of opposing coils which reduces the inductance significantly and therefore allows a much steeper current rise in coil3. In real commutating conditions a strong effect on each other of coils located in the same slots can be expected.
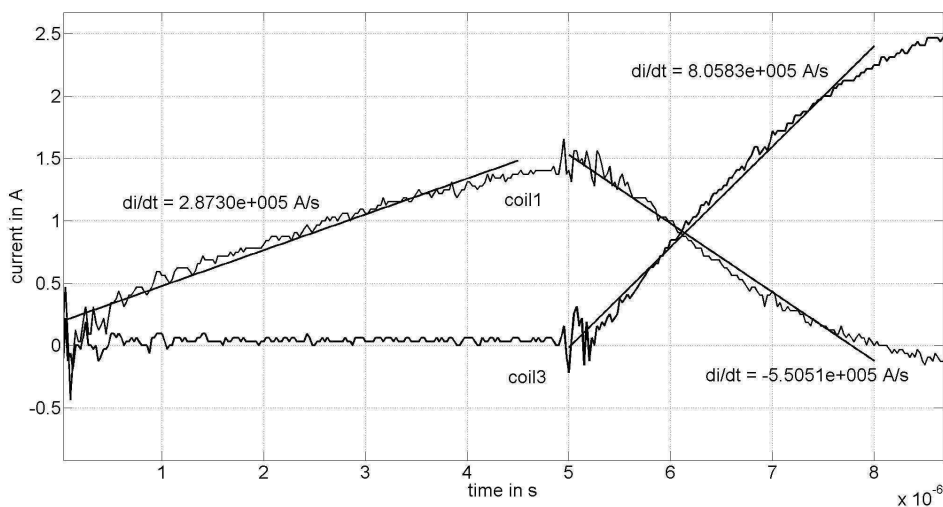
Fig. 7.28 Coil1 and coil3, braking effect

▪ coil1 switched at $t = 0$ and coil2 switched at $t = 5\mu s$ / no source connected to field circuit

This test simulates an asymmetry where both brushes do not switch at the same time. That causes a time delay between the starts of commutation of coil1 and coil2. The time delay is assumed to be large enough so the di/dt in coil1 has changed sign (as if strongly over-

commutating). The influence of the rapid current rise in coil2 on the *di/dt* of coil1 can be observed in Fig. 7.29. It can bee seen that the *di/dt* of the current in coil1 increases by factor 1.477 after coil2 is switched, *i.e.* the coil2 accelerates coil1. This is due to the strong coupling in the d - axis of those two coils. If coil2 is switched its flux induces a voltage in coil1 trying to cancel the effect of coil2. As coil1 carries current producing an opposing field already, the voltage drop induced is in the same direction as the voltage applied. Hence, the coil current is accelerated.
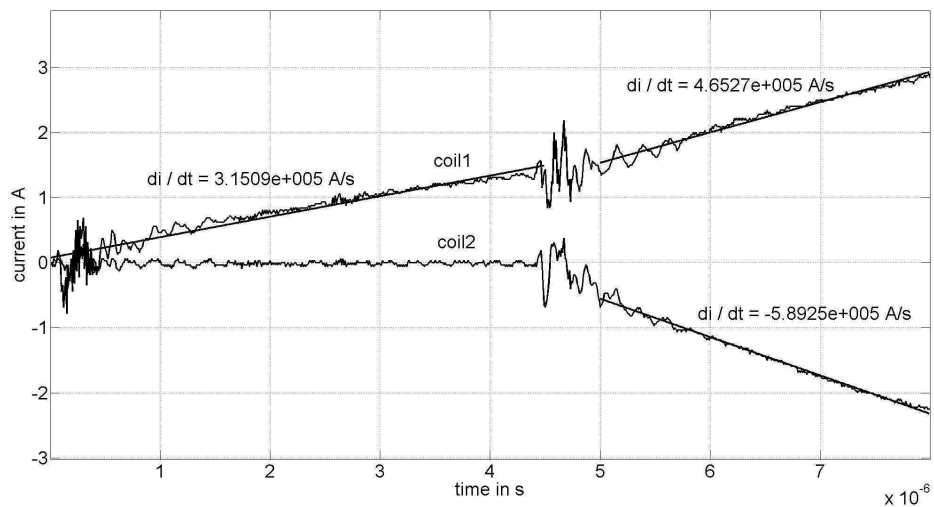
Fig. 7.29 Coil1 and coil2, accelerating effect

■ coil1 switched at *t* = 0 and coil2 switched at *t* = 5μs / 4.2V and 2A DC in the field winding

In this test the influence of the field winding on the accelerating effect observed in the previous test is investigated. In Fig. 7.30 it can be seen that the accelerating effect has vanished. One could even draw the conclusion that coil2 now has a braking effect on coil1 as the *di/dt* of coil1 is significantly lower than before coil2 is switched. Yet on second thought, the *di/dt* of coil2 is very close to value of coil1 before coil2 is switched and therefore it has roughly the same effective inductance as coil1 at *t* < 5μs. This means the coils are not able to build up significant mutual flux as this is impeded by damping of the field winding. The lower *di/dt* of coil1 after the switching of coil2 arises from the sinusoidal shape of the coil currents as the oscillating circuit in Fig. 7.18 is used. (See zoomed out view in Fig. 7.31.)
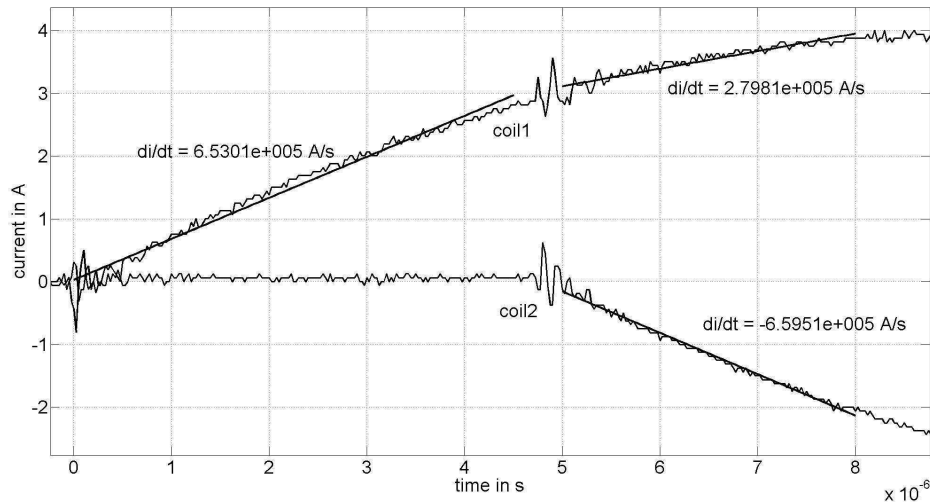
Fig. 7.30 Coil1 and coil2, field winding active
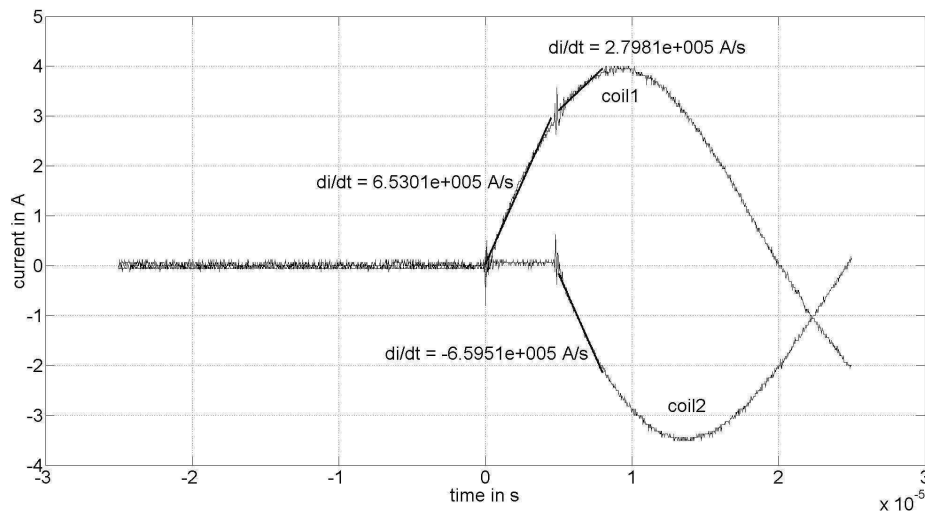
Fig. 7.31 Zoomed out view of Fig. 7.30

■ coil1 and coil2 switched at *t* = 0 and coil3 and coil4 switched at *t* = 5 μs / no source connected to field circuit

This test simulates the transition of the scenarios coil1 and coil2 are undergoing commutation only and coils 1,2,3 and 4 are undergoing commutation. The coil currents are depicted in Fig. 7.32. It can be seen that at the instant where coil3 and coil4 are switched the coils carrying current already show a reversal of current direction. This is due to the tight coupling of the coils. The pair coil1 and coil3 is located in the same slots as well as the pair coil2 and coil4. The sudden current rise in coils coil3 and coil4 induces voltages in coil1 and coil2 that oppose

140

the applied voltages. As the current rise in coil3 and coil4 is very steep and, as stated earlier, the coupling is very tight the induced voltage exceeds the applied voltage and causes the current to reverse.
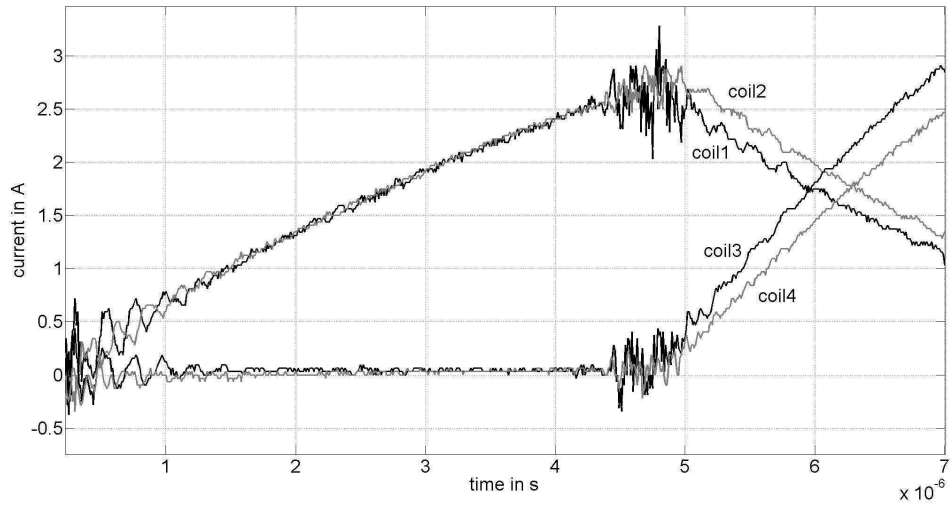
Fig. 7.32 Four coils switched

■ coil3 switched at t = 0 and coil5 switched at $t = 5\mu s$ / no source connected to field circuit

Similar as in the test where coil1 switched at $t = 0$ and coil3 switched at $t = 5\mu s$ a pair of coils connected to adjacent commutator bars was switched with a 5μs time delay. In Fig. 7.28 it can be seen that at the switching instant of the second coil the current of the first coil is reversed. Those two coils are located in the same slots and therefore the coupling is very tight. As coil3 and coil5 are not located in the same slots the effect is much weaker. The coil currents are depicted in Fig. 7.33.
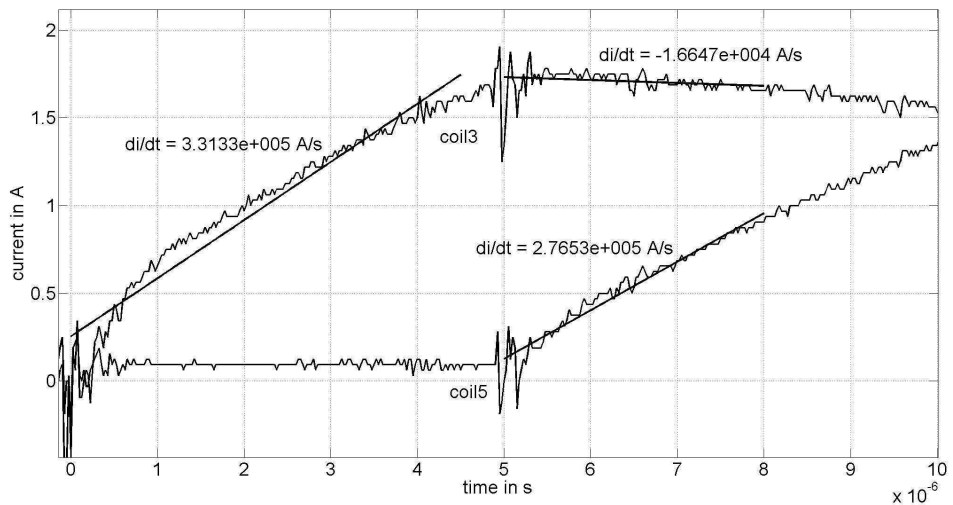
Fig. 7.33 Coil3 and coil5, braking effect

■ coil3 switched at $t = 0$ and coil5 switched at $t = 5\mu s$ / 4.2V and 2A DC in the field winding

The coil currents are shown in Fig. 7.34. The rate of change of current with time of coil3 after coil5 has been switched is now positive. The change of the value of the *di/dt* is due to the sinusoidal shape similar as described above.

Also, a significant increase in initial rate of change of current can be noticed compared to the case where the field winding is left open circuit.
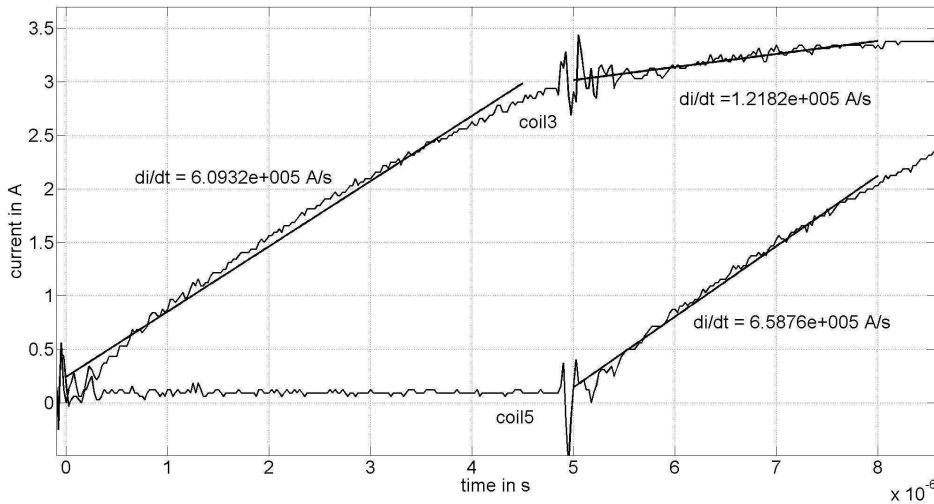
Fig. 7.34 Coil3 and coil5, active field winding

■ coil3 switched at $t = 0$, coil2 switched at $t = 5\mu s$ and coil4 switched at $t = 9\mu s$ / no source connected to field circuit

In this final test a case is simulated where again, due to an asymmetry both brushes do not switch at the same time and the *di/dt* in coil3 has changed sign before the instant coil2 starts carrying current. The coil currents can be seen in Fig. 7.35. A slight accelerating on the current in coil3 can be seen after this point. Subsequently, coil4 is switched after $t = 9\mu s$. A reversing effect of coil4 on coil2 can be noticed which is due to the tight coupling of these two coils (located in the same pair of slots) whereas coil3 does not show a further acceleration as the effect of coil4 in the d - axis is cancelled out by the reversal of the direction of the current in coil2.
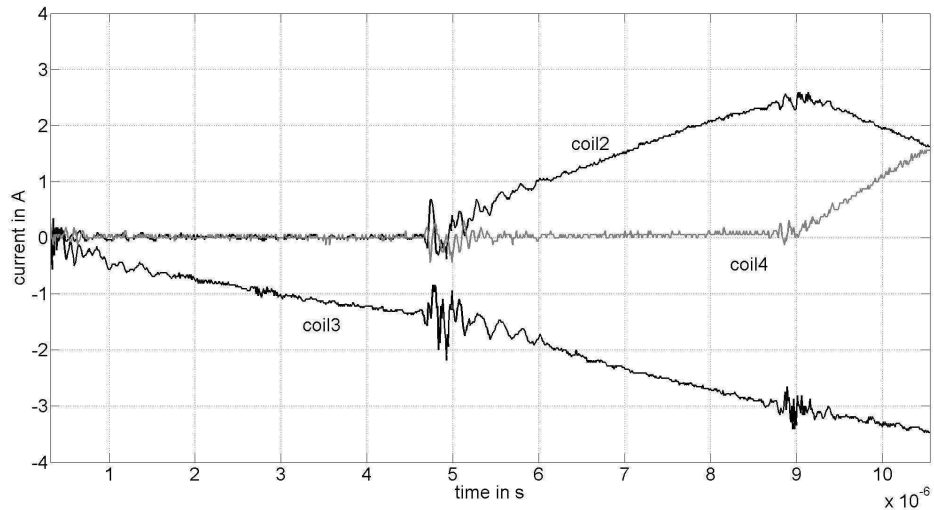
Fig. 7.35 Three coils switched at different times

7.5 Rotational Tests

7.5.1 Test purpose and setup

To investigate the influence on the capability of driving damping currents of the source and cable impedance (the load seen by the harmonic generator) is investigated here. It is assumed that the damping capabilities varies with different field circuits. Therefore different configurations must show different amplitudes in the Fast Fourier Transform (FFT) spectrums of current and voltage at certain frequencies. In [56] motor current and field voltage have already been proposed as useful quantities for universal motor diagnosis and the coupling of the commutating coils with the field winding is described. The simplified equivalent circuit of the universal motor at operating (supply) frequency supplied by a power source and a power cord is shown in Fig. 7.36. Z_p is the source impedance, Z_c is the cord impedance, R_{fa} is the series copper resistance of armature and field winding and L_{fa} is the series inductance of field and armature. Now, regarding the machine as a harmonic generator the equivalent circuit becomes the one shown in Fig. 7.37. To analyse the influence on the damping of Z_p and Z_c several rotational tests have been carried out with different field circuit configurations.

The test bench described in chapter 6 is used for the tests where two universal machines were mounted on a base plate, machine 1 acting as a motor and machine 2 acting as a generator (see Fig. 7.38). Both machines have 12 rotor slots and 24 commutator bars and the same lamination geometry.
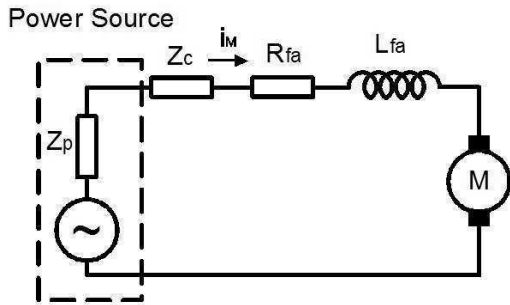
Fig. 7.36 Simplified equivalent circuit for motoring
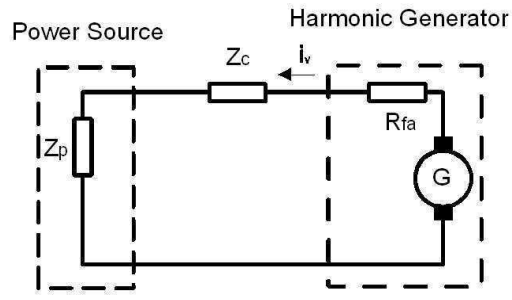
Fig. 7.37 Simplified equivalent circuit if machine is regarded as harmonic generator
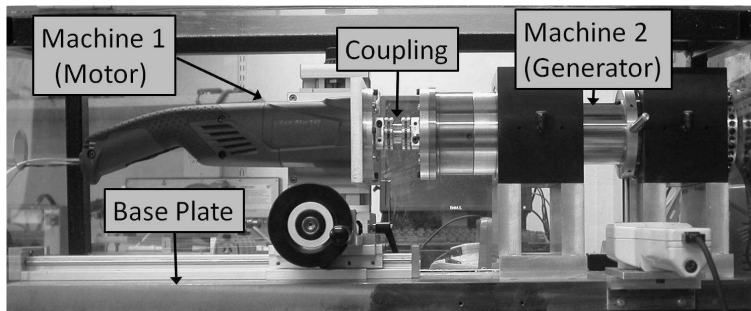
Fig. 7.38 Test setup

7.5.2 Generator tests

The investigation of the field damping on a motoring universal machine is problematic as due to the series connection of the armature and field circuits currents induced in the armature also flow through the field circuit and cause voltage drops there that bias the information in the FFT spectrum with regard to the field damping. Therefore the following test procedure was applied.

Machine 1 drives machine 2 (sitting in an Aluminum tube) at different speeds n = {4000rpm, 8000rpm, 12000rpm}. In machine 2 a DC current of 1 A flows through the armature circuit at all speeds. The armature of machine 2 is supplied by a power source that has an output isolated from the grid. Moreover the impedance of that power source is negligible. Thus, the power source represents a short circuit for harmonic components. The field winding of machine 2 is kept separate from the armature circuit, and the FFT spectrum of the field voltage of the generator is examined for different field circuits. For the different rotor speeds the rotating frequency f_d, the slotting frequency $f_n = 12f_d$ and the commutator frequency $f_c = 24f_d = 2f_n$ are listed in table 7.5.

Table 7.5 Speed dependent frequencies

n [rpm]	f_d [Hz]	f_n [Hz]	f_c [Hz]
4000	200 / 3	800	1600
8000	400 / 3	1600	3200
12000	200	2400	4800

■ Field winding left open circuit

This test serves as a reference where no field damping takes place. In Fig. 7.39 the measured voltage across the field winding and its FFT transform in a frequency range of [0; 10kHz] at a speed of $n = 4000$ rpm can be seen. Similar as in [57], where also the field voltage at open circuit of a machine driven by another one was examined, the component at commutation frequency is predominant. This component represents the repercussions of the commutation for the field winding. Moreover in the graph additional integral multiples of f_c can be observed. This is due to different magnitudes of the peaks in the field voltage as commutation takes place in a sequence of 2 coils commutating - 4 coils commutating simultaneously in this machine where flux variations due to a particularly high rate of change of current in the commutating coils appear at the beginning and the end of commutation. Also, due to manufacturing processes the inductances and resistances of the rotor coils vary and the brushes do not always switch simultaneously. The latter will become more problematic with increasing speed due to the dynamics of the sliding contact (brush vibrations, brush bounce). The damping taking place here is due to coupling between the commutating coils, coupling between commutating coils and non-shorted armature coils, and eddy currents only. For a field circuit that allows damping currents to flow one can expect the voltage components at $m \cdot f_c$ to decrease. ($m \in \mathbb{N}$)

In Fig. 7.40 the armature current as well as its FFT spectrum at the same rotor speed is shown. (DC - component removed from FFT spectrum). In the armature current the component at f_c is not the predominant one. One can observe that there are various significant components at integral multiples of f_d. The component at f_n is due to the slotting of the rotor; the resulting flux variations during motor rotation cause a current ripple at slotting frequency [57], [58]. Moreover, for sequentially manufactured machines of universal motor type multiples of the rotating frequency are common, even in a non-faulty machine, and are caused by mechanical

asymmetries such as slightly elliptic rotors, dynamic eccentricity of the rotor due to sub-optimal bearings, varying inductance and resistance with rotor position [57]. The motor current as a quantity suitable for diagnosis of asymmetries, manufacturing faults or bearing faults is often emphasised [56], [58], [59].

Integral multiples of f_c higher than one do not occur in the FFT spectrum of the armature current due to the weaker coupling of armature winding and commutating coils. Hence, in this study only the field voltage components at commutation frequency are of interest with focus on the field damping of flux variations caused by current reversal. The problems arising with the use of the FFT are that due to limited observation time leakage effects cannot be avoided completely. Therefore spectral components of the observed frequency no longer contain all the energy. Parts of the energy are located at adjacent frequencies. Yet these problems seem to be negligible regarding Fig. 7.39 and Fig. 7.40. One also has to be aware that the speed of the machine is not constant but varies slightly around the measured speed.

Aliasing, which occurs if the sampling frequency is smaller than twice the maximum frequency of the spectrum is avoided by use of a sufficiently high sampling frequency. As a quantity representing the damping capability of the field circuit

$$\gamma = 1 - \frac{\sum_{m=1}^{4} v_m}{\sum_{m=1}^{4} v_{m,open\ circuit}} \tag{178}$$

is introduced where the sum of the 4 most significant field voltage peaks at integral multiples of f_c are related to the corresponding sum in the case of the field winding left open circuit (non-damped case). The obtained values for the case of the field winding left open circuit can be found in table 7.6.
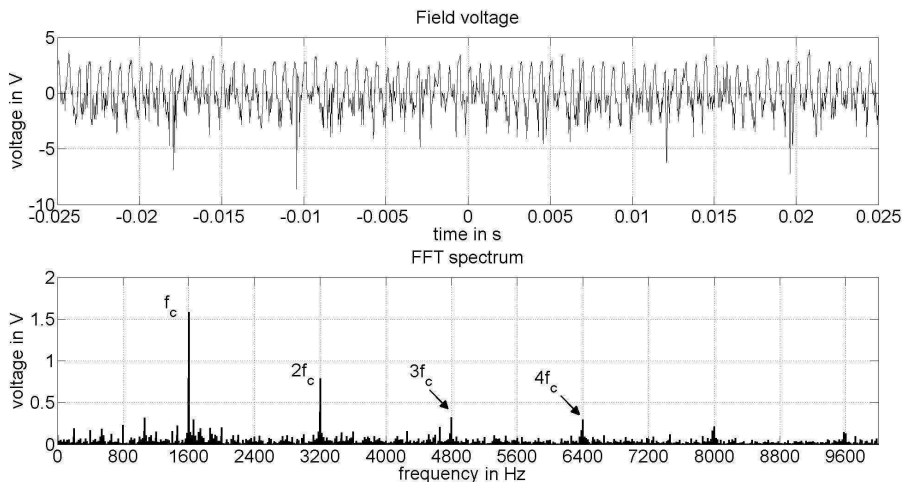
Fig. 7.39 Voltage induced in the field winding at 4000rpm
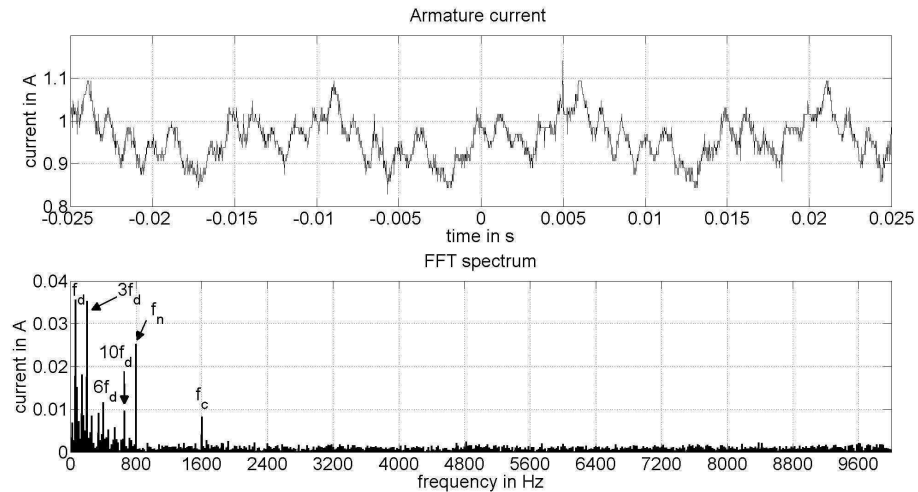
Fig. 7.40 Armature current at 4000rpm

■ Field winding short circuited

The terminals of the field winding were short circuited. This test represents the case of ideal damping with $Z_c = Z_p = 0$ with reference to Fig. 7.37. The results obtained can be found in table 7.7. Voltage components at $m \cdot f_c$ are no longer evident and the damping factor $\gamma \approx 1$ at all observed speeds.

■ Field winding connected to power cord

The terminals of the field winding were connected to a standard power cord for this machine (as a power tool motor) with a length of 4m. The other end of the power cord was short circuited. Typical cables contain lengthwise inductance L_c and resistance R_c as well as transverse capacitance C_c and leakage conductance G_c [60]. Due to the short circuit at the end of the cable only the lengthwise components will have an influence. This configuration simulates a machine acting as a harmonic generator where the impedances in the circuit in Fig. 7.37 are $Z_p = 0$ and $Z_c = R_c + j\omega L_c$ (values not given in datasheet). The results obtained can be found in table 7.8. The influence of the cable is not very significant which implies that the lengthwise components of the cable L_c and R_c are very small. This is in compliance with the fact that the cable is designed to supply the motor from a low voltage grid of 120V. Hence, it has to stand rated currents of up to 12 A and therefore is designed to have minimal losses.

147

■ Field winding connected to long power cord

In the next step the previous test was repeated with a 8m power cord of the same type. Again, one end was connected to the field winding, the other end was short circuited. The results are listed in table 7.9. As in the test with the standard power cord the cable parameters do not reduce the damping factor γ significantly.

■ Field winding connected to inductor

The terminals of the field winding were connected to the terminals of an inductor $L_p = 0.2$H with a resistance of $R_p = 6.5\Omega$. Whilst the plain short circuit of the field winding simulates a motor supplied by an ideal power source and an ideal power cord, the connection to a relatively large inductor can be regarded as a motor supplied by a transformer. Hence, the impedances loaded to the harmonic generator are $Z_c = 0$ and $Z_p = R_p + j\omega L_p$. The results obtained are listed in table 7.10. The damping is significantly lower compared to the conditions with the plain short circuit of the field winding or the field winding connected to a short circuited cable.

■ Field winding connected to power cord and inductor

The field winding was connected to the 4m power cord and other end of the power cord was connected to the inductor used in the previous test. Now, also the transverse capacitance C_c and leakage conductance G_c of the cable are active in the circuit. The impedances are $Z_c = \sqrt{[(R'_c + j\omega L'_c) / (G'_c + j\omega C'_c)]}$ where $'$ indicates quantities in relation to cable length, and $Z_p = R_p + j\omega L_p$. The results listed in table 7.11 show that the damping capability is slightly reduced compared to the previous case.

<table>
<tr><td colspan="3" align="center">Table 7.6 Field open circuit</td><td colspan="3" align="center">Table 7.7 Field short circuit</td></tr>
<tr><td>n [rpm]</td><td>$\sum_{m=1}^{4} v_m$ [V]</td><td>γ</td><td>n [rpm]</td><td>$\sum_{m=1}^{4} v_m$ [V]</td><td>γ</td></tr>
<tr><td>4000</td><td>2.9913</td><td>0</td><td>4000</td><td>0.0036</td><td>0.9988</td></tr>
<tr><td>8000</td><td>4.9107</td><td>0</td><td>8000</td><td>0.0037</td><td>0.9993</td></tr>
<tr><td>12000</td><td>6.7921</td><td>0</td><td>12000</td><td>0.0041</td><td>0.9994</td></tr>
</table>

Table 7.8 Standard power cord

n [rpm]	$\sum_{m=1}^{4} v_m$ [V]	γ
4000	0.0051	0.9983
8000	0.0051	0.9989
12000	0.0049	0.993

Table 7.9 Long power cord

n [rpm]	$\sum_{m=1}^{4} v_m$ [V]	γ
4000	0.0062	0.9979
8000	0.0061	0.9988
12000	0.006	0.9991

Table 7.10 Inductor

n [rpm]	$\sum_{m=1}^{4} v_m$ [V]	γ
4000	2.0857	0.3024
8000	3.5556	0.2758
12000	4.6902	0.3092

Table 7.11 Inductor and power cord

n [rpm]	$\sum_{m=1}^{4} v_m$ [V]	γ
4000	2.3576	0.2115
8000	3.9073	0.2042
12000	4.8576	0.2846

■ Summary of Results

The results of the preceding tests are summarised in Fig. 7.41.Whilst the tests with short circuited field winding, standard and longer power cord connected to the field winding provide almost ideal damping conditions at all observed speeds, the field damping is reduced in the tests with the inductor due to its relatively high inductance and copper resistance.
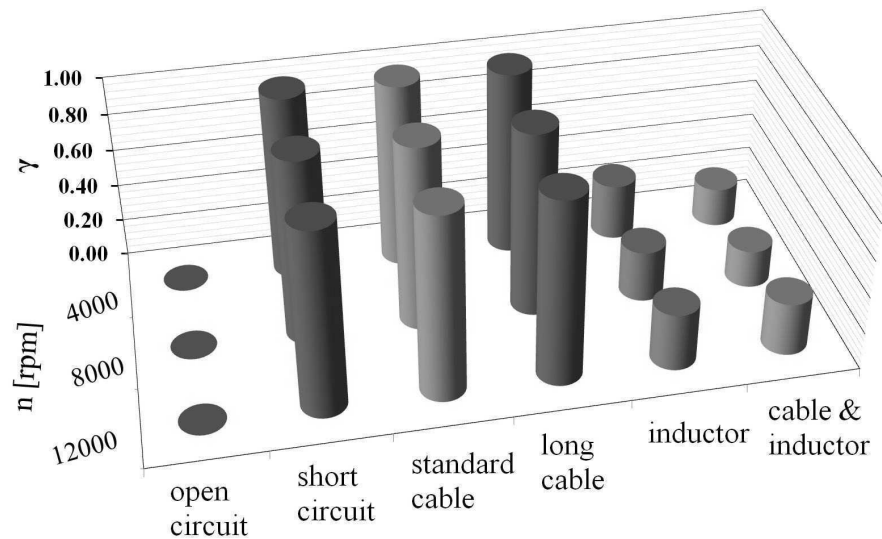
Fig. 7.41 Damping factor γ for all investigated cases

149

7.6   Conclusions

In this chapter several different approaches have been taken to investigate the interaction of the commutating coils and the influence of the damping current in the field winding on the coils undergoing rapid current changes.

In theoretical investigations it was found that a damping current in the field winding, calculated to provide ideal damping, forces all the flux of a single armature coil to leakage paths and therefore cancels out any mutual flux between the armature coil and the field winding.

Moreover, the interaction of certain armature coils was observed using FEA. The single coils interact differently depending whether they are short pitched, full pitched, aiding or opposing. The different flux patterns found from the FEA were confirmed using simple AC measurements where sense coils were used to get an insight about the flux distribution in the motor lamination at different excitations with and without a short circuited field winding.

In the next step an oscillating circuit was used to determine the coil inductances with and without the presence of an active field winding. Capacitors were discharged through certain rotor coils and the periodic time and the logarithmic decrement of the decaying current oscillation were used to determine the inductance. The inductances measured in the presence of an active field winding were significantly lower than the inductances measured with the field winding left open circuit. It has to be pointed out that due to additional wires used for the test setup and the high frequency of the oscillation the inductances measured are unlikely to be the same as under normal operating conditions of the machine. However, one obtains a detailed insight of the change of inductance under the influence of a damping, saturating field winding.

Furthermore, the same circuit was used to observe the effect of coils undergoing a high rate of change of current on each other. The effect (accelerating or braking) is significantly higher if the sides of the coils are located in the same pair of slots. Also the effect of the field winding on the intensity of the rotor coil interaction was found to be significant as the mutual and self inductances are decreased. The effect of eddy currents in the conductors which may cause a significant increase of the effective coil resistance is not discussed at this point.

Subsequently rotational tests were carried out where the machine was driven by another motor and armature and field circuit were kept separate. A DC current was fed through the armature circuit and the FFT spectrum of the field voltage was evaluated for different circuitries

connected to the field winding. The open circuit case served as a reference and was compared to the cases field winding short circuited, standard and long power cord connected to the field winding, inductor connected to the field winding, and a combination of inductor and standard power cord connected to the field winding. The field damping was almost ideal in the cases of plain short circuit of the field winding and standard and long cable connected to the field winding whereas the damping was reduced significantly in the test involving the inductor.

8 Simulation Model

8.1 Deductions from previous Chapters

With regard to the investigations carried out in the previous chapters the following deductions for a simulation model of the commutation are made:

- The use of inductances calculated using FEA is justified as found from comparisons with measurements and analytical calculations. Moreover, the end-winding leakage can be neglected as it only accounts for a very small percentage of the full inductance.

- The brush resistance is a significant element of the commutating circuits and therefore needs to be considered in the simulation.

- The commutation arc can be modelled by a constant voltage where a mean value for anodic and cathodic brushes of 14V gives reasonably precise results.

- The motor line current should not be kept constant during a commutation event in a full simulation model as damping currents in the field winding need to be considered that change the di/dt in the commutating coils significantly. Therefore, the simulation model needs to be voltage-driven.

8.2 Equivalent Circuits of the Machine and their mathematical Analysis

8.2.1 Two commutator bars in contact with one brush

The brush model described in chapter 4 is used the mathematical analysis of the machine. It is limited to the cases of one armature coil short circuited by one brush and two coils short circuited by one brush, and an arcing phase.

Applying the reference system described in chapter 4 and maintaining the coil numbering used in chapter 7, the first case to be discussed is the case of two commutator bars in contact with one brush (see Fig. 8.1).
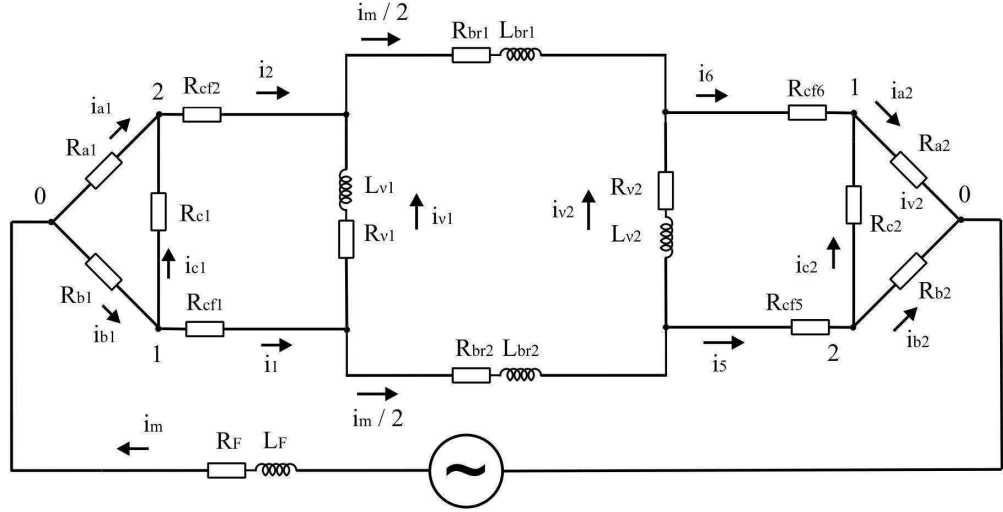
Fig. 8.1 Equivalent circuit of the machine if a brush makes contact with two commutator bars

For the supply voltage v_s one obtains from the circuit ($d\psi_k/dt$ represents the total voltage induced in an inductor L_k)

$$
\begin{aligned}
v_s &= R_F i_m + \frac{d\psi_F}{dt} + R_{a1} i_{a1} + R_{cf2} i_2 + R_{br1} \frac{i_m}{2} + \frac{d\psi_{br1}}{dt} + R_{cf6} i_6 + R_{a2} i_{a2} \\
&= R_F i_m + \frac{d\psi_F}{dt} + R_{b1} i_{b1} + R_{cf1} i_1 + R_{br2} \frac{i_m}{2} + \frac{d\psi_{br2}}{dt} + R_{cf5} i_5 + R_{b2} i_{b2}
\end{aligned}
\tag{179}
$$

which yields

$$
R_{a1} i_{a1} + R_{cf2} i_2 + R_{cf6} i_6 + R_{a2} i_{a2} = R_{b1} i_{b1} + R_{cf1} i_1 + R_{cf5} i_5 + R_{b2} i_{b2}
\tag{180}
$$

where equal armature branch voltages, *i.e.* $R_{br1} i_m / 2 + d\psi_{br1} / dt = R_{br2} i_m / 2 + d\psi_{br2} / dt$ are assumed.

Now, assuming symmetry at both brushes, i.e $R_{a1} = R_{b2} = R_{ab}$, $R_{b1} = R_{a2} = R_{ba}$, $R_{cf1} = R_{cf6} = R_{16}$ and $R_{cf2} = R_{cf5} = R_{25}$, one obtains

$$
0 = R_{ab}(i_{a1} - i_{b2}) + R_{25}(i_2 - i_5) + R_{16}(i_6 - i_1) + R_{ba}(i_{a2} - i_{b1}),
\tag{181}
$$

which always holds if $i_{a1} = i_{b2}$, $i_2 = i_5$, $i_6 = i_1$ and $i_{a2} = i_{b1}$.

For the voltage v_p in the main circuit of the motor one can write

$$v_p = R_{FA}i_m + \frac{d\psi_p}{dt} = v_s - (R_{a1}i_{a1} + R_{cf2}i_2 + R_{cf1}i_1 + R_{b1}i_{b1}) \qquad (182)$$

where R_{FA} is the combined ohmic resistance of the field and armature windings.

For the coil commutating under the left brush with regard to Fig. 8.1 one obtains

$$v_{v1} = R_{v1}i_{v1} + \frac{d\psi_{v1}}{dt} = R_{cf2}i_2 - R_{cf1}i_1 + R_{c1}i_{c1} \qquad (183)$$

and since symmetry at both brushes is assumed one obtains for the coil commutating under the right brush with regard to Fig. 8.1

$$v_{v2} = v_{v1}. \qquad (184)$$

Now, resolving the time derivative of the flux linkage in a coil into the voltage components due to the self inductance L and the mutual inductances M between the coil and all other coils it is magnetically coupled with yields

$$\frac{d\psi}{dt} = \frac{d(Li)}{dt} + \sum_k \frac{d(M_k i_k)}{dt}. \qquad (185)$$

Rewriting the term due to the self inductance with respect to $L = f(i(t), \theta(t))$ where $\theta(t)$ is the rotor position, and $\omega = d\theta / dt$ one obtains

$$\frac{d(Li)}{dt} = \left[\frac{\partial L}{\partial \theta}\omega + \frac{\partial L}{\partial i}\frac{di}{dt} \right] i + L\frac{di}{dt} = \left[L + \frac{\partial L}{\partial i}i \right]\frac{di}{dt} + \frac{\partial L}{\partial \theta}i\omega \qquad (186)$$

and rewriting the term due to a self inductance in the same manner yields

$$\frac{d(Mi)}{dt} = \left[\frac{\partial M}{\partial \theta}\omega + \frac{\partial M}{\partial i}\frac{di}{dt} \right] i + M\frac{di}{dt} = \left[M + \frac{\partial M}{\partial i}i \right]\frac{di}{dt} + \frac{\partial M}{\partial \theta}i\omega \qquad (187)$$

and for the main motor winding one obtains

$$v_p = R_{FA}i_m + \left[L_{FA} + \frac{\partial L_{FA}}{\partial i_m}i_m\right]\frac{di_m}{dt} + \left[\frac{\partial L_{FA}}{\partial \theta}i_m + \sum_k \frac{\partial M_{pk}}{\partial \theta}i_k\right]\omega$$
$$+ \sum_k \left[M_{pk} + \frac{\partial M_{pk}}{\partial i_k}i_k\right]\frac{di_k}{dt} \tag{188}$$

where L_{FA} is the combined armature and field inductance. In the simulation this is calculated using FEA when armature and field winding are excited and therefore contains the mutual effects between armature winding and field winding. M_{pk} represents a mutual inductance between the main machine winding and a commutating coil.

As found in the previous chapter, the current in a single rotor coil does not change the saturation level of the machine considerably and therefore $\partial M_{pk} / \partial i_k \approx 0$. Moreover, if one takes into account that the main electromagnetic torque produced T_{em} is associated with the rate of change of the mutual inductance of the field and armature windings with rotor position, one obtains

$$T_{em} = i_m^2 \frac{\partial M_{FA}}{\partial \theta} \tag{189}$$

which yields

$$\omega \frac{T_{em}}{i_m} = \omega i_m \frac{\partial M_{FA}}{\partial \theta}. \tag{190}$$

Hence, the rotational voltage of the main winding $u_{p\omega}$ can be found as follows

$$u_{p\omega} = \omega \frac{T_{em}}{i_m} \tag{191}$$

where the torque, which depends on the current and rotor position, used in the simulation is found from lookup tables precalculated using FEA (mean value of Maxwell Stress Tensor and Virtual Work Method [55]).

Hence, one can rewrite (188) as follows

$$v_p = R_{FA}i_m + \left[L_{FA} + \frac{\partial L_{FA}}{\partial i_m}i_m\right]\frac{di_m}{dt} + u_{p\omega} + \sum_k M_{pk}\frac{di_k}{dt}. \tag{192}$$

Now, for the voltages in the two coils commutating simultaneously where $\partial L_{v1,2} / \partial i_{v1,2} \approx 0$ and $\partial M_{v1,2} / \partial i_{v1,2} \approx 0$, (183) can be rewritten as

$$v_{v1} = R_{v1}i_{v1} + L_{v1}\frac{di_{v1}}{dt} + M_{v1v2}\frac{di_{v2}}{dt} + \left[M_{v1p} + \frac{\partial M_{v1p}}{\partial i_m}i_m \right]\frac{di_m}{dt} + u_{v1\omega} \qquad (193)$$

and (184) still holds.

These representations of the voltage equations of the machine coils allow the use of inductance and torque matrices precalculated using FEA for a set of 30 rotor positions covering one slot pitch (1° - steps) and a set of 20 motor currents (1A - steps). The data is then interpolated using cubic splines [63]. The rotational voltage $u_{v1\omega}$ in a commutating coil is primarily caused by the rotation of the coil in the field produced by the main motor winding, hence

$$u_{v1\omega} = \omega i_m \frac{\partial M_{v1p}}{\partial \theta} \qquad (194)$$

and for the three windings the governing system of equations is

$$\frac{d\vec{i}}{dt} = [\mathrm{L}]^{-1}(\vec{v} - \vec{u}_r - \vec{u}_\omega) \qquad (195)$$

where

$$\vec{v} = \begin{bmatrix} v_p \\ v_{v1} \\ v_{v2} \end{bmatrix} \qquad (196)$$

$$\vec{u}_r = \begin{bmatrix} R_{FA}i_m \\ R_{v1}i_{v1} \\ R_{v2}i_{v2} \end{bmatrix} \qquad (197)$$

$$\vec{u}_\omega = \begin{bmatrix} u_{p\omega} \\ u_{v1\omega} \\ u_{v2\omega} \end{bmatrix} \qquad (198)$$

and

$$[L] \; = \; \begin{bmatrix} L_{FA} \; + \; \dfrac{\partial L_{FA}}{\partial i_m} i_m & M_{v1p} & M_{v2p} \\[2em] M_{v1p} \; + \; \dfrac{\partial M_{v1p}}{\partial i_m} i_m & L_{v1} & M_{v1v2} \\[2em] M_{v2p} \; + \; \dfrac{\partial M_{v2p}}{\partial i_m} i_m & M_{v1v2} & L_{v2} \end{bmatrix} \qquad (199)$$

where the self - and mutual inductances are found for a certain rotor position and certain values of instantaneous currents in all motor coils. Moreover, reciprocity of the mutual inductances is assumed [61].

The vector of time derivatives of the currents is

$$\frac{d\vec{i}}{dt} \; = \; \frac{d}{dt} \begin{bmatrix} i_m \\ i_{v1} \\ i_{v2} \end{bmatrix} \qquad (200)$$

and for given initial values for i_m, i_{v1} and i_{v2} one can calculate

$$i_1 \; = \; \frac{i_m}{2} \; + \; i_{v1} \qquad (201)$$

and

$$i_2 \; = \; \frac{i_m}{2} \; - \; i_{v1}. \qquad (202)$$

Subsequently, the brush resistances are found from precalculated tables according to the rotor position and the conductance matrix

$$[G] \; = \; \begin{bmatrix} \dfrac{1}{R_{b1}} + \dfrac{1}{R_{c1}} & - \dfrac{1}{R_{c1}} \\[2em] - \dfrac{1}{R_{c1}} & \dfrac{1}{R_{a1}} + \dfrac{1}{R_{c1}} \end{bmatrix} \qquad (203)$$

can be calculated.

Now, with

$$
\begin{bmatrix} v_{B1} \\ v_{B2} \end{bmatrix} = [G]^{-1} \begin{bmatrix} -i_1 \\ -i_2 \end{bmatrix}
\tag{204}
$$

the resistive voltage drop

$$
v_{rd} = R_{cf1}i_1 + R_{cf2}i_2 - v_{B1} - v_{B2},
\tag{205}
$$

can be calculated. Moreover,

$$
v_p = v_s - v_{rd}
\tag{206}
$$

$$
v_{v1} = R_{cf2}i_2 - R_{cf1}i_1 + v_{B1} - v_{B2}
\tag{207}
$$

and

$$
v_{v2} = v_{v1}.
\tag{208}
$$

Subsequently, the numerical integration step is done using Euler's method as follows

$$
{}^{n+1}\vec{i} = {}^{n}\vec{i} + {}^{n}\frac{\overrightarrow{di}}{dt}\Delta t.
\tag{209}
$$

Now, after a certain number of time steps depending on the step size the transition from the cases of two commutator bars in contact with the brush to three commutator bars in contact with the brush needs to be made and the governing circuit is the circuit shown in Fig.8.2.
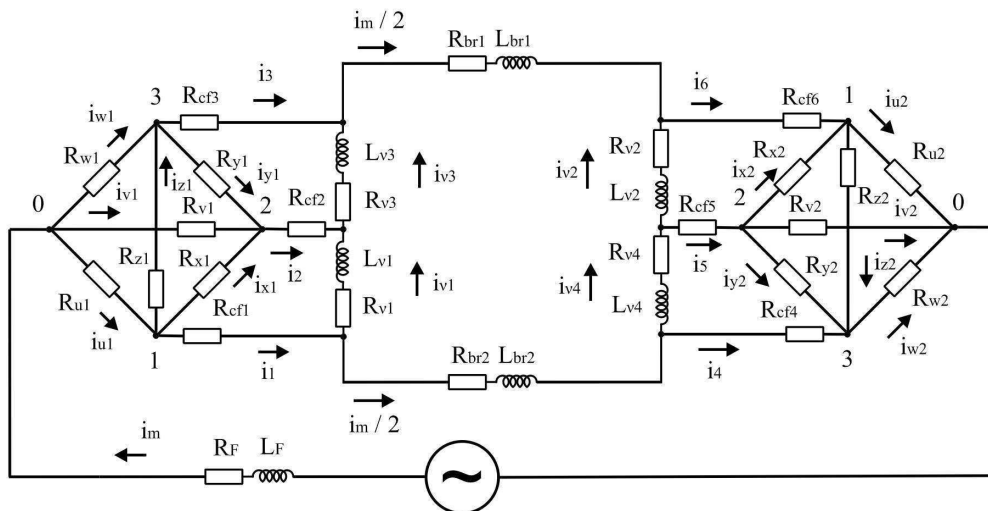
Fig. 8.2 Equivalent circuit of the machine if a brush makes contact with three commutator bars

8.2.2 Three commutator bars in contact with one brush

As in the previous case, symmetry at the brushes and the armature branches is assumed but now, five windings carrying different currents have to be considered. Hence,

$$\vec{v} = \begin{bmatrix} v_p \\ v_{v1} \\ v_{v2} \\ v_{v3} \\ v_{v4} \end{bmatrix} \tag{210}$$

$$\vec{u}_r = \begin{bmatrix} R_{FA} i_m \\ R_{v1} i_{v1} \\ R_{v2} i_{v2} \\ R_{v3} i_{v3} \\ R_{v4} i_{v4} \end{bmatrix} \tag{211}$$

$$\vec{u}_\omega = \begin{bmatrix} u_{p\omega} \\ u_{v1\omega} \\ u_{v2\omega} \\ u_{v3\omega} \\ u_{v4\omega} \end{bmatrix} \tag{212}$$

and

$$[L] = \begin{bmatrix} L_{FA} + \dfrac{\partial L_{FA}}{\partial i_m} i_m & M_{v1p} & M_{v2p} & M_{v3p} & M_{v4p} \\[2ex] M_{v1p} + \dfrac{\partial M_{v1p}}{\partial i_m} i_m & L_{v1} & M_{v1v2} & M_{v1v3} & M_{v1v4} \\[2ex] M_{v2p} + \dfrac{\partial M_{v2p}}{\partial i_m} i_m & M_{v1v2} & L_{v2} & M_{v2v3} & M_{v2v4} \\[2ex] M_{v3p} + \dfrac{\partial M_{v3p}}{\partial i_m} i_m & M_{v1v3} & M_{v2v3} & L_{v3} & M_{v3v4} \\[2ex] M_{v4p} + \dfrac{\partial M_{v4p}}{\partial i_m} i_m & M_{v1v4} & M_{v2v4} & M_{v3v4} & L_{v4} \end{bmatrix}. \tag{213}$$

Moreover,

$$i_1 = \frac{i_m}{2} + i_{v1} \tag{214}$$

$$i_2 = i_{v3} - i_{v1} \tag{215}$$

$$i_3 = \frac{i_m}{2} - i_{v3} \tag{216}$$

and

$$\begin{bmatrix} v_{B1} \\ v_{B2} \\ v_{B3} \end{bmatrix} = [G]^{-1} \begin{bmatrix} i_m \\ -i_1 \\ -i_3 \end{bmatrix}. \tag{217}$$

where [G] is found from (103). The resistive voltage drop v_{rd} is now found as follows

$$v_{rd} = R_{cf1}i_1 + R_{cf3}i_3 + 2v_{B1} - v_{B2} - v_{B3}. \tag{218}$$

Now, the voltage drops in the windings are

$$v_p = v_s - v_{rd} \tag{219}$$

$$v_{v1} = R_{cf2}i_2 - R_{cf1}i_1 + v_{B2} = v_{v2} \tag{220}$$

$$v_{v3} = R_{cf3}i_3 - R_{cf2}i_2 - v_{B3} = v_{v4} \tag{221}$$

and the numerical integration is done using Euler's method where

$$\frac{d\vec{i}}{dt} = \frac{d}{dt} \begin{bmatrix} i_m \\ i_{v1} \\ i_{v2} \\ i_{v3} \\ i_{v4} \end{bmatrix}. \tag{222}$$

8.2.3 Arcing phase

If, after the trailing edge of the brush separates from the commutator segment and therefore interrupts the commutating circuit involving this segment, the difference of the coil current and the armature branch current is greater than a certain I_{min}, (see chapter 5) the ignition of an arc between the trailing brush edge and the commutator segment is assumed and the governing circuit is the one shown in Fig. 8.3.
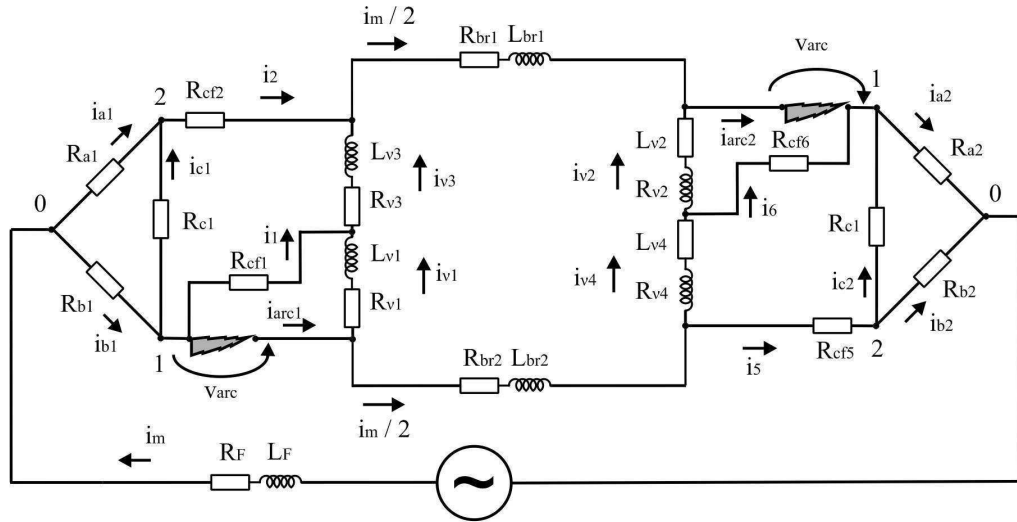
Fig. 8.3 Equivalent circuit of the machine if the arc has ignited

Again, symmetry is assumed in the circuit analysis and for the currents emerging from the brush one obtains

$$i_1 = i_{v3} - i_{v1} \tag{223}$$

$$i_2 = \frac{i_m}{2} - i_{v3} \tag{224}$$

$$i_{arc} = \frac{i_m}{2} + i_{v1} \tag{225}$$

and

$$\begin{bmatrix} v_{B1} \\ v_{B2} \end{bmatrix} = [G]^{-1} \begin{bmatrix} -(i_1 + i_{arc}) \\ -i_2 \end{bmatrix} \tag{226}$$

where [G] is found using (203), and the resistive voltage drops becomes

$$v_{rd} = v_{arc} + R_{cf2}i_2 - v_{B1} - v_{B2}. \tag{227}$$

Hence,

$$v_p = v_s - v_{rd} \tag{228}$$

$$v_{v1} = R_{cf1}i_1 - v_{arc} = v_{v2} \tag{229}$$

$$v_{v3} = R_{cf2}i_2 - R_{cf1}i_1 + v_{B1} - v_{B2} = v_{v4} \tag{230}$$

and the system (195) is again solved using (209).

An overview of the progression of the simulation can be seen in appendix A6.

8.3   Simulation Results, Comparison to Test Data and Discussion

Simulations were carried out for the operational points measured as described in chapter 6. As an example the simulated currents in the case of $n = 4000$ rpm are shown in Fig. 8.4. The simulation data used is listed in table 8.1. Measured resistances of the 120V machine were used.
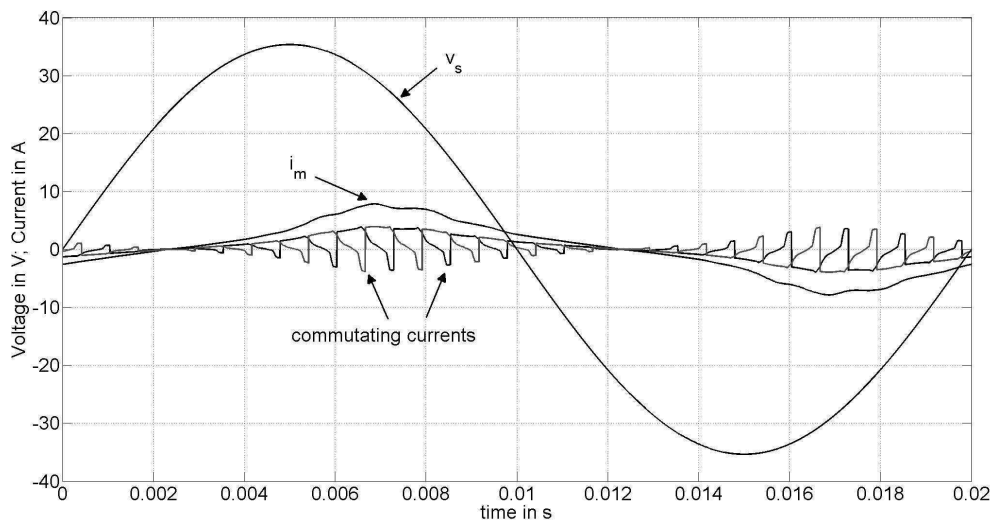
Fig. 8.4 Simulated currents and imposed supply voltage

Table 8.1 Data used in Simulation

```
%Resistances                    %Supply data
Rnu(1…4) = 0.11Ohm;             Vmax = sqrt(2)*25V;
RFA = 1.74Ohm;                  frq = 50Hz;
                                ts = 1E5s;
%Arc parameters                 Tp = 1/frq;
v_arc = 14V;                    t = linspace(0,Tp,ts);
Iarc_min = 0.22A;               vs = Vmax*sin(2*pi*frq*t);

%shaft speed [rpm]              %pre-allocation (comp. time)
n = 4000rpm;                    i_m = zeros(1,length(t));
omega = 2*pi*rpm/60;            i_nu1 = zeros(1,length(t));
dth = omega*dt;                 i_nu2 = zeros(1,length(t));
                                i_nu3 = zeros(1,length(t));
                                i_nu4 = zeros(1,length(t));
```

The simulation was set up in a way that the instantaneous currents of the coils undergoing commutation are written consecutively in pre-allocated vectors. This explains the jumps from $-i_m/2$ to $i_m/2$ (at positive i_m, at negative i_m the jump is in opposite direction) in the simulation graphs. One coil finishes commutation and the next one starts at $i_m/2$. In the simulated time waveforms the influence of the commutating coils on each other as well as the signature of the commutation in the main current i_m can be seen. To observe the influence of commutation in the main current however, one needs to zoom in considerably (see Fig. 8.5).
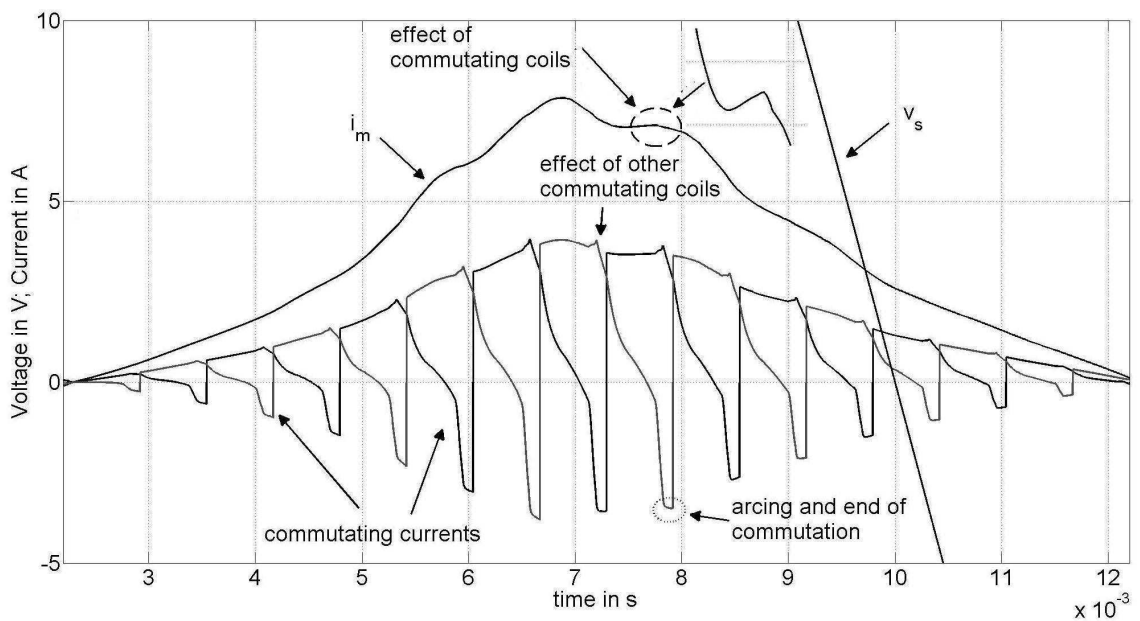
Fig. 8.5 Simulated currents at positive half cycle of i_m

163

Moreover, the arcing phase can be observed as well zooming into the commutating current waveform of a coil (see Fig. 8.6). It can be seen that after the instant of separation (if the ignition conditions are met) the current progression is exponential rather than linear which could be expected with regard to the investigations carried out in chapter 5.
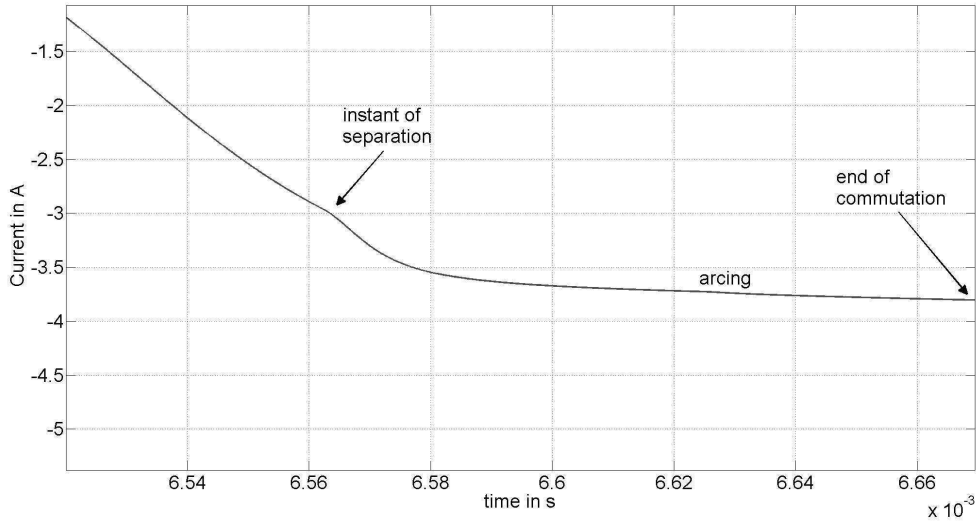
Fig. 8.6 Arcing phase

The simulated and the measured motor main currents are compared in Fig. 8.7.
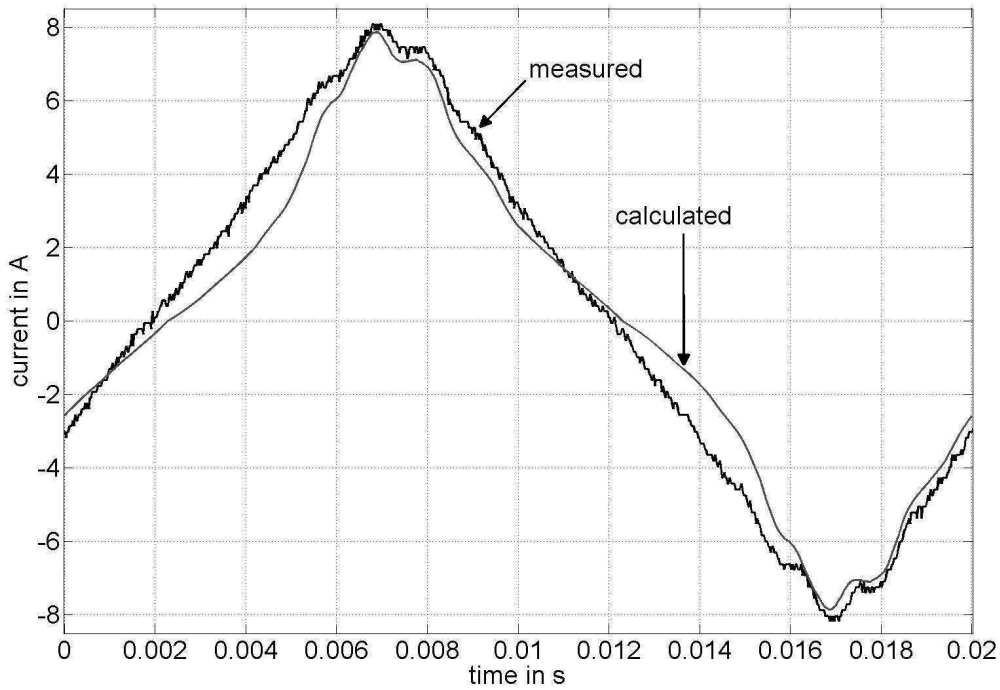
Fig. 8.7 Comparison of simulated and measured motor current

Good agreement of simulated and measured current can be observed. The slotting effect is clearly visible around the peak values of the current. The saturation effect seems a bit stronger in the simulated current. This is due to the fact that the steel data of a standard motor lamination steel [55] was used rather than data of the actual lamination steel of the machine used in the measurements which seems to cause less curvature in the current rise towards the peak value.

However, the most critical quantities in the simulation are the commutating currents and it is essential to examine whether they have been determined reasonably precisely. The main current i_m is not suitable for this examination as the signature of the commutation in i_m is very small (see Fig. 8.5) and the measured current contains a considerable amount of noise (see Fig. 8.7) which practically prevents any meaningful comparison at the small-scale commutation signature. Also, direct measurement of the commutating currents is not taken into consideration. As explained in chapter 5 the space does not allow costly slip ring arrangements, moreover, direct measurement requires interference with the commutating circuits which is likely to distort the results.

As a quantity in order to compare commutation in simulation and measurement the voltage across the field winding is taken into account. The field voltage is often emphasised as a quantity suitable to evaluate commutation quality [16], [21], [22], [56], [62].

To compare the calculated and measured field voltage, the simulated field voltage was found as follows

$$v_F = R_F i_m + \left[L_F + M_{FA} + \frac{\partial (L_F + M_{FA})}{\partial i_m} i_m \right] \frac{di_m}{dt} + \sum_k M_{Fk} \frac{di_k}{dt} \tag{231}$$

where the rotational voltage induced in the field winding is neglected, and the measured field voltage was recorded using a digital oscilloscope. Subsequently, the measured and calculated field voltages were filtered using a bandpass consisting of a 3rd order Butterworth high pass filter and a 3rd order Butterworth low pass filter [63] to minimise the components in the signal that are not of commutation frequency $m \cdot f_c$ ($m = \{1, 2, 3, 4\}$). The filtered signals calculated and measured at a shaft speed of 4000 rpm can be seen in Fig. 8.8.
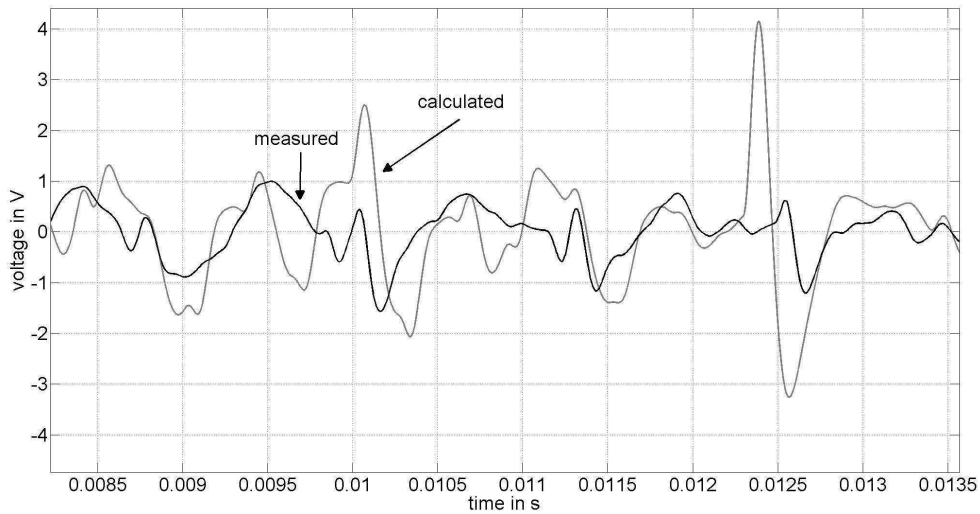
Fig. 8.8 Calculated and measured field voltage after filtering at 4000 rpm

Even though the agreement of the two signals is not ideal, the calculated curve follows the measured curve in tendency. Generally, the calculated values seem to be too high, particularly at some salient voltage pulses. This could be due to the fact that eddy current damping is not considered in the calculations. At a rapid flux variation in the motor due to a commutation event the induced eddy currents may be significant and damp out a considerable part of the flux variations so that the reaction of the field winding is lower than it would be without the eddy currents.

Moreover, the state of wear of the contact members changes during the measurements and other mechanical effects such as changing brush pressure and sightly displaced brushes which are not considered in the calculations might cause these differences between test data and simulation results.

However, the tendency of the calculated values to follow the measured values is promising that the electromagnetic behaviour of the machine including the complex problem of brush commutation could be simulated reasonably well, despite all the simplifications introduced in the mathematical and circuit analysis.

Chapter 09

9 Conclusions

In this thesis theoretical and experimental investigations on the commutation of uncompensated single phase universal motors are outlined that have been carried out in order to get a better insight into the problem of current reversal in these machines. The factors affecting the commutation are of electromagnetic, mechanical, chemical and thermal nature. However, this thesis focuses on the electromagnetic behaviour of the machine with regard to commutation analysis including the sliding contact comprising the commutator and the carbon brushes. It is expected that a successful mathematical model of the commutation of the universal machine can be established if mathematical approaches for the most critical aspects of brush commutation can be identified, that model the physics of the machine with satisfactory precision and that ideally can be tested separately before putting them together in an overall simulation model of the commutation of the universal machine. The discussion confines itself to motors with full sine wave excitation.

Therefore, at the beginning relevant literature was reviewed in order to establish a sound base of knowledge as a starting point of the research. This included classical text books dealing with the commutation of large or medium sized DC or AC commutator machines and more recent publications presenting mathematical models of the commutation of universal motors. In the text books classical analytical approaches have been taken in order to analyze commutation mathematically where simplifications were introduced that hold for large or medium sized machines. In recent scientific articles about the subject more modern approaches can be found using numerical field calculations and coupled magnetic field - and electrical circuit transient solvers. The accuracy improvements obtained by these methods permit the application of those methods to commutation analysis in small uncompensated single phase universal motors where the simplifications introduced for larger machines tend to be too coarse. In the literature review the most critical aspects of commutation modeling could be identified which are the motor inductances, the brush resistance, the commutation arc and the interaction of the commutating coils with other motor coils.

Based on the knowledge acquired in the literature review investigations were carried out whether or not the use of inductances calculated by numerical methods, essentially FEA, is justified in the mathematical analysis of commutation. Inductances are commonly used in the analysis of commutation and represent the capability of a coil to built up a magnetic field that opposes any change in flux that links the coil and therefore are important indicators of how strongly the current reversal is affected by currents in other coils. Moreover, the inductances depend on the magnetic circuit, *i.e.* the cross section geometry of the motor and the position of the rotor, and the state of saturation of the steel. Hence, the inductances reveal how the coupling of the coils changes with rotor position, modifications of the motor geometry and the choice of steel. A selection of important inductances is calculated using FEA and compared to inductances calculated analytically and measured in order to verify the application of numerical magnetostatic field analysis. It is demonstrated that, for unsaturated universal machines, analytical calculations of self and mutual inductances of salient pole machines are an important comparative method in order to verify the use of FEA in motor analysis. The agreement of the analytical calculations and FEA is satisfying and the correction for end winding leakage does not seem to be necessary in the FE-calculated inductances. Moreover, in the analytical equations the influence of certain geometry parameters is highlighted which, despite the limitations with regard to magnetic saturation and slotting effects, makes the analytical calculation an essential tool in motor analysis.

Furthermore, measurement techniques are applied to verify the mathematical analysis. It is shown that with the method proposed in [31] good accuracy can be achieved whereas a simple AC method proves to be inadequate for electrical machine inductances. With regard to a machine simulation model FEA was found capable of dealing with variations of the machine inductances with rotor position and motor current. Hence, FEA is applied to calculate the machine inductances in the overall simulation model.

Another important subject to look into is the brush resistance and the brush to bar contact constriction and film resistance as it is essential in the mathematical analysis of commutation. Although other authors already presented approaches in order to include the brush resistance in the commutation analysis that are quite practical, in this thesis a more rigorous method using resistor networks is developed . The highly nonlinear contact resistance between the brush and the commutator bar taken from experimental work provides reliable data in support of this method. The resistor networks proposed are considerably different from the networks

established by other authors. They are established for both a three-resistor case and a six-resistor case. It is shown that the brush body resistances are influenced by anisotropy and radial brush height. The anisotropy has a stronger effect on the resistances in transversal direction than on the resistances in orthogonal direction with respect to the commutator. Moreover, it could be observed that the influence of the radial brush height has significant influence on the resistances in orthogonal direction whereas its influence on the resistances in transversal direction seems negligible. In a simplified application example commutation transients are shown as well as the influence of the brush body resistances on the progression of the commutating currents. The commutation was fastest with increased transverse resistances by factor 20 and increased orthogonal resistance by factor 5 within the examined range. The progression of the calculated currents shows that the brush resistance is a critical quantity in commutation analysis and the model was included into the full simulation model of the machine.

A complete commutation analysis also contains the analysis of the arcing phase at the conclusion of sub-optimal commutation. Therefore the parameters and currents in the commutating coil and the commutation arc due to a non - zero current difference at contact separation are discussed and used in a mathematical analysis of the arcing phase. The analysis is strictly carried out from a circuit point of view. The different time intervals after contact separation are analysed theoretically and mathematical expressions for the build up of the critical voltage drop across the inter-segment capacity and the progression of current in the commutating coil and the arc current are derived. Certain simplifications have to be applied that were adopted after an extensive literature review on the subject. It is shown that, taking into account the inter-segment and parasitic coil capacitance, the theoretical voltage rise time to a typical arc ignition voltage is less than a nanosecond. The inter-segment and parasitic coil capacitance is neglected in the mathematical analysis of the arcing phase and it was found that, taking the brush resistance into account, the arc current as well as the current in the commutating coil during arcing decrease exponentially towards their designated values. Equations for arc energy and arc duration are derived that reveal the strong dependency of both quantities on brush resistance, coil resistance, effective coil inductance and the difference of armature branch current and the coil current at separation. The mathematical analysis is based on the assumption of a constant arc voltage adopted from reviewed literature. Moreover, a

simplified measurement technique is proposed in order to verify the theoretical analysis. Even though the technique is limited to the arcing phase the results suggest that the equations established model the commutation arc reasonably precisely and thus can be applied in an overall motor simulation model including commutation.

Furthermore, as the commutation causes high rates of changes of flux in the magnetic circuit of the motor the interaction of the commutating coils as well their interaction with the field winding is of interest as the time needed to reverse a current in a rotor coil in machine will be affected by the interaction of coils. Several publications by other authors show graphs of either calculated or measured commutating currents that react strongly on the beginning or the conclusion of the commutation of other rotor coils. The analysis of the influence of the field winding is often reduced to the transformer voltage and the damping effect is only rarely mentioned. In this thesis several different approaches have been taken to investigate the interaction of the commutating coils and the influence of the damping current in the field winding on the coils undergoing rapid current changes.

In theoretical investigations it was found that a damping current in the field winding, calculated to provide ideal damping, forces all the flux of a single armature coil to leakage paths and therefore cancels out any mutual flux between the armature coil and the field winding.

Moreover, an oscillating circuit was used to determine the coil inductances with and without the presence of an active field winding. Capacitors were discharged through certain rotor coils and the periodic time and the logarithmic decrement of the decaying current oscillation were used to determine the inductance. The inductances measured in the presence of an active field winding were significantly lower than the inductances measured with the field winding left open circuit.

Furthermore, the same circuit was used to observe the effect of coils undergoing a high rate of change of current on each other. The effect (accelerating or braking) is significantly higher if the sides of the coils are located in the same pair of slots. Also the effect of the field winding on the intensity of the rotor coil interaction was found to be significant as the mutual and self inductances are decreased.

Subsequently rotational tests were carried out where the machine was driven by another motor and armature and field circuit were kept separate. A DC current was fed through the armature circuit and the FFT spectrum of the field voltage was evaluated for different circuitries

connected to the field winding. The open circuit case served as a reference and was compared to the cases field winding short circuited, standard and long power cord connected to the field winding, inductor connected to the field winding, and a combination of inductor and standard power cord connected to the field winding. The field damping was almost ideal in the cases of plain short circuit of the field winding and standard and long cable connected to the field winding whereas the damping was reduced significantly in the test involving the inductor.

For the simulation model of the machine the following deductions can be made from the analysis mentioned above. The use of inductances calculated using FEA is justified as found from comparisons with measurements and analytical calculations. Moreover, the end-winding leakage can be neglected as it only accounts for a very small percentage of the full inductance. Moreover, the brush resistance is a significant element of the commutating circuits and therefore needs to be considered in the simulation. The commutation arc can be modelled by a constant voltage where a mean value for anodic and cathodic brushes of 14V gives reasonably precise results, and the motor line current should not be kept constant during a commutation event in a full simulation model as damping currents in the field winding need to be considered that change the *di/dt* in the commutating coils significantly. Therefore, the simulation model needs to be voltage-driven.

The simulation model proposed uses precalculated inductances (PC-FEA) as well as precalculated brush resistances. These precalculated quantities are used in a transient circuit solver for three different cases. The first of the analysed cases is each of the two brushes making contact with two commutator bars and therefore one coil is undergoing commutation under each brush. Subsequently, after the transition to the case of each of the two brushes is making contact with three commutator bars, *i.e.* two coils are undergoing commutation under each brush, the circuit to be analysed needs to be extended. Then, if at the next transition back to the case of a brush making contact with two commutator bars the ignition conditions of the arc are met a circuit including a constant arc voltage drop is analysed.

The algorithm comprises significant simplifications such as perfect symmetry at both brushes and both branches of the armature winding. The system of all coil voltage equations is established and solved numerically using Euler's method. The brush circuits established in this thesis are used to represent the brush in the simulation and all internal brush voltage drops are found using nodal voltage analysis.

To verify the calculated time waveforms tests have been carried out using a motor test bench that has been built that allows to measure the motor performance according to the principle of the reaction dynamometer. The load machine is mounted on air bearings to minimize possible torque errors in the measurements. The speed is measured using the built in speed sensor comprising a ferrite ring and a hall sensor. The noisy voltage signal of that sensor is transformed into a series of voltage pulses and evaluated by a FCIV controller in order to find the speed. The simulated and measured motor currents show good agreement, and as a quantity in order to compare commutation in simulation and measurement the voltage across the field winding was taken into account. The measured and simulated signals were filtered and compared. Even though the agreement of the two signals is not found to be ideal, the calculated curve follows the measured curve in tendency which is promising that the electromagnetic behaviour of the machine, including the complex problem of brush commutation, could be simulated reasonably well, despite all the simplifications introduced in the mathematical and circuit analysis.

The model proves to give a reasonably good prediction of the steady state motor performance like the models for example presented in [64], [65] and [66].

It can be concluded that a successful model of the machine, including the commutation process, could be established, based on the calculation of the machine inductances, the brush resistance, the commutation arc and the consideration of coil interactions. These critical aspects were modelled and tested separately before combining them to an overall simulation model.

In future work the model can be developed further in order to achieve better agreement between measured and calculated field voltage. The field voltage is used as an indicator, that the simulation of the commutation gives a good prediction of the actual commutation quality in the machine. Possible ways to improve the model are a finer resolution in the precalculated brush resistances and inductances *i.e.* the angular steps and current steps in the pre-calculation can be refined. Also a more detailed analysis of the brush contact resistance [67] possibly by taking the state of wear of brush and commutator [68] into account could improve the accuracy in the commutation analysis. Another way of improving the model is the inclusion of a detailed eddy current model [69] in the simulation to account for eddy current damping at high rates of changes of motor flux due to commutation. A model with improved accuracy can then be used to predict the quality of the commutation of a new machine design and help

the machine designer to increase brush life [70], [71], [72] and decrease electrical (RFI) [73] and audible [74] noise emitted by the machine.

Moreover, as the model is voltage-driven, in future work it can be used to simulate the machine supplied by power electronics [75], [76], [77], [78] and the influence of the shape of the supply voltage on commutation can be observed.

Appendix A1 - Winding Diagram of Armature Lap Winding

```
Lap Winding:
Throw = 5
Coil sides per
layer = 2
Coil sides per
slot = 4
Number of rotor
slots = 12
Number of
brushes = 2
Number of
parallel arm.
branches = 2

Created using
PC - WFC
Winding Editor
```
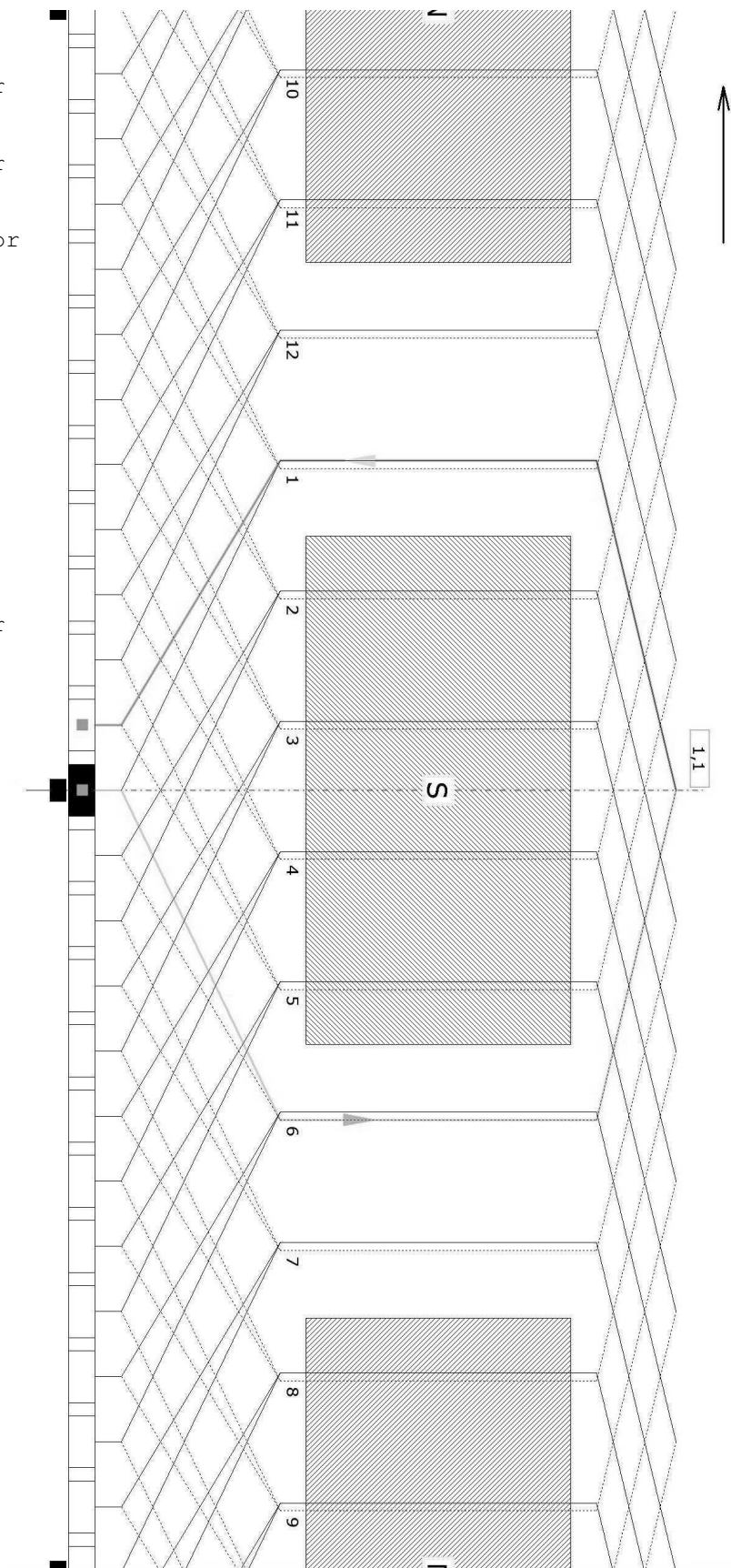

Fig. A1.1 Winding diagram

Appendix A2 - Check of Numerical Algorithm against Analytical Solution

To check the numerical calculation five test cases have been established which have also been treated analytically. Different Dirichlet boundary conditions were set on the edges of the brush in every test case as depicted in Fig. A2.1. Moreover seven random points were selected to compare the analytical and numerical results for a brush with the height b = 10mm and the width a = 5mm. The position of those points can be seen in Fig. A.2.2
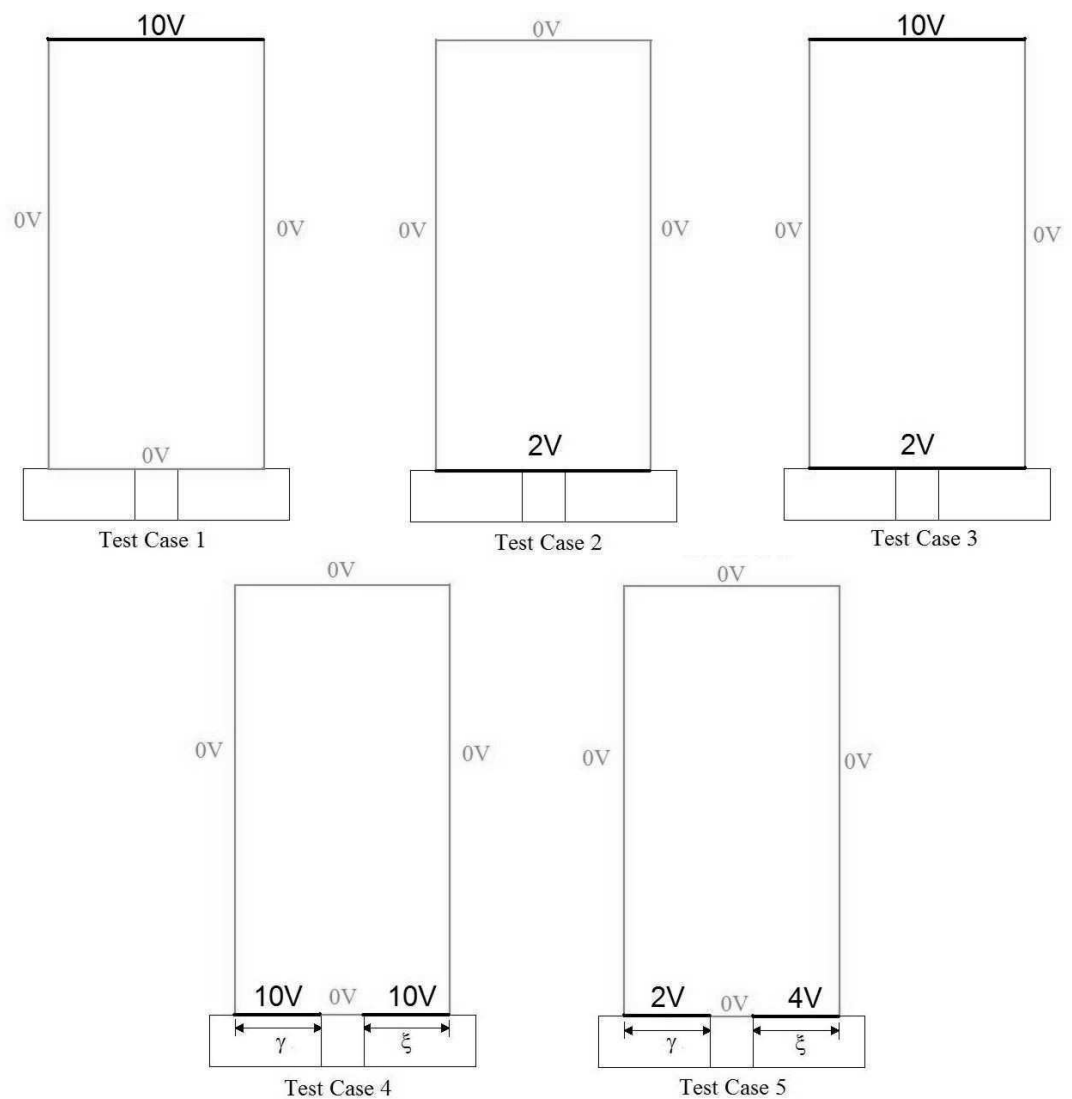
Fig. A2.1 Test cases
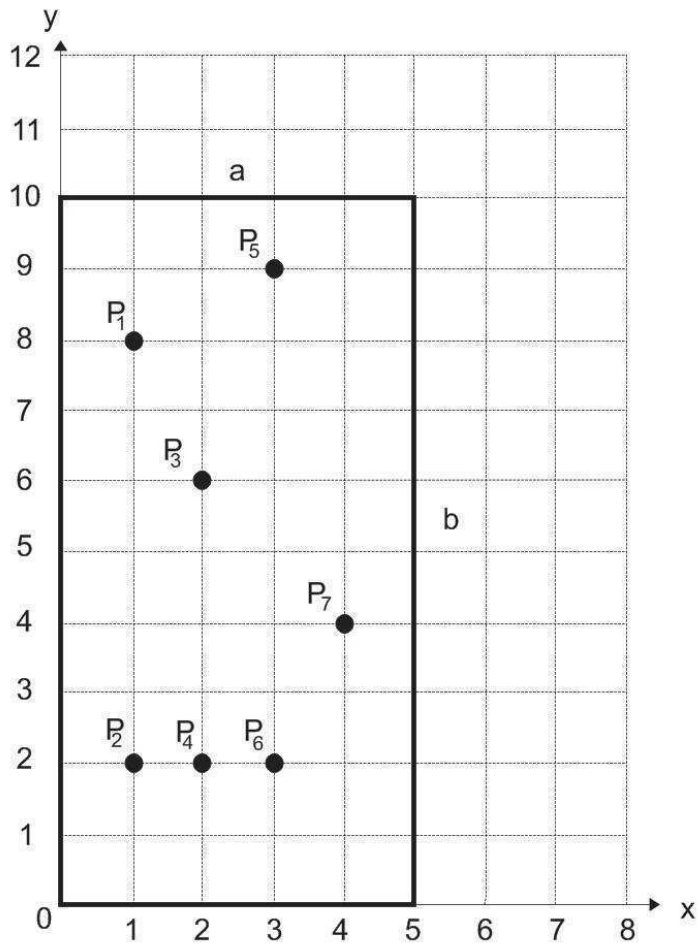
Fig. A2.2 Test points

■   General analytical solution of Laplace's equation (71):

Separation gives

$$\varphi(x,y) \ = \ X(x)\,Y(y) \tag{A2.1}$$

which yields

$$\frac{1}{X}\,\frac{\partial^2 X}{\partial x^2} \ = \ -\,\frac{1}{Y}\,\frac{\partial^2 Y}{\partial y^2} \tag{A2.2}$$

where both sides of (A2.2) must be equal to a constant. For convenience this constant is chosen to be m^2. Hence one obtains

$$\frac{\partial^2 X}{\partial x^2} - m^2 X = 0 \tag{A2.3}$$

and

$$\frac{\partial^2 Y}{\partial y^2} + m^2 Y = 0 \tag{A2.4}$$

with the solutions for X

$$X = A\cos(mx) + B\sin(mx) \tag{A2.5}$$

and Y

$$Y = Ce^{my} + De^{-my} \tag{A2.6}$$

The general solution of (71) can now be written as a linear combination of all particular solutions with the separation parameter m as follows

$$\varphi(x,y) = \sum_{m=1}^{\infty} (A_m\cos(mx) + B_m\sin(mx))\cdot(C_m e^{my} + D_m e^{-my}) \tag{A2.7}$$

■   Test case 1

Boundary conditions: From Fig. A2.1 it can be seen that

$$\varphi(0,y) = A(Ce^{my} + De^{-my}) = 0 \tag{A2.8}$$

which indicates that $A = 0$.

Moreover,

$$\varphi(a,y) = B\sin(ma)\cdot(Ce^{my} + De^{-my}) = 0 \tag{A2.9}$$

requires that $m = \alpha\pi / a$.

The third condition is

$$\varphi(x,0) = B\sin\left[\frac{\alpha\pi}{a}x\right]\cdot(C + D) = 0 \qquad\text{(A2.10)}$$

where $C = -D$ can be found directly.

Now, (A2.7) becomes

$$\varphi(x,y) = \sum_{\alpha=1}^{\infty} K_\alpha \sin\left[\frac{\alpha\pi}{a}x\right]\cdot\sinh\left[\frac{\alpha\pi}{a}y\right] \qquad\text{(A2.11)}$$

where $K_\alpha = 2B_\alpha C_\alpha$.

There is still one boundary condition that has to be taken into account.

$$\varphi(x,b) = \sum_{\alpha=1}^{\infty} K_\alpha \sin\left[\frac{\alpha\pi}{a}x\right]\cdot\sinh\left[\frac{\alpha\pi}{a}b\right] = 10\,V \qquad\text{(A2.12)}$$

If we write (A2.12) as

$$\sum_{\alpha=1}^{\infty} K_\alpha \sin\left[\frac{\alpha\pi}{a}x\right] = \frac{10\,V}{\sinh\left[\frac{\alpha\pi}{a}b\right]} \qquad\text{(A2.13)}$$

then K_α can be found as the coefficients of the Fourier sine series for the constant term on the right side of (A2.13) follows

$$K_\alpha = \frac{2}{a}\int_0^a \frac{10\,V}{\sinh\left[\frac{\alpha\pi}{a}b\right]}\cdot\sin\left[\frac{\alpha\pi}{a}x\right]dx = \frac{2\cdot10\,V}{\sinh\left[\frac{\alpha\pi}{a}b\right]}\cdot\frac{1 - (-1)^\alpha}{\alpha\pi} \qquad\text{(A2.14)}$$

The analytical solution for test case 1 is therefore (A2.11) with K_α calculated from (A2.14). The numerically and analytically calculated scalar potentials in V can be found in table A2.1.

Table A2.1 Numerical vs Analytical Results Test Case 1

Test Point	analytical	numerical solution / grid points			
		36	171	741	3081
P1	2.220	2.286	2.243	2.228	2.224
P2	0.045	0.051	0.047	0.045	0.045
P3	0.979	1.021	0.990	0.982	0.980
P4	0.073	0.082	0.075	0.074	0.073
P5	6.090	5.981	6.057	6.082	6.088
P6	0.073	0.082	0.075	0.074	0.073
P7	0.171	0.187	0.175	0.172	0.172

From table A2.1 it can be seen that the scalar potentials (in V) converge to the analytical result with a rising number of grid points. Good results can be obtained even with a relatively small number of points.

■   Test case 2

Boundary conditions: Analogously to test case 1, $A = 0$ and $m = \alpha\pi / a$. This time the potential on the top of the brush is set to 0. Hence

$$\varphi(x,b) = B\sin\left[\frac{\alpha\pi}{a}x\right]\cdot(Ce^{\frac{\alpha\pi}{a}b} + De^{-\frac{\alpha\pi}{a}b}) = 0 \qquad (A2.15)$$

and therefore $D = -Ce^{\,2b\alpha\pi / a}$. The general solution for test case 2 is

$$\varphi(x,y) = \sum_{\alpha=1}^{\infty} K_\alpha \sin\left[\frac{\alpha\pi}{a}x\right]\cdot(e^{\frac{\alpha\pi}{a}y} - e^{\frac{\alpha\pi}{a}(2b-y)}) \qquad (A2.16)$$

where K_α can be obtained using the last boundary condition *i.e.*

$$\varphi(x,0) = \sum_{\alpha=1}^{\infty} K_\alpha \sin\left[\frac{\alpha\pi}{a}x\right]\cdot(1 - e^{\frac{\alpha\pi}{a}2b}) = 2V \qquad (A2.17)$$

hence

$$K_\alpha \ = \ \frac{2}{a} \int_0^a \frac{2V}{1 - e^{\frac{\alpha\pi}{a}2b}} \cdot \sin\left[\frac{\alpha\pi}{a}x\right] dx \ = \ \frac{2\cdot 2V}{1 - e^{\frac{\alpha\pi}{a}2b}} \cdot \frac{1 - (-1)^\alpha}{\alpha\pi} \cdot$$ (A2.18)

The results can be found in table A2.2.

Table A2.2 Numerical vs Analytical results Test Case 2

Test Point	analytical	numerical solution / grid points			
		36	171	741	3081
P1	0.009	0.010	0.009	0.009	0.009
P2	0.445	0.457	0.449	0.446	0.445
P3	0.055	0.060	0.057	0.056	0.056
P4	0.678	0.676	0.677	0.678	0.678
P5	0.006	0.007	0.006	0.006	0.006
P6	0.678	0.676	0.677	0.678	0.678
P7	0.122	0.128	0.123	0.122	0.122

The convergence in test case 2 is similar as in test case 1.

■   Test case 3

Boundary conditions:

A problem like this (see Fig. A2.1) can be solved by superposition *i.e.* the result is the sum of the solution for test case 1 and test case 2.

Hence, the analytical solution is

$$\varphi(x,y) \ = \ \sum_{\alpha=1}^{\infty} \sin\left[\frac{\alpha\pi}{a}x\right]\left\{K_{\alpha 1}\sinh(\frac{\alpha\pi}{a}y) \ + \ K_{\alpha 2}(e^{\frac{\alpha\pi}{a}y} \ - \ e^{\frac{\alpha\pi}{a}(2b-y)})\right\}$$ (A2.19)

where $K_{\alpha 1}$ is taken from (A2.14) and $K_{\alpha 2}$ is taken from (A2.18). The results can be found in table A2.3.

Table A2.3 Numerical vs Analytical Results Test Case 3

Test Point	analytical	numerical solution / grid points			
		36	171	741	3081
P1	2.232	2.296	2.252	2.237	2.233
P2	0.490	0.508	0.495	0.491	0.490
P3	1.034	1.081	1.047	1.038	1.035
P4	0.751	0.758	0.752	0.751	0.751
P5	6.097	5.988	6.063	6.088	6.095
P6	0.758	0.758	0.752	0.751	0.751
P7	0.293	0.315	0.299	0.294	0.293

In general the numerical results agree well with the analytical results. Only point P6 shows a deviating behaviour; for a very low number of points the analytical and numerical result are identical but the numerical result converges to a smaller value with an increasing number of grid points. Nevertheless the error of 0.9 % at point P6 is still reasonable.

■   Test case 4

Boundary conditions: Similar to test case 2 $A = 0$, $m = \alpha\pi / a$ and $D = -Ce^{2b\alpha\pi/a}$. In addition $(x,0) = g(x)$, where

$$g(x) = \begin{cases} 10V & 0 \leq x \leq \gamma \\ 0 & \gamma < x < a - \xi \\ 10V & a - \xi \leq x \leq a \end{cases} \tag{A2.20}$$

which can also be expressed as a Fourier series as follows

$$g(x) = \frac{2 \cdot 10V(\gamma + \xi)}{a} + \sum_{n=1}^{\infty} \frac{2 \cdot 10V}{n\pi}\left[\sin(\frac{n\pi}{a}\gamma) - \sin(\frac{n\pi}{a}(a - \xi))\right] \cdot \cos(\frac{n\pi}{a}x) \tag{A2.21}$$

Again, K_α in (A2.16) has to be determined by using a Fourier sine series

$$K_\alpha = \frac{2}{a(1 - e^{\frac{\alpha\pi}{a}2b})} \int_0^a g(x) \cdot \sin\left[\frac{\alpha\pi}{a}x\right]dx$$

$$= \left\{\frac{2 \cdot 10V(\gamma + \xi)}{a} \cdot \frac{1 - (-1)^\alpha}{\alpha\pi} + \sum_{n=1}^{\infty} \frac{2 \cdot 10V}{n\pi}\left[\sin(\frac{n\pi}{a}\gamma) - \sin(\frac{n\pi}{a}(a - \xi))\right]\right. \tag{A2.22}$$

$$\left. \cdot \left[\frac{1 - \cos(\pi(\alpha + n))}{\pi(\alpha + n)} + \frac{1 - \cos(\pi(\alpha - n))}{\pi(\alpha - n)}\right]\right\} \cdot \frac{1}{1 - e^{\frac{\alpha\pi}{a}b}}$$

The results can be found in table A2.4.

Table A2.4 Numerical vs Analytical Results Test Case 4

Test Point	analytical	numerical solution / grid points				
		36	171	741	3081	7021
P1	0.031	0.051	0.039	0.035	0.033	0.032
P2	1.513	2.286	1.959	1.794	1.715	1.689
P3	0.191	0.301	0.239	0.214	0.202	0.199
P4	2.213	3.378	2.807	2.541	2.409	2.366
P5	0.021	0.034	0.026	0.023	0.022	0.022
P6	2.380	3.378	2.807	2.541	2.409	2.366
P7	0.430	0.641	0.521	0.469	0.445	0.438

In table A2.4 most of the test points agree reasonably well with the analytical results. Only the points P2, P4 and P6 seem to converge slower. Those points are located very close to the boundary condition $(x,0) = g(x)$. It is obvious from (A2.16) and (A2.22) that the analytical solution comprises two infinite sums which necessarily become finite in the calculation. Hence, in table 4 two approximations are compared and therefore a maximum error of 10.4 % at 7021 grid points is a reasonable result. It should be pointed out that the numerical calculation (FDM) for this number of grid points is very fast (approx. 1s). Analytical calculations were done using the parameters $\gamma = \xi = 2$.

■   Test case 5

Boundary conditions: Similar to test case 2 $A = 0$, $m = \alpha\pi / a$ and $D = -Ce^{2b\alpha\pi / a}$. In addition $(x,0) = h(x)$, where

$$h(x) = \begin{cases} 2V & 0 \leq x \leq \gamma \\ 0 & \gamma < x < a - \xi \\ 4V & a - \xi \leq x \leq a \end{cases} \tag{A2.23}$$

with the Fourier series

$$h(x) = \frac{2 \cdot (2V \cdot \gamma + 4V \cdot \xi)}{a} + \sum_{n=1}^{\infty} \frac{2}{n\pi} \left[2V \cdot \sin(\frac{n\pi}{a}\gamma) - 4V \cdot \sin(\frac{n\pi}{a}(a - \xi)) \right] \cdot \cos(\frac{n\pi}{a}x) \tag{A2.24}$$

and

$$K_\alpha = \frac{2}{a(1 - e^{\frac{\alpha\pi}{a}2b})} \int_0^a h(x)\cdot\sin\left[\frac{\alpha\pi}{a}x\right]dx = \left\{ \frac{2(2V\cdot\gamma + 4V\cdot\xi)}{a} \cdot \frac{1 - (-1)^\alpha}{\alpha\pi} \right.$$

$$+ \sum_{n=1}^{\infty} \frac{2}{n\pi}\left[2V\cdot\sin(\frac{n\pi}{a}\gamma) - 4V\cdot\sin(\frac{n\pi}{a}(a - \xi))\right] \qquad (A2.25)$$

$$\left.\cdot\left[\frac{1-\cos(\pi(\alpha + n))}{\pi(\alpha + n)} + \frac{1-\cos(\pi(\alpha - n))}{\pi(\alpha - n)}\right]\right\} \cdot \frac{1}{1 - e^{\frac{\alpha\pi}{a}b}} \cdot$$

The results can be found in table A2.5.

Table A2.5 Numerical vs Analytical Results Test Case 5

Test Point	analytical	numerical solution / grid points				
		36	171	741	3081	7021
P1	0.009	0.015	0.012	0.010	0.010	0.010
P2	0.335	0.566	0.486	0.443	0.423	0.416
P3	0.057	0.089	0.071	0.064	0.060	0.059
P4	0.632	0.926	0.778	0.704	0.667	0.655
P5	0.006	0.010	0.008	0.007	0.007	0.007
P6	0.777	1.100	0.906	0.820	0.778	0.764
P7	0.136	0.206	0.165	0.149	0.141	0.139

In this case only point P2 seems to converge very slow. The reasons for this are probably the same ones as in case 4. Again calculations were done using the parameters $\gamma = \xi = 2$.

Appendix A3 - Relationship of external and internal Resistances in Case of 3 Segments in Contact with the Brush

$$R_{01} = \frac{R_u(R_u R_x R_x + R_v R_w R_y + R_v R_x R_y + R_w R_x R_z + R_w R_y R_z + R_x R_y R_z)}{R_u R_v R_x + R_u R_w R_x + R_v R_w R_x + R_u R_w R_y + R_v R_w R_y + R_u R_x R_z + R_v R_x R_z + R_w R_x R_z + R_u R_y R_z + R_v R_y R_z + R_w R_y R_z + R_x R_y R_z} \tag{A3.1}$$

$$R_{02} = \frac{R_v(R_u R_w R_y + R_u R_x R_y + R_w R_x R_z + R_w R_y R_z + R_x R_y R_z)}{R_u R_v R_x + R_u R_w R_x + R_v R_w R_x + R_u R_w R_y + R_v R_w R_y + R_u R_x R_z + R_v R_x R_z + R_w R_x R_z + R_u R_y R_z + R_v R_y R_z + R_w R_y R_z + R_x R_y R_z} \tag{A3.2}$$

$$R_{03} = \frac{R_w(R_u R_x R_x + R_u R_x R_y + R_v R_x R_y + R_u R_y R_z + R_v R_y R_z + R_x R_y R_z)}{R_u R_v R_x + R_u R_w R_x + R_v R_w R_x + R_u R_w R_y + R_v R_w R_y + R_u R_x R_z + R_v R_x R_z + R_w R_x R_z + R_u R_y R_z + R_v R_y R_z} \tag{A3.3}$$

$$R_{12} = \frac{R_x(R_u R_v R_y + R_u R_w R_y + R_v R_w R_y + R_v R_w R_z + R_u R_y R_z + R_v R_y R_z)}{R_u R_v R_x + R_u R_w R_x + R_v R_w R_x + R_u R_w R_y + R_v R_w R_y + R_u R_x R_z + R_v R_x R_z + R_w R_x R_z + R_u R_y R_z + R_v R_y R_z} \tag{A3.4}$$

$$R_{23} = \frac{R_y(R_u R_v R_x + R_u R_w R_x + R_v R_w R_x + R_u R_v R_z + R_u R_w R_z + R_v R_w R_z)}{R_u R_v R_x + R_u R_w R_x + R_v R_w R_x + R_u R_w R_y + R_v R_w R_y + R_u R_x R_z + R_v R_x R_z + R_w R_x R_z + R_u R_y R_z + R_v R_y R_z} \tag{A3.5}$$

$$R_{13} = \frac{R_z(R_u R_v R_x + R_u R_w R_x + R_v R_w R_x + R_u R_v R_y + R_u R_w R_y + R_v R_w R_y)}{R_u R_v R_x + R_u R_w R_x + R_v R_w R_x + R_u R_w R_y + R_v R_w R_y + R_u R_x R_z + R_v R_x R_z + R_w R_x R_z + R_u R_y R_z + R_v R_y R_z} \tag{A3.6}$$

Appendix A4 - Diagram of Speed Sensor Circuit

Speed Sensor Circuit
Ian Young, October 2011
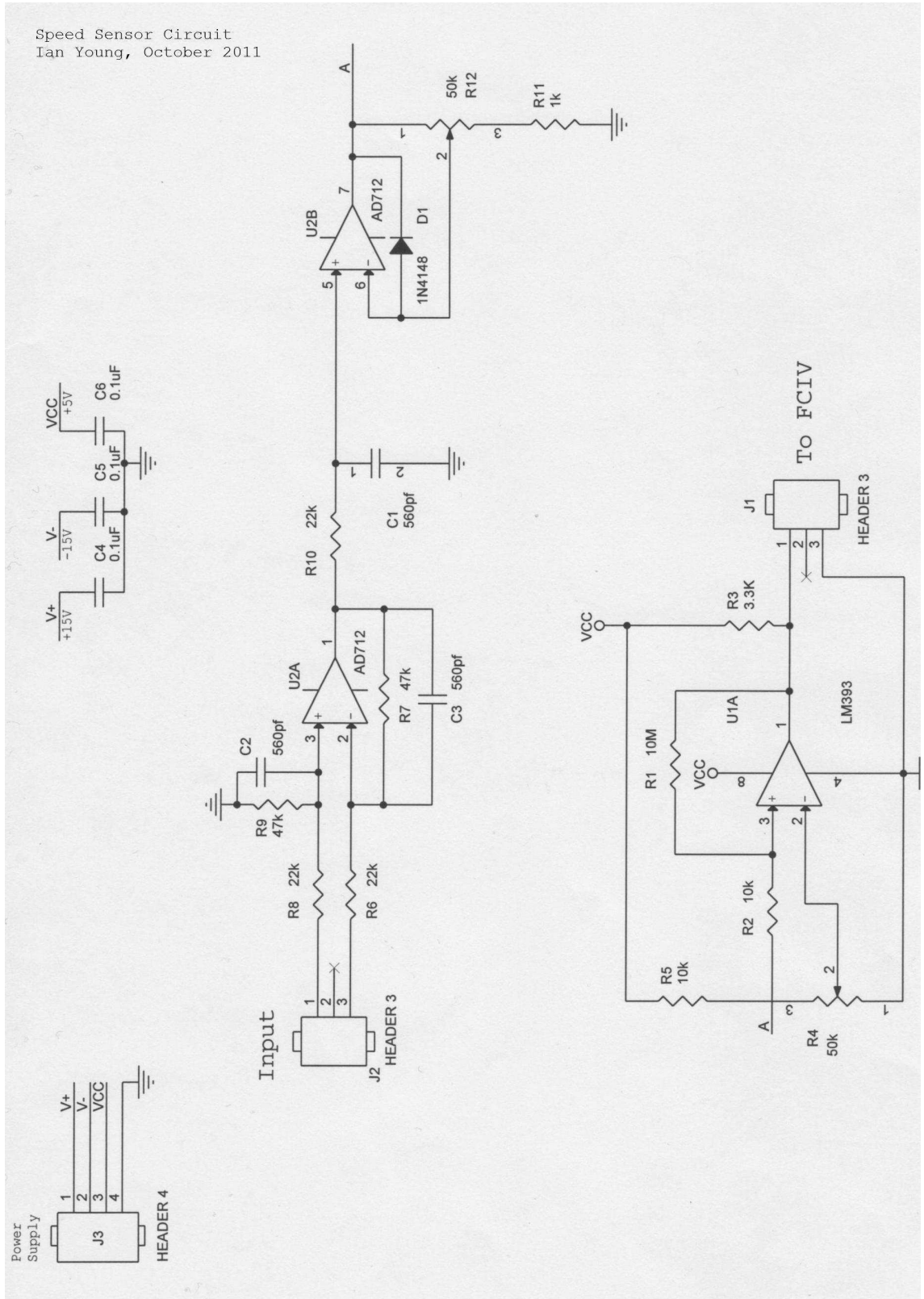
Appendix A5 - Diagrams and Pictures of Oscillating Circuit

```
Coil Driver Circuit
Ian Young, May 2011
```

Setup

Full charge circuit
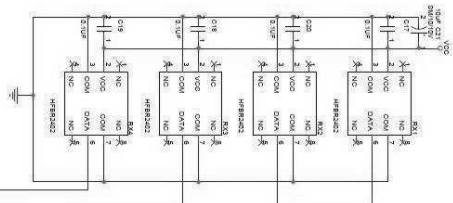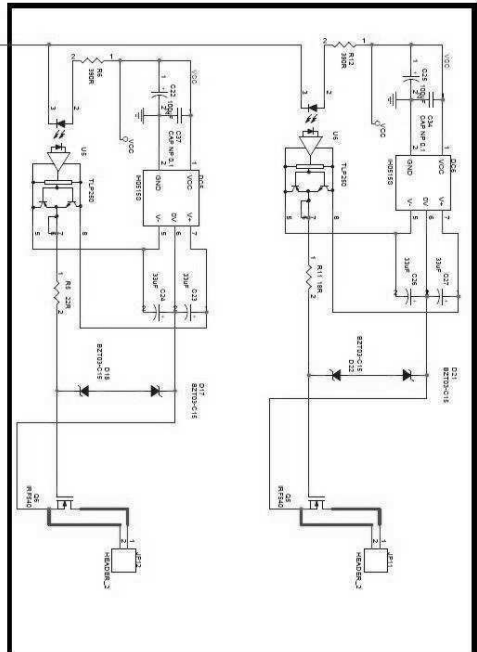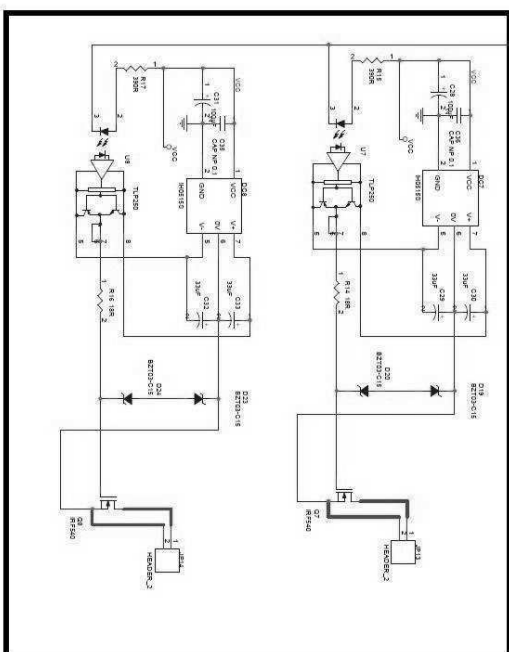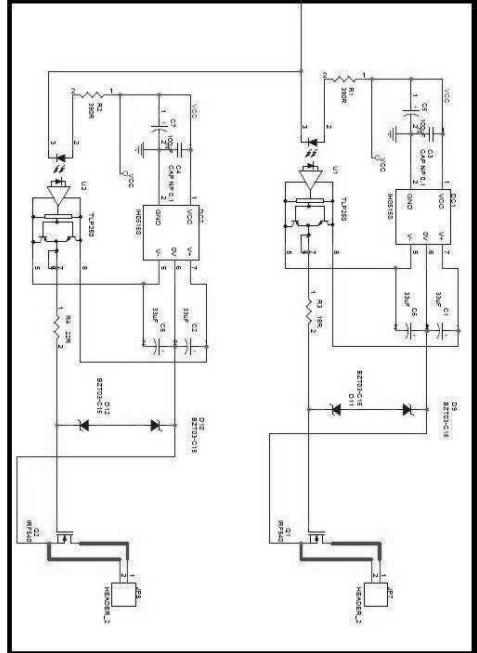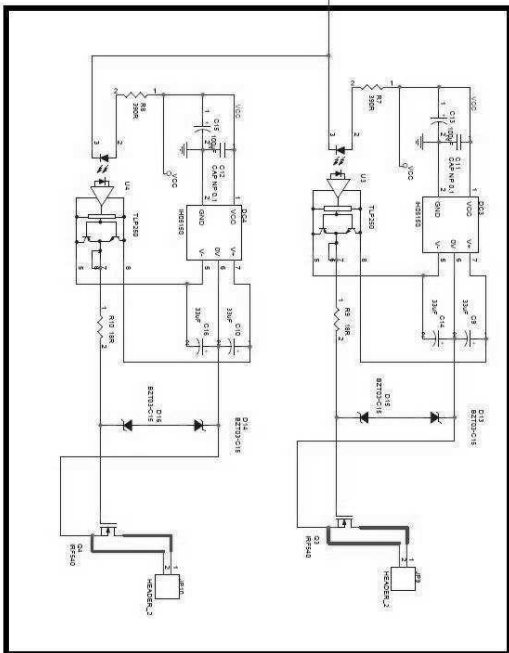
Full discharge circuit
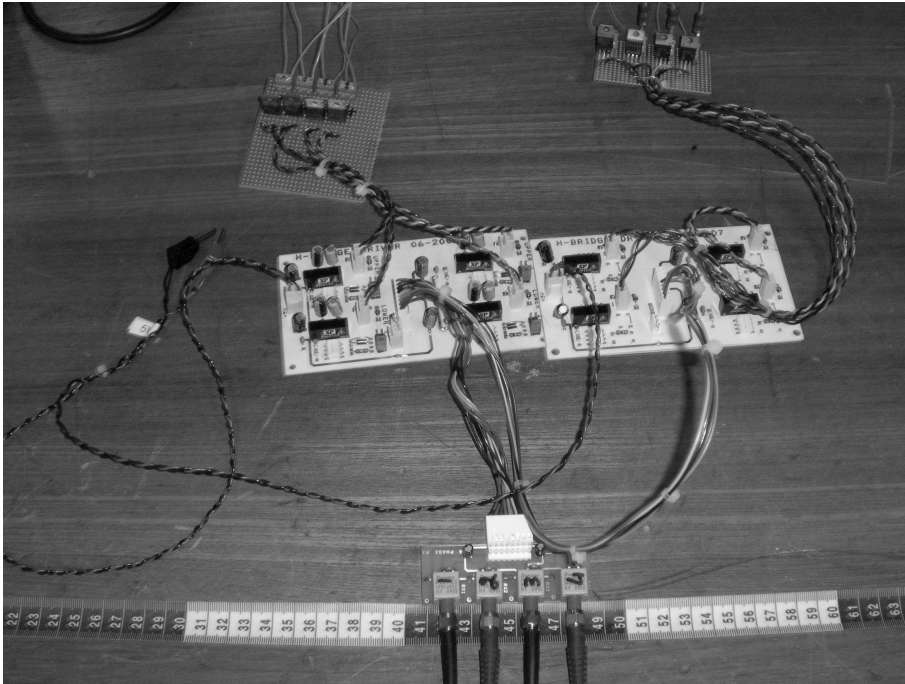
Interface
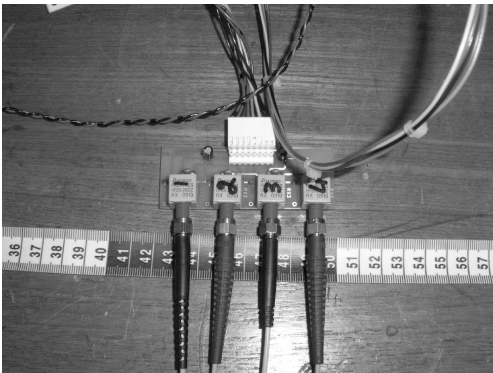
Gate drive circuit
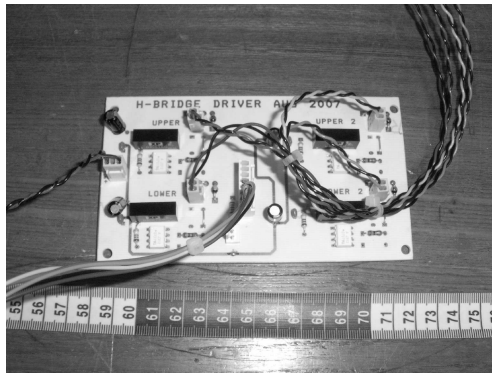
Appendix A6 - Flow Chart of Machine Simulation

START

Initialisation:
n, R_{FA}, R_{v1234},
V_a, I_{min}, v_s, Δt

$\omega = 2\pi n$
$\Delta\theta = \omega\Delta t$

Initial values:
i_m, i_{v1}, i_{v2}

$t = 0$, $\theta = 0$, $n = 1$

Bars in contact with brush = 2 — no

yes

Calculate $\vec{u}_r$ (197)

Calculate $\vec{v}$ (196) $\frac{\theta}{R}$

Pre-calculated brush resistances

Calculate $\vec{u}_\omega$ (198) θ, i_m

Pre-calculated inductances and torques (FEA)

$T_{em}, \partial M_{vp}/\partial\theta$

Calculate [L] (199) θ, i_m

$L, M, \partial L/\partial i_m, \partial M/\partial i_m$

Bars in contact with brush = 3 — no

yes

Calculate $\vec{u}_r$ (211)

Calculate $\vec{v}$ (210) $\frac{\theta}{R}$

Calculate $\vec{u}_\omega$ (212) θ, i_m

$T_{em}, \partial M_{vp}/\partial\theta$

Calculate [L] (213) θ, i_m

Arc ignited — no

yes

Calculate $\vec{u}_r$ (211)

Calculate $\vec{v}$ (210)

Calculate $\vec{u}_\omega$ (212)

Calculate [L] (213)

$\frac{d\vec{i}}{dt} = [L]^{-1}(\vec{v} - \vec{u}_r - \vec{u}_\omega)$

${}^{n+1}\vec{i} = {}^{n}\vec{i} + \frac{{}^{n}d\vec{i}}{dt}\Delta t$

$t = n\Delta t$, $\theta = n\Delta\theta$

$n = n+1$

Arc extinguished — no

yes

$\frac{d\vec{i}}{dt} = [L]^{-1}(\vec{v} - \vec{u}_r - \vec{u}_\omega)$

${}^{n+1}\vec{i} = {}^{n}\vec{i} + \frac{{}^{n}d\vec{i}}{dt}\Delta t$

$t = n\Delta t$, $\theta = n\Delta\theta$

$n = n+1$

Complete AC cycle — no

yes

Converged — no

yes

Invalid condition

END

References

[1]   R. Fischer: Elektrische Maschinen, 12th Edition, Carl Hanser Verlag, 2004

[2]   T. Heidrich: "*Systematisierung des Einsatzbereichs von mechanisch und elektronisch kommutierten Motoren,*" 18. Kleinmaschinenkolloquium, Technical University of Ilmenau, 2010

[3]   R. Goldschmidt: The Alternating Current Commutator Motor, London, "The Electrician," Printing and Publishing Company, Ltd., 1909

[4]   E. Openshaw Taylor: The Performance and Design of A. C. Commutator Motors, London, Sir Isaac Pitman & Sons, Ltd., 1958

[5]   A. E. Clayton: The Performance and Design of Direct Current Machines, London, Sir Isaac Pitman & Sons, Ltd., 1945

[6]   M. Liwschitz-Garik: Direct - Current Machines, D. Van Nostrand Company, Inc. Princeton, New Jersey, 2nd Edition, 1956

[7]   C. C. Hawkins: The Dynamo, Volume II, London, Sir Isaac Pitman & Sons, Ltd., 6th Edition, 1923

[8]   R. Richter: Elektrische Maschinen, Band V, Springer Verlag, 1950

[9]   A. Di Gerlando, R. Perini: "*Model of the Commutation Phenomena in a Universal Motor*," IEEE Transactions on Energy Conversion, Vol. 21, 2006, pp 27-33

[10]   R. H. Wang, R. T. Walter: "*Modelling of Universal Motor Performance and Brush Commutation Using Finite Element Computed Inductance and Resistance Matrices,*" IEEE Transactions on Energy Conversion, Vol. 15, No. 3, 2000, pp 257-263

[11]   R. H. Wang, R. T. Walter: "*Computer Aided Simulation of Performance and Brush Commutation for Universal Motors with Two Coils per Armature Slot,*" Proceedings IEMD , 1999, pp 559-561

[12]   B. Benedičič, F. Pavlovčič, J. Nastran, J. Rejec: "*A Commutator with Integrated Capacitors,*" Informacije MIDEM Vol. 34, No. 1, 2004, pp 43-53

[13]   K. Kurihara, K. Yamamoto, T. Kubota: "*Commutation Analysis of Universal Motors Taking into Account Brush-to-Bar Voltage Drop,*" Transactions ICEMS 2009, Tokyo, Japan

[14]   T. Matsuda, T. Moriyama, N. Konda, Y. Suzuki, Y. Hashimoto: " *Method for analysing the commutation in small universal motors,*" IEE Proceedings on Electric Power Applications, Vol. 142, Issue 2, 1995, pp 123-130

[15]   T. Fujii: "*Study of Universal Motors with Lag Angle Brushes,*" IEEE Transaction on Power Apparatus and Systems, Vol. PAS - 101, Issue 6, 1982, pp 1288-1296

[16]   T. Fujii, T. Hanazawa: "*Commutation of universal motors,*" IEEE Industry Applications Society Annual Meeting, Vol. 1, 1989, pp 265-271

[17]   M. Doppelbauer: "*Oberfeldtheorie zur Berechnung der Kommutierung und des Betriebsverhaltens von Universalmotoren,*" Electrical Engineering 78, 1995, pp 407-416

[18]   D. Roye, M. Poloujadoff: "*Contribution to the Study of Commutation in Small Uncompensated Universal Motors,*" IEEE Transactions on Power Apparatus and Systems, Vol. PAS-97, No.1, 1978, pp 242-250

[19]   K. J. Bradley, W. M. H. Ismail: "*The performance analysis of the single-phase, AC commutator-motor,*" Fifth International Conference on Electrical Machines and Drives, 1991, London, pp 146-150

[20]   Y. Niwa, Y. Akiyama: "*Propositions for the analysis of commutation phenomenon and the modeling of universal motors based on introducing the state function method into FEM electromagnetic field analysis,*" Transactions ECCE 2009, San Jose, pp 226-233

[21]   A. Möckel, D. Oesingmann: "*Die Abbildung der Stromkommutierung von Kommutatorreihenschlussmaschinen in der Erregerspannung,*" GMM-IMM-Fachtagung, 2001, Mainz, pp 14-21

[22]   A. Möckel, D. Oesingmann: "*Die Analyse des Stromwendevorgangs bei wechselspannungsbetriebenen hochtourigen Kommutatormotoren,*" ETG-GMM-Fachtagung, 2004, Darmstadt, pp 89-93

[23]   T.J.E. Miller, M. Willig: "*Calculation of the Armature Inductance of the Universal AC Commutator Motor*," Transactions ICEM 2010, Rome, Italy

[24]   R. Richter: Elektrische Maschinen, Band I, Springer Verlag, 1967

[25]   T.J.E. Miller, M. I. McGilp, D. A. Staton, J. J. Bremner: "*Calculation of inductance in permanent-magnet DC motors,*" IEE Proceedings on Electric Power Applications, Vol.146, No.2, 1999, pp 129-137

[26]   G. Sostmann, U. Walter: "*Beiträge zur Berechnung und experimentellen Untersuchung von Universalmotoren im Hinblick auf die Erstellung eines mathematischen Modells zur Optimierung,*" Research Report, TH Ilmenau, 1970

[27]   R. Retana, A. Paweletz, H.-G. Herzog: "*Analysis and Detection of Short Circuits in Fractional Horsepower Commutator Machines,*" IEEE Transactions on   Energy Conversion, Vol. 23, No. 2, 2008, pp 484-491

[28]   J.R. Hendershot, T.J.E Miller: Design of Brushless Permanent-Magnet Machines, Motor Design Books LLC, USA, 2010

[29]   W. Nürnberg, R. Hanitsch: Die Prüfung elektrischer Maschinen, 7th Edition, Springer-Verlag, 2001

[30]   J. C. Prescott, A. K. El-Kharashi: "*A Method of measuring Self-Inductances applicable to large Electrical Machines,*" Proceedings of the IEE - Part A: Power Engineering , Vol. 106, No. 26, 1959, pp 169-173

[31]   C. V. Jones: "*An Analysis of Commutation for the Unified-Machine Theory,*" Proceedings of the IEE - Part C: Monographs , Vol. 105, No. 8, 1958, pp 476-488

[32]   W. E. Rogers, Introduction to Electric Fields, McGraw-Hill Book Company Inc., 1954

[33]   A. Quarteroni, R. Sacco, F. Saleri: Numerical Mathematics, Springer Berlin Heidelberg, 2007

[34]   H.-J. Bartsch: Handbook of Mathematical Formulas, New York Academic Press, 1974

[35]   K. J. Binns, P. J. Lawrenson, C. W. Trowbridge: The Analytical and Numerical Solution of Electric and Magnetic Fields, John Wiley and Sons Ltd, 1992

[36]   W. Volkmann: Kohlebürsten, Schunk&Ebe GmbH, Gießen, 8th Edition, 1980

[37]   A. Kost: Numerische Methoden in der Berechnung elektromagnetischer Felder, Springer-Verlag, 1994

[38]   J. Stoer, R. Bulirsch: Introduction to Numerical Analysis, Springer-Verlag, 1991

[39]   CIGRE Working Group: "*Practical application of arc physics in circuit breakers. Survey of calculation methods and application guide,*" Electra No. 118, 1988, pp 65-79

[40]   CIGRE Working Group: "*Applications of black box modelling to circuit breakers,*" Electra No. 149, 1993, pp 41-71

[41]   U. Habedank: "*Application of a New Arc Model for the Evaluation of Short - Circuit Breaking Tests*", IEEE Transactions on Power Delivery, Vol.8, No. 4, 1993, pp 1921-1925

[42]   J. L. Guardado, S. G. Maximov, E. Melgoza, J. L. Naredo, P. Moreno: "*An Improved Arc Model Before Current Zero Based on the Combined Mayr and Cassie Arc Models,*" IEEE Transactions on Power Delivery, Vol. 20, No. 1, 2005, pp 138-142

[43]   K. Padmanabhan, A. Srinivasan,: "*Some Aspects in the Phenomenon of Commutator Sparking,*" IEEE Transactions on Power Apparatus and Systems, Vol. 84, No. 5, 1965, pp 396-404

[44]   G. C. R. Sincero, J. Cros, P. Viarouge: "*Arc Models for Simulation of Brush Motor Commutations,*" IEEE Transactions on Magnetics, Vol. 44, No. 6, 2008, pp 1518-1521

[45]   F. Pavločič: "*The Commutator Optimization due to Electrically Caused Wear,*" Transactions ICEM 2010, Rome

[46]   F. Pavločič, J. Nastran: "*Affinity of Contact Materials to form the electric drawn Arcs,*" Informacije MIDEM Vol. 35, No. 3, 2005, pp 148-157

[47]   B. Herzig: "*Charakteristische Kennwerte der Endphase des Kommutierungsvorgangs,*" Elektrie 27, H.12, 1973, pp 662-665

[48]   D. Oesingmann *et al.*: Chapter 2 "*Motors for Continuous Rotation*" in H.-D. Stölting *et al.*: Handbook of Fractional-Horsepower Drives, Springer-Verlag Berlin Heidelberg, 2008

[49]   K. Binder: "*Grenzbedingungen der Lichtbogenbildung bei der Kommutierung,*" ETZ-A, Bd. 81, H. 16, 1960, pp 558-562

[50]   F. L. Jones: The Physics of Electrical Contacts, Oxford University Press, 1957

[51]   Air Bearing Application and Design Guide, New Way Precision, 2003

[52]   AIR BUSHING - METRIC Specifications, New Way air bearings

[53]   REXNORD / BSD Instructions for installation, Service and Maintenance

[54]   A. Tustin, H. Ward: "*The E.M.F.s induced in the Armature Coils of D.C. Machines during Commutation,*" Proceedings of the IEE - Part C: Monographs , Vol.109, No.16, 1962, pp 456-474

[55]   SPEED Laboratory: PC-FEA Version 5.5 User's Manual, Department of Electronics and Electrical Engineering, University of Glasgow, 2008

[56]   D. Oesingmann, R. Schuder, A. Möckel: "*Spannungsanalyse zur Beurteilung der Kommutierungsverhältnisse,*" 43rd International Scientific Colloquium Technical University of Ilmenau, 1998

[57]   K. Röpke: "Statistische und modellgestützte Verfahren zur Klassenbildung bei der Diagnose von Universalmotoren," Doctoral Thesis, Technical University of Berlin, 1997

[58]   C. Gühmann, D. Filbert: *"Fault Diagnosis of Universal Motors by analyzing the Motor Current,"* Transactions UPEC, 1990, pp 695-698

[59]   G. B. Kliman, J. Stein: "*Methods of Motor Current Signature Analysis,*" Electric Machines & Power Systems, 20:5, 1992, pp 463-474

[60]   A. H. Morton: Advanced Electrical Engineering, Pitman &Sons, 1966

[61]   N. L. Schmitz, D. W. Novotny: Introductory Electromechanics, The Ronald Press, 1965

[62]   A. Biebighäuser: *"Neuartiges Verfahren zur Beurteilung der Kommutierung von Gleichstrommaschinen,"* Electrical Engineering, Vol. 78, 1995, pp 175-187

[63]   MathWorks Matlab User Manual, 1984-2009 The MathWorks, Inc.

[64]   R.N. Ebben, J.R. Brauer, G.C. Lizalek, Z.J. Cendes: *"Performance curves of a series DC motor predicted using parametric finite element analysis,"* IEEE Transactions on Magnetics, Vol.35, No.3, pp 1294-1297, 1999

[65]   R.N. Ebben, J.R. Brauer, Z.J. Cendes, N.A. Demerdash: *"Prediction of performance characteristics of a universal motor using parametric finite element analysis,"* Proceedings IEMD '99, pp 192-194, 1999

[66]   A. Di Gerlando, R. Perini, G. Rapi: *"Equivalent circuit for the performance analysis of universal motors,"* IEEE Transactions on Energy Conversion, Vol.19, No.1, pp 18-27, 2004

[67]   M. F. Gómez: "Characterisation and Modelling of Brush Contacts," Doctoral Thesis, University "Helmut Schmidt," Hamburg, 2005

[68]   A. Wilk, I. Moson: *"The wave character of commutator wear in electrical machines,"* Wear, Vol. 253, No. 9, pp 935-945, 2002

[69]   A. A. Rodriguez, A. Valli: Eddy Current Approximation of Maxwell Equations - Theory, algorithms and applications, Springer-Verlag Italia, 2010

[70]   R. Holm, R.M. Bauer, D.F. Emmett, W.E. Yohe: "*Brush Wear During Commutation,*" IEEE Transactions on Power Apparatus and Systems, Vol. PAS-85, No.1, pp 84-88, 1966

[71]   R. J. Hamilton: "*DC motor brush life,*" IEEE Transactions on Industry Applications, Vol.36, No.6, pp 1682- 1687, 2000

[72]   F. Pavlovčič: "*Commutator wear due to drawn arcs,*" Proceedings ICEM, Marseille, pp 1227-1232, 2012

[73]   C.R. Suriano, J.R. Suriano, G. Thiele, T. W. Holmes: "*Prediction of radiated emissions from DC motors,*" IEEE International Symposium on Electromagnetic Compatibility, Vol.2, pp 790-795, 1998

[74]   U. Benko, J. Petrovčič, Đ. Juričić, J. Tavčar, J. Rejec, A. Stefanovska: "*Fault diagnosis of a vacuum cleaner motor by means of sound analysis,*" Journal of Sound and Vibration, Vol. 276, Issues 3–5, pp 781–806, 2004

[75]   Y. Bahout, P. Rault: "*Universal Motor speed Control,*" Transactions Motor-Con, pp 214-227, 1985

[76]   A. Di Gerlando, R. Perini: "*Modelling and Test Validation of High Speed Universal Motors Fed via a Triac,*" 2005 IEEE International Conference on Electric Machines and Drives, pp 1173-1178, 2005

[77]   G. Schröder, J. Bekiesch, H. Siebel: "*AC-fed universal motor with open loop speed control and PFC,*" Transactions IECON '03. Vol.1, pp 705-708 , 2003

[78]   Z. Glowacz, A. Zdrojewski: "*Spectral Analysis of Field and Armature Currents of Commutator DC Motor,*" 51st International Scientific Colloquium, Technical University of Ilmenau, 2006

[79]   T. J. E. Miller: SPEED's Electric Machines - An outline of some theory in the SPEED software for electric machine design, SPEED Laboratory, University of Glasgow, 2009

Publications of the Author

[P1]   Miller, T.J.E.; Willig, M.: "*Calculation of the armature inductance of the universal AC commutator motor*," Electrical Machines (ICEM), 2010 XIX International Conference on , Rome, 6-8 Sept. 2010

[P2]   Willig, M.; Miller, T. J. E.; Corral, I.: "*A brush model for detailed commutation analysis of universal motors*," Electrical Machines (ICEM), 2012 XX International Conference on , pp 1146-1152, Marseille, 2-5 Sept. 2012

[P3]   Willig, M.; Miller, T. J. E.; Corral, I.: "*Influence of Source and Power Cord Impedance on Damping of Flux Variations induced by Commutation in uncompensated Universal Motors*," Electrical and Power Engineering (EPE), 2012 International Conference and Exposition on, pp 391-396, Iasi, 25-27 October, 2012